New constraints on the axion's coupling to nucleons from a Spin Mass Interaction Limiting Experiment (SMILE)

Junyi Lee

A Dissertation
Presented to the Faculty
of Princeton University
in Candidacy for the Degree
of Doctor of Philosophy

Recommended for Acceptance
by the Department of
Physics
Adviser: Professor Michael V. Romalis

June 2019

Abstract

Long range anomalous spin-mass interactions are a generic feature of many theories beyond the Standard Model. They are typically mediated by a light pseudoscalar boson with CP-violating couplings such as an axion or axion-like particle that is the pseudo Nambu-Goldstone boson of some spontaneously broken U(1) symmetry. In this work, we present the results of a Spin-Mass Interaction Limiting Experiment (SMILE) where we search for possible long range spin-mass interactions using a continuously pumped alkali-noble gas co-magnetometer and two 250 kg Pb source masses and report new constraints on $g_s^N g_p^n$, the product of the axion's scalar and pseudoscalar coupling to nucleons and neutrons, that represent an order of magnitude improvement over existing laboratory limits over two decades of axion mass range from $0.01 - 1$ μeV. Slightly improved limits on $g_s^N g_p^e$, the product of the axion's scalar and pseudoscalar coupling to nucleons and electrons are also presented.

Analysis of correlation data and noise spectrums indicate that significant improvement is possible if unforeseen systematic thermal effects correlated to the position of the source masses at the level of 1 mK are controlled and if the low frequency performance of the co-magnetometer is further improved by decreasing optical rotation and pump deflection noise. We discuss various analyses that pinpoint these problems and suggest strategies to overcome them. The dynamics of hybrid pumping used in this work, in which a dense alkali vapor is polarized via spin-exchange collisions with another sparse optically pumped alkali species, and its implication on co-magnetometer operation are also discussed.

Finally, we present simulation and experimental results of a new pulsed alkali-noble gas co-magnetometer in which alkali atoms are optically pumped by short intense laser pulses and anomalous fields are measured during the alkali's decay in the dark. Unlike its continuously pumped counterpart, the pulsed co-magnetometer can potentially suppress noise due to pump beam deflections while retaining suppression of

ordinary magnetic fields. Moreover, it also possesses simultaneous dual axis sensitivity which we demonstrate by measuring the gyroscopic effect from Earth's rotation.

Acknowledgements

This work is the result of many a long day in the dungeons of Jadwin far beyond the reaches of sunlight and lair, it sometimes seem, of innumerable mischievous gremlins. Yet though the days be long, short indeed are the years and ever shall I look back with fondness at my time here in Princeton. I have thoroughly enjoyed working with my adviser Michael Romalis and I am truly grateful for his kind support over all these years. Mike's passion and diligence has been infectious and inspiring, and I am grateful for his many keen physics insights and sense of humor, especially when work is laborious or when things are not working. I am always impressed by the hacks that Mike comes up with that work surprisingly well for what they cost and his hands on approach to taking things apart and improvising has certainly rubbed off on me. I am especially thankful for the latitude he has given me to explore and experiment even if it means making mistakes along the way. The quality of this dissertation would also have been significantly poorer without Mike's careful reading and for that, I am once again grateful. I am in addition indebted to Waseem Bakr and Mariangela Lisanti for agreeing to be on my final public oral examination committee on short notice and for Christopher Tully who readily agreed to be the second reader of this dissertation.

Of course, the work in this thesis would also not have been possible without the help of many others. Nezih Dural, my *kardeş*, helped with various optics related problems and has always been a valuable aid both in and outside of lab. I am sincerely grateful for the delicious bread that he bakes (and gives me), for our conversations about food and music, and for the time he graciously and readily lent me his car when I urgently needed to be somewhere else in a situation so hilariously bad that it would have belonged on a sit-com set. Atta Almasi taught me how to arc weld and helped with various laborious aspects of SMILE, including the lifting of one too many heavy objects. Marc Smiciklas first showed me the ropes in the Romalis lab and Morgan Hedges, Mark Limes, Nathaniel David McDonough, Vito Lucivero,

Wonjae Lee, William Terrano and Jingyao Wang have all contributed to the congenial atmosphere of the Romalis lab. Members of Waseem Bakr's group have also been helpful and kind in lending us various equipment from time to time and I am especially thankful for the friendship of Peter Brown, Debanyan Mitra and Peter Schauss, with whom David and I had a most memorable adventure-filled ski trip in Vermont.

I am also thankful for many others in the physics department outside of the Romalis and Bakr groups. The glass cells used in this work were all expertly fabricated by the famed glassblower Mike Souza. It is always fascinating to watch Mike work and I wished I had more time to learn glassblowing from him. Steven Lowe regaled me with all sorts of interesting stories while I machined large blocks of metals and patiently taught me almost everything I know about machining. I am thankful for his expertise and friendly help/advice in the machine shop without which I would not have been able to machine parts of SMILE with tight exacting tolerances. William (Bill) Dix was a kind grandfatherly figure in the professional machine shop who helped made numerous laborious components for SMILE and welded critical strength bearing components. Glenn Atkinson machined the large drive shaft for SMILE not once but twice and was always helpful, together with Bill, whenever I needed tools that the student shop did not carry. Handy Seldon, Aric Davala, Ralph Searfoss and Matthay Smith in the facilities team were always ready to assist and they installed the drop-in concrete anchors from which the source masses hang. "Uncle Teddy" Ted Lewis helped with metal cutting in the stockroom before Julio Lopez took over and I am thankful for Uncle Teddy's help first in the stockroom and then later in purchasing. Together with Lauren Callahan, Uncle Teddy processed all our purchasing needs promptly and without fuss. Julio Lopez who took over Uncle Teddy's role in the stockroom was always helpful in locating items and in providing spare backup items when the shelves were empty. SMILE required the moving and lifting of heavy objects from time to time and Darryl Johnson and James (Jim) Kukon were friendly

major helps who lent us lifting slings from time to time whenever we needed them. In addition, Jim helped ensure we had liquid helium whenever we needed to pull cells off. I am also thankful for Antonia Sarchi who patiently handled all our administrative needs within the group and for Catherine Brosowsky who was our helpful graduate student administrator. Thomas Hazard and Mallika Randeria were peers in the dungeons to whom I can relate the perils of being stuck under the surface for too long and I am thankful for their friendship.

Outside of the physics department, I am grateful for the many friends, brothers and sisters that I've had the privilege of meeting and living with over these years. Emily (Gilson) Jones and Taylor Russell were faithful companions with whom I cooked and shared many Sunday dinners with in my first year. Jack Kinyon initiated the weekly Saturday breakfast tradition that continues to this very day long after he has left to pursue his dreams of being a professional artist. Together with Peter Kunze, Joshua Kezele, Ben Jones, Ben Reimold and others, we spent many an enjoyable Saturday morning digging into my favorite meal of the day and many a Thursday evening engaging in all manner of banter at the Alchemist and Barrister. And what shall I say of our Saturday evening game/movie nights and of our almost weekly Sunday evening dinners together? Over the years, I have been blessed with many adventures with these dear friends and they never fail to bring a wistful smile back to me. I have many pleasant memories of a road and car camping trip with Jack to Niagara Falls and Lake Placid while Ben Reimold and I had more than our fair share of adventures together. From the eight grueling peaks of the Pemi Loop in the White Mountains of New Hampshire to an unforgettable ski trip in Vermont with David McDonough and Peter Schauss where we dealt with a lost car key, a flat tire and a snow storm, Ben Reimold has been through it all with me. Ben Jones has been another dear brother and housemate with whom I have enjoyed many morning breakfasts, evening dinners, snow fights and, yes, swashbuckling adventures. I am

indebted to his hospitality when I visited him in California where we toured the mountains, beaches and cities of the Golden State, and it was with great pleasure and honor that I stood beside him as his best man when he wedded Emily Gilson at the start of this year. Joshua Kezele has been a devoted friend and brother all these years and I am forever grateful for his loyal friendship when he drove an hour from church on a Sunday morning to help me free an unbelievably rusted rotor that almost seem welded to the brake pads. James (Jimmy) Passaro has been another amazing house mate who introduced me to the world of professional wrestling and with whom I have many fond memories of sharing my life with as we chatted till late into the night and watched the victory of the hobbits over the dark lord Sauron. More recently, I have been blessed with the companionship of my housemates John Tracey, Federico Pasqualotto and Francisco Carrillo who have made my return to the old pad a very sweet one.

During my years here, I have also the privilege of serving alongside many in Stone Hill church in both the youth and mercy ministry. In particular, I have been blessed to have befriended and/or co-labored with Richard Kantzer, Pete and Jackie Johnsen, Becca Gater, Doug Megill, Tracy Troxel, Matt Ristuccia, Robert Tunstall, Rapheal and Michele Surarez, Michael Sentance, Penny Stone, April Clare, Donna Nitchun, Aly Hamilton, Eric Humcke, Ryan and Denise Manheimer, and Abigail Sargent. Over the last few months, I have also been richly blessed by the Stone Hill choir. Words cannot adequately describe my joy in singing and worshiping with them over the last few months. Seldom have I seen a volunteer choir so gifted and I shall sorely miss being in their presence, yet I rejoice and yearn for the day when I shall sing and worship with them anew again. I am grateful for our choir director, Bob Doll, with his infectious joy and love for our Lord Jesus, and for my fellow tenors George Tilton, Bob Henrie and Arthur Harris, as well as other members of the choir, for so warmly welcoming me into the choir over the last few months.

Last but not least, I am indebted to my parents, Yuenmeng and Kimhong Lee, and my sister Ziyi (Lee) Wong who have lovingly watched and prayed for me from afar over all these years. They have ever been self-sacrificially supportive of my pursuits even when it means that I will be far away from them and I am eternally grateful for the love and care they have showered on me all these years. Looking back over all these years, there is truly much to give thanks for, and as every good and perfect gift comes from the Father of lights above, it would be remiss for me to not thank my Father in heaven for all the blessings and people He has put in my life. Though this work be mean compared to His majesty, yet I dedicate it to my Lord Jesus for it is only fitting that I should give of my best to my King who has given His life for me.

Soli Deo gloria

Contents

List of Tables

List of Figures

Chapter 1

Introduction

Despite the many storied successes of the Standard Model in predicting and explaining a diverse range of physical phenomenon, there remains numerous outstanding problems that continue to befuddle our understanding of the universe. Chief among these problems is the longstanding "strong CP problem", which is so named because although quantum chromodynamics (QCD) naturally predicts CP symmetry breaking in a wide variety of strong interactions, yet extensive experimental searches have only found the contrary to date. In particular, due to the non-abelian nature of QCD and its non-trivial vacuum, the QCD Lagrangian possesses a non-vanishing boundary term [1–4]

$$\mathcal{L}_{\theta,QCD} = \bar{\theta}\frac{g^2}{32\pi^2}G_a^{\mu\nu}\tilde{G}_{a\mu\nu} = \bar{\theta}\frac{g^2}{64\pi^2}\epsilon_{\mu\nu\rho\sigma}G_a^{\mu\nu}G_a^{\rho\sigma}, \tag{1.1}$$

where $a = 1, 2 \ldots, 8$ labels the eight gluon fields and $\bar{\theta} = \theta + \arg(\det M)$ here is the sum of the QCD vacuum angle θ and the complex phase of the determinant of the quark mass matrix M. Due to the asymmetric $\epsilon_{\mu\nu\rho\sigma}$ term, (1.1) is manifestly T and P odd. Equivalently, since CPT must be conserved together [5], (1.1) is CP odd. Consequently, we would expect to observe CP symmetry breaking for $\bar{\theta} \neq 0$ and there is no compelling *a priori* reason why $\bar{\theta}$ should vanish. After all, it comprises

of a sum of two unrelated quantities that would make an accidental cancellation a strange peculiarity. Naively, we would therefore expect $\bar{\theta}$ as an angle to be of $\mathcal{O}(1)$.

As noted in [3, 4], a non-zero $\bar{\theta}$ parameter has measurable CP violating consequences. In particular, it should result in a permanent neutron electric dipole moment (nEDM) that has been calculated via QCD sum rules to be about $d_n = 1.2 \times 10^{-16}\,\bar{\theta}$ e cm [6], which implies a naive nEDM of $\sim 1.2 \times 10^{-16}$ e cm if $\bar{\theta}$ is indeed of $\mathcal{O}(1)$. Unfortunately, a nEDM of that magnitude has never been found and this failure is not due to a want of looking. Indeed, the current experimental constraint on the nEDM is $|d_n| < 3.6 \times 10^{-26}$ e cm at a 95% confidence level [7]. In other words, $\bar{\theta}$ is at least 10 orders of magnitude smaller than our naive expectation. Although there is nothing inherently wrong with $\bar{\theta}$ taking on such a small value through an accidental cancellation, its extreme fine-tuning to zero is suggestive of a more elaborate causal mechanism and our current ignorance of this supposed mechanism constitutes the strong CP problem.

One possible solution to the strong CP problem is to postulate that the lightest quark is actually massless since that would imply that that $\bar{\theta}$ has no physical consequences [1]. However, this proposed solution to the strong CP problem has been almost all but ruled out by lattice QCD calculations [8] and experimental data [9]. In 1977, Peccei and Quinn [10, 11] showed that if there exist an additional global U(1) chiral symmetry, and if at least one of the quarks obtains its mass through the Higgs mechanism, then for any value of $\bar{\theta}$, there is an equivalent theory where $\bar{\theta} = 0$ and consequently, $\bar{\theta}$ has no physical consequence and the strong CP problem is thus resolved. More specifically, they noted that if the quarks obtained their mass through the Higgs mechanism, then the quark mass matrix M depends on the vacuum expectation value $\langle\phi\rangle$ of the Higgs fields. However, although θ is arbitrary, $\langle\phi\rangle$ is not. Rather, it is determined by the minimum of a potential $V(\phi)$ that is itself dependent on θ. Peccei and Quinn showed that the transformation required to make the quark

masses real will, together with the fact that M depends on θ through $\langle\phi\rangle$, ensure that $\arg(\det M) = -\theta$ and consequently, that $\bar{\theta} = 0$ as desired.

Shortly thereafter, Weinberg [12] and Wilczek [13] both independently realized that the spontaneous breaking of the postulated Peccei-Quinn U(1) chiral symmetry associated with the appearance of $\langle\phi\rangle$ necessarily implies the creation of a light pseudo-Nambu-Goldstone boson, which Wilczek named the "axion" after the cleaning detergent made by Colgate Palmolive "since they clean up a problem with an axial current" [14]. To correctly implement the the Peccei-Quinn symmetry, Weinberg and Wilczek initially considered a theory (typically called the Peccei-Quinn-Weinberg-Wilczek or PQWW axion) with two Higgs doublets. The PQWW model had interactions related to the electroweak scale that has since been experimentally ruled out [15, 16]. Nevertheless, there remains classes of "invisible" axion models that remain experimentally viable. These models differ from each other in the way they extend the Standard Model to implement the Peccei-Quinn symmetry. For example, in the Dine-Fischler-Srednicki-Zhitnitsky (DFSZ) model, a new complex singlet scalar is added to the PQWW model to enable it to escape the experimental constraints that doomed the original PQWW axion [17, 18] whereas in the Kim-Shifman-Vainshtein-Zakharov (KSVZ) model, the Standard Model is extended with an additional (weak-interaction) singlet quark and an additional singlet complex scalar [19, 20]. Since then, the number of axion models have greatly proliferated to include among others, hadronic axion models [21], "axi-Majorons" [22, 23], "familons" [24, 25] and "flaxions" [26, 27].

Besides these QCD axion models that have been postulated to solve the strong CP problem in QCD, there are also a whole other group of axion-like particles (ALP) that have been hypothesized over the years. Like the axion, these ALPs are light, pseudo-Nambu-Goldstone bosons that are the result of an additional spontaneously broken U(1) symmetry, which is a fairly generic feature of supersymmetric [28], grand-unified [29] and string theories [30–32]. Unlike the QCD axions however, these ALPs

do not necessarily solve the strong CP problem and their masses are typically not related to the strength of their coupling with fermions in the way that QCD axions are.

Although axions were first postulated to solve the strong CP problem, it was realized not long after their invention that they can also potentially solve another growing problem in astrophysics. Observations of galactic rotation curves by the 1980s revealed a serious discrepancy between the measured orbital velocities of stars and the distribution of visible matter in the galaxy [33]. Those observations suggested that there was a significant amount of non-luminous "dark matter", first suggested in [34–36] about half a century ago, around the center of galaxies. More recently, observations of gravitational lensing from galactic clusters have also suggested that the gravitational potential in those clusters were due predominantly to unseen matter and that modifications of the gravitational force law is insufficient to account for the discrepancy [37, 38]. As the evidence for dark matter continued to increase, axions were soon postulated to potentially be a significant fraction of the universe's cold dark matter (CDM) content and conversely, cosmological dark matter densities were used to constrain the axion's decay constant [39–41].

Given the potential of the axion to solve multiple perplexing problems, it is not surprising that there has been numerous experimental attempts to discover them. Obviously, searches for axions must rely on their couplings to known fields. Broadly speaking, experiments looking for axions either rely on their coupling to the electromagnetic field or their interaction with fermions. For example, helioscopes [42, 43], photon-axion-photon "light shining through wall" [44] and microwave cavity [45, 46] experiments all search for the axion through its electromagnetic coupling while mass-mass [47], spin-mass [48–53], spin-spin [54, 55] long-range force experiments and upcoming NMR-type searches [56–58] all rely on the axion's coupling with nucleons and electrons.

In the bulk of this work, we search for anomalous spin-mass interactions that is motivated by the presence of axions or axion-like particles. The spin-mass interaction arises from a pseudoscalar and scalar coupling of the axion to fermions. Following [59], we may understand the pseudoscalar coupling as arising from a combined SU(N)×U(1) chiral transformation intended to keep the phase of the t' Hooft vertex invariant after a Peccei-Quinn transformation to make the masses of the quarks real and minimize the energy of the Higgs field. More specifically, a pure Peccei-Quinn (PQ) transformation causes

$$m_q \to m_q e^{-i\Delta\theta/3} \quad , \quad q_L \to q_L e^{-i\Delta\theta/6} \quad , \quad q_R \to e^{i\Delta\theta/6} q_R, \tag{1.2}$$

so that the Lagrangian

$$\mathcal{L} = m_u \bar{u}_L u_R + m_d \bar{d}_L d_R + m_s \bar{s}_L s_R + \text{h.c}, \tag{1.3}$$

is invariant under a PQ transformation, where m_i is the mass of the i quark and we are explicitly considering the up, down and strange quarks here. However, the phase of the t' Hooft vertex changes as

$$\arg(\prod_q \bar{q}_L q), \tag{1.4}$$

and so a pure PQ transformation causes a shift $\Delta\theta$ of the phase of the t' Hooft vertex although it leaves the quark mass terms invariant. This is energetically unfavorable and the PQ transformation is therefore compensated by a combined SU(3)×U(1) transformation that keeps the phase of the t' Hooft vertex invariant and minimizes the energy. Indeed, a chiral SU(3)×U(1) transformation causes the quark terms to transform as

$$q_R \to e^{i\nu_q/2} q_R \quad , \quad q_L \to e^{-i\nu_q/2}, \tag{1.5}$$

so that for $\sum_q \nu_q = -\Delta\theta$, a chiral SU(3)×U(1) transformation will compensate for the change in the t' Hooft vertex phase after a PQ transformation (1.2) to give

$$\mathcal{L} = \sum_q m_q e^{-i\Delta\theta_q} \bar{q}_L q_R + \text{h.c} \tag{1.6}$$

$$\approx \frac{1}{2}\sum_q m_q(\bar{q}q + \bar{q}\gamma^5 q)(1 - i\Delta\theta_q) + m_q(\bar{q}q - \bar{q}\gamma^5 q)(1 + i\Delta\theta_q), \tag{1.7}$$

where in the second line we have expanded $\exp(i\Delta\theta_q)$ for small $\Delta\theta_q$. Since the quarks are not massless, there is also an energy cost to the SU(3)×U(1) transformation given by

$$E = \sum_q m_q \langle\bar{q}q\rangle \cos(\Delta\theta_q), \tag{1.8}$$

where $\langle\bar{q}q\rangle = v < 0$ is the vacuum expectation value of the quark bilinears. For small $\Delta\theta_q$, we may expand (1.8) and minimize the $\Delta\theta_q$ subject to the constraint $\sum_q \Delta\theta_q = \Delta\theta$ to yield

$$\Delta\theta_u = \frac{m_d m_s \Delta\theta}{m_d m_s + m_d m_u + m_s m_u} \tag{1.9}$$

$$\Delta\theta_d = \frac{m_s m_u \Delta\theta}{m_d m_s + m_d m_u + m_s m_u} \tag{1.10}$$

$$\Delta\theta_s = \frac{m_d m_u \Delta\theta}{m_d m_s + m_d m_u + m_s m_u}. \tag{1.11}$$

Substituting these angles into (1.7), we obtain

$$\mathcal{L} = -i\frac{m_d m_s m_u}{m_d m_s + m_d m_u + m_s m_u}\Delta\theta(\bar{u}\gamma^5 u + \bar{d}\gamma^5 d + \bar{s}\gamma^5 s) + \sum_q m_q \bar{q}q. \tag{1.12}$$

From the properly normalized axion kinetic energy term $F_a^2(\partial\Delta\theta)^2$, where F_a is the scale at which the PQ symmetry is broken, we may identify $\Delta\theta = a/F_a$, where a is

the axion field. The axion's pseudoscalar coupling with quarks is then

$$\mathcal{L}_{int} = -i\frac{m_d m_s m_u}{(m_d m_s + m_d m_u + m_s m_u)F_a} a(\bar{u}\gamma^5 u + \bar{d}\gamma^5 d + \bar{s}\gamma^5 s). \tag{1.13}$$

Using current algebra, the axion's effective pseudoscalar coupling to nucleons can be calculated to give [15]

$$\mathcal{L}_{\text{eff}} = -ia\bar{\psi}_N\gamma^5(g_p^N + g^{(1)}\tau_3)\psi_N, \tag{1.14}$$

where g_p^N and $g^{(1)}$ are the iso-scalar and iso-vector part of the coupling respectively and τ_3 is a Pauli matrix in iso-spin space. As discussed in [15], the iso-scalar part never vanishes for a theory with more than 2 quarks but the iso-vector component can plausibly vanish for a suitable ratio of the Higgs fields' vacuum expectation value. We shall be mainly interested in the ever present iso-scalar component g_p^N. More generally, we may write the CP-conserving effective Lagrangian of the axion with fermions and photons as [60]

$$\begin{aligned}
\mathcal{L}_{\text{eff}} &= -\frac{g_{a\gamma\gamma}}{4} a F_{\mu\nu}\tilde{F}^{\mu\nu} + \frac{C_f}{2F_a}\bar{\psi}_f\gamma^\mu\gamma_5\psi_f\partial_\mu a \\
&= -\frac{g_{a\gamma\gamma}}{4} a F_{\mu\nu}\tilde{F}^{\mu\nu} - \frac{C_f}{2F_a}\partial_\mu\left[\bar{\psi}_f\gamma^\mu\gamma_5\psi_f\right] a \\
&= -\frac{g_{a\gamma\gamma}}{4} a F_{\mu\nu}\tilde{F}^{\mu\nu} - i\frac{m_f C_f}{F_a}\bar{\psi}_f\gamma_5\psi_f a = -\frac{g_{a\gamma\gamma}}{4} a F_{\mu\nu}\tilde{F}^{\mu\nu} - ig_f^p\bar{\psi}_f\gamma_5\psi_f a
\end{aligned} \tag{1.15}$$

where m_f in the last line is the mass of the fermion, $g_f^p \equiv m_f C_f/F_a$ and we have made use of Dirac's equation in going from the second to last line. Since the axion's effective interactions with the photon and fermions depend upon the exact implementation of the PQ symmetry, the coupling coefficients $g_{a\gamma\gamma}$ and g_f^p are generally model dependent. For example, the axion's coupling to photons $g_{a\gamma\gamma}$ is [61, 62]

$$g_{a\gamma\gamma} = \frac{\alpha}{2\pi F_a}\left(\frac{E}{N} - 1.92(4)\right), \tag{1.16}$$

where α is here the fine-structure constant and E, N are the electromagnetic and color anomalies associated with the chiral current of the axion. In the DFSZ model and in any grand unified theory, $E/N = 8/3$ but it can be zero in the KSVZ model if the electric charge of the new singlet quark is taken to be zero [61] or tuned to 2 in hadronic axion models to give a suppressed axion-photon coupling [62]. We note here that the axion's coupling to photons have both a model dependent E/N part and a model independent (1.92) component[1].

Similarly, the axion's pseudoscalar coupling to nucleons g_N^p has both model independent and model dependent parts. A recent QCD lattice calculation gives the axion's pseudoscalar coupling to protons and neutrons as [63]

$$\begin{aligned} C_p = &-0.47(3) + 0.88(3)C_u - 0.39(2)C_d - 0.038(5)C_s \\ &- 0.012(5)C_c - 0.009(2)C_b - 0.0035(4)C_t \end{aligned} \tag{1.17}$$

$$\begin{aligned} C_n = &-0.02(3) - 0.39(2)C_u + 0.88(3)C_d - 0.038(5)C_s \\ &- 0.012(5)C_c - 0.009(2)C_b - 0.0035(4)C_t, \end{aligned} \tag{1.18}$$

where the C_q, $q = u, d, s, c, b, t$ refer to the model dependent quark pseudoscalar coupling with the axion. We note that the model independent part of the neutron's pseudoscalar coupling to axions, -0.02(3), is consistent with zero and therefore, for hadronic axion models with $C_q = 0$, the neutron's pseudoscalar coupling to axions could well vanish although the proton will still have a non-zero pseudoscalar coupling to axions [60]. For the DFSZ model, the quarks' pseudoscalar coupling with the axions are

$$C_u = C_c = C_t = \frac{1}{3}\cos^2\beta \tag{1.19}$$

$$C_d = C_s = C_b = \frac{1}{3}\sin^2\beta, \tag{1.20}$$

[1]This is computed from a ratio of quark masses.

where $\tan\beta = v_u/v_d$ is the ratio of vacuum expectation value v_u of the Higgs field that gives masses to the up type quarks to the vacuum expectation value v_d of the Higgs field that gives masses to the down type quarks [60].

In the KSVZ model, the axion's pseudoscalar coupling to electrons vanishes at tree level although it has a radiatively induced coupling at the one-loop level [61]. On the other hand, in the DFSZ model, the axion's pseudoscalar coupling to electrons is [60, 61]

$$C_e = \frac{\sin^2\beta}{3}, \tag{1.21}$$

where β is as defined in (1.20).

Although the mechanism suggested by Peccei and Quinn to solve the strong CP problem does yield $\bar{\theta} = 0$ in the context of a QCD Lagrangian, CP violating effects from weak interactions can nevertheless cause $\bar{\theta} \neq 0$ in a more complete Lagrangian [10, 11]. These effects have been estimated to be quite small [1, 2] but it is nevertheless possible that $\bar{\theta}$ has a small but non-zero value even with the existence of an axion. If this is true, then the axion will, in addition to the pseudoscalar coupling (1.13), also have scalar couplings to quarks [59]. This scalar coupling may be observed by absorbing the remnant CP violating $\bar{\theta}$ back into the quark mass sector (1.3) via another combined SU(N)×U(1) chiral transformation and minimizing the energy. Performing the minimization and expanding (1.3) as before (with the $\bar{\theta}$ and $\Delta\theta$ transformations), one can show that there are terms proportional to $\Delta\theta\bar{\theta}\bar{q}q = \bar{\theta}a\bar{q}q/F_a$, which give the axion's scalar coupling to quarks. At the nucleon level, we may write an effective scalar coupling of the axion to nucleons as

$$\mathcal{L}_{\text{eff}} = -ig_s^N a\bar{\psi}_N\psi_N. \tag{1.22}$$

Clearly, there is still much uncertainty regarding the axion's coupling to known fields. In this work we experimentally search for the axion's generic scalar and

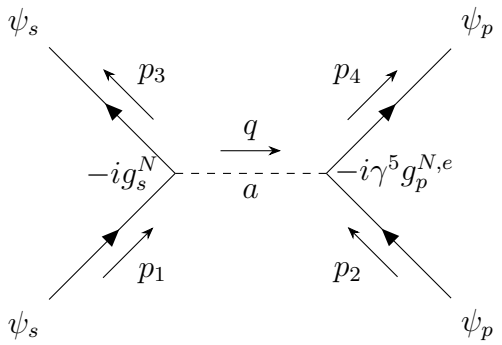

Figure 1.1: Tree level Feynman diagram of an anomalous spin-mass interaction.

pseudoscalar couplings to nucleons and electrons without reference to any particular model. We therefore write the axion's Lagrangian with nucleons and electrons simply as

$$\mathcal{L}_{\text{eff}} = -ig_p^N a\bar{\psi}_N\gamma^5\psi_N - ig_s^N a\bar{\psi}_N\psi_N - ig_p^e a\bar{\psi}_e\gamma^5\psi_e, \tag{1.23}$$

where g_p^N, g_p^e and g_s^N are the axion's pseudoscalar coupling to nucleons, electrons and scalar coupling to nucleons respectively.

At tree level, the interactions in (1.23) give rise to the Feynman diagram in Figure 1.1, where ψ_s, the Dirac particle that couples to the axion with a scalar vertex is a nucleon and ψ_p, the Dirac particle that couples to the axion via a pseudoscalar vertex can be either a nucleon or electron with coupling constants g_p^N, g_p^e respectively. The reduced scattering amplitude of the Feynman diagram in Figure 1.1 is

$$\mathscr{M} = -g_s^N g_p^{N,e}\,\bar{u}^{r'}(p_3)u^r(p_1)\frac{i}{(p_1-p_3)^2 - m_a^2}\bar{u}^{s'}(p_4)\gamma^5 u^s(p_2), \tag{1.24}$$

where m_a is here the mass of the axion. In Dirac's representation, the Dirac spinor for a particle can be generally written as

$$u^s(p) = \sqrt{E+m}\begin{pmatrix} \chi^s \\ \frac{\boldsymbol{\sigma}\cdot\mathbf{p}}{E+m}\chi^s \end{pmatrix} \tag{1.25}$$

$$\approx \sqrt{2m}\begin{pmatrix} \chi^s \\ \frac{\boldsymbol{\sigma}\cdot\mathbf{p}}{2m}\chi^s \end{pmatrix}, \tag{1.26}$$

where in the second line we have made the non-relativistic approximation $m \gg |\mathbf{p}|$. E, m and $\mathbf{p}$ are here the energy, rest mass and 3-momentum of the particle while $\boldsymbol{\sigma}$ are the Pauli matrices and χ^s is a 2-D basis spinor with $s = 0, 1$ for spin up/down. We therefore have in the non-relativistic limit

$$\begin{aligned}\overline{u}^{r'}(p_3)u^r(p_1) &\approx 2m_s\begin{pmatrix}\chi^{\dagger r'} & \chi^{\dagger r'}\frac{\boldsymbol{\sigma}\cdot\mathbf{p_3}}{2m_s}\end{pmatrix}\begin{pmatrix}1 & 0\\ 0 & -1\end{pmatrix}\begin{pmatrix}\chi^r \\ \frac{\boldsymbol{\sigma}\cdot\mathbf{p_1}}{2m_s}\chi^r\end{pmatrix} \\ &= 2m_s\left(\chi^{\dagger r'}\chi^r - \chi^{\dagger r'}\frac{\boldsymbol{\sigma}\cdot\mathbf{p_3}}{2m_s}\frac{\boldsymbol{\sigma}\cdot\mathbf{p_1}}{2m_s}\chi^r\right) \\ &\approx 2m_s\chi^{\dagger r'}\chi^r = 2m_s\delta^{r'r},\end{aligned} \tag{1.27}$$

and

$$\begin{aligned}\overline{u}^{s'}(p_4)\gamma^5 u^s(p_2) &\approx 2m_p\begin{pmatrix}\chi^{\dagger s'} & \chi^{\dagger s'}\frac{\boldsymbol{\sigma}\cdot\mathbf{p_4}}{2m_p}\end{pmatrix}\begin{pmatrix}1 & 0\\ 0 & -1\end{pmatrix}\begin{pmatrix}0 & 1\\ 1 & 0\end{pmatrix}\begin{pmatrix}\chi^s \\ \frac{\boldsymbol{\sigma}\cdot\mathbf{p_2}}{2m_p}\chi^s\end{pmatrix} \\ &= 2m_p\left(\chi^{\dagger s'}\frac{\boldsymbol{\sigma}\cdot\mathbf{p_2}}{2m_p}\chi^s - \chi^{\dagger s'}\frac{\boldsymbol{\sigma}\cdot\mathbf{p_4}}{2m_p}\chi^s\right) \\ &= \chi^{\dagger s'}\boldsymbol{\sigma}\cdot(\mathbf{p_2}-\mathbf{p_4})\chi^s = (\mathbf{p_2}-\mathbf{p_4})\cdot\chi^{\dagger s}\boldsymbol{\sigma}\chi^s \\ &= (\mathbf{p_2}-\mathbf{p_4})\cdot\langle\hat{\boldsymbol{\sigma}}_p\rangle\,,\end{aligned} \tag{1.28}$$

where in the third line we have made use of the fact from (1.27) that for a non-zero amplitude, $r' = r$ and therefore, by conservation of angular momentum, $s' = s$. Also, we note that $\langle\hat{\boldsymbol{\sigma}}_p\rangle$ here is the expectation value of the particle's spin at the

pseudoscalar vertex with unit length since χ^s is normalized and the $\boldsymbol{\sigma}$ operators are unitary. In the CM frame, the reduced scattering amplitude for elastic scattering (space-like momentum transfer $q \equiv p_1 - p_3 = \mathbf{p}_3 - \mathbf{p}_1$) is then

$$\mathscr{M} = -g_s^N g_p^{N,e}\, 2m_s \frac{i}{\mathbf{q}^2 + m_a^2} \mathbf{q} \cdot \langle \hat{\boldsymbol{\sigma}}_p \rangle \,. \tag{1.29}$$

To obtain a non-relativistic potential from the scattering process in Figure 1.1, we may perform the inverse Born approximation by taking the Fourier transform of the reduced scattering amplitude $\mathscr{M}$

$$V(\mathbf{r}) = \int \frac{\mathbf{dq}}{(2\pi)^3} - \frac{g_s^N g_p^{N,e}\, 2m_s}{(2m_s)(2m_p)} \frac{i}{\mathbf{q}^2 + m_a^2} \mathbf{q} \cdot \langle \hat{\boldsymbol{\sigma}}_p \rangle \, e^{i\mathbf{q}\cdot\mathbf{r}}, \tag{1.30}$$

where we have included the additional factors of $2m_s$ and $2m_p$ in the denominator to remove the relativistic normalization in the Dirac spinors. The integral in (1.30) may be evaluated by fixing the angle between $\mathbf{r}$ and $\langle \hat{\boldsymbol{\sigma}}_p \rangle$ before performing the angular integrals. This can be accomplished by, for example, choosing $\mathbf{r}$ to lie along the z-axis and $\langle \hat{\boldsymbol{\sigma}}_p \rangle$ to lie in the x-z plane. Indeed, if θ_0 is the polar angle between $\langle \hat{\boldsymbol{\sigma}}_p \rangle$ and $\mathbf{r}$, then we may write $V(\mathbf{r})$ as

$$\begin{aligned} V(\mathbf{r}) &= -\frac{i g_s^N g_p^{N,e}}{16\pi^3 m_p} \int_0^{2\pi} \int_{-1}^{1} \int_0^{\infty} q^2 d\phi d(\cos\theta) dq \, \frac{1}{q^2 + m_a^2} \\ &\qquad \times (q \sin\theta \cos\phi \sin\theta_0 + q \cos\theta \cos\theta_0) e^{iqr\cos\theta} \\ &= -\frac{i g_s^N g_p^{N,e}}{8\pi^2 m_p} \cos\theta_0 \int_0^{\infty} dq \, \frac{q^3}{q^2 + m_a^2} \frac{1}{iqr} \left[e^{iqr} + e^{-iqr} - \frac{1}{iqr} \left(e^{iqr} - e^{-iqr} \right) \right]. \end{aligned} \tag{1.31}$$

The remaining radial integral may be evaluated using contour integrals as follows

$$\begin{aligned}
&\int_0^\infty dq\, \frac{q^3}{q^2+m_a^2}\frac{1}{iqr}\left[e^{iqr}+e^{-iqr}-\frac{1}{iqr}\left(e^{iqr}-e^{-iqr}\right)\right] \\
&= \frac{1}{ir}\left[\int_0^\infty dq\, \frac{q^2}{q^2+m_a^2}e^{iqr}-\int_0^{-\infty} dq\, \frac{q^2}{q^2+m_a^2}e^{iqr}\right] \\
&\qquad + \frac{1}{r^2}\left[\int_0^\infty dq\, \frac{q}{q^2+m_a^2}e^{iqr}-\int_0^{-\infty} dq\, \frac{q}{q^2+m_a^2}e^{iqr}\right] \\
&= \frac{1}{ir}\int_{-\infty}^\infty dq\, \frac{q^2}{q^2+m_a^2}e^{iqr}+\frac{1}{r^2}\int_{-\infty}^\infty dq\, \frac{q}{q^2+m_a^2}e^{iqr} \\
&= \frac{1}{ir}\oint dq\, \frac{q^2}{q^2+m_a^2}e^{iqr}+\frac{1}{r^2}\oint dq\, \frac{q}{q^2+m_a^2}e^{iqr} \\
&= i\pi\left(\frac{m_a}{r}+\frac{1}{r^2}\right)e^{-m_a r},
\end{aligned} \tag{1.32}$$

where in the second last line the contour for both integral runs along the real line and is closed in the positive $\mathbb{I}\mathrm{m}$ plane, which implies that the residues of the two integrands at $q = im_a$ are given by

$$\lim_{q\to im_a}(q-im_a)\frac{q^2}{q^2+m_a^2}e^{iqr} = \lim_{q\to im_a}(q-im_a)\left(1-\frac{m_a^2}{q^2+m_a^2}\right)e^{iqr} = -\frac{m_a}{2i}e^{-m_a r} \tag{1.33}$$

$$\lim_{q\to im_a}(q-im_a)\frac{q}{q^2+m_a^2}e^{iqr} = \frac{1}{2}e^{-m_a r}. \tag{1.34}$$

Substituting (1.32) back into (1.31) and recognizing that $\cos\theta_0 = \hat{\mathbf{r}}\cdot\langle\hat{\boldsymbol{\sigma}}_p\rangle$, we obtain the non-relativistic anomalous spin-mass potential

$$\begin{aligned}
V(\mathbf{r}) &= \frac{g_s^N g_p^{N,e}}{8\pi m_p}\hat{\mathbf{r}}\cdot\langle\hat{\boldsymbol{\sigma}}_p\rangle\left(\frac{m_a}{r}+\frac{1}{r^2}\right)e^{-m_a r} \\
&= \frac{\hbar^2 g_s^N g_p^{N,e}}{8\pi m_p}\left(\frac{m_a c}{\hbar r}+\frac{1}{r^2}\right)e^{-r m_a c/\hbar}\,\hat{\mathbf{r}}\cdot\langle\hat{\boldsymbol{\sigma}}_p\rangle\,,
\end{aligned} \tag{1.35}$$

where we have restored $\hbar$ and c back in the appropriate places in the second line to obtain a more experimentally useful form. $\mathbf{r}$ here, as the conjugate vector to

$\mathbf{q}$, the 3-momentum transfer from the scalar vertex to the pseudoscalar vertex, is the displacement vector from the particle at the scalar vertex to the particle at the pseudoscalar vertex. We note that any axion or ALP with a non-zero scalar coupling will be capable of mediating the interaction in Figure 1.1 leading to the potential (1.35) between spin unpolarized particles (at the scalar vertex) and spin-polarized particles (at the pseudoscalar vertex). Moreover, a very light spin-1 Z' boson with CP-violating couplings has been shown to be also capable of mediating an interaction of the form (1.35) [64, 65].

For an electron at the pseudoscalar vertex, we can write $\langle \hat{\boldsymbol{\sigma}}_p \rangle = g_s \langle \mathbf{S} \rangle$, where $\mathbf{S}$ is the electron spin operator. In that case, we may from (1.35) define the anomalous electron-coupling field

$$\boldsymbol{\beta}^e = \frac{\hbar^2 g_s^N g_p^e}{8\pi m_p g_s \mu_B} \left(\frac{m_a c}{\hbar r} + \frac{1}{r^2} \right) e^{-r m_a c/\hbar} \, \hat{\mathbf{r}}, \tag{1.36}$$

so that we have $V(\mathbf{r}) = g_s \mu_B \langle \mathbf{S} \rangle \cdot \boldsymbol{\beta}^e$. Similarly, we may define the anomalous neutron-coupling field

$$\boldsymbol{\beta}^n = -\frac{\hbar^2 g_s^N g_p^n K}{8\pi m_p \mu_K} \left(\frac{m_a c}{\hbar r} + \frac{1}{r^2} \right) e^{-r m_a c/\hbar} \, \hat{\mathbf{r}}, \tag{1.37}$$

so that $V(\mathbf{r}) = -\mu_K \langle \mathbf{K} \rangle \cdot \boldsymbol{\beta}^n / K$, where $\mathbf{K}$ is the valence neutron spin operator on a noble gas atom.

In this work, we search for a general anomalous spin-mass interactions of the form in (1.35) between two unpolarized 250 kg Pb source masses and spin-polarized atoms in a K-^{3}He co-magnetometer. Equivalently, we look for anomalous electron and neutron coupling magnetic-like fields of the form (1.36) and (1.37). In chapter 2 we give an overview of the fundamental atomic physics processes relevant to operation of the co-magnetometer including collisions, light-atom interactions, optical pumping and other relaxation mechanisms. We next describe in chapter 3 the behavior of the cou-

pled alkali and noble-gas spin ensembles in the co-magnetometer and detail various features and advantages of using an alkali-noble gas co-magnetometer to search for tiny anomalous magnetic-like spin-mass interactions. Since this work employed hybrid optical pumping, we also describe how such a technique affects co-magnetometer operation. In chapter 4, we report new constraints on $g_p^n g_s^N$, the product of the axion's pseudoscalar and scalar coupling to neutron and nucleons respectively, which represents an order of magnitude improvement over existing laboratory limits over two decades of axion mass range. Slightly improved limits on $g_p^e g_s^N$, the product of the axion's pseudoscalar and scalar coupling to the electron and nucleons respectively, are also presented. Details of the Spin-Mass Interaction Limiting Experiment (SMILE) including various design choices, experimental setup, co-magnetometer characterization, data analysis and systematic effects are all discussed too. Finally, we present work on a new pulsed co-magnetometer in chapter 5 whereby alkali atoms in a co-magnetometer cell are optically pumped by short intense laser pulses. Compared to traditional continuously pumped alkali-noble gas co-magnetometer, the pulsed co-magnetometer has dual-axis sensitivity to anomalous fields and can potentially suppress noise due to pump beam drift, which is a significant source of un-suppressed noise in continuously pumped co-magnetometers. We conclude with an outlook of future precision measurements with alkali-noble gas co-magnetometers.

Chapter 2

Theoretical Background

2.1 Alkali Atoms

Alkali atoms have, owing to their hydrogen-like electronic structure, long been extensively studied. Their relatively low melting points allow experimentalists to generate a vapor of alkali atoms by heating a sample of pure alkali metal above its melting point in an evacuated or inert enviroment. Moreover, a good number of transistions within alkali atoms are today conveniently accessible by commericially available diode lasers, making them even easier than ever to work with.

In this thesis, we work mainly with potassium and rubidium atoms in our alkali-noble gas co-magnetometers, where alkali and noble gas atoms are co-located within the same volume in an aluminosilicate (GE180) glass cell. During operation of the co-magnetometer, the cell is heated in an oven to around 180 - 200 °C to create a dense ($\sim 10^{14}$ cm^{-3}) vapor of alkali atoms. Potassium melts at 63.38 °C and rubidium melts at 39.31 °C [66]. Their respective (gaseous) number densities [67] at temperatures

above their melting points are empirically given by:

$$n_K = \frac{1}{k_B T}\, 10^{3.4077 - 4453/T} \quad \text{cm}^{-3}, \quad 337 < T < 550\, K \tag{2.1}$$

$$n_{Rb} = \frac{133.322}{k_B T}\, 10^{1.193 - 4040/T} \quad \text{cm}^{-3}, \quad 298 < T < 550\, K, \tag{2.2}$$

where T is the temperature in Kelvins and k_B is the Boltzmann constant. In the equations above, we have taken the liberty to convert the vapor pressures given in [67], which have a quoted accuracy of $\pm 5\%$ within the specified temperature range, to number densities in units of cm^{-3} assuming ideal gas behavior. Fig 2.1 below shows the alkali densities over a range of accessible temperatures in a co-magnetometer.

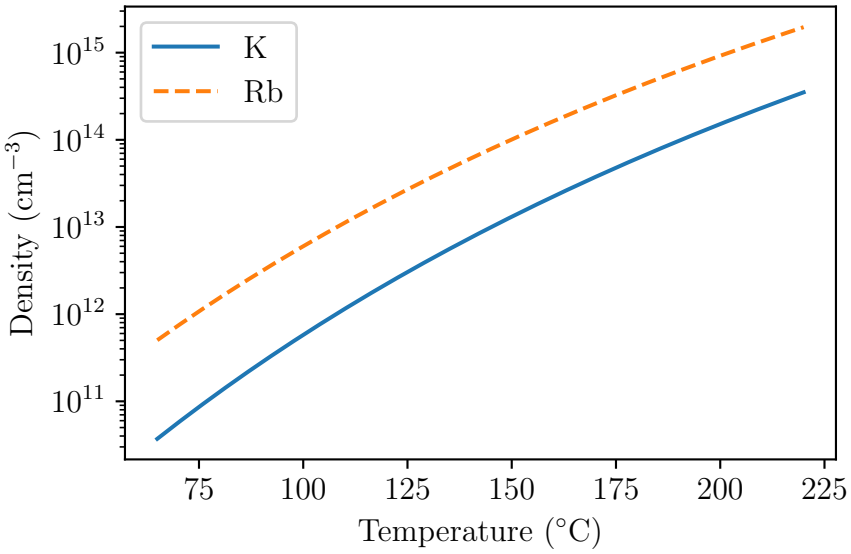

Figure 2.1: Number density of K and Rb as a function of temperature.

We note that in general, the heavier alkali metals have lower melting points due to weaker metallic bonds and that they consequently, as Fig 2.1 demonstrates, also have higher vapor pressures compared to lighter alkali metals. Despite the stated accuracy of these density numbers, we note that the actual alkali number density in a co-magnetometer cell can vary significantly (by a factor of 2 or more) [68, 69] from the measured temperature of the oven since the actual gas temperature of the cell

can, depending on the circumstance, be appreciably higher or lower than the oven's temperature. For example, large poorly insulated windows (or lack thereof) on the oven that provide optical access to the cell can cause significant loss of heat due to black body radiation, resulting in a cell that is colder than the oven. On the other hand, strong optical pumping of the cell can also cause significant self-heating, leading in extreme cases, to a reported 95 °C increase in gas temperature due to a deposition of 22 W of laser power into the cell [70]. The equations above should therefore only be used as a rough guide to estimate the alkali density within the cell. The discrepancy between the oven and cell temperatures can be estimated by performing absorption measurements at lower temperatures.

Alkali atoms have a single, unpaired valence electron in a $^2S_{1/2}$ ground state that is coupled to a non-zero nuclear spin through the hyperfine coupling, which splits the ground state into two energetically distinct hyperfine manifolds. The first two (fine structure) excited states are the $^2P_{1/2}$ and $^2P_{3/2}$ states with orbital angular momentum $L = 1$ and total electronic angular momentum $J = 1/2$ and $J = 3/2$ respectively. These excited fine structure states are further split by the hyperfine interaction into 6 distinct hyperfine manifolds. Application of a magnetic field then breaks the degeneracy of the m_F states within each hyperfine manifold as schematically depicted in Figure 2.2. We note however, that in our high pressure co-magnetometer cells, the collisional broadening due to noble gas atoms is typically so large that the hyperfine structure is not resolved.

The ground state spin Hamiltonian is

$$H_g = A_g \mathbf{I} \cdot \mathbf{S} + g_s \mu_B \mathbf{S} \cdot \mathbf{B} - \frac{\mu_I}{I} \mathbf{I} \cdot \mathbf{B} + g_s \mu_B \mathbf{S} \cdot \boldsymbol{\beta}_e, \tag{2.3}$$

where $\boldsymbol{\beta}_e$ is any possible magnetic-like anomalous field, A_g is the ground state hyperfine coupling constant, g_s is the electron spin g-factor, μ_B is the Bohr magneton,

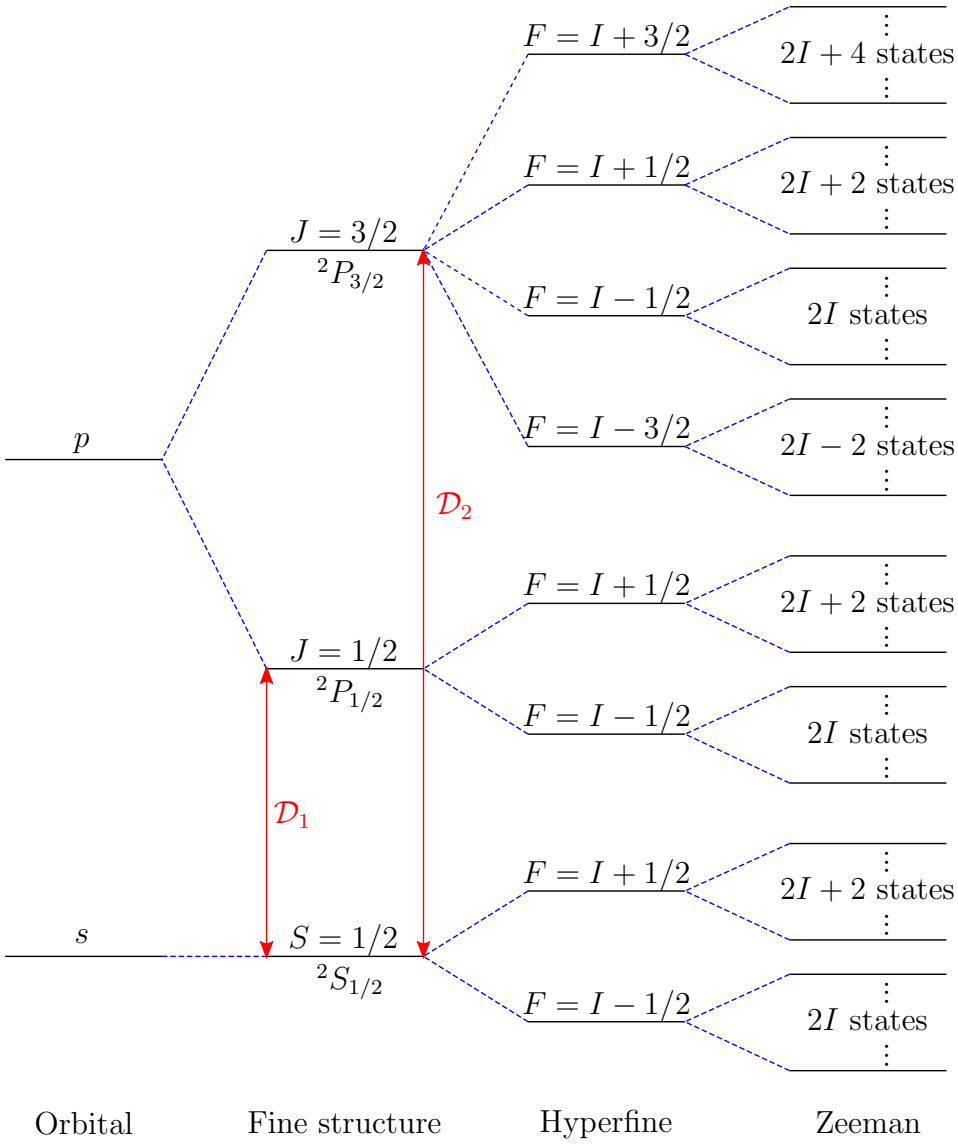

Figure 2.2: Ground and the first two (fine structure) excited states of an alkali atom. The spacing of the energy levels are not drawn to scale.

μ_I is the nuclear dipole moment and I is the nuclear spin. **S** and **I** are the electron and nuclear spin operators respectively while **B** is the magnetic field. The nuclear dipole moment term is typically a factor of ~ 1000 smaller than the Bohr magneton term due to the mass difference between a nucleon and an electron. Consequently, we note that the nuclear dipole term can be considered a small perturbation of the much larger electron dipole term.

In the absence of a magnetic field, the total angular momentum $\mathbf{F}$ is conserved and the $|F, m_F\rangle$ states are eigenstates of the hamiltonian. Indeed, since, $\mathbf{F} = \mathbf{I} + \mathbf{S}$ and $F^2 = \mathbf{F} \cdot \mathbf{F}$, we may re-write the ground state Hamiltonian in the absence of a magnetic field as

$$H_g = \frac{A_g}{2}\left(F^2 - I^2 - S^2\right), \tag{2.4}$$

where $|F, m_F\rangle$ is manifestly an eigenstate of the Hamiltonian. Moreover, since $S = 1/2$, there are two hyperfine manifolds, $F_a = I + 1/2$ and $F_b = I - 1/2$ with different energies although different m_F states within each hyperfine manifold is degenerate. On application of a magnetic field, $\mathbf{F}$, as we will show later, is no longer rigorously conserved and the degeneracy of the m_F states within each hyperfine manifold is broken. In the co-magnetometer, we are (for reasons we shall explain more fully in a later section) primarily concerned with the behavior of the alkali's atom electron spin $\mathbf{S}$. More specifically, our probe beam measures a projection of the expectation value of $\mathbf{S}$, which can be expressed as

$$\begin{aligned}\langle \mathbf{S} \rangle &= \langle \psi \left| \mathbf{S} \right| \psi \rangle \\ &= \sum_{f f' m_f m'_f} \langle f, m_f | \psi \rangle \langle \psi | f', m'_f \rangle \langle f', m'_f \left| \mathbf{S} \right| f, m_f \rangle \, e^{-i\left(\omega_{f,m_f} - \omega_{f',m'_f}\right)t},\end{aligned} \tag{2.5}$$

where we have expanded $|\psi\rangle$ in terms of the $\{|f, m_f\rangle\}$ basis states and we have defined $\omega_{f,m_f} \equiv E_{f,m_f}/\hbar$ where E_{f,m_f} is the energy of the $|f, m_f\rangle$ state. Evidently, $\langle \mathbf{S} \rangle$ precesses at the frequency(ies)[1] $\omega_{f,m_f} - \omega_{f',m'_f}$. To obtain a more explicit result for these frequencies, we shall need to solve (2.3) for E_{f,m_f}. To do so, we note that during typical co-magnetometer operation, the longitudinal magnetic field is typically on the scale of ~ 5 mGs so $g_s \mu_B B_z$ is of order ~ 60 peV. On the other hand, A_g, the

[1] We note that there is a sum of different frequencies if $\omega_{f,m_f} - \omega_{f',m'_f}$ are not the same for different (f,m_f) and (f',m'_f) pairs, as is the case for sufficiently large B fields. In that case, the precession will exhibit beating.

hyperfine coupling constant for ^{41}K[2] is of order $\sim 0.5\ \mu$eV [71] so that under typical co-magnetometer operation, the magnetic field terms in the ground-state hamiltonian is a tiny perturbation compared to the hyperfine coupling. Consequently, we may solve for E_{f,m_f} in (2.3) to second order in $g_s\mu_B B_z$ using degenerate perturbation theory. We begin by making the convenient definitions $\lambda \equiv \mu_B B_z g_s$ and $\alpha \equiv \mu_I/(g_s\mu_B I)$. In the absence of transverse magnetic fields, the ground state Hamiltonian is then

$$H_g = \underbrace{\frac{A_g}{2}\left(F^2 - I^2 - S^2\right)}_{h_0} + \lambda \underbrace{(S_z - \alpha I_z)}_{V}, \tag{2.6}$$

where we have denoted the unperturbed hamiltonian as h_0 and the perturbation as V with a parameter λ that is small compared to $A_g/2$. Since the m_F states within each hyperfine manifold are degenerate, we shall need to find a basis of states in each degenerate subspace such that V is diagonal in each subspace. More precisely, if $|m_i\rangle$ for $i \in [1, d], i \in \mathbb{N}$ is the i^{th} degenerate eigenstate of h_0 such that $P_0 = \sum_i |m_i\rangle \langle m_i|$ is the projector to that degenerate subspace, then we seek a basis of states such that $\lambda P_0 V P_0$ is diagonal in that basis. The matrix elements of V in the $\{|f, m_f\rangle\}$ basis may be computed by expanding $|f, m_f\rangle$ in the uncoupled $|I, m_i\rangle |S, m_s\rangle$ basis states

$$\begin{aligned}
\left\langle f', m'_f \left| S_z - \alpha I_z \right| f, m_f \right\rangle &= \sum_{m_i m_s} \sum_{m'_i m'_s} \langle m'_i m'_s | S_z - \alpha I_z | m_i m_s \rangle \\
&\qquad \times C(ISf'; m'_i m'_s m'_f) C(ISf, m_i m_s m_f) \\
&= \sum_{m_i m_s} \sum_{m'_i m'_s} (m_s - \alpha m_i) \delta_{m'_i, m_i} \delta_{m'_s, m_s} \\
&\qquad \times C(ISf'; m'_i m'_s m'_f) C(ISf, m_i m_s m_f) \\
&= \sum_{m_i m_s} C(ISf'; m_i m_s m'_f) C(ISf; m_i m_s m_f) (m_s - \alpha m_i) \delta_{m_f, m'_f},
\end{aligned} \tag{2.7}$$

[2]The hyperfine coupling for ^{39}K, ^{87}Rb and ^{85}Rb are all even larger.

where in the last line we have made use of the Clebsch-Gordan property (A.55a). The m_f states are therefore automatically diagonal. However, we note that in general, if $f' \neq f$ in the full hamiltonian, then by (2.7), $\langle f', m'_f | S_z - \alpha I_z | f, m_f \rangle$ is non-zero. In other words, V is, as expected, not diagonal in the $\{|f, m_f\rangle\}$ basis so that as mentioned before, F is no longer a good quantum number on application of a magnetic field. Nevertheless, because the m_f states are automatically diagonal, the $\{|f, m_f\rangle\}$ are still diagonal within each hyperfine manifold. Consequently, the basis of states that we seek such that $\lambda P_0 V P_0$ is diagonal within each hyperfind manifold is the $\{|f, m_f\rangle\}$ states themselves. By degenerate perturbation theory, the first order correction to the energy $\Delta E^{(1)}$ is then $\lambda \langle f, m_f | V | f, m_f \rangle$ [72]. Since $S = 1/2$, we may compute this from (2.7) using (A.65) and (A.66). For $F = I + 1/2$, we obtain

$$\begin{aligned} \Delta E^{(1)}_{F=I+1/2} &= \lambda \langle I + {}^1\!/_2, m_F | S_z - \alpha I_z | I + {}^1\!/_2, m_F \rangle \\ &= \frac{B_z m_F}{2I+1} \left(\mu_B g_s - 2\mu_I \right), \end{aligned} \tag{2.8}$$

while for $F = I - 1/2$, we get

$$\begin{aligned} \Delta E^{(1)}_{F=I-1/2} &= \lambda \langle I - {}^1\!/_2, m_F | S_z - \alpha I_z | I - {}^1\!/_2, m_F \rangle \\ &= -\frac{B_z m_F}{2I+1} \left(\mu_B g_s + \frac{2(I+1)}{I} \mu_I \right). \end{aligned} \tag{2.9}$$

From perturbation theory [72], the second-order correction to the energy of states in the $F = I \pm 1/2$ manifold is

$$\begin{aligned} \Delta E^{(2)}_{F=\pm 1/2, m_F} &= \lambda^2 \sum_{m'_F} \frac{\left| \langle I \mp {}^1\!/_2, m'_F | V | I \pm {}^1\!/_2, m_F \rangle \right|^2}{E^{(0)}_{F=I\pm 1/2, m_F} - E^{(0)}_{F=I\mp 1/2, m'_F}} \\ &= \lambda^2 \frac{\left| \langle I \mp {}^1\!/_2, m_F | V | I \pm {}^1\!/_2, m_F \rangle \right|^2}{E^{(0)}_{F=I\pm 1/2, m_F} - E^{(0)}_{F=I\mp 1/2, m_F}}, \end{aligned} \tag{2.10}$$

where in the second line we have made use of the fact from (2.7) that the m_F states are automatically diagonal and $E^{(0)}_{F=I\pm1/2,m_F}$ are the unperturbed energies of the different hyperfine manifolds, which from (2.4) is given by

$$E^{(0)}_{F=I\pm1/2,m_F} = \frac{A_g}{2}\left(\pm I - \frac{1}{2}\left(1 \mp 1\right)\right). \tag{2.11}$$

The off-diagonal matrix-elements may be computed using (A.65) and (A.66) as before. We obtain in this case

$$\lambda \left\langle I - {}^1\!/_2, m_F \left| S_z - \alpha I_z \right| I + {}^1\!/_2, m_F \right\rangle = -\frac{\lambda}{2I+1}\sqrt{\left(I+\frac{1}{2}\right)^2 - m_F^2}\,(1+\alpha)\,. \tag{2.12}$$

The second-order corrections are then

$$\Delta E^{(2)}_{F=I\pm1/2} = \pm\frac{2B_z^2}{\left(2I+1\right)^3 A_g}\left[\left(I+\frac{1}{2}\right)^2 - m_F^2\right]\left(\mu_B g_S + \frac{\mu_I}{I}\right)^2, \tag{2.13}$$

so that the energies of the states in the $F = I \pm 1/2$ hyperfine manifold are (to second-order)

$$\begin{aligned} E_{F=I+1/2,m_F} = {} & \frac{A_g}{2}I + \frac{B_z m_F}{2I+1}\left(\mu_B g_s - 2\mu_I\right) \\ & + \frac{2B_z^2}{\left(2I+1\right)^3 A_g}\left[\left(I+\frac{1}{2}\right)^2 - m_F^2\right]\left(\mu_B g_s + \frac{\mu_I}{I}\right)^2, \end{aligned} \tag{2.14}$$

and

$$\begin{aligned} E_{F=I-1/2,m_F} = {} & -\frac{A_g}{2}\left(I+1\right) - \frac{B_z m_F}{2I+1}\left(\mu_B g_s + \frac{2\left(I+1\right)}{I}\mu_I\right) \\ & - \frac{2B_z^2}{\left(2I+1\right)^3 A_g}\left[\left(I+\frac{1}{2}\right)^2 - m_F^2\right]\left(\mu_B g_s + \frac{\mu_I}{I}\right)^2. \end{aligned} \tag{2.15}$$

Consequently, for $|F, m_F\rangle \rightarrow |F, m_F - 1\rangle$ transitions within the same hyperfine manifold, the resonance frequencies are

$$\omega_{F=I+1/2,\overline{m}} = \frac{B_z}{(2I+1)\hbar}(\mu_B g_s - 2\mu_I) - \frac{4B_z^2\overline{m}}{(2I+1)^3 A_g \hbar}\left(\mu_B g_s + \frac{\mu_I}{I}\right)^2, \tag{2.16}$$

and

$$\omega_{F=I-1/2,\overline{m}} = -\frac{B_z}{(2I+1)\hbar}\left[\mu_B g_s - \frac{2(I+1)}{I}\mu_I\right] + \frac{4B_z^2\overline{m}}{(2I+1)^3 A_g \hbar}\left(\mu_B g_s + \frac{\mu_I}{I}\right)^2, \tag{2.17}$$

where we have followed [73] in defining $\overline{m} \equiv (2m_F - 1)/2$ as the mean azimuthal quantum number of the transition. We note that if μ_I, which is much smaller than μ_B is neglected, then to first order in B_z, the resonance frequencies are given simply by

$$\omega_{F=I\pm1/2,\overline{m}} \approx \pm\frac{\mu_B g_s B_z}{(2I+1)\hbar} = \pm\frac{\gamma_e B_z}{2I+1}, \tag{2.18}$$

where in the last equality $\gamma_e = \mu_B g_s/\hbar$ is the gryomagnetic ratio of the free electron. We therefore see that neglecting the small perturbation of the nuclear dipole moment, states in different hyperfine manifolds precess at the same rate but in opposite directions for a sufficiently small B_z field. This will later turn out to be important in understanding the spin-exchange relaxation free (SERF) regime in which relaxation of the alkali atoms' spins due to spin-exchange collisions is strongly suppressed in the limit of high alkali atom number densitiy and zero magnetic field. Also, we note that the effect of the nuclear spin and the strong hyperfine coupling here is to slow down the precession rate of the free electron by a factor of $2I + 1$. Figure 2.3 shows the energy splitting (2.14), (2.15) over an extended range of B_z values encountered during co-magnetometer operation.

(2.3) describes the Hamiltonian of an alkali atom in an inertial frame. To transform it to a rotating frame with angular velocity $\mathbf{\Omega}$, we may make use of the rotation

operator $R(t) = \exp(-i\mathbf{\Omega}\cdot\mathbf{F}t)$. The transformed Hamiltonian $\tilde{H}$ can be read off from writing

$$\begin{aligned}\tilde{H}R\left|\psi\right\rangle = i\hbar\frac{d}{dt}R\left|\psi\right\rangle &= i\hbar\left(-i\mathbf{\Omega}\cdot\mathbf{F}R\left|\psi\right\rangle + \frac{1}{i\hbar}RH\left|\psi\right\rangle\right) \\ &= \underbrace{\left(\hbar\mathbf{\Omega}\cdot\mathbf{F} + RHR^{-1}\right)}_{\tilde{H}}R\left|\psi\right\rangle, \end{aligned} \tag{2.19}$$

to give

$$\begin{aligned}\tilde{H} &= \hbar\mathbf{\Omega}\cdot\mathbf{F} + e^{i\mathbf{\Omega}\cdot\mathbf{F}t}\left(A_g\mathbf{I}\cdot\mathbf{S} + g_s\mu_B\mathbf{S}\cdot(\mathbf{B}+\boldsymbol{\beta}_e) - \frac{\mu_I}{I}\mathbf{I}\cdot\mathbf{B}\right)e^{-i\mathbf{\Omega}\cdot\mathbf{F}t} \\ &\approx \hbar\mathbf{\Omega}\cdot\mathbf{F} + A_g\mathbf{I}\cdot\mathbf{S} + g_s\mu_B\mathbf{S}\cdot(\mathbf{B}+\boldsymbol{\beta}_e) - \frac{\mu_I}{I}\mathbf{I}\cdot\mathbf{B} \\ &\approx \hbar\mathbf{\Omega}\cdot\mathbf{F} + A_g\mathbf{I}\cdot\mathbf{S} + g_s\mu_B\mathbf{S}\cdot(\mathbf{B}+\boldsymbol{\beta}_e), \end{aligned} \tag{2.20}$$

where in the second line we have approximated $\exp^{\pm i\mathbf{\Omega}\cdot\mathbf{F}t} \approx 1$, since the coherence time of the ground state Hamiltonian is so short in between collisions with other atoms that the argument $\mathbf{\Omega}\cdot\mathbf{F}t \approx 0$. Also, since μ_I is, as explained above, about a 1000 times smaller than μ_B, we have dropped it in the last line of (2.20) which we shall frequently use as the approximate ground-state Hamiltonian of the alkali atom.

As will be described in greater detail later, alkali atoms in this thesis are optically pumped via the $\mathcal{D}_1(^2S_{1/2} \rightarrow {}^2P_{1/2})$ transition. While in the excited state, the alkali atom evolves under a hamiltonian that is, ignoring the anomalous field, analogous to the ground state hamiltonian:

$$H_e = A_e\mathbf{I}\cdot\mathbf{J} + g_J\mu_B\mathbf{J}\cdot\mathbf{B} - \frac{\mu_I}{I}\mathbf{I}\cdot\mathbf{B}, \tag{2.21}$$

where A_e is now the hyperfine coupling of the excited state, g_J is the Landé g-factor and $\mathbf{J} = \mathbf{S} + \mathbf{L}$ is the total electronic angular momentum operator.

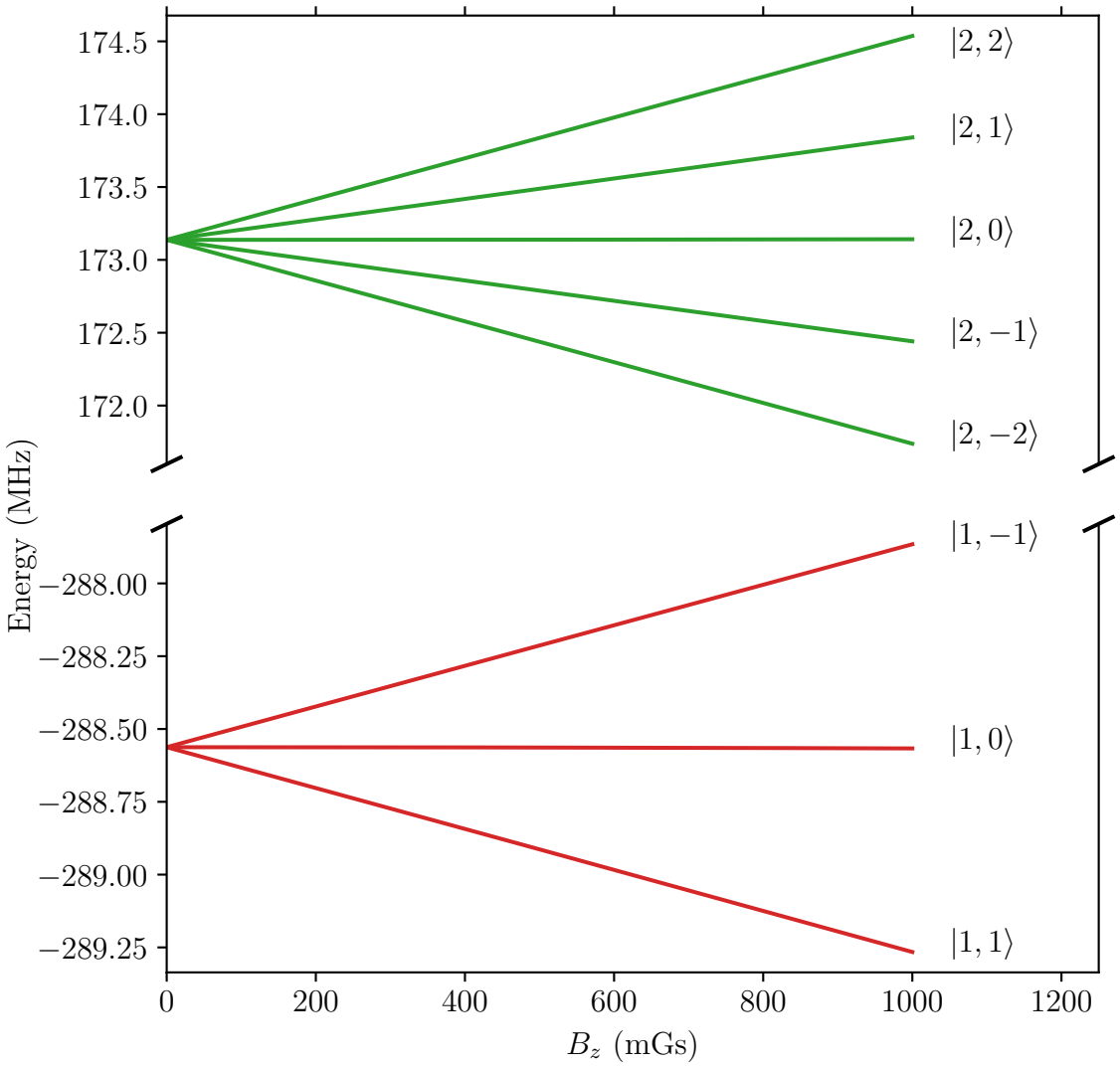

Figure 2.3: Zeeman (and hyperfine) splitting of the $^2S_{1/2}$ ground state of ^{39}K over an extended range of B_z values encountered during co-magnetometer operation.

2.2 The Density Matrix

In a co-magnetometer cell, there are vast numbers ($\sim 10^{13}$ - 10^{15}) of alkali atoms interacting with an even greater number of noble gas atoms ($\sim 10^{19}$ - 10^{20}). Our measurement of the system with a linearly polarized off-resonant probe beam transversing through the length of the co-magnetometer cell is therefore an ensemble average measurement. It is convenient, as reviewed by Fano in [74], to describe such an ensemble

of atoms using the density matrix ρ. In this section, we define the density matrix and list a few pertinent properties relevant to this thesis.

Following [74], we define the density matrix ρ as the operator such that for any operator Q, the ensemble average $\langle Q \rangle$ of an ensemble consisting of N identical atoms is

$$\langle Q \rangle = \frac{1}{N} \sum_n \langle \psi_n | Q | \psi_n \rangle \equiv \mathrm{Tr}\left[Q\rho\right], \tag{2.22}$$

where $|\psi_n\rangle$ is here the wavefunction of the n^{th} atom. From this definition, it follows that

$$\frac{1}{N} \sum_n \sum_{ij} \langle \psi_n | i \rangle \langle i | Q | j \rangle \langle j | \psi_n \rangle = \sum_{ij} \langle i | Q | j \rangle \langle j | \rho | i \rangle, \tag{2.23}$$

where the sums over i,j are over a complete set of eigenstates spanning the space of $|\phi_n\rangle$, and therefore the matrix elements of ρ may be identified to be

$$\rho_{ji} = \frac{1}{N} \sum_n \langle j | \psi_n \rangle \langle \psi_n | i \rangle, \tag{2.24}$$

or in operator form,

$$\rho = \frac{1}{N} \sum_n |\psi_n\rangle \langle \psi_n|. \tag{2.25}$$

In particular, if we let $|m\rangle$ and $|\mu\rangle$ denote excited and ground states eigenstates respectively so that the wavefunction of the n^{th} wavefunction may be expanded as

$$|\psi_n(t)\rangle = \sum_m a_m^n e^{-i\omega_m t} |m\rangle + \sum_\mu a_\mu^n e^{-i\omega_\mu t} |\mu\rangle, \tag{2.26}$$

then from (2.24), the ground state density matrix is

$$\rho^g_{\mu\nu} = \frac{1}{N} \sum_n \langle \mu | \psi_n \rangle \langle \psi_n | \nu \rangle = \frac{1}{N} \sum_n a_\mu^n a_\nu^{n*} e^{i\omega_{\nu\mu} t} = \langle a_\mu a_\nu^* \rangle e^{i\omega_{\nu\mu} t}, \tag{2.27}$$

where we have defined $\omega_{\nu\mu} \equiv \omega_\nu - \omega_\mu = (E_\nu - E_\mu)/\hbar$. In between collisions with other atoms, the ground state alkali atom evolves under the ground state hamiltonian (2.3) according to the Schrödinger equation

$$i\hbar \frac{d}{dt} |\psi\rangle = H_g |\psi\rangle , \tag{2.28}$$

so that in between collisions, the density matrix ρ evolves according to the Liouville equation

$$\begin{aligned} \frac{d\rho}{dt} &= \frac{1}{N} \sum_n \left[\left(\frac{d}{dt} |\psi_n\rangle \right) \langle \psi_n| + |\psi_n\rangle \left(\frac{d}{dt} \langle \psi_n| \right) \right] \\ &= \frac{1}{i\hbar} \left(H \frac{1}{N} \sum_n |\psi_n\rangle \langle \psi_n| - \frac{1}{N} \sum_n |\psi_n\rangle \langle \psi_n| H \right) \\ &= \frac{1}{i\hbar} [H, \rho] . \end{aligned} \tag{2.29}$$

From the definition of ρ in (2.25), it is evident that ρ is Hermitian, which implies that the eigenvalues of ρ are real. Moreover, it is easy to show that these eigenvalues must be non-negative since if we let μ be an eigenvalue of ρ corresponding to the eigenvector $|\mu\rangle$, then

$$\mu = \langle \mu | \rho | \mu \rangle = \frac{1}{N} \sum_n \langle \mu | \psi_n \rangle \langle \psi_n | \mu \rangle = \frac{1}{N} \sum_n |\langle \mu | \psi_n \rangle|^2 \geq 0. \tag{2.30}$$

If we take the trace of ρ, we see that

$$\mathrm{Tr}[\rho] = \sum_\mu \mu = \sum_\mu \langle \mu | \rho | \mu \rangle = \frac{1}{N} \sum_n \underbrace{\sum_\mu \langle \mu | \psi_n \rangle \langle \psi_n | \mu \rangle}_{=1} = 1. \tag{2.31}$$

Consequently, each eigenvalue μ of ρ is bounded between $0 \leq \mu \leq 1$. Accordingly, if μ is an energy eigenstate, then we can interpret $\mu = \rho_{\mu\mu} = \left(\sum_n \langle \mu | \psi_n \rangle |\psi_n\rangle \langle \mu| \right)/N$ as the probability that an atom selected at random from the ensemble will be in the

eigenstate $|\mu\rangle$. The diagonal elements of ρ are for this reason called the populations while off-diagonal matrix elements are called coherences.

Compared to the electron spin, the nuclear spin of an alkali atom is generally more shielded from its environment. Consequently, physical processes tend to affect them in significantly different ways and it is therefore convenient to separate the density matrix into components with and without electron polarization. To do so, we note that we can expand the density matrix in terms of spherical basis operators. In particular, we may expand ρ in the uncoupled spherical basis operators (A.23) as

$$\rho = \sum_{KMLN} \rho(KM;LN) T^K_M(I,I) T^L_N(S,S), \tag{2.32}$$

where $\rho(KM;LN)$ are the expansion coefficents. Since $S = 1/2$, we may write down $T^L_N(S,S)$ explicitly as in (A.25) and so the expansion becomes

$$\begin{aligned}\rho &= \sum_{KM} \rho(KM;00) T^K_M(I,I) \underbrace{T^0_0(\tfrac{1}{2},\tfrac{1}{2})}_{1/\sqrt{2}} + \sum_N \sum_{KM} \rho(KM;1N) T^K_M(I,I) \underbrace{T^1_N(\tfrac{1}{2},\tfrac{1}{2})}_{\sqrt{2}S_N} \\ &= \phi + \boldsymbol{\Theta}\cdot\mathbf{S},\end{aligned} \tag{2.33}$$

where we have defined the purely nuclear operators ϕ and $\boldsymbol{\Theta}$ in the second line as

$$\phi \equiv \frac{1}{\sqrt{2}} \sum_{KM} \rho(KM;00) T^K_M(I,I) \tag{2.34}$$

$$\Theta_N \equiv \sqrt{2} \sum_{KM} \rho(KM;1N) T^K_M(I,I). \tag{2.35}$$

Since $\rho = \phi + \boldsymbol{\Theta}\cdot\mathbf{S}$, it is evident that ϕ, which is a purely nuclear operator, is the part of the density matrix without any electron polarization whereas $\boldsymbol{\Theta}\cdot\mathbf{S}$ is, by virtue of its electron spin operators, the part of the density matrix that contains electron polarization. We may obtain an expression for ϕ in terms of ρ and $\mathbf{S}$ by means of a simple trick. Multiplying (2.33) on the right by $\mathbf{S}$ and taking the inner product on

the left with $\mathbf{S}$, we obtain

$$\begin{aligned}\mathbf{S}\cdot\rho\mathbf{S} &= \phi\mathbf{S}\cdot\mathbf{S} + \Theta^i S_j S_i S^j \\ &= \frac{3}{4}\phi - \frac{1}{4}\mathbf{\Theta}\cdot\mathbf{S},\end{aligned} \tag{2.36}$$

where we have used the identity (A.49) to obtain the second line. Solving (2.33) and (2.36) simultaneously then gives us

$$\phi = \frac{1}{4}\rho + \mathbf{S}\cdot\rho\mathbf{S} \tag{2.37}$$

$$\mathbf{\Theta}\cdot\mathbf{S} = \frac{3}{4}\rho - \mathbf{S}\cdot\rho\mathbf{S}. \tag{2.38}$$

Evidently, the term $\mathbf{S}\cdot\rho\mathbf{S}$ is a frequently recurring term and we therefore here state a few useful identities related to expressions of this form that can be easily derived using (A.48) and (A.35).

$$\mathbf{S}\cdot\rho\mathbf{S}\mathbf{S} = S_j\rho S^j S^i = S_j\rho\left(\frac{1}{4}\delta^{ji} + \frac{i}{2}\epsilon^{jik}S_k\right) = \frac{1}{4}\mathbf{S}\rho - \frac{i}{2}\mathbf{S}\times\rho\mathbf{S} \tag{2.39}$$

$$\mathbf{S}\mathbf{S}\cdot\rho\mathbf{S} = S^i S_j\rho S^j = \frac{1}{4}\rho\mathbf{S} - \frac{i}{2}\mathbf{S}\times\rho\mathbf{S} \tag{2.40}$$

$$S_j\rho S^i S^j = \frac{1}{4}\mathbf{S}\rho + \frac{i}{2}\mathbf{S}\times\rho\mathbf{S} \tag{2.41}$$

$$S_j S^i\rho S^j = \frac{1}{4}\rho\mathbf{S} + \frac{i}{2}\mathbf{S}\times\rho\mathbf{S}. \tag{2.42}$$

The trace of $\mathbf{S}\times\rho\mathbf{S}$ is

$$\begin{aligned}\mathrm{Tr}[\mathbf{S}\times\rho\mathbf{S}] &= \mathrm{Tr}[\epsilon^{ijk}S_j\rho S_k] = \mathrm{Tr}[\epsilon^{ijk}\rho S_k S_j] \\ &= \mathrm{Tr}\left[\epsilon^{ijk}\rho\left(\frac{1}{4}\delta_{kj} + \frac{i}{2}\epsilon_{kjl}S^l\right)\right] \\ &= \frac{i}{2}\,\mathrm{Tr}[\underbrace{\epsilon^{ijk}\epsilon_{kjl}}_{-2\delta^i_l}\rho S^l] = -i\,\langle\mathbf{S}\rangle\,,\end{aligned} \tag{2.43}$$

so that

$$\mathrm{Tr}[\mathbf{S}\cdot\rho\mathbf{S}\mathbf{S}] = \mathrm{Tr}[\mathbf{S}\mathbf{S}\cdot\rho\mathbf{S}] = -\frac{1}{4}\langle\mathbf{S}\rangle \tag{2.44}$$

$$\mathrm{Tr}[S_j\rho S^i S^j] = \mathrm{Tr}[S_j S^i\rho S^j] = \frac{3}{4}\langle\mathbf{S}\rangle\,. \tag{2.45}$$

We note that

$$\mathrm{Tr}[\mathbf{S}\rho\mathbf{S}] = \mathrm{Tr}[S_j\rho S^j] = \mathrm{Tr}[\rho S^j S_j] = \frac{3}{4}, \tag{2.46}$$

and therefore $\mathrm{Tr}[\phi] = 1$ while $\mathrm{Tr}[\mathbf{\Theta}\cdot\mathbf{S}] = 0$. Moreover,

$$\mathrm{Tr}[\mathbf{S}\cdot\rho\mathbf{S}\mathbf{I}] = \mathrm{Tr}[\mathbf{I}\mathbf{S}\cdot\rho\mathbf{S}] = \mathrm{Tr}[\rho\mathbf{I}S^j S_j] = \frac{3}{4}\langle\mathbf{I}\rangle\,. \tag{2.47}$$

We shall also have occasion to run into expressions of the form $\phi\mathbf{S}$ and we note that this may be expanded using (2.37), (2.39) and (2.40) to obtain

$$\phi\mathbf{S} = \mathbf{S}\phi = \frac{1}{4}\{\rho,\mathbf{S}\} - \frac{i}{2}\mathbf{S}\times\rho\mathbf{S}, \tag{2.48}$$

where the curly bracket denotes the anti-commutator. With these identities, it is easy to verify that as expected,

$$\mathrm{Tr}[\phi\mathbf{S}] = \frac{1}{2}\langle\mathbf{S}\rangle - \frac{i}{2}\left(-i\langle\mathbf{S}\rangle\right) = 0 \tag{2.49}$$

$$\mathrm{Tr}[\phi\mathbf{I}] = \frac{1}{4}\langle\mathbf{I}\rangle + \frac{3}{4}\langle\mathbf{I}\rangle = \langle\mathbf{I}\rangle\,, \tag{2.50}$$

and

$$\mathrm{Tr}[\mathbf{\Theta}\cdot\mathbf{S}\,\mathbf{S}] = \frac{3}{4}\langle\mathbf{S}\rangle + \frac{1}{4}\langle\mathbf{S}\rangle = \langle\mathbf{S}\rangle \tag{2.51}$$

$$\mathrm{Tr}[\mathbf{\Theta}\cdot\mathbf{S}\,\mathbf{I}] = \frac{3}{4}\langle\mathbf{I}\rangle - \frac{3}{4}\langle\mathbf{I}\rangle = 0. \tag{2.52}$$

2.3 Collisional Evolution

In a co-magnetometer vapor cell, alkali atoms undergo collisions of various types with noble gas atoms, other buffer gas atoms (such as N_2 that is mainly used for quenching[3]), and of course, with other alkali atoms. Due to the different physical origins of the collisions, these collisions affect the macroscopic spin polarization of the vapor in different ways but in general, these collisions serve to randomize the macroscopic spin polarization of the alkali vapor with the notable exception of spin-exchange collisions, which conserves the total angular momentum of the colliding atoms.

During a collision, the (ground state) free atom's Hamiltonian is modified to become

$$H = H_g + H_c, \tag{2.53}$$

where H_g is the ground state Hamiltonian in (2.3) and H_c is the collisional Hamiltonian.

For a collision of duration τ, the evolution of the n^{th} alkali atom with wavefunction $|\psi^n\rangle$ may be represented with the S-matrix[4] as

$$|\psi_c^n\rangle = S(H,\tau)\,|\psi^n\rangle\,, \tag{2.54}$$

so that the density matrix ρ_c after a small time Δt is

$$\begin{aligned}\rho_c &= \frac{\Delta t}{T_c}\frac{1}{N}\left\langle \sum_n S(H,\tau)\,|\psi^n\rangle\,\langle\psi^n|\,S^\dagger(H,\tau)\right\rangle \\ &= \frac{\Delta t}{T_c}\left\langle S\rho S^\dagger\right\rangle,\end{aligned} \tag{2.55}$$

[3] To be described in greater detail in section 2.7 on optical pumping.
[4] This should not be confused with the electron spin operator **S**.

where the average above is over all possible impact parameters and orbital planes, and T_c, the ensemble averaged rate of collisions, is

$$\frac{1}{T_c} = n \langle \sigma \overline{v} \rangle , \tag{2.56}$$

where n here is the number density of the colliding species and $\langle \sigma \overline{v} \rangle$ is the ensemble averaged rate constant. Accordingly, collisions with other atoms cause the density matrix to evolve as

$$\frac{d\rho_c}{dt} = \frac{1}{T_c} \left\langle S\rho S^\dagger - \rho \right\rangle . \tag{2.57}$$

The detailed computation to obtain $\left\langle S\rho S^\dagger - \rho \right\rangle$ from the collisional Hamiltonian H_c for each of the different types of collisions will take us too far afield and the interested reader should refer to [75] for more details. In the sections below, we simply delineate the different types of collisions that are relevant to the operation of the co-magnetometer cell, explain their physical origins and state how these collisions affect the evolution of the density matrix. Even though three-body collisions involving the formation of van der Waals molecules are possible, we shall be mainly interested in binary collisions since van der Waals molecules formation are mostly only significant with heavier noble gases such as Xe and in any case, van der Waals molecules are rapidly destroyed in our high pressure co-magnetometer cells so that only binary collisions are important. Similarly, we note that formation of alkali-alkali singlet or triplet dimer molecules is not favored in our high pressure cells, although there has been claims in the literature that alkali-alkali triplet dimer molecules are responsible for a significant amount alkali self-relaxation even at multi-atmosphere pressures [76], which we further discuss in section 2.3.4. However, we omit a discussion of alkali-alkali singlet dimers, which only contribute to significant spin relaxation in the regime of high alkali density and low buffer gas pressure [77] that is not relevant to our high pressure co-magnetometer cells.

2.3.1 Spin-exchange collisions with alkali atoms

Spin-exchange collisions are, as their name suggests, collisions in which the colliding partners have, on average, the orientation of their electronic spin, interchanged. The mechanism of such a collision was first identified in 1956 by Wittke and Dicke [78] as well as Purcell and Field [79] in an astrophysical context to account for the rate of the ubiquitous and now famous "21-cm" hydrogen line in radio astronomy. In a spin-exchange collision, two hydrogen-like atoms form a molecule whose overall wavefunction is a linear combination of an anti-symmetric singlet spin state and a symmetric triplet spin state with a corresponding symmetric and anti-symmetric spatial wavefunction with a large energy splitting (on the order of an eV) that is electrostatic in nature. Due to this large energy splitting, the cross-section for spin-exchange collisions are typically rather large $\sim 10^{-14}$ cm^2. The spin-exchange interaction can be represented by an potential of the form

$$V(\mathbf{r}) = V_0(\mathbf{r}) + \mathbf{S}_A \cdot \mathbf{S}_B V_1(\mathbf{r}), \tag{2.58}$$

where $\mathbf{S}_A$ and $\mathbf{S}_B$ are the spin operators of atoms A and B respectively [80]. It can be shown [73, 81, 82] that this interaction causes the density matrix to evolve like

$$\begin{aligned}\frac{d\rho^i_{ex}}{dt} &= \sum_j \frac{1}{T^{ij}_{ex}} \left(\phi^i \left(1 + 4\left\langle \mathbf{S}^j \right\rangle \cdot \mathbf{S}^i\right) - \rho^i\right) + \frac{1}{i\hbar}\left[\delta\mathscr{E}^{ij}_{ex}, \rho^i\right] \\ &\approx \sum_j \frac{1}{T^{ij}_{ex}} \left(\phi^i \left(1 + 4\left\langle \mathbf{S}^j \right\rangle \cdot \mathbf{S}^i\right) - \rho^i\right),\end{aligned} \tag{2.59}$$

where the indices i, j label different alkali species present in the vapor, and we have dropped the frequency-shift operator $\delta\mathscr{E}^{ij}_{ex}$ [83, 84]

$$\delta\mathscr{E}^{ij}_{ex} = \frac{2\hbar\kappa_{ex}}{T^{ij}_{ex}} \left\langle \mathbf{S}^j \right\rangle \cdot \mathbf{S}^i, \tag{2.60}$$

in the second line since the dimensionless parameter κ_{ex} in (2.60) is typically only a few percent [73]. The spin-exchange rate $1/T_{ex}$ is

$$\frac{1}{T_{ex}^{ij}} = n_j \sigma_{ex}^{ij} \overline{v}, \tag{2.61}$$

where n_j is the number density of the j^{th} species, σ_{ex}^{ij} is the cross-section of spin-exchange collisions between species i and j, and $\overline{v}$, the mean relative velocity of the colliding atoms (in the center of mass frame), is

$$\overline{v} = \sqrt{\frac{8 k_B T}{\pi \mu}}, \tag{2.62}$$

where k_B is the Boltzmann's constant, T is the temperature and μ is the reduced mass of the two colliding atoms. In order to see that spin-exchange collisions conserve the total angular momentum of the colliding atoms, we may compute $\langle \dot{\mathbf{F}} \rangle$ by multiplying (2.59) by $\mathbf{F}$ and taking its trace. Using (2.48) we may re-write (2.59) as

$$\frac{d\rho_{ex}^i}{dt} = \sum_j \frac{1}{T_{ex}^{ij}} \left(\phi^i - \rho^i + \left\langle \mathbf{S}^j \right\rangle \cdot \{\rho^i, \mathbf{S}^i\} - 2i \left\langle \mathbf{S}^j \right\rangle \cdot \mathbf{S}^i \times \rho^i \mathbf{S}^i \right). \tag{2.63}$$

The traces may be evaluated with the help of these identities[5]

$$\mathrm{Tr}([S^j,\rho]S^i) = i\epsilon^{ijk}\langle S_k\rangle \tag{2.64}$$

$$\mathrm{Tr}([S^j,\rho]I^i) = 0 \tag{2.65}$$

$$\mathrm{Tr}(\{S^j,\rho\}S^i) = \frac{1}{2}\delta^{ij} \tag{2.66}$$

$$\mathrm{Tr}(\{S^j,\rho\}I^i) = 2\left\langle I^i S^j\right\rangle \tag{2.67}$$

$$\mathrm{Tr}(\epsilon^{ijk}S_j\rho S_k S^l) = \frac{i}{4}\delta^{il} \tag{2.68}$$

$$\mathrm{Tr}(\epsilon^{ijk}S_j\rho S_k I^l) = -i\left\langle I^l S^i\right\rangle \tag{2.69}$$

$$\tag{2.70}$$

. Using (2.66) and (2.67), we have[6]

$$\mathrm{Tr}(\left\langle \mathbf{S}^j\right\rangle \cdot \{\mathbf{S}^i,\rho^i\}\mathbf{F}^i) = \frac{1}{2}\left\langle \mathbf{S}^j\right\rangle + 2\left\langle \mathbf{S}^j\right\rangle \cdot \left\langle \mathbf{S}^i\mathbf{I}^i\right\rangle, \tag{2.71}$$

while from (2.68) and (2.69) we obtain

$$\mathrm{Tr}(\left\langle \mathbf{S}^j\right\rangle \cdot (\mathbf{S}^i \times \rho^i\mathbf{S}^i)\mathbf{F}^i) = i\left(\frac{1}{4}\left\langle \mathbf{S}^j\right\rangle - \left\langle \mathbf{S}^j\right\rangle \cdot \left\langle \mathbf{S}^i\mathbf{I}^i\right\rangle\right). \tag{2.72}$$

Therefore, we see from (2.63) that

$$\frac{d}{dt}\left\langle \mathbf{F}^i\right\rangle = \sum_j \frac{1}{T_{ex}^{ij}}\left(\left\langle \mathbf{S}^j\right\rangle - \left\langle \mathbf{S}^i\right\rangle\right) \tag{2.73}$$

and consequently, we note that if only one species of alkali atoms are present (i.e. there is only value of j and $j = i$), then spin-exchange collisions do indeed conserve the total angular momentum of the atoms. However, since they can flip the electronic spins of atoms, we note that spin-exchange collisions do tend to distribute the angular

[5]The indices here refer to the components of the operators and should not be confused with i, j indices used elsewhere in this section to denote different species of alkali atoms.

[6]Note that the indices here refer again to the i, j species of atoms.

momentum of the atoms over various m_F sublevels. Indeed, as will be discussed in more detail in section 2.4, at sufficiently high spin-exchange rates, a spin-temperature equilibrium is reached in which the ensemble averaged spin polarization of the atoms uniquely determines the population distribution of the various m_F sublevels. On the other hand, we note that if there is more than one species of alkali atoms present, then the net effect of spin-exchange collisions is to drive the total angular momentum **F** of each species until the electronic spin polarization of both species are the same. This will turn out to be important in allowing us to use a hybrid pumping technique that we describe further in section 2.7.4. For now, we conclude this discussion by listing the experimentally measured spin-exchange cross-sections of several alkali atom pairs below.

Species	σ (10^{-14} cm^2)	Temperature (°C)	Reference
^{23}Na-^{23}Na	1.0 ± 0.1	427	[85]
^{23}Na-^{23}Na	1.109 ± 0.005	117	[86]
Na-Rb	2.6 ± 0.9	139	[87]
^{39}K-^{39}K	1.5 ± 0.2	327	[85]
^{85}Rb-^{85}Rb	1.9 ± 0.3	277	[85]
^{85}Rb-^{87}Rb	1.7 ± 0.2	90	[88]
^{87}Rb-^{87}Rb	1.9 ± 0.2	277	[85]
^{87}Rb-^{87}Rb	1.9 ± 0.2	78	[89]
^{133}Cs-^{133}Cs	2.0 ± 0.3	227	[85]
^{133}Cs-^{133}Cs	2.0 ± 0.3	27	[90]
^{87}Rb-^{133}Cs	2.3 ± 0.2	78	[89]

Table 2.1: Experimental alkali-alkali spin-exchange cross-sections

We note from Table 2.1 that the spin-exchange cross-sections are for our purposes, independent of temperature. Also, although there are not many measurements (that this author is aware of) of spin-exchange cross-sections between different alkali metals, the few measurements performed on such systems indicate that the spin-exchange cross-section between two different alkali metals tend to follow the larger (self) spin-exchange cross section of the two and in any case, the range of cross-sections listed above all span between 1 to 2.3 (10^{-14} cm^2).

2.3.2 Spin-exchange collisions with noble gas atoms

Despite having the same nominal name of "spin-exchange", a spin-exchange collision between an alkali and noble gas atom is of vastly different physical origin as compared to an alkali-alkali spin-exchange collision described in the preceding section. Indeed, in this case spin-exchange collisions between alkali and noble gas atoms occur due to the interaction of the alkali atom's valence electron with magnetic fields produced by the noble-gas nucleus. The magnetic (dipole) field at displacement $\mathbf{r}$ due to the noble gas atom is

$$\mathbf{B}_b(\mathbf{r}) = \frac{8\pi\mu_K}{3K}\mathbf{K}\delta(\mathbf{r}) + \frac{\mu_K}{K}\mathbf{K}\cdot\frac{3\mathbf{r}\mathbf{r} - r^2\mathbb{1}}{r^5}, \tag{2.74}$$

where $\mathbf{K}$ is the nuclear spin of the noble gas atom and μ_K is the magnetic dipole moment of the noble gas nucleus. The first term of (2.74) gives rise to the isotropic magnetic dipole Fermi-contact hyperfine[7] interaction first discovered by Fermi [91] when, during a collision, the wavefunction of the alkali's atom valence electron overlaps with the nucleus of the noble gas atom and the two spins interact via the magnetic fields of their respective dipole moments. This interaction can be represented by a potential of the form

$$V_{iso}(\mathbf{r}) = A_b(\mathbf{r})\mathbf{K}\cdot\mathbf{S}, \tag{2.75}$$

where $\mathbf{r}$ is the separation between the alkali and noble gas atom, $\mathbf{S}$ is the electron spin of the alkali atom and A_b is strongly dependent on $\mathbf{r}$. The coupling constant A_b is given by [92]

$$A_b(\mathbf{r}) = \frac{8\pi g_s\mu_B\mu_K}{3K}\left|\eta\psi_0(\mathbf{r})\right|^2, \tag{2.76}$$

where μ_B is the Bohr magneton, g_s is the electron spin g-factor, ψ_0 is the ground-state wavefunction of the alkali atom in the absence of the noble gas atom and η is an enhancement factor.

[7] That is a coupling of the form $\mathbf{I}\cdot\mathbf{S}$.

The second term of (2.74) gives rise to the anisotropic magnetic-dipole hyperfine interaction that may be represented by a potential of the form

$$V_{ani}(\mathbf{r}) = B_b(\mathbf{r})\mathbf{K} \cdot (3\hat{\mathbf{z}}\hat{\mathbf{z}} - \mathbb{1}) \cdot \mathbf{S}. \tag{2.77}$$

The anisotropic coupling is typically a few percent compared to the isotropic coupling. Indeed, Walter, Happer and Walker [93] estimates that for K-^{3}He and Rb-^{3}He systems, the anisotropic coupling is 3.7% and 3.0% respectively of the isotropic coupling, and this fraction is even smaller for other noble gases. We note that the anisotropic coupling tends to polarize $\langle \mathbf{K} \rangle$ in the opposite direction of $\langle \mathbf{S} \rangle$ so that it will, in general, set a theoretical limit to how much $\langle \mathbf{K} \rangle$ can be polarized. This can be a problem for applications requiring hyperpolarized ^{3}He, such as magnetic resonance imaging with hyperpolarized noble gases but since we typically only polarize our noble gas atoms to a few percent in the co-magnetometer cell, the anisotropic hyperfine coupling is frequently ignored. As a result, we take the spin-exchange interaction potential to be simply given by (2.75).

Despite the different physical origin of this interaction as compared to the alkali-alkali spin-exchange collisions, it can be shown [73] that for $K = 1/2$ the potential (2.75) causes the density matrix of the alkali atom to evolve as

$$\frac{d\rho_{se}}{dt} = \frac{1}{T_{se}} \left(\phi \left(1 + 4 \langle \mathbf{K} \rangle \cdot \mathbf{S} \right) - \rho \right) + \frac{1}{i\hbar} [\delta \mathscr{E}_{se}, \rho], \tag{2.78}$$

in an analogous fashion to the evolution of the density matrix due to alkali-alkali spin-exchange collisions. The frequency-shift operator $\delta \mathscr{E}_{se}$ is given by [73]

$$\delta \mathscr{E}_{se} = n_b \frac{8\pi g_s \mu_B \mu_K}{3K} \kappa_0 \langle \mathbf{K} \rangle \cdot \mathbf{S}, \tag{2.79}$$

where n_b is the number density of noble gas atoms, κ_0 is a dimensionless enhancement coefficient that is bigger than 1, and the rate of alkali-noble gas spin-exchange collisions (for an alkali atom) is

$$\frac{1}{T_{se}} = n_b \left\langle \sigma_{se} \overline{v} \right\rangle , \tag{2.80}$$

where $\left\langle \sigma_{se} \overline{v} \right\rangle$ is the rate constant of spin-exchange collisions between alkali and noble gas atoms. The first term of (2.78) causes the ensemble averaged total angular momentum $\mathbf{F}$ to evolve as

$$\frac{1}{T_{se}} \left(\mathrm{Tr}((\phi - \rho)\mathbf{F}) + \mathrm{Tr}\left(\langle \mathbf{K} \rangle \cdot \{\rho, \mathbf{S}\}\mathbf{F} \right) - 2i \, \mathrm{Tr}(\langle \mathbf{K} \rangle \cdot (\mathbf{S} \times \rho \mathbf{S}) \, \mathbf{F}) \right) . \tag{2.81}$$

Letting $\langle \mathbf{S}^j \rangle \to \langle \mathbf{K} \rangle$ and dropping all of the i indices (since we are only considering one alkali species here) in (2.71) and (2.72), we have

$$\mathrm{Tr}(\langle \mathbf{K} \rangle \cdot \{\rho, \mathbf{S}\}\mathbf{F}) = \frac{1}{2} \langle \mathbf{K} \rangle + 2 \langle \mathbf{K} \rangle \cdot \langle \mathbf{IS} \rangle \tag{2.82}$$

$$\mathrm{Tr}(\langle \mathbf{K} \rangle \cdot (\mathbf{S} \times \rho \mathbf{S})\mathbf{F}) = i \left(\frac{1}{4} \langle \mathbf{K} \rangle - \langle \mathbf{K} \rangle \cdot \langle \mathbf{IS} \rangle \right) , \tag{2.83}$$

and so the first term's (in (2.78)) contribution to $\langle \dot{\mathbf{F}} \rangle$ is,

$$\frac{1}{T_{se}} \left(\langle \mathbf{K} \rangle - \langle \mathbf{S} \rangle \right) . \tag{2.84}$$

It remains to be seen how the second term of (2.78) contributes to $\langle \dot{\mathbf{F}} \rangle$. The trace of the second term (multiplied by $\mathbf{F}$) comes down to the trace of $[\langle \mathbf{K} \rangle \cdot \mathbf{S}, \rho]\mathbf{F}$. From (2.64) and (2.65) however, we get

$$\mathrm{Tr}([\langle \mathbf{K} \rangle \cdot \mathbf{S}, \rho]\mathbf{F}) = i \langle \mathbf{K} \rangle \times \langle \mathbf{S} \rangle , \tag{2.85}$$

and therefore we have

$$\begin{aligned}\mathrm{Tr}\left(\frac{1}{i\hbar}\left[\delta\mathscr{E}_{se},\rho\right]\mathbf{F}\right) &= \kappa_0\frac{8\pi}{3}n_b\mu_K\frac{\langle\mathbf{K}\rangle}{K}\times\frac{g_s\mu_B}{\hbar}\langle\mathbf{S}\rangle \\ &= \lambda M_n\mathbf{P}_n\times\gamma_e\langle\mathbf{S}\rangle\,, \end{aligned} \tag{2.86}$$

where $\gamma_e = g_s\mu_B/\hbar$ is the gyromagnetic ratio of the free electron, $\mathbf{P}_n = \langle\mathbf{K}\rangle/K$ is the spin polarization of the noble gas atoms, and we have defined λ and M_n in the second line as

$$\lambda \equiv \frac{8\pi\kappa_0}{3} \tag{2.87}$$

$$M_n \equiv n_b\mu_K. \tag{2.88}$$

We note that M_n as defined above is the magnetization of fully polarized noble gas atoms and $8\pi/3$ is the geometrical factor[8] to obtain the magnetic field from a uniformly magnetized sphere and so written in this way, it is clear that the net effect of the second term in (2.78) is to create an enhanced (because of $\kappa_0 > 1$) effective magnetic field that the electron spin of the alkali atoms precess about.

Adding (2.84) and (2.86) together, we see that alkali-noble gas spin-exchange collisions causes the ensemble averaged total angular momentum $\mathbf{F}$ of the alkali atoms to evolve as

$$\frac{d}{dt}\langle\mathbf{F}_{se}\rangle = \frac{1}{T_{se}}\left(\langle\mathbf{K}\rangle - \langle\mathbf{S}\rangle\right) + \lambda M_n\mathbf{P}_n\times\gamma_e\langle\mathbf{S}\rangle\,. \tag{2.89}$$

Since these collisions originate from a magnetic interaction which requires the overlap of the alkali atom's electron into the noble gas nucleus, they have a substantially smaller cross-section as compared to the spin-exchange collisions between alkali-alkali atoms. Indeed, the cross-sections of alkali-noble gas spin-exchange collisions are of the order $\sim 10^{-20}$ cm^2, which are about six orders of magnitudes smaller

[8] This is in c.g.s units. In S.I units, this would be simply 2/3.

than the cross-sections of alkali-alkali spin-exchange collisions. For easy reference, we list the experimentally measured spin-exchange rates between various alkali-noble gas pairs below.

Species	k_{se} (10^{-20} cm^3/s)	Temperature (°C)	Reference
Rb-^{3}He	6.7 ± 0.6	$90 - 180$	[94]
Rb-^{3}He	6.8 ± 0.2	$140 - 180$	[69]
Rb-^{21}Ne	8 ± 1	140	[95]
K-^{3}He	6.1 ± 0.7	150	[96]
K-^{3}He	6.1 ± 0.4	$140 - 180$ (?)	[97]
K-^{3}He	5.5 ± 0.2	?	[98]
K-^{3}He	7.1 ± 0.6	$230 - 290$	[99]
K-^{21}Ne	2.7 ± 0.4	140	[95]

Table 2.2: Experimental alkali-noble gas spin-exchange rate constants

We note that for the most part, these experimental measurements measure the sum of the isotropic and anisotropic contributions to the spin-exchange rate but since the anisotropic contribution is only a few percent of the isotropic contributions, we shall take these measurements to be measurements of the isotropic hyperfine coupling. Moreover, most measurements have assumed that the rate constant is independent of temperature, and calculations in [93] seem to indicate that this is indeed valid for noble gases heavier than helium, where the repulsive potential is so steep that it effectively defines the distance of closest approach regardless of the kinetic energy of the colliding atoms. For alkali-^{3}He systems however, the calculations of [93] predict some temperature dependence, although they caution that since there is significant uncertainty in the potentials of the ^{3}He systems used in their calculations, the temperature dependence could possibly be vanishingly small. Measurements of the spin-exchange rate constants in Rb-^{3}He systems have not observed any temperature dependence [69, 94] but discrepancies in measurements [97, 99] of the rate constants in K-^{3}He systems was suggested by [99] to be due to a temperature dependence that is in agreement with more recent *ab initio* quantum scattering calculations [100].

The parameter κ_0 in (2.79) is a measure of the strength of the Fermi-contact interaction between the noble gas nucleus and the valence electron on the alkali atom. We list below experimentally measured κ_0 values for a variety of alkali-noble gas pairs.

Species	κ_0	Temperature (°C)	Reference
K-^{3}He	5.99 ± 0.11	200	[101]
K-^{3}He	6.01 ± 0.11	200	[94]
K-^{21}Ne	31 ± 3	140	[95]
Rb-^{21}Ne	32 ± 3	128	[102]
Rb-^{21}Ne	36 ± 4	140	[95]

Table 2.3: Experimental κ_0 parameter

These parameters are expected to have some temperature dependence and for Rb-He systems, [101] and [103] respectively give the temperature dependence of κ_0 as

$$\kappa_0^{Rb-He} = 6.39 + 0.00914(T - 200\,(^\circ\mathrm{C})) \quad , 150 < T < 350\,^\circ C \tag{2.90}$$

$$\kappa_0^{Rb-He} = 4.52 + 0.00934(T(^\circ\mathrm{C})) \quad , 110 < T < 172\,^\circ C. \tag{2.91}$$

For K-^{3}He systems, [101] gives the temperature dependence of κ_0 as

$$\kappa_0^{K-He} = 5.99 + 0.0086(T - 200\,(^\circ\mathrm{C})). \tag{2.92}$$

2.3.3 Spin-rotation collisions

In contrast to the two types of spin-exchange collisions described above, spin-rotation collisions do not conserve the total angular momentum of the colliding atoms and are an important mechanism of spin relaxation for the alkali atoms. Physically, spin-rotation collisions arise from a spin-orbit interaction of the alkali atom's valence electron with either the noble/buffer gas' core and/or its own core during the duration of the collision as the two atoms rotate about each other [104, 105].

We note that in general, the strength of a spin-orbit interaction increases with the atomic number Z of the atom since it is (partly) due to the magnetic field produced by an orbiting (from the electron's frame of reference) nucleus whose electric field is imperfectly screened by other electrons. For heavier noble gas atoms, measurements of the alkali-noble gas spin-rotation rates [106–109] indicate that the spin-orbit interaction of the alkali's valence electron mainly originate from within the noble gas core [110] since the spin-rotation rates show a marked proportional increase with the atomic number Z of the colliding noble gas atom, as would be expected for a spin-orbit interaction within the noble gas atom's core whose own spin-orbit splitting show the same dependence on Z [111]. This is also naively to be expected since a ground state valence alkali atom electron in a $L = 0$ s spherically symmetric orbital around its own nucleus cannot have a non-zero $\mathbf{L} \cdot \mathbf{S}$ spin-orbit interaction with its own nucleus, which implies that any spin-orbit interaction must originate from within the colliding atom's core. However, in reality, the alkali's valence electron's spherically symmetric s orbital is perturbed by the colliding atom during a collision and mixes with $L = 1$ p orbitals that can now give it a non-zero spin-orbit splitting with its own core [105]. In collisions with heavier noble/buffer gas atoms with far larger spin-orbit splittings of their own, this is a small contribution and most of the spin-rotation interaction is due to the noble/buffer gas atom's core rotating about the electron. However, for lighter noble gas atoms like He that also have small spin-orbit splittings, the dominant contribution to the spin-rotation interaction can come from the perturbed alkali's valence electron's spin-orbit interaction with its own core [105]. This is supported by measurements of the spin-rotation rates between Na-He [112, 113], which are significantly smaller as compared to Rb-He [68], which would be expected if the dominant spin-orbit interaction here is due to the alkali's own core since Na is considerably lighter compared to Rb and its spin-orbit splitting will therefore be accordingly smaller.

In addition to undergoing spin-rotation collisions with other noble/buffer gas atoms, alkali atoms can also undergo spin-rotation collisions with other alkali atoms [114]. However, it is evident from the reasons stated above that the rates for these collisions will be significantly smaller compared to the rates from collisions with noble/buffer gas atoms. Indeed, since the spin-orbit splitting in an alkali ground state atom is only non-zero because of the small admixture of $L = 1$ p orbitals in its perturbed ground state wavefunction, the cross-section for alkali-alkali spin-rotation collisions will be significantly smaller compared to a alkali-noble/buffer gas spin rotation collision. For light noble gas atoms like He that also have small spin-orbit splittings, it is conceivable that the alkali-alkali spin rotation cross section would be comparable to the alkali-He spin rotation cross section. However, in a high pressure co-magnetometer cell, the alkali-alkali spin rotation rate will still be significantly smaller than the alkali-He spin rotation rate since the number density of He is usually at least 5 orders of magnitude larger than that of the alkali atoms. Accordingly, we consider only spin rotation collisions between alkali and noble/buffer gas atoms in the rest of this section.

Since spin-rotation collisions originate from a spin-orbit coupling that is due to the orbital motion of the colliding atoms as they rotate about each other, we expect that its rate will scale with the velocity and therefore temperature of the colliding atoms [105]. Moreover, since lighter atoms move, for the same temperature, faster than heavier atoms, we expect that this temperature dependence will be especially strong in lighter atoms. Indeed, for Rb-He, measurements of its spin-rotation rates at different temperatures reveal a strong $\sim T^4$ (in Kelvins) dependence in the spin-rotation rate [94].

During a spin-rotation collision, the alkali and colliding gas atom rotate around each other at a frequency

$$\omega = \frac{\hbar \mathbf{N}}{\mu r^2}, \tag{2.93}$$

where $\mathbf{N}$ is the relative angular momentum of the rotating pair, μ is the reduced mass and r is the distance between the two atoms. If we transform into the rest frame of the alkali's valence electron, the electron experiences a Coriolis interaction given by [115]

$$V_\omega = -\hbar\boldsymbol{\omega} \cdot \mathbf{L}. \tag{2.94}$$

This Coriolis interaction needs to be taken into account in calculating the first-order correction of the alkali's wavefunction $\left|\psi^{(1)}\right\rangle$ due to collision with the colliding atom, which as mentioned above, will contain small admixtures of $L = 1$ p orbitals. The potential of the spin-rotation collision can then be written as the expectation value of the spin-orbit interaction

$$V = \left\langle \psi^{(1)} \left| V_{SO} \right| \psi^{(1)} \right\rangle = \gamma \mathbf{N} \cdot \mathbf{S}, \tag{2.95}$$

where γ here depends on the the details of spin-orbit interaction (i.e. whether it is from within an alkali or noble/buffer gas core) and is strongly temperature dependent [116]. In general, the spin-rotation interaction can lead to depolarization of the alkali's spin either through binary collisions or during the formation of an alkali-noble/buffer gas Van der Waals molecule [107]. Nevertheless, in our high pressure co-magnetometer cell where the rate of collisions with other noble/buffer gas atoms is extremely high, the lifetimes of these Van der Waals molecules is sufficiently short that spin relaxation due to them is practically indistinguishable from relaxation due to binary collisions. Moreover, since the duration of these binary collisions are much shorter than the alkali's ground state hyperfine frequency, the collision effectively randomizes the alkali's electron spin without affecting the nuclear spin. We may therefore write the density matrix's evolution under the influence of spin-rotation collisions as

$$\frac{d\rho_{NS}}{dt} = -\frac{1}{T_{NS}}(\rho - \phi), \tag{2.96}$$

since from (2.33) $\rho = \phi + \mathbf{\Theta}\cdot\mathbf{S}$ and ϕ, $\mathbf{\Theta}\cdot\mathbf{S}$ are purely nuclear and electronic operators respectively.

As usual, the rate of spin-rotation collisions $1/T_{NS}$ is

$$\frac{1}{T_{NS}} = n_b \sigma_{NS} \overline{v}, \tag{2.97}$$

where n_b is the number density of the colliding atom, σ_{NS} is the (temperature-dependent) spin-rotation cross-section and $\overline{v}$ is the mean relative velocity of the colliding atoms given in (2.62). Not surprisingly, the ensemble-averaged total angular momentum of the alkali atoms evolve as

$$\frac{d}{dt}\langle \mathbf{F} \rangle = \mathrm{Tr}\left[\frac{d\rho}{dt}\mathbf{F}\right] = -\frac{1}{T_{NS}}\mathrm{Tr}\left[\boldsymbol{\theta}\cdot\mathbf{S}\,\mathbf{F}\right] = -\frac{1}{T_{NS}}\langle \mathbf{S} \rangle, \tag{2.98}$$

where the last equality follows from (2.51) and (2.52). We conclude this discussion by listing some measured spin-rotation cross-sections of K and Rb with He, Ne and N_2[9].

Species	σ (10^{-25} cm^2)	Temperature (°C)	Reference
K-He	5.0 ± 0.2	150	[96]
K-Ne	110 ± 10	140	[95]
Rb-He	87	150	[94]
Rb-Ne	190 ± 20	140	[95]
Rb-N_2	1440 ± 30	150	[68]

Table 2.4: Experimental alkali-noble gas spin-rotation cross-sections

2.3.4 Spin-axis collisions with alkali atoms

Although the dominant spin-exchange collisions between alkali atoms discussed in section 2.3.1 conserve the total angular momentum of colliding alkali atoms, mea-

[9] As mentioned above, spin relaxation due to alkali-alkali spin rotation collisions in a high pressure co-magnetometer cell is insignificant compared to alkali-noble/buffer gas spin-rotation collisions and are therefore not considered here.

surements of the spin polarization in a dense Cs vapor revealed limits to the maximum attainable polarization in an alkali vapor and suggested the existence of an alkali-alkali spin destruction collision [117]. Measurement of the cross-section for this collision yielded a number that is too large to be explained by spin-rotation collisions between alkali-alkali atoms and it was therefore proposed [114] that this relaxation was due to a spin-axis collisions arising mainly from an anisotropic magnetic dipole spin-spin coupling[10] and a second order spin-orbit interaction [76, 118] between the two colliding atoms with the interaction potential

$$V_{sa} = \frac{2\lambda}{3}\mathbf{S}\cdot(3\hat{\boldsymbol{\zeta}}\hat{\boldsymbol{\zeta}} - \mathbb{1})\cdot\mathbf{S}, \tag{2.99}$$

where $\mathbf{S}$ is the total electron spin of the colliding atoms, $\hat{\boldsymbol{\zeta}}$ is a unit vector lying along the atoms' inter-nuclear axis, and λ is a coupling constant that is known to be sufficiently large from the case of O_2 molecules [119] and SO radicals [120] to potentially explain the alkali-alkali relaxation rate observed in [114].

Despite a flurry of studies seeking to understand the precise physical nature of spin-axis collisions, there still seems to be some uncertainty within the literature concerning multiple aspects of this interaction. Firstly, it was argued in 1998 [76] that a significant fraction of spin relaxation due to spin-axis relaxations was not due to sudden binary collisions since the relaxation rates can be reduced by a factor of 3 by applying external magnetic fields of the order of a few kGs. The rationale for this was that at magnetic fields of ~ 1 kGs, the precession frequency of the (free) electron is $\sim 2\pi \times 2.8$ GHz and so there is negligible precession of the electron spin about the applied magnetic field during the binary collision duration of 1 ps, which implies that application of $\mathbf{B}$ fields of ~ 1 kGs should not affect the relaxation rates. It is therefore claimed that the observed reduction of relaxation rates due to external

[10] Compare the form of the spin-axis interaction below (2.99) with the anisotropic magnetic dipole coupling in spin-exchange collisions between alkali and noble gas atoms (2.77).

B fields of a few kGs is evidence for a significant fraction of the relaxation occurring in triplet dimer molecules. However, as acknowledged in [76], this is contrary to the persistence of the relaxation at high buffer gas pressures, which should in theory cause rapid breakup of such triplet dimer molecules and result in a substantial reduction of the relaxation rate. It appears that there has, as of 2017 [121], been no resolution in the literature to this difficulty in the interpretation of the magnetic decoupling data from [76].

However, we note that it has been experimentally shown in [122] that **B** fields of a few kGs is sufficient to slow down the relaxation rate from *binary* spin rotation collisions between alkali and noble/buffer gas atoms so it's not obvious if the claims of significant spin-axis relaxation due to triplet molecules in [76] is accurate since their observed reduction in spin-axis relaxation rates at **B** fields of a few kGs could, according to [122], be due simply to a decrease of spin relaxation from binary collisions. If so, this will also explain the persistence of the spin-axis relaxation at high buffer gas pressures. We note that the reason given for the reduction in relaxation rates in [122] does not depend on the specifics of the spin-rotation interaction and applies quite generally to all sudden binary collisions. Accordingly, there is no obvious reason why the results in [122], if correct, cannot be applied to [76]. Indeed, as explained in [122], real alkali atoms store a significant fraction of their angular momentum in the nuclear spin at low **B** fields where **I** and **S** are tightly coupled (i.e. F is a good quantum number). Consequently, even though sudden binary collisions only relax the electronic spin polarization, yet because of the relatively strong hyperfine coupling, the nuclear spin polarization is also eventually destroyed through the hyperfine coupling. However, at sufficiently high **B** fields of a few kGs, **I** and **S** decouple (i.e. F is no longer a good quantum number) and hence, sudden binary collisions can no longer easily cause relaxation of the nuclear spin polarization. Accordingly, relaxation of the

total angular momentum due to sudden binary collisions can be substantially slowed down by applying **B** fields of a few kGs.

Furthermore, although the observation of magnetic resonances peaks in [118] strongly suggest that an interaction of the form in (2.99) is responsible for a significant amount of spin relaxation in alkali-alkali collisions, *ab initio* calculations of the cross-section for these collisions are off from experimentally measured values by a factor of $10-100$, which suggest that either (2.99) or the spin independent potentials used to perform the averaging in computing the scattering cross-section from (2.99) is wrong [123].

The effect of spin-axis collisions on the density matrix will depend on whether or not it is due primarily to binary collisions, to triplet dimers, or to both. Before [123], spin-axis collisions were historically treated as sudden binary collisions that only destroy the electronic spin polarization without affecting the nuclear spin polarization so that in analogy to (2.96), the density matrix evolves as

$$\frac{d\rho_{SS}}{dt} = -\frac{1}{T_{SS}}(\rho - \phi), \tag{2.100}$$

where ϕ is as defined in (2.37) and the rate of spin-axis collisions $1/T_{SS}$ is

$$\frac{1}{T_{SS}} = n_a \langle \sigma_{SS} v \rangle , \tag{2.101}$$

where n_a is the number density of alkali atoms and $\langle \sigma_{SS} v \rangle$ is the temperature independent [94] spin-axis collision rate constant. The ensemble averaged total angular momentum evolves, in analogy to (2.98), as

$$\frac{d}{dt} \langle \mathbf{F} \rangle = -\frac{1}{T_{SS}} \langle \mathbf{S} \rangle . \tag{2.102}$$

We note that these equations are, strictly speaking, only valid for sudden binary collisions. If a significant amount of spin-axis collisions at high buffer gas pressures is indeed due to triplet molecules, then we note that the density matrix will evolve differently from that indicated in (2.100). We conclude this section by listing some alkali-alkali spin destruction rate constants that have been attributed to spin-axis collisions.

Species	$\langle\sigma_{SS}v\rangle$ (10^{-13} cm^3/s)	Reference
K	1.8 ± 0.2	[124]
Rb	7.8 ± 0.8	[124]
Rb	8.1 ± 0.3	[68]
Rb	4.2 ± 0.4	[94]
Rb	4.7 ± 0.4	[76]

Table 2.5: Experimental alkali-alkali spin-axis collision rate constants

We note that the rate constants for Rb-Rb spin-axis collisions are a factor of 2 larger in [76, 94] as compared to in [68, 124]. [94] suggests the discrepancies could be due to the fact that the other measurements did not take into account the temperature dependence of the spin-rotation cross-section (see section 2.3.3). However, this is true of [76], which [94] agrees with, and of the two earlier measurements that [94] disagrees with. Consequently, it is still unfortunately not immediately obvious why the later two measurements are a factor of two larger than the two earlier measurements.

2.4 Spin Temperature Equilibrium

As discussed in section 2.3, spin-exchange collisions between alkali atoms is by far the collisional process with the largest cross-section owing to the large energy splitting between the singlet and triplet states of two approaching alkali atoms. Indeed, a cursory glance at the measured cross-sections for different types of collisions show that whereas spin-exchange collisions between alkali atoms have a cross-section on the order of 10^{-14} cm^2 (Table 2.1), the cross-sections for alkali-noble gas spin exchange

collisions, alkali-noble/buffer gas spin-rotation collisions and alkali-alkali spin-axis collisions are on the order of 10^{-20} (Table 2.2), $10^{-22} - 10^{-25}$ (Table 2.4) and 10^{-16} cm^2 (Table 2.5)[11] respectively. Consequently, the rate of spin-exchange collisions at our operating temperature ($\sim 200°$) typically far exceed any other collisional rates. We acknowledge however, that for a sufficiently strong pump beam, the effective[12] pumping rate can plausibly be comparable or even exceed the rate of spin-exchange collisions. Nevertheless, in the absence of extremely strong pumping, which is typically the case for a continuously pumped co-magnetometer, spin-exchange collisions do occur much faster than any other process affecting the alkali atoms.

As first noted in [125], when there is an absence of any transverse spin polarization and when the rate of spin-exchange greatly exceeds any other processes, the rapid spin-exchange collisions re-distributes the populations of the various m_F sub-levels among the atoms and drives the populations into a distribution that is uniquely characterized by the longitudinal macroscopic ensemble-averaged electronic spin $\langle S_z \rangle$. We may derive this distribution from a purely statistical argument that is analogous to the derivation of the canonical ensemble for the case of a small sub-system that is in thermal equilibrium with a larger thermal reservoir that together with the smaller sub-system, is otherwise completely insulated from their environment. In our case, we may take the smaller sub-system to be an individual alkali atom that exchanges its longitudinal angular momentum m_F with a reservoir of other alkali atoms in the vapor through spin-exchange collisions. Since the total longitudinal angular momentum of the vapor F_{tot} is conserved, we may write that the probability an individual alkali

[11] Table 2.5 gives the temperature independent rate constants of spin-axis collisions. However, it is easy enough to convert it into an cross-section for comparison with the other collisional processes using (2.62). In fact, some older references like [124] give both.

[12] We say effective because if the atoms are fully polarized, then even a strong pump beam does not actually pump the atoms (see section 2.7.3).

atom has angular momentum m_F is

$$p(m_F) = \frac{\Omega_2(F_{tot} - m_F)}{\Omega_{1+2}(F_{tot})}, \tag{2.103}$$

where $\Omega_i(f)$ is the number of micro-states in system i that could correspond with system i having total longitudinal angular momentum f, and we are denoting the individual atom of interest and the rest of the atoms as sub-systems 1 and 2 respectively so that system $1+2$ consists of all the atoms in the vapor. If we define a "spin entropy" $s(f) \equiv \log(\Omega(f))$, we may write from (2.103)

$$\begin{aligned} \log(p) &= s_2(F_{tot} - m_F) - s_{1+2}(F_{tot}) \\ &\approx s_2(F_{tot}) - \underbrace{\left.\frac{ds_2}{df}\right|_{f=F_{tot}}}_{\beta} m_F - s_{1+2}(F_{tot}), \end{aligned} \tag{2.104}$$

where we have expanded $s_2(F_{tot} - m_F)$ around F_{tot} in the second line and have made the approximation that since sub-system 2 (the reservoir) is much larger than sub-system 1 (the individual atom), changes to its spin entropy due to small amounts of changes of its angular momentum from spin exchange with an individual atom is at most linear. Or in other words, higher derivatives of ds_2/df is zero. This is analogous to saying that the thermal bath is so much larger than the smaller sub system that its temperature (we note that in usual thermodynamics, $ds/dE = 1/T$) does not change in response to small energy exchanges with the smaller sub system. With this approximation, we may then write

$$\begin{aligned} p(m_F) &\approx e^{\beta m_F} e^{s_2(F_{tot}) + s_{1+2}(F_{tot})} \propto e^{\beta m_F} \\ \implies p(m_F) &= \frac{1}{Z} e^{\beta m_F}, \end{aligned} \tag{2.105}$$

where Z is the partition function that normalizes $p(m_F)$ so that $\sum_{m_F} p(m_F) = 1$. We note here that the sum over m_F is not merely over all distinct m_F but rather over all the micro-states. This is an important distinction since certain m_F values are degenerate in the sense that there are more than one micro-state (i.e. combination of m_I and m_S) that corresponds to a given m_F value. The correct partition function Z is therefore

$$Z = \sum_{m_F} e^{\beta m_F} = \underbrace{\sum_{m_I=-I}^{I} e^{\beta m_I}}_{Z_I} \underbrace{\sum_{m_S=-S}^{S} e^{\beta m_S}}_{Z_S}. \tag{2.106}$$

We note that for arbitrary spin J, the spin partition function Z_J is given by

$$Z_J = \sum_{m=-J}^{J} e^{\beta m} = e^{-\beta J} \sum_{m=0}^{2J} \left(e^{\beta}\right)^m = \frac{e^{-\beta J} - e^{\beta J + \beta}}{1 - e^{\beta}} = \frac{\sinh \beta \left(J + \frac{1}{2}\right)}{\sinh \frac{\beta}{2}}. \tag{2.107}$$

Although (2.105) as we have derived it refers to the probability that an individual atom has longitudinal angular momentum m_F, we note that for a vapor with no transverse spin polarization, its density matrix is diagonal. Moreover, as discussed in section 2.2, the diagonal element $\langle m_F | \rho | m_F \rangle$ of the density matrix may be interpreted as the probability that an atom selected at random from the ensemble will be in the eigenstate $|m_F\rangle$. Consequently, for a vapor with no transverse spin polarization and spin-exchange rates greatly exceeding that of other rates, the alkali atoms settle into a "spin-temperature equilibrium" where their density matrix is given by (2.105). The mean electronic spin is

$$\langle S_z \rangle = \sum_{m_S} m_S \sum_{m_I} \frac{e^{\beta m_I} e^{\beta m_S}}{Z_I Z_S} = \frac{d}{d\beta} \log Z_S = \frac{1}{2} \tanh \frac{\beta}{2}, \tag{2.108}$$

where we have used $Z_S = \sinh\beta/\sinh(\beta/2)$ from (2.107) in the last equality. If we, as usual, define the polarization $P_z^e \equiv \langle S_z\rangle / S$, then we have

$$P_z^e = \tanh\frac{\beta}{2}, \tag{2.109}$$

so that, as promised, in the limit of spin temperature equilibrium, the density matrix (or the populations of the m_F sub-levels) is uniquely determined by the longitudinal electronic spin polarization. Similarly, the ensemble averaged total angular momentum $\langle F_z\rangle$ is given by

$$\langle F_z\rangle = \sum_{m_F}\frac{m_F e^{\beta m_F}}{Z} = \frac{d}{d\beta}\log Z = \frac{2I+1}{2}\coth\left(\frac{2I+1}{2}\beta\right) - \coth\beta - \coth\frac{\beta}{2}, \tag{2.110}$$

so that the ratio of $\langle F_z\rangle$ / $\langle S_z\rangle$ is

$$\frac{\langle F_z\rangle}{\langle S_z\rangle} = \frac{(2I+1)\coth\left(\frac{2I+1}{2}\beta\right) - 2\coth\beta - 2\coth\frac{\beta}{2}}{\tanh\frac{\beta}{2}}. \tag{2.111}$$

This may be simplified using the Brillouin function [126], which is defined as

$$B_J(x) = \frac{2J+1}{2J}\coth\left(\frac{2J+1}{2J}x\right) - \frac{1}{2J}\coth\left(\frac{1}{2J}x\right), \tag{2.112}$$

so that we have

$$\frac{\langle F_z\rangle}{\langle S_z\rangle} = \frac{2IB_I(I\beta) + B_{1/2}\left(\frac{\beta}{2}\right)}{B_{1/2}\left(\frac{\beta}{2}\right)} = 1 + \epsilon(I,\beta), \tag{2.113}$$

where the paramagnetic coefficient $\epsilon(I,\beta)$ is defined to be

$$\epsilon(I,\beta) \equiv 2I\frac{B_I(I\beta)}{B_{1/2}\left(\frac{\beta}{2}\right)} \tag{2.114}$$

By using (2.109), we may re-write $\epsilon(I, \beta)$ in terms of the electronic polarization P[13]. For the typical cases of $I = 3/2$ (e.g K and ^{87}Rb) and $I = 5/2$ (e.g. ^{85}Rb), we have

$$\epsilon\left(\frac{3}{2}, P\right) = \frac{5 + P^2}{1 + P^2} \tag{2.115}$$

$$\epsilon\left(\frac{5}{2}, P\right) = \frac{35 + 42P^2 + 3P^4}{3 + 10P^2 + 3P^4}. \tag{2.116}$$

Tabulated expressions of $\epsilon(I, P)$ are available from [73] for $I = 0$ to $I = 7/2$ in half integer increments.

2.5 Spin-Exchange Relaxation Free Regime

Although spin-exchange collisions between alkali atoms do not contribute to the relaxation of the alkali's vapor longitudinal polarization, they do contribute to the relaxation of the macroscopic transverse polarization [78]. This is potentially problematic for atomic magnetometers (and co-magnetometers) since they typically work by measuring the (transverse) precession of the atomic vapor's macroscopic spin polarization and consequently, their sensitivity to magnetic fields δB scales inversely with the coherence time of the vapor's transverse spin polarization. More precisely, the spin-projection noise of the atomic magnetometer is [127]

$$\delta B = \frac{1}{\gamma\sqrt{nT_2Vt}}, \tag{2.117}$$

where γ is the (effective) gyromagnetic ratio, n is the number density of alkali atoms, T_2 is the transverse polarization coherence time and V, t are the measurement volume and time respectively. In the presence of spin-exchange collisions, T_2 is frequently limited by the rate of spin-exchange collisions, which prevents atomic magnetometers

[13] We drop the sub and superscripts for convenience.

from achieving high sensitivity to magnetic fields (i.e. small δB). Physically, spin-exchange collisions contribute to relaxation of the macroscopic transverse polarization because they can cause ground state alkali atoms to transition from one hyperfine manifold to another. However, according to (2.18), alkali atoms in the $F = I + 1/2$ hyperfine manifold precess in the opposite direction from atoms in the $F = I - 1/2$ manifold. It is evident then, that spin-exchange collisions, by causing individual atoms to randomly transition from one hyperfine manifold to another, will cause individual atoms to randomly precess in different directions and cause the macroscopic transverse polarization to decohere.

Nevertheless, as was first discovered by Happer and Tang [128], there exist a "spin-exchange relaxation free" (SERF) regime where transverse relaxation due to spin-exchange collisions can be eliminated at sufficiently high alkali densities and low magnetic fields. Although a rigorous mathematical description of this phenomenon is not trivial (the evolution of the density matrix under spin-exchange collisions is not linear), it is not difficult to paint a physical picture that informs the origins of SERF. Essentially, at sufficiently high alkali densities and low magnetic fields so that the rate of spin-exchange collisions greatly exceeds the precession frequency, the spin of an alkali atom has hardly precessed in one direction before it begins to precess in the opposite direction after undergoing a spin-exchange collision with another alkali atom. All other things being equal, this implies that there will be little to no precession of the macroscopic polarization. However, since there are more m_F sub-levels in the $F = I + 1/2$ manifold compared to the $F = I - 1/2$ manifold, the alkali atom will on average populate the $F = I + 1/2$ manifold more frequently as compared to the $F = I - 1/2$ manifold. Consequently, there is on the whole still a net coherent albeit slowed down precession of the macroscopic polarization.

Another way of stating the SERF regime is to say that the spin-exchange rate is so much faster than the Larmor precession that spin temperature equilibrium is

maintained even in the presence of small transverse excitation. In that case, we may easily write down the effect of the SERF regime on small transverse excitation. From (2.3), the ground state Hamiltonian is

$$\begin{aligned} H_g &= A_g \mathbf{I}\cdot\mathbf{S} + g_s\mu_B \mathbf{S}\cdot(\mathbf{B}+\boldsymbol{\beta}_e) - \frac{\mu_I}{I}\mathbf{I}\cdot\mathbf{B} \\ H_g &\approx A_g \mathbf{I}\cdot\mathbf{S} + g_s\mu_B \mathbf{S}\cdot\mathbf{B} \equiv H_{hf} + H_B, \end{aligned} \tag{2.118}$$

where we have dropped the term involving μ_I since that is typically ~ 1000 times smaller than μ_B and have for convenience defined H_{hf} and H_B as the parts of the Hamiltonian due to the hyperfine and magnetic interaction respectively. Moreover, since $\boldsymbol{\beta}_e$ has basically the same form as $\mathbf{B}$, we have for brevity dropped it here since it is obvious that it will, in this context, have the same behavior as $\mathbf{B}$. From (2.29), the ground state Hamiltonian causes the density matrix to evolve as

$$\frac{d\rho_g}{dt} = \frac{1}{i\hbar}[H_{hf},\rho] + \frac{1}{i\hbar}[H_B,\rho], \tag{2.119}$$

while from (2.59)[14], spin-exchange collisions with like alkali atoms cause the density matrix to evolve as

$$\frac{d\rho_{ex}}{dt} \approx \frac{1}{T_{ex}}\left(\phi\left(1+4\left\langle\mathbf{S}\right\rangle\cdot\mathbf{S}\right)-\rho\right). \tag{2.120}$$

The evolution of the macroscopic ensemble averaged total angular momentum $\langle\mathbf{F}\rangle$ is then

$$\frac{d\left\langle\mathbf{F}\right\rangle}{dt} = \mathrm{Tr}\left[\frac{d\rho_g}{dt}\mathbf{F}\right] + \mathrm{Tr}\left[\frac{d\rho_{ex}}{dt}\mathbf{F}\right]. \tag{2.121}$$

From (2.73), we know that the spin-exchange collisions conserve $\langle\mathbf{F}\rangle$ and so it remains to compute the first term on the r.h.s above. The first term itself comprises of two terms: $\mathrm{Tr}([H_{hf},\rho]\mathbf{F})/i\hbar$ and $\mathrm{Tr}([H_B,\rho]\mathbf{F})/i\hbar$. Since the hyperfine interaction conserves the total angular momentum, we expect that $A_g\,\mathrm{Tr}([\mathbf{I}\cdot\mathbf{S},\rho]\mathbf{F})/i\hbar$ is zero.

[14] We consider only species and drop the i, j indices here.

Indeed, using (A.48) and the fact that $\mathbf{I}$ and $\mathbf{S}$ commutes, it is straightforward to show that

$$\mathrm{Tr}([\mathbf{I}\cdot\mathbf{S},\rho]\mathbf{S}) = i\,\mathrm{Tr}(\mathbf{I}\times\rho\mathbf{S}), \tag{2.122}$$

and

$$\mathrm{Tr}([\mathbf{I}\cdot\mathbf{S},\rho]\mathbf{I}) = -i\,\mathrm{Tr}(\mathbf{I}\times\rho\mathbf{S}) \tag{2.123}$$

so that

$$\mathrm{Tr}([\mathbf{I}\cdot\mathbf{S},\rho]\mathbf{F}) = \mathrm{Tr}([\mathbf{I}\cdot\mathbf{S},\rho](\mathbf{I}+\mathbf{S})) = 0. \tag{2.124}$$

Therefore $\mathrm{Tr}([H_{hf},\rho]\mathbf{F})/i\hbar = 0$ as expected and it remains to compute $\mathrm{Tr}([H_B,\rho]\mathbf{F})/i\hbar = g_s\mu_B(\mathrm{Tr}([\mathbf{S}\cdot\mathbf{B},\rho]\mathbf{S}) + \mathrm{Tr}([\mathbf{S}\cdot\mathbf{B},\rho]\mathbf{I}))/i\hbar$. To do so, we note that

$$\mathrm{Tr}[\mathbf{S}\cdot\mathbf{B}\rho\mathbf{I}] = B^i\,\mathrm{Tr}[S_i\rho I^j] = B^i\,\mathrm{Tr}[I^jS_i\rho], \tag{2.125}$$

and

$$\mathrm{Tr}[\rho\mathbf{S}\cdot\mathbf{B}\mathbf{I}] = B^i\,\mathrm{Tr}[\rho S_iI^j] = B^i\,\mathrm{Tr}[S_iI^j\rho] = B^i\,\mathrm{Tr}[I^jS_i\rho], \tag{2.126}$$

so that $\mathrm{Tr}([\mathbf{S}\cdot\mathbf{B},\rho]\mathbf{I})$=0. Moreover, by making use of (A.48) we have

$$\begin{aligned}\mathrm{Tr}[\mathbf{S}\cdot\mathbf{B}\rho\mathbf{S}] = \mathrm{Tr}[B^i\rho S^jS_i] &= \mathrm{Tr}\left[\frac{\rho}{4}B^j + \frac{i}{2}\rho\epsilon^j{}_i{}^kB^iS_k\right]\\ &= \frac{\mathbf{B}}{4} + \frac{i}{2}\mathbf{B}\times\langle\mathbf{S}\rangle\,,\end{aligned} \tag{2.127}$$

and

$$\begin{aligned}\mathrm{Tr}[\rho\mathbf{S}\cdot\mathbf{B}\mathbf{S}] = \mathrm{Tr}[\rho B_iS^iS^j] &= \mathrm{Tr}\left[\frac{\rho}{4}B^j - \frac{i}{2}\epsilon^{jik}B_i\rho S_k\right]\\ &= \frac{\mathbf{B}}{4} - \frac{i}{2}\mathbf{B}\times\langle\mathbf{S}\rangle\,,\end{aligned} \tag{2.128}$$

so that $\mathrm{Tr}([\mathbf{S}\cdot\mathbf{B},\rho]\mathbf{S}) = i\mathbf{B}\times\langle\mathbf{S}\rangle$. Consequently,

$$\mathrm{Tr}\left[\frac{d\rho_g}{dt}\mathbf{F}\right] = \frac{1}{i\hbar}\mathrm{Tr}([H_B,\rho]\mathbf{F}) = \frac{g_s\mu_B}{\hbar}\mathbf{B}\times\langle\mathbf{S}\rangle = \gamma_e\mathbf{B}\times\langle\mathbf{S}\rangle\,, \tag{2.129}$$

and the precession of $\langle\mathbf{F}\rangle$ is therefore

$$\frac{d\langle\mathbf{F}\rangle}{dt} = \mathrm{Tr}\left[\frac{d\rho_g}{dt}\mathbf{F}\right] + \mathrm{Tr}\left[\frac{d\rho_{ex}}{dt}\mathbf{F}\right] = \gamma_e\mathbf{B}\times\langle\mathbf{S}\rangle\,, \tag{2.130}$$

where $\gamma_e \equiv g_s\mu_B/\hbar$ is here the gryomagnetic ratio of the free electron. In the SERF regime when the alkali atoms maintain spin-exchange equilibrium even in the presence of small transverse excitation, we may approximate (2.113) as

$$\frac{\langle F_z\rangle}{\langle S_z\rangle} = 1+\epsilon(I,\beta) \approx \frac{\langle\mathbf{F}\rangle}{\langle\mathbf{S}\rangle}, \tag{2.131}$$

so that in the SERF regime, we may from (2.130) obtain

$$\frac{d\langle\mathbf{S}\rangle}{dt} = \frac{\gamma_e}{1+\epsilon(I,\beta)}\mathbf{B}\times\langle\mathbf{S}\rangle = \frac{\gamma_e}{Q(I,\beta)}\mathbf{B}\times\langle\mathbf{S}\rangle\,, \tag{2.132}$$

where as expected, we see a precession frequency that is slowed down by a factor

$$Q(I,\beta) \equiv 1+\epsilon(I,\beta). \tag{2.133}$$

We note that $Q(I,\beta)$ here depends on the polarization P through the spin-temperature β and it includes the slowing down factor (from the precession of a free electron) due to both the hyperfine interaction and spin-exchange collisions. For the common case of $I = 3/2$, we may use (2.115) to write $Q(I,\beta)$ in terms of the polarization $P = \langle S\rangle/S$ to obtain

$$Q\left(\frac{3}{2},P\right) = 2+\frac{4}{1+P^2}. \tag{2.134}$$

The results above are strictly speaking only completely exact at infinitely high spin-exchange rates. In reality, there is, of course, a continuum between the SERF regime and non-SERF regime. The precession frequency ω and transverse coherence time T_2 (due to spin-exchange collisions) in this intermediate region can be non-trivial to calculate, particularly at high alkali polarizations since the spin-exchange operators has terms that are quadratic in ρ. Nevertheless, in the limit of low polarization so that terms quadratic in ρ can be ignored, and for the usual case whereby the hyperfine coupling A_g is much larger than both the spin-exchange rate T_{se} and $\omega_0 = \gamma_e B/(2I+1)$, a perturbative treatment yields an analytic expression for T_2 and ω [129]

$$\frac{1}{T_2} + i\omega = \frac{(2I+1)^2+2}{3T_{ex}(2I+1)^2} - \sqrt{-\omega_0^2 + \left(\frac{(2I+1)^2+2}{3T_{ex}(2I+1)^2}\right)^2 - i\frac{2\omega_0}{T_{ex}(2I+1)}}, \tag{2.135}$$

where T_2, $\omega \in \mathbb{R}$ and T_{ex}, the time in between spin-exchange collisions, is as defined in (2.61). In the limit of fast spin-exchange so that $\omega_0 T_{ex} \ll 1$, the radical in (2.135) may be expanded to give [129]

$$\omega \approx \frac{\omega_0}{C} + \frac{\omega_0^3 T_{ex}^2 (2I+1)^2 (1-C^{-2})}{2C^3} \tag{2.136}$$

$$\frac{1}{T_2} \approx \frac{\omega_0^2 T_{ex}(2I+1)(1-C^{-2})}{2C} - \frac{(\omega_0 T_{ex}(2I+1))^3 (1-6C^{-2}+5C^{-4})}{8C^3}, \tag{2.137}$$

where C is, for convenience, defined as

$$C \equiv \frac{(2I+1)^2+2}{3(2I+1)}. \tag{2.138}$$

We note that to first order, $1/T_2$ is proportional to the square of the magnetic field (since $\omega_0 \propto B$). These expressions are useful in relating T_2 and ω_0 with the spin-

exchange rate $1/T_{ex}$ and can allow us to determine T_{ex} (and by extension the density of alkali atoms n_a) by measuring T_2 while varying ω_0.

2.6 Light-Atom Interactions

The interactions of alkali atoms with light give the experimentalist a convenient way to control and manipulate alkali atoms. In this section, we discuss the interactions between alkali atoms and light that is relevant to the co-magnetometer. It suffices to describe the light classically at the laser wavelengths and intensities pertinent to the operation of the co-magnetometer and we therefore start by quoting Maxwell's equations[15]:

$$\nabla \cdot \mathbf{E} = 4\pi\rho \tag{2.139}$$

$$\nabla \cdot \mathbf{B} = 0 \tag{2.140}$$

$$\nabla \times \mathbf{E} = -\frac{1}{c}\frac{\partial \mathbf{B}}{\partial t} \tag{2.141}$$

$$\nabla \times \mathbf{H} = \frac{4\pi}{c}\mathbf{J}_f + \frac{1}{c}\frac{\partial \mathbf{D}}{\partial t}. \tag{2.142}$$

The auxillary fields are defined in Gaussian CGS units as:

$$\mathbf{D} = \mathbf{E} + 4\pi\mathbf{P} \tag{2.143}$$

$$\mathbf{B} = \mathbf{H} + 4\pi\mathbf{M}. \tag{2.144}$$

In a neutral non-magnetic atomic vapor, $\rho = 0$ (to a good approximation on the scale of the laser wavelengths of interest) and $\mathbf{J}_f = \mathbf{M} = 0$ and so taking the curl on

[15] We use Gaussian CGS units here primarily because the polarizability tensor $\overleftrightarrow{\alpha}$, which we shall soon discuss, is typically given in CGS units in the literature.

both sides of (2.141) gives

$$\nabla \times (\nabla \times \mathbf{E}) = -\frac{1}{c}\frac{\partial}{\partial t}\nabla \times \mathbf{B} \tag{2.145}$$

$$\implies \nabla^2 \mathbf{E} - \frac{1}{c^2}\frac{\partial^2 \mathbf{E}}{\partial t^2} = \frac{4\pi}{c^2}\frac{\partial^2 \mathbf{P}}{\partial t^2}. \tag{2.146}$$

$\mathbf{P}$ is the macroscopic polarization density of the atomic vapor and can be expressed as $\mathbf{P} = n\langle \mathbf{p} \rangle$, where n is the density of alkali atoms and $\langle \mathbf{p} \rangle$ is the ensemble averaged dipole moment of an alkali atom[16]. The dipole moment $\langle \mathbf{p} \rangle$ depends on the electric field $\mathbf{E}$ via the polarizability tensor and is given by $\langle \mathbf{p} \rangle = \langle \overleftrightarrow{\alpha} \rangle \cdot \mathbf{E}$. Equation (2.146) then becomes

$$\nabla^2 \mathbf{E} - \frac{1}{c^2}\frac{\partial^2 \mathbf{E}}{\partial t^2} = \frac{4\pi n}{c^2}\frac{\partial^2}{\partial t^2}\langle \overleftrightarrow{\alpha} \rangle \cdot \mathbf{E}. \tag{2.147}$$

Evidently, understanding light-atom interactions comes down to understanding the origins of the polarizability tensor $\langle \overleftrightarrow{\alpha} \rangle$. The derivation of $\langle \overleftrightarrow{\alpha} \rangle$ in this context was first carefully derived by Happer and Mathur in [130] and we detail that derivation below since a variety of light-atom phenomenon relevant to the co-magnetometer trace their origins back to the polarizability tensor.

2.6.1 Polarizability tensor

Since the polarizability tensor is defined via the relation $\langle \mathbf{p} \rangle = \langle \overleftrightarrow{\alpha} \rangle \cdot \mathbf{E}$, we can derive an expression for it if we can compute $\langle \mathbf{p} \rangle$ from first principles. To do so, we note that $\langle \mathbf{p} \rangle$, which is the ensemble averaged dipole moment of an alkali atom, is given by the expectation value $\langle \psi | \mathbf{p} | \psi \rangle$ of the dipole moment operator $\mathbf{p}$ for a single atom, averaged over the collisional history and velocity distribution of the atom. If the mean time between collisions is given by $1/\gamma_c$, then the probability $P(t - t')\, dt'$ that

[16] The ensemble average here includes an average over the different velocities and collisional histories of the atom

the last collision happened at time t' (for $t' < t$) is given by:

$$P(t-t')\,dt' = \gamma_c\, e^{-\gamma_c(t-t')}\,dt'. \tag{2.148}$$

Moreover, for the alkali densities ($\sim 10^{13} - 10^{14}$ cm^{-3}) of interest in a co-magnetometer, the atoms can be viewed as mostly non-interacting particles except for brief periods during collisions. As such, we expect their velocities to obey the Maxwell-Boltzmann distribution and the probability of finding an atom with velocity $\mathbf{v}$ is thus[17]

$$N(\mathbf{v})\,d\mathbf{v} = \left(\frac{m_a}{2\pi k_B T}\right)^{3/2} e^{-\frac{m_a v^2}{2k_B T}}\,d\mathbf{v}, \tag{2.149}$$

and so $\langle \mathbf{p} \rangle$ is given by:

$$\langle \mathbf{p} \rangle = \int_{-\infty}^{t} dt'\, P(t-t') \int d\mathbf{v}\, N(\mathbf{v}) \langle \psi\, |\mathbf{p}|\, \psi \rangle\,. \tag{2.150}$$

To make further progress, we will have to compute $\langle \psi\, |\mathbf{p}|\, \psi \rangle$. The wavefunction of the atom can be expanded in terms of the eigenfunctions of the ground state $\{|\mu\rangle\}$ and of the excited state $\{|m\rangle\}$ in between collisions[18]

$$|\psi(t)\rangle = \sum_m a_m e^{-iE_m t/\hbar}\,|m\rangle + \sum_\mu a_\mu e^{-iE_\mu t/\hbar}\,|\mu\rangle\,, \tag{2.151}$$

and the expectation value of the dipole moment operator $\mathbf{p}$ for a single atom is therefore

$$\langle \psi\, |\mathbf{p}|\, \psi \rangle = \sum_{\nu m} a_\nu^* a_m e^{i\omega_{\nu m} t} \mathbf{p}_{\nu m} + \text{c.c}, \tag{2.152}$$

[17] We use m_a here to denote the mass of the alkali atom to avoid confusion with m which is later used in this section as an index for excited states. k_B is, as usual, the Boltzmann constant and T is the temperature.

[18] We use curly brackets to denote a set. For example, $\{|\mu\rangle\}$ denotes the set of ground state eigenfunctions. Also, throughout this section, we will use Latin alphabet to denote excited states and Greek alphabet to denote ground states.

where we have used the shorthand notation $\omega_{\nu m} \equiv (E_\nu - E_m)/\hbar$, $\mathbf{p}_{\nu m} \equiv \langle \nu \left| \mathbf{p} \right| m \rangle$. We now wish to find an expression for a_m, the excited state amplitudes. During intervals between collisions, the wavefunction of the alkali atom evolves according to Schrodinger's equation:

$$i\hbar \frac{\partial}{\partial t} \left| \psi(t) \right\rangle = \left(H_0 - \mathbf{p} \cdot \mathbf{E} \right) \left| \psi(t) \right\rangle . \tag{2.153}$$

Substituting (2.151) into (2.153) and recalling that $\langle m \left| \mathbf{p} \cdot \mathbf{E} \right| n \rangle = 0$ by the dipole selection rule then gives us

$$i\dot{a}_m = -i\frac{\Gamma}{2} a_m - \sum_\mu \left\langle m \left| \frac{\mathbf{E} \cdot \mathbf{p}}{\hbar} \right| \mu \right\rangle a_\mu e^{i\omega_{m\mu} t}, \tag{2.154}$$

where the first term of (2.154) was added to account for relaxation from the excited state via spontaneous emission and $1/\Gamma$ is the radiative lifetime of the excited state.

For simplicity and without loss of generality, we shall treat $\mathbf{E}$ as a monochromatic laser field:

$$\mathbf{E}(\mathbf{r}, t) = \frac{E_0}{2} e^{i(\mathbf{k}\cdot\mathbf{r} - \omega t)} \mathbf{e} + \text{c.c.} \tag{2.155}$$

The complex polarization vector $\mathbf{e}$ is normalized so that $\mathbf{e} \cdot \mathbf{e}^* = \mathbf{e}^* \cdot \mathbf{e} = 1$. Without loss of generality, we may also define our co-ordinates so that the atom's position $\mathbf{R}$ at time $t = 0$ is at the origin and therefore $\mathbf{R}(t) = \mathbf{v}t$. Substituting $\mathbf{E}(\mathbf{R}, t)$ into (2.154) and integrating from t' to t then yields, after dropping an rapidly oscillating term,

$$\begin{aligned} i a_m(t) =& i a_m(t') e^{-\Gamma/2 (t - t')} \\ & - \frac{E_0}{2\hbar} e^{i(\mathbf{k}\cdot\mathbf{R} - \omega t)} \sum_\mu \mathbf{p}_{m\mu} \cdot \mathbf{e}\, e^{i\omega_{m\mu} t} a_\mu \frac{1 - e^{-i(\omega_{m\mu} - \omega + \mathbf{k}\cdot\mathbf{v} - i\Gamma/2)(t - t')}}{i\left(\omega_{m\mu} - \omega + \mathbf{k}\cdot\mathbf{v} - i\Gamma/2\right)}, \end{aligned} \tag{2.156}$$

where we have assumed that the ground state amplitude a_μ are slowly varying with respect to to the excited state decay rate Γ and can be approximated as constant over a time interval t to t' in between collisions. The expectation value of the dipole moment operator (2.152) is therefore

$$\begin{aligned}\langle\psi\,|\mathbf{p}|\,\psi\rangle = &\sum_{\nu m} a_\nu^* \mathbf{p}_{\nu m} a_m(t') e^{i\omega_{\nu m} t} e^{-\Gamma/2(t-t')} \\ &- \frac{E_0}{i2\hbar} e^{i(\mathbf{k}\cdot\mathbf{R}-\omega t)} \sum_{m\nu\mu} \Big[a_\nu^* \mathbf{p}_{\nu m} \left(\mathbf{p}_{m\mu}\cdot\mathbf{e}\right) e^{i\omega_{\nu\mu} t} a_\mu \\ &\times \frac{1 - e^{-i(\omega_{m\mu}-\omega+\mathbf{k}\cdot\mathbf{v}-i\Gamma/2)(t-t')}}{i\left(\omega_{m\mu}-\omega+\mathbf{k}\cdot\mathbf{v}-i\Gamma/2\right)} \Big] + \text{c.c.} \end{aligned} \tag{2.157}$$

With this expression in hand, we can now average (2.157) over the collisional histories and possible velocities of the atom to obtain the ensemble averaged dipole moment $\langle\mathbf{p}\rangle$. To do this, we first note that the excited state amplitude $a_m(t')$ in the first term of (2.157) will average to zero since it is rapidly randomized by each collisions. On the other hand, the ground state amplitudes $\{a_\mu\}$, as we have noted earlier, vary slowly on these time scales (for a discussion about the different relaxation behaviors of the ground and excited state of alkali atoms see [75]) and $a_\mu a_\nu^*$ in the second term of (2.157) can therefore be replaced by an average value $\langle a_\mu a_\nu^*\rangle$. Performing the time integral and re-writing the velocity integral with the help of the plasma dispersion function $Z(\xi)$, we obtain

$$\langle\mathbf{p}\rangle = \sum_{\nu\mu m} a_\mu a_\nu^* e^{i\omega_{\nu\mu} t} \frac{1}{k}\sqrt{\frac{m_a}{2k_B T}} Z\left(\xi\left(\omega_{m\mu}\right)\right) \frac{1}{\hbar}\mathbf{p}_{\nu m}\left(\mathbf{p}_{m\mu}\cdot\frac{E_0}{2} e^{i(\mathbf{k}\cdot\mathbf{R}-\omega t)}\mathbf{e}\right) + \text{c.c}, \tag{2.158}$$

where the plasma dispersion function $Z(\xi)$ is [131]

$$Z(\xi(\omega_{m\mu})) = \frac{1}{\sqrt{\pi}}\int_{-\infty}^{\infty} du\, \frac{e^{-u^2}}{u-\xi}, \tag{2.159}$$

and its argument $\xi(\omega_{m\mu})$ is defined as

$$\xi \equiv \frac{1}{k}\sqrt{\frac{m_a}{2k_BT}}\left[\omega - \omega_{m\mu} + i\left(\frac{\Gamma}{2} + \gamma_c\right)\right]. \tag{2.160}$$

We may rewrite (2.158) in the form $\langle \mathbf{p} \rangle = \langle \overleftrightarrow{\alpha} \rangle \cdot \mathbf{E}$ by writing the plasma-dispersion function (profile function) $Z(\xi(\omega_{m\mu}))$ as

$$\begin{aligned} Z(\omega_{m\mu}) &= \sum_{\nu} \delta_{\mu\nu}\delta_{\nu\mu} Z(\omega_{m\nu}) \\ &= \sum_{\nu} \langle \mu | \nu \rangle \langle \nu | \mu \rangle Z(\omega_{m\nu}) \\ &= \langle \mu | z(m) | \mu \rangle , \end{aligned}$$

where

$$z(m) = \sum_{\nu} |\nu\rangle \langle \nu| Z(\omega_{m\nu}), \tag{2.161}$$

and we therefore have from (2.158)

$$\begin{aligned} \langle \mathbf{p} \rangle = & \sum_{\nu\mu} \langle a_\mu a_\nu^* \rangle e^{i\omega_{\nu\mu}t} \\ & \times \left(\langle \nu | \frac{1}{k\hbar}\sqrt{\frac{m_a}{2k_BT}} \sum_m \mathbf{p} |m\rangle \langle m| \mathbf{p} |\mu\rangle \langle \mu | z(m) | \mu \rangle \right) \cdot \frac{E_0}{2} e^{i(\mathbf{k}\cdot\mathbf{R} - \omega t)} \mathbf{e} + \text{c.c} \\ & = \left(\sum_{\nu\mu} \rho_{\mu\nu} \overleftrightarrow{\alpha}_{\nu\mu} \right) \cdot \frac{E_0}{2} e^{i(\mathbf{k}\cdot\mathbf{R} - \omega t)} \mathbf{e} + \text{c.c} \\ & = \langle \overleftrightarrow{\alpha} \rangle \cdot \frac{E_0}{2} e^{i(\mathbf{k}\cdot\mathbf{R} - \omega t)} \mathbf{e} + \text{c.c}, \end{aligned} \tag{2.162}$$

where in the third line above, we have identified the ground state density matrix ρ (2.27) and the polarizability operator $\overleftrightarrow{\alpha}$ as

$$\rho = \sum_{\mu\nu} |\mu\rangle \langle\nu| \langle a_\mu a_\nu^* \rangle e^{i\omega_{\nu\mu}t} \tag{2.163}$$
$$\overleftrightarrow{\alpha} \equiv \frac{1}{k\hbar}\sqrt{\frac{m_a}{2k_BT}} \sum_m \mathbf{p}\,|m\rangle \langle m|\,\mathbf{p}\, z(m),$$

so that

$$\sum_{\nu\mu} \rho_{\mu\nu} \overleftrightarrow{\alpha}_{\nu\mu} = \mathrm{Tr}[\rho \overleftrightarrow{\alpha}] = \langle \overleftrightarrow{\alpha} \rangle .$$

Moreover, we can split the sum of m over all excited states in the definition of $\overleftrightarrow{\alpha}$ above into a double sum of F_e and m, where F_e is an excited state hyperfine manifold and m is now a Zeeman state within the F_e excited state hyperfine manifold. In that case, we have

$$\begin{aligned} \overleftrightarrow{\alpha} &\equiv \sum_{F_e} \frac{1}{k\hbar}\sqrt{\frac{m_a}{2k_BT}} \sum_m \mathbf{p}\,|F_e, m\rangle \langle F_e, m|\,\mathbf{p}\, z(m) \\ &\approx \sum_{F_e} \frac{1}{k\hbar}\sqrt{\frac{m_a}{2k_BT}} \kappa(F_e) \mathbf{p}\, z(F_e), \end{aligned} \tag{2.164}$$

where we have defined the effective ground state operator $\kappa(F_e)$ as

$$\kappa(F_e) \equiv \sum_m \mathbf{p}\,|F_e, m\rangle \langle F_e, m|\,\mathbf{p}, \tag{2.165}$$

and have made the approximation that since the alkali atoms in a co-magnetometer are in a near zero magnetic field environment during normal co-magnetometer operation, the Zeeman splitting of the hyperfine states are therefore negligibly small compared to the (Doppler broadened) splitting of the hyperfine manifolds and therefore $Z(\omega_{m\mu}) \approx Z(\omega_{F_eF_g})$, which implies $z(m) \approx z(F_e)$.

Expanding $\kappa(F_e)$ in spherical basis using the basis dyadics $\mathbf{Q}^L_{\rho+\sigma}$ (A.11) and spherical tensor operator $T^{\Lambda}_{\mu-\mu'}$ (A.19) and simplifying the matrix elements with the Wigner-Eckhart theorem (A.89), we obtain after some computation with the aid of identities in section A.3

$$\kappa(F_e) = \sum_{\substack{F_g F'_g \\ LM}} (-1)^{M+1} \mathbf{Q}^L_{-M} T^L_M \sqrt{(2F_g+1)(2F_e+1)} W(11F_g F'_g; LF_e) \times \langle F_g \,||\mathbf{p}||\, F_e\rangle \langle F_e \,||\mathbf{p}||\, F_g\rangle \,, \tag{2.166}$$

where W here is a Racah W co-efficient. The reduced matrix elements may be computed by using (A.90) and the Wigner-Eckhart theorem (A.89) by noting that firstly, the total transition rate from the excited electronic state $J_e = L_e + S$ to the ground state $J_g = L_g + S$ [132] is

$$\Gamma(J_e \to J_g) = \frac{1}{2J_e+1} \frac{64\pi^4}{h\lambda^3} \sum_{m\mu} |\langle J_e m \,|p_z|\, J_g \mu\rangle|^2 \,, \tag{2.167}$$

and secondly, that the transition rate $\Gamma(J_e \to J_g)$ is related to the oscillator strength f_{ge} of that transition by the relation [133]

$$\Gamma(J_e \to J_g) = \frac{2e^2\omega^2}{m_e c^3} \frac{2J_g+1}{2J_e+1} f_{ge}. \tag{2.168}$$

Using these relations, we obtain[19]

$$\langle F_g \,||\mathbf{p}||\, F_e\rangle \langle F_e \,||\mathbf{p}||\, F_g\rangle = (-1)^{F_e-F_g}\frac{3\hbar e^2 f_{ge}}{2m_e\omega}(2J_g+1)\sqrt{(2F_e+1)(2F_g'+1)} \times W(J_eF_eJ_gF_g;I1)W(J_eF_eJ_gF_g';I1), \tag{2.169}$$

and therefore

$$\kappa(F_e) = \hbar k\sqrt{\frac{2k_BT}{m_a}}\sum_{\substack{F_gF_g'\\LM}}\xi^L(F_g,F_g',F_e)(-1)^M\mathbf{Q}^L_{-M}T^L_M(F_g,F_g'), \tag{2.170}$$

where the coefficient ξ^L is

$$\xi^L(F_g,F_g',F_e) = 3G(-1)^{F_e-F_g+1}(2J_g+1)(2F_e+1)\sqrt{(2F_g+1)(2F_g'+1)} \times W(11F_gF_g';LF_e)W(J_eF_eJ_gF_g;I1)W(J_eF_eJ_gF_g';I1), \tag{2.171}$$

and G is here defined as

$$G = \frac{\lambda^2e^2f_{ge}}{8\pi^2m_ec}\sqrt{\frac{m_a}{2k_BT}}. \tag{2.172}$$

Substituting our expression for $\kappa(F_e)$ back into (2.164), we have at last our desired expression for the polarizability tensor $\overleftrightarrow{\alpha}$

$$\overleftrightarrow{\alpha} = \sum_L \overleftrightarrow{\alpha}^L, \tag{2.173}$$

[19] We note that there is, unfortunately, a sign discrepancy in (2.169) compared to [130]. Whereas we have $(-1)^{F_e-F_g}$, [130] has $(-1)^{F_e-F_g'}$. This discrepancy seems to stem from the sign factor in (A.90). As far as this author can tell, (A.90) as quoted is correct. However, this discrepancy isn't a major issue since [130] consistently uses (A.90) with a different sign factor and consequently, the multipole components of the polarizability tensor we eventually arrive at are identical because there is a corresponding sign difference in our expansion of the ground state operators.

where the L^{th} multipole component of $\overleftrightarrow{\alpha}$ is

$$\begin{aligned}\overleftrightarrow{\alpha}^L &= \sum_{\substack{F_g F_g' \\ M}} (-1)^M \mathbf{Q}^L_{-M} T^L_M(F_g, F_g') \sum_{F_e} \xi^L(F_g, F_g', F_e) Z(F_e, F_g') \\ &= \sum_{\substack{F_g F_g' \\ M}} (-1)^M \mathbf{Q}^L_{-M} T^L_M(F_g, F_g') A^L(F_g, F_g'), \end{aligned} \tag{2.174}$$

and

$$A^L(F_g, F_g') = \sum_{F_e} \xi^L(F_g, F_g', F_e) Z(F_e, F_g'). \tag{2.175}$$

$Z(F_e, F_g')$ here is the profile factor $Z(\omega_{F_e F_g'}) \approx Z(\omega_{m\mu})$ first defined in (2.159) and $\xi^L(F_g, F_g', F_e)$ is as defined in (2.171). We conclude this section by observing from (2.166) that $L = 0, 1, 2$ and the polarizability operator (and hence light-atom interactions) $\overleftrightarrow{\alpha}$ can therefore be neatly separated into a scalar $\overleftrightarrow{\alpha}^0$ component, a vector $\overleftrightarrow{\alpha}^1$ component, as well as a tensor $\overleftrightarrow{\alpha}^2$ component.

2.6.2 Multipole components of the polarizability tensor

Having obtained the polarizability tensor in the section above, we further compute the multipole components of the polarizability tensor here, which will give rise to different physical light-atom interactions. We shall, for the most part, consider alkali atoms where the energy splittings between the different excited hyperfine manifolds are small compared to the (Doppler broadened) splittings between the ground and excited state hyperfine manifolds. This is true for K, which is the main alkali atom of interest in the K-^{3}He co-magnetometer. For atoms like Rb (which is used in the pulsed co-magnetometer) where this is not true, a relatively straightforward generalization exist, which we shall discuss at the end of this section. In the case where this approximation

holds, we may approximate the profile factor $Z(F_e, F'_g)$ as

$$Z(F_e, F'_g) \approx Z(F'_e, F'_g) = Z(F'_g) \equiv Z_{F'_g}. \tag{2.176}$$

The coefficient A^L (2.175) can then be approximated as

$$\begin{aligned} A^L(F_g, F'_g) &\approx Z_{F'_g} \sum_{F_e} \xi^L(F_g, F'_g, F_e) \\ &= Z_{F'_g} 3G(2J_g+1)\sqrt{(2F_g+1)(2F'_g+1)} \\ &\times \sum_{F_e} (-1)^{F_e - F_g + 1}(2F_e+1) W(11F_gF'_g; LF_e) W(J_eF_eJ_gF_g; I1) W(J_eF_eJ_gF'_g; I1). \end{aligned} \tag{2.177}$$

The sum over the three W coefficient is most easily evaluated by first converting them into Wigner 6-J symbols (A.83), applying the Wigner 6-J symmetry relations and then using (A.87):

$$\begin{aligned} &\sum_{F_e} (-1)^{F_e}(2F_e+1) W(11F_gF'_g; LF_e) W(J_eF_eJ_gF_g; I1) W(J_eF_eJ_gF'_g; I1) \\ &= (-1)^{2\left(F_g+F'_g+J_e+J_g\right)} \sum_{F_e} (-1)^{3F_e}(2F_e+1) \begin{Bmatrix} 1 & 1 & L \\ F'_g & F_g & F_e \end{Bmatrix} \begin{Bmatrix} J_e & F_e & I \\ F_g & J_g & 1 \end{Bmatrix} \begin{Bmatrix} J_e & F_e & I \\ F'_g & J_g & 1 \end{Bmatrix} \\ &= (-1)^{2\left(F_g+F'_g+J_e+J_g\right)} \sum_{F_e} (-1)^{3F_e}(2F_e+1) \begin{Bmatrix} 1 & F_e & F_g \\ F'_g & L & 1 \end{Bmatrix} \begin{Bmatrix} I & F_e & J_e \\ 1 & J_g & F'_g \end{Bmatrix} \begin{Bmatrix} 1 & F_e & F_g \\ I & J_g & J_e \end{Bmatrix} \\ &= (-1)^{-3+L+2F_g-F'_g} W(F_gLIJ_g; F'_gJ_g) W(1LJ_eJ_g; 1J_g), \end{aligned} \tag{2.178}$$

where we have also made use of the fact that $F'_g + J_e - I, L \in \mathbb{Z}$ in the last line. Substituting this into (2.177), we obtain

$$A^L(F_g, F'_g) \approx Z_{F'_g} \xi^L(F_g, F'_g), \tag{2.179}$$

where[20]

$$\xi^L(F_g, F_g') = (-1)^{F_g - F_g' + L} 3G(2J_g + 1)\sqrt{(2F_g + 1)(2F_g' + 1)} \times W(F_g L I J_g; F_g' J_g) W(1 L J_e J_g; 1 J_g). \tag{2.180}$$

The scalar component of the polarizability tensor $\overleftrightarrow{\alpha}^0$ is then, after using (A.78),(A.12), (A.18) and the Clebsch-Gordan properties in section A.3

$$\begin{aligned} \overleftrightarrow{\alpha}^0 &\approx \sum_{F_g F_g' M} \xi^0(F_g, F_g') Z_{F_g'} (-1)^M \mathbf{Q}^0_{-M} T^0_M(F_g, F_g') \\ &= G \sum_{F_g \mu} |F_g, \mu\rangle \langle F_g, \mu| Z_{F_g}. \end{aligned} \tag{2.181}$$

The vector component of the polarizability tensor $\overleftrightarrow{\alpha}^1$ can be computed in a similar manner. From (2.174) and (2.179), we have

$$\overleftrightarrow{\alpha}^1 = \sum_{F_g F_g' M} \xi^1(F_g, F_g') Z_{F_g'} (-1)^M \mathbf{Q}^1_{-M} T^1_M(F_g, F_g'), \tag{2.182}$$

where from (2.180) and for $J_g = 1/2$,

$$\xi^1(F_g, F_g') = -(-1)^{F_g - F_g'} 6G\sqrt{(2F_g + 1)(2F_g' + 1)} W\left(F_g 1 I \frac{1}{2}; F_g' \frac{1}{2}\right) W\left(1 1 J_e \frac{1}{2}; 1 \frac{1}{2}\right). \tag{2.183}$$

The last W coefficient can be evaluated by applying the symmetry relation (A.81) and using (A.88) to obtain

$$W\left(1 1 J_e \frac{1}{2}; 1 \frac{1}{2}\right) = \frac{11 - 4J_e(J_e + 1)}{24}, \tag{2.184}$$

[20] We note the sign discrepancy with [130] here that arises from the earlier discrepancy in (2.169).

and therefore, after applying the symmetry relation (A.80) to the first W coefficient, we obtain

$$\overleftrightarrow{\alpha}^1 \approx -\frac{G}{4}\left(11-4J_e\left(J_e+1\right)\right)\sum_M(-1)^M\mathbf{Q}^1_{-M}\sum_{F_gF_g'}\sqrt{(2F_g+1)(2F_g'+1)}$$
$$\times W\left(1\frac{1}{2}F_gI;\frac{1}{2}F_g'\right)T^1_M(F_g,F_g')Z_{F_g'}. \tag{2.185}$$

The expression above for $\overleftrightarrow{\alpha}^1$ may be expressed in terms of the familiar magnetic dipole moment operator $\boldsymbol{\mu}=-g_J\mu_B\mathbf{J}$ by noting from (A.32) that the M^{th} component μ_M of the magnetic dipole moment operator is (for $J_g=1/2$)

$$\mu_M=-\frac{g_J\mu_B}{\sqrt{2}}\sum_{F_gF_g'}\eta_M(F_g,F_g')\sum_\mu\left|F_g,\mu\right\rangle\left\langle F_g',\mu-M\right|, \tag{2.186}$$

where we have, for convenience, defined η as

$$\eta_M(F_g,F_g')=(-1)^{\mu-M-F}\sqrt{(2F_g'1+1)(2F_g+1)}W\left(1\frac{1}{2}F_gI;\frac{1}{2}F_g'\right)C(F_gF_g'1,\mu,M-\mu). \tag{2.187}$$

The vector component of the polarizability tensor can then be written, after some manipulation, as

$$\overleftrightarrow{\alpha}^1 \approx \frac{G\sqrt{2}}{4g_J\mu_B}(11-4J_e(J_e+1))\sum_M(-1)^M\mathbf{Q}^1_{-M}$$
$$\times\left(\sum_f p(f)\mu_M p(f)Z_f+\sum_{f\neq f'}p(f)\mu_M p(f')Z_{f'}\right), \tag{2.188}$$

where we have defined the hyperfine ground state projection operator $p(f)$ as

$$p(f)=\sum_\nu\left|f,\nu\right\rangle\left\langle f,\nu\right|. \tag{2.189}$$

For alkali atoms with insignificant excited hyperfine structure, that is where the energy splittings between the different excited hyperfine manifolds are small compared to the (Doppler broadened) splittings between the ground and excited state hyperfine manifolds, the $L = 2$ component of the polarizability tensor $\overleftrightarrow{\alpha}^2$ is approximately zero. In order to see this, we note that under the approximation $Z(F_e, F'_g) \approx Z(F'_e, F'_g) = Z_{F'_g}$, the $L = 2$ component is, from (2.174) and (2.179) given by

$$\overleftrightarrow{\alpha}^2 = \sum_{F_g F'_g M} \xi^2(F_g, F'_g) Z_{F'_g} (-1)^M \mathbf{Q}^2_{-M} T^2_M(F_g, F'_g), \tag{2.190}$$

where from (2.180) and for $J_g = 1/2$,

$$\xi^2(F_g, F'_g) = (-1)^{F_g - F'_g} 6G \sqrt{(2F_g + 1)(2F'_g + 1)} W\left(F_g 2 I \frac{1}{2}; F'_g \frac{1}{2}\right) W\left(12 J_e \frac{1}{2}; 1\frac{1}{2}\right). \tag{2.191}$$

However, the second W coefficient $W\left(12 J_e \frac{1}{2}; 1\frac{1}{2}\right)$ is identically zero since $j_2 = 2, j_3 = 1/2, j'' = 1/2$ does not satisfy the triangular condition (A.79b) and therefore, $\overleftrightarrow{\alpha}^2$ is identically zero in this approximation.

We conclude this section by briefly summarizing the main results derived by neglecting the excited state hyperfine structure and we close by noting how these results can be generalized to the case when the excited state hyperfine structure cannot be safely ignored. For alkali atoms with insignificant excited state hyperfine structure so that $Z(F_e, F'_g) \approx Z(F'_e, F'_g) = Z_{F'_g}$, the multipole components of the polarizability

tensor are given by:

$$\overleftrightarrow{\alpha}^0 \approx G \sum_f p(f) Z_f \tag{2.192}$$

$$\begin{aligned}\overleftrightarrow{\alpha}^1 \approx & \frac{G\sqrt{2}}{4 g_J \mu_B}(11 - 4J_e(J_e+1)) \sum_M (-1)^M \mathbf{Q}^1_{-M} \\ & \times \left(\sum_f p(f) \mu_M p(f) Z_f + \sum_{f \neq f'} p(f) \mu_M p(f') Z_{f'} \right)\end{aligned} \tag{2.193}$$

$$\overleftrightarrow{\alpha}^2 \approx 0, \tag{2.194}$$

where $p(f)$ is the hyperfine ground state projection operator defined in (2.189) and the factor G is defined in (2.172). In the case where the excited state hyperfine structure cannot be safely ignored, the approximation $A^L(F_g, F'_g) = \sum_{F_e} \xi^L(F_g, F'_g, F_e) Z(F_e, F'_g) \approx Z_{F'_g} \xi^L(F_g, F'_g)$ cannot be made but the form of the approximate $A^L(F_g, F'_g)$ can be retained by writing

$$\begin{aligned} A^L(F_g, F'_g) &= \sum_{F_e} \xi^L(F_g, F'_g, F_e) Z(F_e, F'_g) \\ &= \xi^L(F_g, F'_g) \frac{\sum_{F_e} \xi^L(F_g, F'_g, F_e) Z(F_e, F'_g)}{\xi^L(F_g, F'_g)} \\ &= \xi^L(F_g, F'_g) \zeta^L(F_g, F'_g), \end{aligned} \tag{2.195}$$

which has the same form as the approximate $A^L(F_g, F'_g) \approx Z_{F'_g} \xi^L(F_g, F'_g)$ with $Z_{F'_g} \to \zeta^L(F_g, F'_g)$. Consequently, the approximate results (2.192) and (2.193) for $\overleftrightarrow{\alpha}^0$ and $\overleftrightarrow{\alpha}^1$ can be applied to the general case by simply making the replacement $Z_{F'_g} \to \zeta^L$ where

$$\zeta^L(F_g, F'_g) = \frac{\sum_{F_e} \xi^L(F_g, F'_g, F_e) Z(F_e, F'_g)}{\xi^L(F_g, F'_g)}. \tag{2.196}$$

We do note however, that in the general case, there will be a $L = 2$ component $\overleftrightarrow{\alpha}^2$ to the polarizability tensor, which is otherwise absent when the excited state hyperfine

structure is neglected and that this component can be calculated by using (2.174) and the full expression (2.175) for $A^L(F_g, F_g')$.

2.6.3 Light propagation in a co-magnetometer

In this section, we consider how the different multipole components of the polarizability tensor $\overleftrightarrow{\alpha}$ obtained in section 2.6.2 gives rise to different physical effects. In particular, we shall consider the paramagnetic Faraday rotation of an off-resonance linearly polarized probe beam, the absorption cross-section of a circularly polarized pump beam through a partially polarized ensemble of alkali atoms and the absorption cross-section of a linearly polarized beam through an unpolarized ensemble of alkali atoms. The first two processes are integral to the operation of the co-magnetometers described in this work since they represent the means by which the spin polarization of the atoms are probed and pumped respectively while the third process is frequently used to determine the density of the alkali vapor[21]. We begin this discussion by noting that the vapor cells used in the co-magnetometers described in this work are high pressure vapor cells containing large quantities of a noble gas species. For example, a typical K-^{3}He high pressure vapor cell would contain roughly 10 a.t.m of ^{3}He at room temperature and at such pressures, the hyperfine structure of the alkali atoms are not optically resolved. This represents a major simplification since the profile factors Z_{F_g} introduced in the preceding section are all approximately the same i.e. $Z_{F_g} \approx Z_{F_g'}$ and the multipole components of the polarizability tensor can thus be further simplified to

$$\overleftrightarrow{\alpha}^0 \approx G \sum_f p(f) Z_f \approx G Z_{F_g} \sum_f p(f) = G Z_{F_g} \tag{2.197}$$

[21] We note however, that this method is only reliable for lower alkali densities ($<\sim 10^{14}$ cm^{-3}).

and

$$\begin{aligned}
\overleftrightarrow{\alpha}^1 &\approx \frac{G\sqrt{2}}{4g_J\mu_B}(11-4J_e(J_e+1))\sum_M(-1)^M\mathbf{Q}^1_{-M} \\
&\quad\times\left(\sum_f p(f)\mu_M p(f)Z_f+\sum_{f\neq f'}p(f)\mu_M p(f')Z_{f'}\right) \\
&\approx \frac{GZ_{F_g}\sqrt{2}}{4g_J\mu_B}(11-4J_e(J_e+1))\sum_M(-1)^M\mathbf{Q}^1_{-M} \\
&\quad\times\sum_{fg}p(f)\mu_M p(g) \\
&= \frac{\overleftrightarrow{\alpha}^0\sqrt{2}}{4g_J\mu_B}(11-4J_e(J_e+1))\sum_M(-1)^M\mathbf{Q}^1_{-M}\mu_M. \qquad (2.198)
\end{aligned}$$

Furthermore, at high buffer gas pressures where the rate of collisions γ_c is such that $\gamma_c\sqrt{m_a/2k_BT}/k \gg 1$, the argument of the profile factor $Z(\xi(F_g,F_e,\gamma_c))$ (2.160) is such that $|\xi(F_g,F_e,\gamma_c)| \gg 1$ and the plasma dispersion function (profile factor) can therefore be approximated as [131]:

$$\begin{aligned}
Z(\xi)\approx -\frac{1}{\xi} &= -k\sqrt{\frac{2k_BT}{m_a}}\frac{1}{\left(\omega-\omega_{F_eF_g}\right)+i\left(\Gamma/2+\gamma_c\right)} \\
&= -k\sqrt{\frac{2k_BT}{m_a}}\frac{1}{\left(\omega-\omega_{F_eF_g}\right)+i\left(\gamma_{tot}\right)} \\
&= -k\sqrt{\frac{2k_BT}{m_a}}\frac{1}{\left(\omega-\omega_{F_eF_g}\right)+i\left(2\pi\Gamma_{tot}\right)}, \qquad (2.199)
\end{aligned}$$

where in the second line, we have made the replacement $\Gamma/2+\gamma_c \rightarrow \gamma_{tot}$ for convenience and in the third line, we have defined Γ_{tot} as the non-angular version of γ_{tot}, which is the collision broadened (angular) HWHM of the transition. We are primarily interested in the propagation of plane waves through the co-magnetometer cell and we shall therefore write the laser field as

$$\mathbf{E}(\mathbf{r},t)=\mathbf{E}_0(\hat{k}\cdot\mathbf{r},t)e^{i(\mathbf{k}\cdot\mathbf{r}-\omega t)}, \qquad (2.200)$$

where $\mathbf{E}_0$ can, in general, be complex but as is typical in such situations, we always mean to take the real part of the RHS to represent the physical electric field of the light. Moreover, the envelope function $\mathbf{E}_0$ is, to a good approximation, a slowly varying function in space and time compared to the oscillatory factor so that

$$\begin{aligned}
\nabla \cdot \mathbf{E} &= (\nabla \cdot \mathbf{E}_0)\, e^{i(\mathbf{k}\cdot\mathbf{r}-\omega t)} + \mathbf{E}_0 \cdot \nabla e^{i(\mathbf{k}\cdot\mathbf{r}-\omega t)} \\
&= (\nabla \cdot \mathbf{E}_0 + i\mathbf{k} \cdot \mathbf{E}_0)\, e^{i(\mathbf{k}\cdot\mathbf{r}-\omega t)} \\
&\approx i\mathbf{k} \cdot \mathbf{E}_0 e^{i(\mathbf{k}\cdot\mathbf{r}-\omega t)} \qquad (2.201) \\
\implies &|\nabla \cdot \mathbf{E}_0| \ll |\mathbf{k} \cdot \mathbf{E}_0|\,, \qquad (2.202)
\end{aligned}$$

and similarly,

$$\left|\partial^j E_0^j\right| \ll |k^j E_0^j|, \qquad (2.203)$$

where no summation is implied in the repeated indices above and lastly

$$\begin{aligned}
\frac{\partial \mathbf{E}}{\partial t} &= \left(\frac{\partial \mathbf{E}_0}{\partial t} - i\omega \mathbf{E}_0\right) e^{i(\mathbf{k}\cdot\mathbf{r}-\omega t)} \\
&\approx -i\omega \mathbf{E}_0 e^{i(\mathbf{k}\cdot\mathbf{r}-\omega t)} \qquad (2.204) \\
\implies &\left|\frac{\partial \mathbf{E}_0}{\partial t}\right| \ll |\omega \mathbf{E}_0|. \qquad (2.205)
\end{aligned}$$

Consequently, from (2.202) $\nabla \cdot \mathbf{E} = 4\pi\rho \approx i\mathbf{k} \cdot \mathbf{E} \approx 0$, since to an excellent approximation, $\rho \approx 0$ on the scale of the laser wavelengths of interest. This implies that $\mathbf{k} \cdot \mathbf{E} \approx 0$ and the polarization of the light through a co-magnetometer cell is hence primarily transverse to the light's propagation direction and equation (2.147) can thus be written as

$$\nabla^2 \mathbf{E} - \frac{1}{c^2}\frac{\partial^2 \mathbf{E}}{\partial t^2} = \frac{4\pi n}{c^2}\frac{\partial^2}{\partial t^2}\langle \overleftrightarrow{\alpha}_\perp \rangle \cdot \mathbf{E}, \qquad (2.206)$$

where by $\langle \overleftrightarrow{\alpha}_\perp \rangle$ we mean the transverse component of $\langle \overleftrightarrow{\alpha} \rangle$, which is given by

$$\begin{aligned}\langle \overleftrightarrow{\alpha}_\perp \rangle &= \overleftrightarrow{T} \cdot \langle \overleftrightarrow{\alpha} \rangle \cdot \overleftrightarrow{T} \\ &= \overleftrightarrow{T} \cdot \left(\langle \overleftrightarrow{\alpha}^0 \rangle + \langle \overleftrightarrow{\alpha}^1 \rangle + \langle \overleftrightarrow{\alpha}^2 \rangle \right) \cdot \overleftrightarrow{T} \\ &\approx \overleftrightarrow{T} \cdot \left(\langle \overleftrightarrow{\alpha}^0 \rangle + \langle \overleftrightarrow{\alpha}^1 \rangle \right) \cdot \overleftrightarrow{T}, \end{aligned} \tag{2.207}$$

since $\overleftrightarrow{\alpha}^2$ is approximately 0 (see (2.194) and the discussion there) and $\overleftrightarrow{T}$ is, in terms of the unit wavevector $\hat{k}$, defined as

$$\overleftrightarrow{T} = \mathbf{1} - \hat{k}\hat{k}. \tag{2.208}$$

Taking the propagation direction to be along the z axis and making use of the approximations (2.203) and (2.205), the propagation equation (2.206) at steady state becomes

$$\frac{\partial \mathbf{E}_0}{\partial z} \approx i 2\pi n k \, \langle \overleftrightarrow{\alpha}_\perp \rangle \cdot \mathbf{E}_0. \tag{2.209}$$

Moreover, the scalar component of the polarizability tensor $\overleftrightarrow{\alpha}^0$ is, under the approximations (2.197) and (2.199), given by

$$\overleftrightarrow{\alpha}^0 \approx G Z_{F_g} \approx -\frac{r_e f_{osc} c^2}{2\omega} \frac{1}{\omega - \omega_0 + i\gamma_{tot}}, \tag{2.210}$$

where we have, for convenience, made the replacement $\omega_{F_e F_g} \to \omega_0$. Similarly, the vector component of the polarizability tensor $\overleftrightarrow{\alpha}^1$ is, under the approximations (2.198) and (2.199), given by

$$\overleftrightarrow{\alpha}^1 \approx -\frac{G Z_{F_g} \sqrt{2}}{4} (11 - 4J_e(J_e+1)) \sum_M (-1)^M \mathbf{Q}^1_{-M} S_M, \tag{2.211}$$

where we have used the definition $\mathbf{S} = -\mu_B g_J \boldsymbol{\mu}$. The expectation values of $\overleftrightarrow{\alpha}^0$ and $\overleftrightarrow{\alpha}^1$ under the approximations (2.198) and (2.199) are then

$$\left\langle \overleftrightarrow{\alpha}^0 \right\rangle \approx -\frac{r_e f_{osc} c^2}{2\omega} \frac{1}{\omega - \omega_0 + i\gamma_{tot}} \equiv \alpha^0, \tag{2.212}$$

where we have defined the last equality as α^0 since this is now just a scalar quantity, and

$$\left\langle \overleftrightarrow{\alpha}^1 \right\rangle \approx -\frac{\alpha^0 \sqrt{2}}{4}(11 - 4J_e(J_e+1)) \sum_M (-1)^M \mathbf{Q}^1_{-M} \left\langle S_M \right\rangle . \tag{2.213}$$

Accordingly, the transverse component of the polarizability tensor $\langle \overleftrightarrow{\alpha}_\perp \rangle$ is then

$$\langle \overleftrightarrow{\alpha}_\perp \rangle = \alpha^0 \left(\overleftrightarrow{T} - \frac{\sqrt{2}}{4}(11 - 4J_e(J_e+1)) \sum_M (-1)^M \overleftrightarrow{T} \cdot \mathbf{Q}^1_{-M} \cdot \overleftrightarrow{T} \left\langle S_M \right\rangle \right). \tag{2.214}$$

However, by expanding $\mathbf{Q}^1_{-M}$ (A.10) and remembering that $\overleftrightarrow{T} = \mathbf{i}_{-1}\mathbf{i}^*_{-1} + \mathbf{i}_1 \mathbf{i}^*_1$ (since we have taken $\hat{k} = \hat{z}$), the sum over M in the second term can be simplified as

$$\begin{aligned}
&\sum_M (-1)^M \overleftrightarrow{T} \cdot \mathbf{Q}^1_{-M} \cdot \overleftrightarrow{T} \left\langle S_M \right\rangle = \sum_{M\mu} (-1)^{\mu+1} C(111, \mu, -M-\mu) \left\langle S_M \right\rangle \\
&\quad \times \left[\delta_{1\mu}\delta_{\mu+M,1} \mathbf{i}_1 \mathbf{i}^*_1 + \delta_{1\mu}\delta_{\mu+M,-1} \mathbf{i}_1 \mathbf{i}^*_{-1} + \delta_{-1,\mu}\delta_{\mu+M,1} \mathbf{i}_{-1} \mathbf{i}^*_1 + \delta_{-1,\mu}\delta_{\mu+M,-1} \mathbf{i}_{-1} \mathbf{i}^*_{-1} \right] \\
&= C(111, 1, -1) \left\langle S_0 \right\rangle \mathbf{i}_1 \mathbf{i}^*_1 + C(111, -1, 1) \left\langle S_0 \right\rangle \mathbf{i}_{-1} \mathbf{i}^*_{-1} \\
&= \frac{1}{\sqrt{2}} (\mathbf{i}_1 \mathbf{i}^*_1 - \mathbf{i}_{-1} \mathbf{i}^*_{-1}) \left\langle S_z \right\rangle ,
\end{aligned} \tag{2.215}$$

where we have used the Clebsch-Gordan symmetry relation (A.58) in the second line and the fact that $C(111, 1, -1) = 1/\sqrt{2}$ in the third line. Consequently, we obtain

$$\langle \overleftrightarrow{\alpha}_\perp \rangle = \mathbf{i}_1 \mathbf{i}^*_1 \left(\alpha^0 + \alpha_{gt} \left\langle S_z \right\rangle \right) + \mathbf{i}_{-1} \mathbf{i}^*_{-1} \left(\alpha^0 - \alpha_{gt} \left\langle S_z \right\rangle \right), \tag{2.216}$$

where the gyrotropic polarizability α_{gt} is defined as

$$\alpha_{gt} = -\alpha_0 \frac{11 - 4J_e(J_e+1)}{4}. \tag{2.217}$$

As expected, the eigenvectors of the transverse polarizability in (2.216) are $\mathbf{i}_1$ and $\mathbf{i}_{-1}$, which means that the transverse $\mathbf{E}_0$ is also an eigenvector. Consequently, the general solution of the (approximate) propagation equation at steady state (2.209) is

$$\mathbf{E}_0(z) = e^{i\phi}\left(e^{i\theta}\mathbf{i}_1\mathbf{i}_1^* + e^{-i\theta}\mathbf{i}_{-1}\mathbf{i}_{-1}^*\right)\mathbf{E}_0(0), \tag{2.218}$$

where ϕ and θ and are here defined as

$$\phi = 2\pi nk\alpha^0 z \tag{2.219}$$

$$\begin{aligned}\theta &= 2\pi nk\alpha_{gt}\langle S_z\rangle z \\ &= -2\pi nk\alpha^0 \frac{11 - 4J_e(J_e+1)}{4}\langle S_z\rangle z.\end{aligned} \tag{2.220}$$

We note that in general, $\phi \in \mathbb{C}$ and $\theta \in \mathbb{C}$, since $\alpha^0 \in \mathbb{C}$. Furnished with this solution, we can now derive several important results that are integral to the operation of the co-magnetometers described in this work.

2.6.4 Faraday rotation of off-resonance linearly polarized light

The macroscopic spin polarization of the alkali atoms in a co-magnetometer vapor cell is read out using the paramagnetic Faraday rotation of an off-resonance linearly polarized probe beam. In order to derive this effect, we first note that if the probe laser is sufficiently far detuned from the resonance, then $|\omega - \omega_0| \gg \gamma_{tot}$ and we can therefore neglect the imaginary part of α^0. Furthermore, without loss of generality,

let us take the light to be initially polarized in the x-direction so that

$$\mathbf{E}_0(0) = \frac{E_0}{\sqrt{2}}(\mathbf{i}_{-1} - \mathbf{i}_1). \tag{2.221}$$

Then (2.218) reduces to

$$\begin{aligned}\mathbf{E}_0(z) &\approx \frac{E_0}{\sqrt{2}} e^{i\phi}(-e^{i\,\mathbb{R}\mathrm{e}[\theta]}\mathbf{i}_1 + e^{-i\,\mathbb{R}\mathrm{e}[\theta]}\mathbf{i}_{-1}) \\ &= E_0 e^{i\phi}\left(\cos\left(\mathbb{R}\mathrm{e}[\theta]\right)\,\mathbf{i}_x - \sin\left(\mathbb{R}\mathrm{e}[\theta]\right)\,\mathbf{i}_y\right),\end{aligned} \tag{2.222}$$

and from (2.220) and (2.212)

$$\begin{aligned}\mathbb{R}\mathrm{e}[\theta] &= -2\pi n k\,\mathbb{R}\mathrm{e}[\alpha^0]\frac{11 - 4J_e(J_e+1)}{4}\langle S_z\rangle\, z \\ &= \pi n k \frac{r_e f_{osc} c^2}{\omega}\frac{\omega - \omega_0}{(\omega-\omega_0)^2 + \gamma_{tot}^2}\frac{11 - 4J_e(J_e+1)}{4}\langle S_z\rangle\, z,\end{aligned} \tag{2.223}$$

so that the polarization of the initially x-polarized light is indeed rotated by $\mathbb{R}\mathrm{e}[\theta]$ after propagating through a distance z. For the $\mathcal{D}_1$ transition, $J_e = 1/2$ and $\mathbb{R}\mathrm{e}[\theta]$ becomes

$$\theta_{\mathcal{D}_1} = \frac{1}{2} n r_e f_{\mathcal{D}_1} c \frac{\nu - \nu_{\mathcal{D}_1}}{(\nu - \nu_{\mathcal{D}_1})^2 + (\gamma_{tot}/2\pi)^2} P_z z, \tag{2.224}$$

where we have made the replacement $\langle S_z\rangle \to P_z/2$ and have for the experimentalist's convenience, expressed the frequency in non-angular units. Similarly, the Faraday rotation due to the $\mathcal{D}_2$ transition with $J_e = 3/2$ is

$$\theta_{\mathcal{D}_2} = -\frac{1}{4} n r_e f_{\mathcal{D}_2} c \frac{\nu - \nu_{\mathcal{D}_2}}{(\nu - \nu_{\mathcal{D}_2})^2 + (\gamma_{tot}/2\pi)^2} P_z z, \tag{2.225}$$

where $\gamma_{tot}/2\pi$ is now the HWHM of the $\mathcal{D}_2$ transition (in non-angular units). For a sufficiently far detuned laser beam so that $|\omega - \omega_0| \gg \gamma_{tot}$ and $\mathbb{I}\mathrm{m}[\alpha^0]$ is negligible, the rotation from both $\mathcal{D}_1$ and $\mathcal{D}_2$ transitions are additive and the total optical rotation

is therefore

$$\theta_{FR} = \frac{1}{2} n r_e c P_z z \left(f_{\mathcal{D}_1} \frac{\nu - \nu_{\mathcal{D}_1}}{\left(\nu - \nu_{\mathcal{D}_1}\right)^2 + \left(\Gamma_{tot}^{\mathcal{D}_1}\right)^2} - \frac{1}{2} f_{\mathcal{D}_2} \frac{\nu - \nu_{\mathcal{D}_2}}{\left(\nu - \nu_{\mathcal{D}_2}\right)^2 + \left(\Gamma_{tot}^{\mathcal{D}_2}\right)^2} \right), \quad (2.226)$$

where as before, n is the density of alkali atoms, r_e is the classical electron radius, c is the speed of light, P_z is the polarization of the atoms along the direction of the light, z is the distance of light propagation through the cell, $f_{\mathcal{D}_{1,2}}$ are the oscillator strengths of the respective transitions, and ν, $\nu_{\mathcal{D}_{1,2}}$ and $\Gamma_{tot}^{\mathcal{D}_{1,2}}$ are respectively the laser frequency, transition frequencies and collisional broadened HWHM in non-angular units. We note here that the Faraday rotation is dispersive in that it is zero on resonance.

2.6.5 Absorption of circularly polarized light

In the section above, we considered the effect of a partially (spin) polarized ensemble of alkali atoms on linearly polarized off-resonance light propagating through the ensemble. For sufficiently far detuned light, the net effect of the polarized atoms was to rotate the polarization of the light and this effect is used to read out the macroscopic (spin) polarization of the atoms. In this section, we consider the attenuation of circularly polarized pump light through a partially (spin) polarized ensemble of alkali atoms. We begin by noting that the (time-averaged) intensity of the light is (in c.g.s units) given by

$$I(z) = \frac{c}{8\pi} \mathbb{R}\mathrm{e}[\mathbf{E}(z)\mathbf{E}^*(z)] = \frac{c}{8\pi} \mathbf{E}_0(z)\mathbf{E}_0^*(z), \quad (2.227)$$

where $\mathbf{E}(z)$ and $\mathbf{E}_0(z)$ are defined in (2.200). However, $\mathbf{E}_0(z)$ is given by (2.218) and so

$$I(z) = \frac{c}{8\pi} e^{-2\,\mathbb{I}\mathrm{m}[\phi]} \left(e^{-2\,\mathbb{I}\mathrm{m}[\theta]} \left|\mathbf{i}_1^* \cdot \mathbf{E}_0(0)\right|^2 + e^{2\,\mathbb{I}\mathrm{m}[\theta]} \left|\mathbf{i}_{-1}^* \cdot \mathbf{E}_0(0)\right|^2 \right). \quad (2.228)$$

Evidently, for circularly polarized light, i.e $\mathbf{E}_0(0) = E_0\mathbf{i}_{\pm 1}$, the intensity of the light through the cell varies as

$$I^{\pm}(z) = \frac{c}{8\pi} e^{-2\,\mathbb{I}\mathrm{m}[\phi]\mp 2\,\mathbb{I}\mathrm{m}[\theta]} E_0^2 = e^{-2\,\mathbb{I}\mathrm{m}[\phi]\mp 2\,\mathbb{I}\mathrm{m}[\theta]} I^{\pm}(0), \tag{2.229}$$

where the argument of the exponential above is from (2.219), (2.220) and (2.212) given by

$$\begin{aligned} -2\,\mathbb{I}\mathrm{m}\left[\phi\right] \mp 2\,\mathbb{I}\mathrm{m}\left[\theta\right] &= -4\pi nk\left(1 \mp \frac{11 - 4J_e(J_e+1)}{4}\left\langle S_z\right\rangle\right)\mathbb{I}\mathrm{m}[\alpha^0]z \\ &= -n\frac{r_e f_{osc} c\left(\gamma_{tot}/2\pi\right)}{\left(\nu-\nu_0\right)^2 + \left(\gamma_{tot}/2\pi\right)^2}\left(1 \mp \frac{11 - 4J_e(J_e+1)}{8}\left\langle P_z\right\rangle\right)z, \end{aligned} \tag{2.230}$$

and we have, as before, made the replacement $\langle S_z\rangle \to \langle P_z\rangle/2$ in the last line. (2.229) and (2.230) together give us the intensity profile of a circularly polarized beam propagating through a partially polarized ensemble of atoms. However, the treatment here is somewhat of an oversimplification since it assumes that the polarization $\langle P_z\rangle$ is uniform across the cell. In practice, this is usually not the case since the attenuation of the pump light (which is the means by which the atoms are polarized) necessarily implies, to the extent that the diffusion time of the alkali atom is long compared to its spin relaxation time, that there exist some polarization gradient within the cell. However, this can be mitigated through the use of hybrid optical pumping techniques that we discuss in section 2.7.4.

(2.229) and (2.230) not only gives us the intensity profile of the a circularly polarized beam through a uniformly partially polarized ensemble of atoms, but they also allow us to extract the absorption cross-section of an alkali atom to circularly polarized light. To see this we note that by definition, the absorption cross-section is the ratio between the power absorbed by the atom to the intensity of the laser beam impinging upon it. Equivalently, the absorption cross-section is the ratio between the

power loss in the beam to its intensity:

$$\sigma \equiv \frac{P_{loss}}{I(z)}. \tag{2.231}$$

The corresponding drop in intensity of the beam is then

$$\begin{aligned} I(z+dz) - I(z) &= -\sigma I(z) n\, dz \\ \implies \frac{dI}{dz} &= -n\sigma I(z). \end{aligned} \tag{2.232}$$

On the other hand, differentiating (2.229) gives us

$$\frac{dI^{\pm}}{dz} = -nr_e f_{osc} c \frac{(\gamma_{tot}/2\pi)}{(\nu-\nu_0)^2 + (\gamma_{tot}/2\pi)^2} \left(1 \mp \frac{11 - 4J_e(J_e+1)}{8} \langle P_z \rangle\right) I^{\pm}(z), \tag{2.233}$$

and so comparison with (2.232) yields the absorption cross-section of partially polarized alkali atoms to circularly polarized light

$$\sigma^{\pm} = r_e f_{osc} c \frac{(\gamma_{tot}/2\pi)}{(\nu-\nu_0)^2 + (\gamma_{tot}/2\pi)^2} \left(1 \mp \frac{11 - 4J_e(J_e+1)}{8} \langle P_z \rangle\right). \tag{2.234}$$

Furthermore, we can compute the rate of absorption of photons from the circularly polarized pump beam by noting that R_{abs} is simply

$$R_{abs} = \frac{P_{loss}}{h\nu}, \tag{2.235}$$

but R_{abs} is also the rate R_{dp} at which the alkali atoms are depopulated out of the ground state by the circularly polarized light and so from (2.231), $R_{dp} = R_{abs}$ is just

$$\begin{aligned} R_{dp} = \frac{\sigma I}{h\nu} &= I \frac{r_e f_{osc} c}{h\nu} \frac{\gamma_{tot}/2\pi}{(\nu-\nu_0)^2 + (\gamma_{tot}/2\pi)^2} \left(1 \mp \frac{11 - 4J_e(J_e+1)}{8} \langle P_z \rangle\right) \\ &= R_p \left(1 \mp \frac{11 - 4J_e(J_e+1)}{8} \langle P_z \rangle\right), \end{aligned} \tag{2.236}$$

where we have defined the mean pumping rate of unpolarized atoms out of the ground state as

$$R_p \equiv I \frac{r_e f_{osc} c}{h\nu} \frac{\Gamma_{tot}}{(\nu - \nu_0)^2 + (\Gamma_{tot})^2}. \tag{2.237}$$

I is here the intensity of the light and h is Planck's constant. All other variables are as defined in (2.226). For the $\mathcal{D}_1$ pumping used in the co-magnetometers described in this work, $J_e = 1/2$ and $R_{dp} = R_{abs}$ is then

$$R_{abs} = R_{dp} = R_p \left(1 \mp \langle P_z \rangle\right), \tag{2.238}$$

where the $\mp$ corresponds to the $\pm$ polarity of the circularly polarized light.

2.6.6 Absorption of linearly polarized light

We conclude our discussion of light propagation through the co-magnetometer cell with a quick derivation of the absorption of linearly polarized light through an atomic ensemble. Without loss of generality, we shall take our light to be linearly polarized in the x-direction so that $\mathbf{E}_0(0)$ is given by (2.221). In this case, (2.228) reduces to

$$I(z) = \frac{c}{8\pi} e^{-\beta} \cosh\left(-\beta \frac{11 - 4J_e(J_e+1)}{8} \langle P_z \rangle\right) E_0^2, \tag{2.239}$$

where

$$\beta = n r_e f_{osc} c \frac{\gamma_{tot}/2\pi}{(\nu - \nu_0)^2 + (\gamma_{tot}/2\pi)^2} z. \tag{2.240}$$

Moreover, for an unpolarized vapor with $\langle P_z \rangle = 0$, (2.239) becomes simply

$$I(z) = \exp\left(-n r_e f_{osc} c \frac{\gamma_{tot}/2\pi}{(\nu - \nu_0)^2 + (\gamma_{tot}/2\pi)^2} z\right) I_0, \tag{2.241}$$

and we can, in this case, write down the absorption cross-section of linearly polarized light in an (spin) unpolarized atomic ensemble:

$$\frac{dI}{dz} = -nr_e f_{osc} c \frac{\gamma_{tot}/2\pi}{(\nu - \nu_0)^2 + (\gamma_{tot}/2\pi)^2} I(z) \tag{2.242}$$

$$\implies \sigma_{lin} = r_e f_{osc} c \frac{\gamma_{tot}/2\pi}{(\nu - \nu_0)^2 + (\gamma_{tot}/2\pi)^2}. \tag{2.243}$$

2.6.7 The effective ground-state Hamiltonian

In the preceding section, we have made use of the polarizability tensor to demonstrate how an ensemble of partially (spin) polarized atoms can affect a propagating laser beam. In this section, we investigate how a laser beam can in turn affect an ensemble of alkali atoms[22]. In particular, we would like to understand how the laser beam affects the evolution of the ground-state density matrix. As before, the wavefunction of the alkali atom evolves according to (2.153) during the intervals between collisions and the ground-state density matrix is defined as in (2.163). The evolution of the ground-state density matrix is then given by

$$\frac{d}{dt}\left[e^{i\omega_{\mu\nu}t}\rho_{\mu\nu}\right] = \langle \dot{a}_\mu a_\nu^* \rangle + \langle a_\mu \dot{a}_\nu^* \rangle \,. \tag{2.244}$$

To make further progress, we would require an expression for $\dot{a}_\mu$. Taking the inner product with $|\mu\rangle$ on both sides of (**??**), we obtain

$$i\dot{a}_\mu = -\sum_m \left\langle \mu \left| \frac{\mathbf{p}\cdot\mathbf{E}}{\hbar} \right| m \right\rangle a_m e^{i\omega_{\mu m}t}. \tag{2.245}$$

We shall take (2.155) as the electric field of the laser beam of interest. The excited state amplitude $a_m(t)$ is given by (2.156) and substitution of both $\mathbf{E}$ and $a_m(t)$ into

[22] As before, this section is based on [130].

the above yields (after dropping a fast oscillating term)

$$\begin{aligned}\dot{a}_\mu = i\sum_m \left\langle \mu \left| \frac{\mathbf{p}\cdot\mathbf{E}}{\hbar} \right| m \right\rangle a_m(t') e^{-\Gamma(t-t')/2} e^{i\omega_{\mu m} t} \\ - \frac{|E_0|^2}{i4\hbar^2} \sum_{m\sigma} \left(\mathbf{e}^* \cdot \rho_{\mu m}\right)\left(\rho_{m\sigma}\cdot\mathbf{e}\right) a_\sigma e^{i\omega_{\mu\sigma}t} \\ \times \frac{1 - e^{-i(\omega_{m\sigma}-\omega+\mathbf{k}\cdot\mathbf{v}-i\Gamma/2)(t-t')}}{(\omega_{m\sigma}-\omega+\mathbf{k}\cdot\mathbf{v}-i\Gamma/2)}.\end{aligned} \tag{2.246}$$

The averages in (2.244) is over the atom's collisional history and velocity distribution. As before, the probability that the last collision happened at time t' (for $t' < t$) is given by (2.148) and we expect that since the atoms are mostly non-interacting particles in between collisions, their velocities should follow the Maxwell-Boltzmann distribution (2.149). The average $\langle \dot{a}_\mu a_\nu^* \rangle$ is then

$$\langle \dot{a}_\mu a_\nu^* \rangle = \int_{-\infty}^{t} dt'\, \gamma_c e^{-\gamma_c(t-t')} \int d\mathbf{v}\, N(\mathbf{v}) \dot{a}_\mu a_\nu^*, \tag{2.247}$$

where $N(\mathbf{v})$ is defined as in (2.149). As before, the first term of (2.246) (multiplied by a_ν^*) averages to zero in (2.247) due to the randomization of the excited state amplitude a_m in between collisions. The time average of the second term in (2.246) (multiplied by a_ν^*) then gives

$$\int_{-\infty}^{t} dt'\, \gamma_c e^{-\gamma_c(t-t')} \frac{1 - e^{-i(\omega_{m\nu}-\omega+\mathbf{k}\cdot\mathbf{v}-i\Gamma/2)(t-t')}}{(\omega_{m\nu}-\omega+\mathbf{k}\cdot\mathbf{v}-i\Gamma/2)} = \frac{1}{\omega_{m\sigma}-\omega+\mathbf{k}\cdot\mathbf{v}-i\left(\Gamma/2+\gamma_c\right)}, \tag{2.248}$$

while the average over $\mathbf{v}$ yields as before

$$\begin{aligned}\int d\mathbf{v} \frac{N(\mathbf{v})}{\omega_{m\sigma}-\omega+\mathbf{k}\cdot\mathbf{v}-i\left(\Gamma/2+\gamma_c\right)} &= \frac{1}{k}\sqrt{\frac{m_a}{2k_BT}} Z(m,\sigma) \\ &= \frac{1}{k}\sqrt{\frac{m_a}{2k_BT}} \left\langle \sigma \left| z(m) \right| \sigma \right\rangle,\end{aligned} \tag{2.249}$$

where $Z(m,\sigma)$ and $z(m)$ are as defined in (2.159) and (2.161). We therefore have

$$\langle \dot{a}_\mu a_\nu^* \rangle = -\frac{|E_0|^2}{i4\hbar} \sum_\sigma \langle \mu | \, \mathbf{e}^* \cdot \left(\frac{1}{\hbar k} \sqrt{\frac{m_a}{2k_B T}} \sum_m \mathbf{p} \, |m\rangle \langle m| \, \mathbf{p} \, |\sigma\rangle \langle \sigma| \, z(m) \right) \cdot \mathbf{e} \, |\sigma\rangle \times \langle a_\sigma a_\nu^* \rangle \, e^{i\omega_{\mu\sigma} t}, \tag{2.250}$$

but since $\omega_{\mu\sigma} \equiv (E_\mu - E_\sigma) = \omega_{\nu\sigma} + \omega_{\mu\nu}$, then from the definitions of ρ and $\overleftrightarrow{\alpha}$ in (2.163), we have

$$\langle \dot{a}_\mu a_\nu^* \rangle = -\frac{|E_0|^2}{i4\hbar} \langle \mu \, | \mathbf{e}^* \cdot \overleftrightarrow{\alpha} \cdot \mathbf{e} \, \rho | \, \nu \rangle \, e^{i\omega_{\mu\nu} t}. \tag{2.251}$$

By making the replacement $\mu \leftrightarrow \nu$ in (2.251) and then taking its complex conjugate, we likewise get

$$\begin{aligned} \langle a_\mu \dot{a}_\nu^* \rangle &= \frac{|E_0|^2}{i4\hbar} \left\langle \sigma \left| (\mathbf{e}^* \cdot \overleftrightarrow{\alpha} \cdot \mathbf{e} \, \rho)^\dagger \right| \nu \right\rangle e^{-i\omega_{\nu\mu} t} \\ &= \frac{|E_0|^2}{i4\hbar} \left\langle \sigma \left| \rho \, (\mathbf{e}^* \cdot \overleftrightarrow{\alpha} \cdot \mathbf{e})^\dagger \right| \nu \right\rangle e^{i\omega_{\mu\nu} t}, \end{aligned} \tag{2.252}$$

and so from (2.244) we obtain

$$\begin{aligned} i\hbar \frac{d\rho_{\mu\nu}}{dt} = (E_\mu - E_\nu)\rho_{\mu\nu} &+ \langle \mu | \left(-\frac{|E_0|^2}{4} \mathbf{e}^* \cdot \overleftrightarrow{\alpha} \cdot \mathbf{e} \, \rho \right) | \nu \rangle \\ &- \langle \mu | \left(-\rho \, \frac{|E_0|^2}{4} \, (\mathbf{e}^* \cdot \overleftrightarrow{\alpha} \cdot \mathbf{e})^\dagger \right) | \nu \rangle . \end{aligned} \tag{2.253}$$

Recognizing that $(E_\mu - E_\nu)\rho_{\mu\nu}$ is simply $[H_0, \rho]_{\mu\nu}$, where H_0 is the atomic Hamiltonian without the influence of the light (of which $\{|\mu\rangle\}$ are eigenstates of), it is evident that the influence of the light can be captured by the effective ground-state Hamiltonian δH

$$\delta H = -\frac{|E_0|^2}{4} \mathbf{e}^* \cdot \overleftrightarrow{\alpha} \cdot \mathbf{e}, \tag{2.254}$$

so that (2.253) in operator form is simply the Liouville equation

$$i\hbar\frac{d\rho}{dt} = [H_0, \rho] + (\delta H\rho - \rho\delta H^\dagger). \tag{2.255}$$

In general, δH will not be Hermitian since the number of ground-state atoms are not conserved in optical pumping. However, δH can be written as a linear combination of the Hermitian light-shift operator $\delta\mathscr{E}$ and the Hermitian light absorption operator $\delta\Gamma$ here defined as

$$\delta\mathscr{E} = \frac{\delta H + \delta H^\dagger}{2} = -\frac{|E_0|^2}{8}\left(\mathbf{e}^* \cdot \overleftrightarrow{\alpha} \cdot \mathbf{e} + \mathbf{e} \cdot \overleftrightarrow{\alpha}^\dagger \cdot \mathbf{e}^*\right), \tag{2.256}$$

and

$$\delta\Gamma = \frac{i}{\hbar}(\delta H - \delta H^\dagger) = -i\frac{|E_0|^2}{4\hbar}\left(\mathbf{e}^* \cdot \overleftrightarrow{\alpha} \cdot \mathbf{e} - \mathbf{e} \cdot \overleftrightarrow{\alpha}^\dagger \cdot \mathbf{e}^*\right), \tag{2.257}$$

so that (2.255) may be re-written as

$$i\hbar\frac{d\rho}{dt} = [(H_0 + \delta\mathscr{E}), \rho] - \frac{i\hbar}{2}(\delta\Gamma\,\rho + \rho\,\delta\Gamma), \tag{2.258}$$

and (2.254) becomes

$$\delta H = \frac{\delta H + \delta H^\dagger}{2} - \frac{i\hbar}{2}\frac{i}{\hbar}\left(\delta H - \delta H^\dagger\right) = \delta\mathscr{E} - \frac{i\hbar}{2}\delta\Gamma. \tag{2.259}$$

Evidently, the diagonal elements of $\delta\mathscr{E}$ will cause shifts in the ground state energy levels while its off-diagonal elements can cause transitions between the different sublevels of the atomic ground state. The interpretation of $\delta\Gamma$ is also readily apparent when we consider that the rate of loss of atoms from the ground state is given by $-\operatorname{Tr}[\dot{\rho}]$ and from (2.258), this is simply

$$-\operatorname{Tr}\left[\frac{d\rho}{dt}\right] = \operatorname{Tr}[\delta\Gamma\,\rho] \equiv \langle\delta\Gamma\rangle\,, \tag{2.260}$$

so that the light absorption operator $\delta\Gamma$ is aptly named since the expectation value of $\delta\Gamma$ gives the pumping rate of the atoms out of the ground state. Indeed, from (2.256) and (2.257),

$$\delta\mathscr{E} = -\frac{|E_0|^2}{4}\,\mathbb{R}\mathrm{e}\left[\mathbf{e}^* \cdot \overleftrightarrow{\alpha} \cdot \mathbf{e}\right], \tag{2.261}$$

and

$$\delta\Gamma = \frac{|E_0|^2}{2\hbar}\,\mathbb{I}\mathrm{m}\left[\mathbf{e}^* \cdot \overleftrightarrow{\alpha} \cdot \mathbf{e}\right], \tag{2.262}$$

but at the high buffer gas pressures prevalent in our co-magnetometer cells, we have from (2.210) and (2.211),

$$\mathbf{e}^* \cdot \overleftrightarrow{\alpha} \cdot \mathbf{e} \approx \overleftrightarrow{\alpha}^0 - \frac{\sqrt{2}}{4}\overleftrightarrow{\alpha}^0(11 - 4J_e(J_e+1))\mathbf{e}^* \cdot \sum_M (-1)^M \mathbf{Q}^1_{-M} S_M \cdot \mathbf{e}. \tag{2.263}$$

This can be further simplified by noting that

$$\begin{aligned}
\mathbf{e}^* \cdot \sum_M (-1)^M \mathbf{Q}^1_{-M} S_M \cdot \mathbf{e} &= \sum_{M\mu} (-1)^{-\mu-M-1} e^*_{-\mu} e_{-\mu-M} C(111, \mu, -M-\mu) S_M \\
&= -\sum_{M\mu} e^*_{-\mu} e_{-\mu-M} C(111; -M, M+\mu) S_M \\
&= \frac{1}{\sqrt{2}} \mathbf{S} \cdot \mathbf{s},
\end{aligned} \tag{2.264}$$

where we have used (A.60) and (A.57) in the second line, (A.17) in the third line and $\mathbf{s}$ is the mean photon spin vector defined in (A.16). Substituting $\overleftrightarrow{\alpha}^0$ from (2.210), (2.263) is then

$$\mathbf{e}^* \cdot \overleftrightarrow{\alpha} \cdot \mathbf{e} = -\frac{r_e f_{osc} c^2}{2\omega} \frac{1}{\omega - \omega_0 + i\gamma_{tot}} \left(1 - \frac{11 - 4J_e(J_e+1)}{4} \mathbf{S} \cdot \mathbf{s}\right). \tag{2.265}$$

Consequently, the light-shift and light absorption operators become

$$\delta\mathscr{E} = \mathscr{E}_p(1 - \mathbf{q} \cdot \mathbf{S}), \tag{2.266}$$

and

$$\delta\Gamma = R_p(1 - \mathbf{q}\cdot\mathbf{S}), \tag{2.267}$$

where $\mathbf{q}$ is for convenience, defined as

$$\mathbf{q} \equiv \frac{11 - 4J_e(J_e+1)}{4}\mathbf{s} \quad = \begin{cases} 2\mathbf{s} \text{ for } \mathcal{D}_1 & \text{(2.268a)} \\ -\mathbf{s} \text{ for } \mathcal{D}_2, & \text{(2.268b)} \end{cases}$$

and $\mathbf{s}$ is the mean photon spin (A.16), R_p is the mean pumping rate of unpolarized atoms out of the ground state (2.237), and $\mathscr{E}_p$ is defined as

$$\mathscr{E}_p \equiv \frac{R_p\hbar}{2\Gamma_{tot}}(\nu - \nu_0), \tag{2.269}$$

where Γ_{tot}, ν and ν_0 are the transition's HWHM, laser frequency and transition frequency respectively in non-angular units. Multiplying (2.267) by ρ and taking the trace, we then recover (2.236) as expected

$$\langle\delta\Gamma\rangle = R_p(1 - \mathbf{q}\cdot\langle\mathbf{S}\rangle). \tag{2.270}$$

2.6.8 Scalar light-shift

As demonstrated above, the effective ground state Hamiltonian due to the light allows us to capture the optical pumping action of the light on an ensemble of alkali atoms. Besides optically pumping the atoms, resonant light can also cause shifts in the energy levels of the atoms that are collectively termed light-shifts. In the co-magnetometer, we are typically more concerned with the vector, magnetic-like light-shift where the energy shifts are in the Zeeman levels of the alkali atoms. This has the overall effect of making the light look like an effective magnetic field. More generally however, resonant light can also cause an overall shift in the ground state energy levels of the alkali atoms (which is not detectable in the co-magnetometer) and an effective

shift in A, the hyperfine magnetic dipole coupling (that is also not detectable at the high buffer gas pressures pertinent to our co-magnetometers). These two effects result from the scalar component of the polarizability tensor and are referred to as the scalar light-shift. Although unimportant for the co-magnetometer's operation, it requires little additional work to derive them and we therefore present them (worked out in [130]) here for completeness.

We begin by noting that in the ground state with electronic angular momentum $J_g = 1/2$ and nuclear spin I, there are only two hyperfine manifolds $a = I + 1/2$ and $b = I - 1/2$. Consequently, the ground-state hyperfine projection operators $p(f)$ (2.189) can be written in terms of the ground-state operator $\mathbf{I} \cdot \mathbf{J}$ by noting that $p(f) |g, \mu\rangle = \delta_{fg} |g, \mu\rangle$ and

$$\mathbf{I} \cdot \mathbf{J} |F, \mu\rangle = \begin{cases} \frac{1}{2} I & , F = I + \frac{1}{2} \\ -\frac{1}{2}(I+1) & , F = I - \frac{1}{2}, \end{cases} \tag{2.271}$$

so that

$$p(a) = \frac{I + 1 + 2\mathbf{I} \cdot \mathbf{J}}{2I + 1}, \tag{2.272}$$

and

$$p(b) = \frac{I - 2\mathbf{I} \cdot \mathbf{J}}{2I + 1}. \tag{2.273}$$

Accordingly, the scalar component of the polarizability tensor $\overleftrightarrow{\alpha}^0$ from (2.192) can be re-written as

$$\overleftrightarrow{\alpha}^0 = G \left(Z^+ + \frac{Z^-}{2I+1} \right) + \frac{4GZ^-}{2I+1} \mathbf{I} \cdot \mathbf{J}, \tag{2.274}$$

where

$$Z^+ = \frac{Z_a + Z_b}{2}, \tag{2.275}$$

and

$$Z^- = \frac{Z_a - Z_b}{2}. \tag{2.276}$$

The scalar component of the light-shift operator $\delta\mathscr{E}$ (2.256) is given by

$$\delta\mathscr{E}^0 = -\frac{|E_0|^2}{8}(\mathbf{e}^* \cdot \overleftrightarrow{\alpha}^0 \cdot \mathbf{e} + \mathbf{e} \cdot \overleftrightarrow{\alpha}^{0\dagger} \cdot \mathbf{e}^*), \tag{2.277}$$

which upon subsitution of (2.274) yields

$$\delta\mathscr{E}^0 = \delta\mathscr{E}_{cg} + h\,\delta A\,\mathbf{I}\cdot\mathbf{J}, \tag{2.278}$$

where

$$\delta\mathscr{E}_{cg} = -G\frac{|E_0|^2}{4}\,\mathbb{R}\mathrm{e}\left[Z^+ + \frac{Z^-}{2I+1}\right], \tag{2.279}$$

and

$$\delta A = -\frac{G}{h}\frac{|E_0|^2}{2I+1}\,\mathbb{R}\mathrm{e}[Z^-]. \tag{2.280}$$

Evidently, $\delta\mathscr{E}_{cg}$ represents an overall shift in the ground state energy levels of the atoms and δA is an effective shift in the hyperfine magnetic dipole coupling constant. However, as we have noted before, the co-magnetometer is insensitive to the overall energy shift $\delta\mathscr{E}_{cg}$ and since the ground state hyperfine structure is not resolved due to the high buffer gas pressure in our co-magnetometer cells, $Z_a \approx Z_b$ and therefore $Z^- \approx 0$, which implies that $\delta A \approx 0$ in the co-magnetometer.

2.6.9 Vector light-shift

The vector component of the light-shift operator $\delta\mathscr{E}$ (2.256) is

$$\delta\mathscr{E}^1 = -\frac{|E_0|^2}{8}(\mathbf{e}^* \cdot \overleftrightarrow{\alpha}^1 \cdot \mathbf{e} + \mathbf{e} \cdot \overleftrightarrow{\alpha}^{1\dagger} \cdot \mathbf{e}^*), \tag{2.281}$$

where $\overleftrightarrow{\alpha}^1$ is given by (2.193). Substituting (2.193) into (2.281) will result in terms proportional to $\sum_M (-1)^M \mu_M \mathbf{e}^* \cdot \mathbf{Q}^1_{-M} \cdot \mathbf{e}$ that can be expanded and simplified as

$$\begin{aligned}
&\sum_M (-1)^M \mu_M \mathbf{e}^* \cdot \mathbf{Q}^1_{-M} \cdot \mathbf{e} \\
&\quad = \sum_{M\mu\nu\rho} (-1)^{\mu+\nu+\rho-1} \mu_M e^*_\mu e_\rho \underbrace{\mathbf{i}^*_{-\mu} \cdot \mathbf{i}_\nu}_{\delta_{-\mu,\nu}} \underbrace{\mathbf{i}^*_{\nu+M} \cdot \mathbf{i}_{-\rho}}_{\delta_{\nu+M,-\rho}} C(111; \nu, -M-\nu) \\
&\quad = \sum_{M\mu} (-1)^{-M+\mu-1} \mu_M e^*_\mu e_{\mu-M} C(111; -\mu, \mu-M) \\
&\quad = -\sum_{M\mu} \mu_M e^*_{-\mu} e_{-\mu-M} C(111; -M, M+\mu) \\
&\quad = \frac{1}{\sqrt{2}} \boldsymbol{\mu} \cdot \mathbf{s},
\end{aligned} \tag{2.282}$$

in which we have expanded the first line according to (A.9),(A.10),(A.8) and have used the Clebsch-Gordan symmetry relations (A.60) and (A.57) in going from the second to third line. In the last line, we have made used of (A.17) and $\mathbf{s}$ is here the mean photon spin as defined in (A.16). The term $\mathbf{e}^* \cdot \overleftrightarrow{\alpha}^1 \cdot \mathbf{e}$ is then

$$\mathbf{e}^* \cdot \overleftrightarrow{\alpha}^1 \cdot \mathbf{e} = \frac{G}{4 g_J \mu_B} (11 - 4J_e(J_e+1)) \mathbf{s} \cdot \left[\sum_f p(f) \boldsymbol{\mu} p(f) Z_f + \sum_{f \neq f'} p(f) \boldsymbol{\mu} p(f') Z_{f'} \right], \tag{2.283}$$

and its complex conjugate is

$$\mathbf{e} \cdot \overleftrightarrow{\alpha}^{1\dagger} \cdot \mathbf{e}^* = \frac{G}{4 g_J \mu_B} (11 - 4J_e(J_e+1)) \mathbf{s} \cdot \left[\sum_f p(f) \boldsymbol{\mu} p(f) Z^*_f + \sum_{f \neq f'} p(f') \boldsymbol{\mu} p(f) Z^*_{f'} \right]. \tag{2.284}$$

$\delta\mathscr{E}^1$ is then

$$\begin{aligned}
\delta\mathscr{E}^1 = -\frac{|E_0|^2}{8} \frac{G}{4 g_J \mu_B} (11 - 4J_e(J_e+1)) \mathbf{s} \cdot \Bigg[& 2 \sum_f p(f) \boldsymbol{\mu} p(f)\, \mathbb{R}\mathrm{e}[Z_f] + \\
& \sum_{f \neq f'} p(f) \boldsymbol{\mu} p(f') Z_{f'} + \sum_{f \neq f'} p(f') \boldsymbol{\mu} p(f) Z^*_{f'} \Bigg].
\end{aligned} \tag{2.285}$$

The on-diagonal elements of $\delta\mathscr{E}^1$ are the vector light-shifts caused by the light while the non-diagonal elements cause transitions between different ground-state sub-levels. The expected energy shift due to the vector light-shift is therefore

$$\begin{aligned}\left\langle \delta\mathscr{E}_L^1 \right\rangle &= \mathrm{Tr}[\delta\mathscr{E}_L^1\rho] \\ &= -C\mathbf{s}\cdot\sum_{f'\nu}\sum_{f\sigma\tau}\underbrace{\langle f',\nu|\, f,\sigma\rangle}_{\delta_{ff'}\delta_{\nu\sigma}}\langle f,\sigma\,|\boldsymbol{\mu}|\, f,\tau\rangle\,\langle f,\tau\,|\rho|\, f',\nu\rangle\,\mathbb{R}\mathrm{e}[Z_f] \\ &\approx -C\,\mathbb{R}\mathrm{e}[Z]\mathbf{s}\cdot\sum_{f\sigma\tau}\langle f,\sigma\,|\boldsymbol{\mu}|\, f,\tau\rangle\,\langle f,\tau\,|\rho|\, f',\nu\rangle = -C\,\mathbb{R}\mathrm{e}[Z]\mathbf{s}\cdot\langle\boldsymbol{\mu}\rangle\,, \end{aligned} \tag{2.286}$$

where in the second line we have made use of the fact that at the high buffer gas pressures relevant in the co-magnetometer, the hyperfine levels are not resolved and hence $Z_f \approx Z$. Also, we have denoted the expectation value of the dipole moment operator $\boldsymbol{\mu}$ as $\langle\boldsymbol{\mu}\rangle$ and have, for convenience, defined C here as

$$C = \frac{|E_0|^2}{8}\frac{G}{4g_J\mu_B}(11-4J_e(J_e+1)). \tag{2.287}$$

The form of (2.286) suggests that the light acts as an effective magnetic field $\mathbf{L}$ that we can define as

$$\mathbf{L} \equiv C\,\mathbb{R}\mathrm{e}[Z]\mathbf{s}. \tag{2.288}$$

Substituting C into (2.288) and making use of (2.172), (2.199), as well as the fact that the gyromagnetic ratio γ_e is given by $\gamma_e = g_J\mu_B/\hbar$, the classical electron radius r_e is given by $r_e = e^2/(m_ec^2)$ and that the intensity of the light is given by $I = |E_0|^2c/(8\pi)$, we obtain

$$\begin{aligned}\mathbf{L} &= -\frac{I}{h\nu}\frac{r_ef_{osc}c}{8\gamma_e}(11-4J_e(J_e+1))\frac{\nu-\nu_0}{(\nu-\nu_0)^2+\left(\gamma_{tot}/2\pi\right)^2}\mathbf{s} \\ &= -\frac{\mathscr{E}_p}{\hbar\gamma_e}\mathbf{q}, \end{aligned} \tag{2.289}$$

where in the second line we have made use of the definitions (2.269) and (2.268a)/(2.268b). We note here that since $\mathbf{q}$ has different signs for $\mathcal{D}_1/\mathcal{D}_2$ pumping, the lightshift $\mathbf{L}$ also has different signs for $\mathcal{D}_1/\mathcal{D}_2$ pumping. For $\mathcal{D}_1$ transitions with $J_e = 1/2$, this reduces to

$$\mathbf{L} = -\frac{I}{h\nu}\frac{r_e f_{osc} c}{\gamma_e}\frac{\nu - \nu_0}{(\nu - \nu_0)^2 + \Gamma_{tot}^2}\mathbf{s}, \tag{2.290}$$

where Γ_{tot} is the transition's HWHM in non-angular units. We note that the vector light-shift, like the Faraday rotation of linearly polarized light, is dispersive in that it is zero on resonance.

2.7 Optical Pumping

Optical pumping has been developed since the 1950s and there exists a number of review articles on this topic, including the comprehensive review by Happer [80] in 1972, and a number of later papers [73, 116, 121] that focused more on the spin-exchange pumping of noble gases (primarily Xe and He) via optically pumped alkali atoms and even a book [75] that focuses on performing numerical simulations in this area. Spin-exchange optical pumping (SEOP) of noble gas nuclei via optically pumped atoms find applications in many diverse areas including spin-polarized targets for nuclear and particle physics scattering experiments [134–136], neutron spin filters [137], magnetic resonance imaging [138, 139], and of course, precision measurements [55, 140] and the work in this thesis. Clearly, SEOP is a fascinating field in its own right and we note that despite its relatively long history, there are still elements of it that are not well understood, particularly in the case of SEOP of hyperpolarized Rb-^{3}He systems where there is an as yet unexplained ^{3}He relaxation mechanism that is proportional to Rb's density [121]. Furthermore, even in the optical pumping of alkali atoms, there remain areas which have escaped much study such as the role

of quenching gases [141] and we note that there has been misleading claims in the literature regarding the role of relaxation in the excited state as it pertains to the maximum attainable alkali spin polarization. Given that optical pumping is not a central focus of this thesis however, we can only point out in passing the areas of optical pumping or SEOP that are not currently well understood in the hopes that an interested reader may one day uncover some of their present day mysteries. We begin with a quick motivation for why optical pumping is required in the work of this thesis.

An isolated alkali atom in the absence of any fields that might break rotational symmetry has no well defined quantization axis and its total spin angular momentum $\mathbf{F}$ may, with equal probability, be oriented in any direction. Consequently, in the absence of any fields, there is no net ensemble averaged spin angular momentum in a macroscopic ensemble of alkali atoms. Upon application of a magnetic field however, the ground state hamiltonian (2.3) implies that there is an energy cost between different orientations of the spin angular momentum and it is now possible to speak of a macroscopic spin polarization in an ensemble where, on average, the spins of the alkali atoms in their ground states are more likely to point along a certain direction. In order to search for anomalous spin interactions with a macroscopic ensemble of atoms, it is obviously necessary to have a significant amount of spin polarized along a certain direction. However, since the energy splittings between the Zeeman levels are miniscule, the thermal spin polarization of the alkali atoms at our operating temperatures is far too small to be useful in searches for anomalous spin interactions. Consequently, it is necessary to polarize the spins of the alkali atoms using circularly polarized resonant light that carry a quantized angular momentum of 1 (in units of $\hbar$) along their direction of travel.

Conservation of energy and angular momentum implies that when an atom absorbs resonant circularly polarized light, it must be excited to a higher energy state and that

the transition must be subject to the selection rule $\Delta m_F = 1$, $\Delta E = E_e - E_g = h\nu$, where E_e, E_g are the energies of the excited and ground states respectively and ν is the frequency of the light. For $\mathcal{D}_1(^2S_{1/2} \rightarrow^2 P_{1/2})$ pumping where the total electronic angular momentum $J = 1/2$ in the excited state is the same as the ground state, the hyperfine coupling results in states with the same F, m_F numbers in both the excited and ground state. Consequently, the selection rule $\Delta m_F = 1$ implies that the pumping light pumps all but the $|F, F\rangle$ state in the ground state and by doing so, is polarizing the ground state by selectively depopulating it. However, this is only half the story since the excited atoms will eventually decay back to the ground state where they can, in general, repopulate any of the $|F, m_F\rangle$ ground states. The probability that an excited atom will end up in a particular ground state depends on the nature of the decay channel and on which excited state the atom is currently in. The total optical pumping is therefore dependent on both the depopulation and repopulation processes.

2.7.1 Depopulation pumping

As we have already seen from section 2.6.7, the ground state atoms evolve according to an effective Hamiltonian δH (2.259) as a result of the pump beam. According to the Liouville equation (2.29), the pumping light then causes the ground state density matrix to evolve as

$$\begin{aligned}\frac{d\rho_{dp}}{dt} = \frac{1}{i\hbar}\left[\delta H, \rho\right] &= \frac{1}{i\hbar}\left(\left(\mathscr{E}_p - \frac{i\hbar}{2}R_p\right)(1 - \mathbf{q}\cdot\mathbf{S})\,\rho - \rho\left(\mathscr{E}_p + \frac{i\hbar}{2}R_p\right)(1 - \mathbf{q}\cdot\mathbf{S})\right) \\ &= \frac{\mathscr{E}_p}{i\hbar}\left[\rho, \mathbf{q}\cdot\mathbf{S}\right] - R_p\left(\rho - \frac{1}{2}\left\{\mathbf{q}\cdot\mathbf{S}, \rho\right\}\right), \end{aligned} \tag{2.291}$$

where $\mathscr{E}_p$, R_p and $\mathbf{q}$ are as defined in (2.269), (2.237) and (2.268a)/(2.268b) for $(\mathcal{D}_1/\mathcal{D}_2)$ pumping respectively. We note that since $\mathrm{Tr}([\rho, \mathbf{q}\cdot\mathbf{S}]) = 0$, the rate of

atoms leaving the ground state is simply

$$\frac{d}{dt}\,\mathrm{Tr}[\rho] = -R_p\left(1 - \mathrm{Tr}\left[\mathbf{q}\cdot\mathbf{S}\rho\right]\right) = -R_p\left(1 - \mathbf{q}\cdot\langle\mathbf{S}\rangle\right), \tag{2.292}$$

in agreement with(2.236) and (2.270). Evidently, the term $[\rho, \mathbf{q}\cdot\mathbf{S}]$ corresponds not to atoms leaving the ground state but to the vector light-shift described in section 2.6.9.

2.7.2 Repopulation pumping

Once excited to the excited state, the probability that an atom in an excited state $|e\rangle$ will decay to a particular ground state $|g\rangle$ depends on the matrix element $\langle g\,|\mathbf{r}|\,e\rangle$ and the lifetime of the excited state is therefore dependent on the sum of all these different amplitudes. For excited alkali atoms in the first $^2P_{1/2}$ states, this lifetime is typically on the order of 20 ns. Measurements of the natural lifetime of the $4^2P_{1/2}$ state in K yields $\sim$ 26 ns while the analogous measurement of the $5^2P_{1/2}$ state in Rb gives $\sim$ 29 ns [142]. However, decaying via spontaneous emission is undesirable for optical pumping since the polarization of the emitted photon is random and its absorption by a nearby alkali atom will in general result in the randomization of that atom's electronic angular momentum. Since our co-magnetometer cell consists of a dense alkali vapor that is optically thick, most of this fluorescence light never escapes the cell and can consequently cause significant depolarization within the alkali vapor. A common solution to this "radiation trapping" problem, which can be significant at alkali number densities as low as $\sim 3\times10^{11}$ cm^{-3} [143], is to introduce quenching gas into the cells.

It has been known since at least the 1960s that radiationless decay of excited alkali atoms are possible via inelastic "quenching" collisions with molecules [144–146] that carry away the excess energy of the excited alkali atom. Experimental

measurements have indicated that whereas noble gas atoms such as He have extremely small quenching cross sections with excited alkali atoms (for example, $< 10^{-19}$ cm^2 with Cs [147]), molecular buffer gas such as N_2 have considerably larger (on the order of $\sim 5 \times 10^{-15}$ cm^2) quenching cross sections due to their vibrational states [143] and can effectively quench excited alkali atoms before they decay via spontaneous emission. A study of electronic and nuclear spin polaization transfers due to quenching collisions suggests that the duration of a quenching collision is so short compared to the spin-orbit $\mathbf{L} \cdot \mathbf{S}$ period that the orientation of the alkali's electronic (and hence nuclear) spin is conserved during a quenching collision [148]. In the optical pumping literature, it is typically assumed that sufficient quenching gas is added so that the average time for a quenching collision to occur T_Q is ~ 1 ns, which is much less than the ~ 25 ns natural lifetime of the excited state in alkali atoms [73] so that to a good approximation, an excited alkali atom can be assumed to decay via a quenching collision.

However, before decaying via a quenching collision in ~ 1 ns after being excited from the ground state, the alkali atom is typically assumed to have lost all of its electronic polarization due to "J-damping" collisions with noble and buffer gas atoms. As its name implies, these J-damping collisions randomize the electronic spin of the excited alkali atom but leaves the nuclear spin untouched. Physically, this is due to the fact that the duration of these collisions are so short that they are unable to substantially affect the nuclear spin through the hyperfine interaction. For a Rb-^{3}He high pressure cell with 10 amagats of ^{3}He, these J-damping collisions typically happen at an average rate of once every ~ 10 ps [73], which is significantly faster than the rate of quenching collisions. Consequently, it is typically assumed that by the time an alkali atom decays via a quenching collision, it would have lost all of its electronic polarization but none of its nuclear polarization [73, 116]. Given these assumptions, we can easily write down the evolution of the ground state density matrix due to the

repopulation term. Since only the nuclear polarization of the atoms depopulated out of the ground state is preserved and the nuclear part of a density matrix operator ρ is given by (2.37), we have

$$\frac{d\rho_{rp}}{dt} = -\frac{1}{4}\frac{d\rho_{dp}}{dt} - \mathbf{S}\cdot\frac{d\rho_{dp}}{dt}\mathbf{S}. \tag{2.293}$$

2.7.3 Total pumping

The evolution of the ground state density matrix due to optical pumping is then

$$\frac{d\rho_{op}}{dt} = \frac{3}{4}\frac{d\rho_{dp}}{dt} - \mathbf{S}\cdot\frac{d\rho_{dp}}{dt}\mathbf{S}. \tag{2.294}$$

We note that from (2.41) and (2.42)

$$\mathbf{S}\cdot[\rho,\mathbf{q}\cdot\mathbf{S}]\mathbf{S} = q_i S_j[\rho,S^i]S^j = q_i\left(S_j\rho S^i S^j - S_j S^i\rho S^j\right) = \frac{1}{4}[\mathbf{q}\cdot\mathbf{S},\rho], \tag{2.295}$$

and

$$\mathbf{S}\cdot\{\mathbf{q}\cdot\mathbf{S},\rho\}\mathbf{S} = q_i S_j\{S^i,\rho\}S^j = \frac{1}{4}\{\mathbf{q}\cdot\mathbf{S},\rho\} + i\mathbf{q}\cdot(\mathbf{S}\times\rho\mathbf{S}). \tag{2.296}$$

Consequently, under the influence of the pumping light, the density matrix evolves as

$$\begin{aligned}\frac{d\rho_{op}}{dt} &= -\frac{\mathscr{E}_p}{i\hbar}[\mathbf{q}\cdot\mathbf{S},\rho] - R_p\left(\rho - \phi - \frac{1}{4}\mathbf{q}\cdot(\{\mathbf{S},\rho\} - 2i(\mathbf{S}\times\rho\mathbf{S}))\right)\\ &= -\frac{\mathscr{E}_p}{i\hbar}[\mathbf{q}\cdot\mathbf{S},\rho] + R_p(\phi(1+\mathbf{q}\cdot\mathbf{S}) - \rho),\end{aligned} \tag{2.297}$$

where we have made use of (2.48) in going from the first to second line. Experimentally, we measure ensemble average quantities and it is therefore useful to turn (2.297) into one that involves such quantities. At the low magnetic fields pertinent to co-magnetometer operation, the total angular momentum $\mathbf{F}$ is, as discussed in section 2.1, approximately conserved whereas the nuclear spin $\mathbf{I}$ and electron spin $\mathbf{S}$ are not.

We are therefore interested in the evolution of the ensemble average of $\mathbf{F}$ as a result of the pumping light, which may be obtained by multiplying (2.297) by $\mathbf{F}$ and taking the trace.

Letting $\langle \mathbf{S} \rangle \to \mathbf{q}$ in (2.71) and (2.72), we have

$$\mathrm{Tr}(\mathbf{q} \cdot \{\mathbf{S}, \rho\}\mathbf{F}) = \frac{1}{2}\mathbf{q} + 2q_j \left\langle S^j \mathbf{I} \right\rangle \tag{2.298}$$

$$\mathrm{Tr}(\mathbf{q} \cdot (\mathbf{S} \times \rho\mathbf{S})\mathbf{F}) = i\left(\frac{1}{4}\mathbf{q} - q_j \left\langle S^j \mathbf{I} \right\rangle\right), \tag{2.299}$$

while from (2.85) and letting $\langle \mathbf{K} \rangle \to \mathbf{q}$, we get

$$\mathrm{Tr}([\mathbf{q} \cdot \mathbf{S}, \rho]\mathbf{F}) = i\mathbf{q} \times \langle \mathbf{S} \rangle . \tag{2.300}$$

Consequently, we derive from (2.297)

$$\begin{aligned}
\frac{d\left\langle \mathbf{F} \right\rangle_{op}}{dt} &= \mathrm{Tr}\left(\frac{d\rho}{dt}\mathbf{F}\right) = -\frac{\mathscr{E}_p}{i\hbar}\mathrm{Tr}([\mathbf{q} \cdot \mathbf{S}, \rho]\mathbf{F}) \\
&\quad + R_p\left(-\mathrm{Tr}((\rho - \phi)\mathbf{F}) + \frac{1}{4}\mathrm{Tr}(\mathbf{q} \cdot \{\mathbf{S}, \rho\}\mathbf{F}) - \frac{i}{2}\mathrm{Tr}(\mathbf{q} \cdot (\mathbf{S} \times \rho\mathbf{S})\mathbf{F})\right) \\
&= -\frac{\mathscr{E}_p}{\hbar}\mathbf{q} \times \langle \mathbf{S} \rangle + R_p\left(\frac{1}{4}\mathbf{q} - \langle \mathbf{S} \rangle\right) \\
&= \gamma_e \mathbf{L} \times \langle \mathbf{S} \rangle + R_p\left(\frac{1}{4}\mathbf{q} - \langle \mathbf{S} \rangle\right),
\end{aligned} \tag{2.301}$$

where in the last line we have made use of (2.289). We therefore see that the the pump light has a two-fold effect: it behaves like an effective magnetic field $\mathbf{L}$ (the light-shift) and it pumps the vapor since the angular momentum increases at a rate of $R_p(\mathbf{q}/4 - \langle \mathbf{S} \rangle)$. It is worth noting that since $\mathbf{q} = 2\mathbf{s}$ for $\mathcal{D}_1$ pumping but is $-\mathbf{s}$ for $\mathcal{D}_2$ pumping, the maximum polarization attainable for $\mathcal{D}_2$ pumping is 0.5. Moreover, we note that $\mathcal{D}_2$ pumping results in angular momentum being built up in the opposite direction from the mean photon spin $\mathbf{s}$. Since $\mathcal{D}_2$ pumping can only polarize the alkali atoms up to 50%, we use $\mathcal{D}_1$ pumping in this work.

We note that Equation (2.301) is valid under the assumptions that the hyperfine structure is not resolved due to collisional broadening (i.e. the assumptions made in (2.197) and (2.199)), that most of the excited state alkali atoms decay via quenching collisions, and that there is no depolarization of the nuclear spin's polarization while the alkali atom is in the excited state.

2.7.4 Hybrid pumping

As we shall discuss in greater detail later, the continuously pumped co-magnetometer achieves maximum sensitivity at an alkali polarization of 50%. However, this implies that the alkali atoms are not fully polarized and consequently, according to (2.238), there will continue to be significant absorption of the pumping light throughout the cell. This results in considerable attenuation of the pumping light throughout the length of the cell, which translates into an alkali polarization gradient across the length of the cell that makes it impossible for all parts of the cell to achieve the nominal 50% polarization condition required for optimal sensitivity. We note that in our high pressure co-magnetometer cells, the time it would take for an alkali atom to diffuse through the volume of the cell is typically much longer compared to its spin relaxation life time. Accordingly, the polarization gradient cannot be removed by diffusive means. A large polarization gradient in the cell also means that some parts of the cell are not exactly satisfying the "compensation point" condition whereby the sum of the alkali and noble-gas magnetization cancels out the applied $\mathbf{B}$ field. As we discuss later, the co-magnetometer needs to be operated at this "compensation point" to ensure good suppression of ordinary magnetic field while retaining high sensitivity to anomalous fields, which are both properties that are crucial to measuring a tiny anomalous spin-mass interaction without serious systematic effects from magnetic interactions. To mitigate these problems [149], we employ a hybrid pumping technique [97, 150] wherein we optically pump an optically thin ^{87}Rb vapor, which

then spin polarizes an optically thick K vapor via spin-exchange collisions. By pumping an optically thin ^{87}Rb vapor, the attenuation of the pump beam through the cell is reduced, which translates to more uniform optical pumping and hence alkali polarization throughout the cell.

Consider two species of alkali atoms labeled r (receiver) and d (donor) where we optically pump the optically thin donor vapor. From our discussions in sections 2.1, 2.2, 2.3 and 2.7.3, we can write down the density matrix evolution of the two species under $\mathcal{D}_1$ pumping of the donor species as

$$\frac{d\rho^r}{dt} = \frac{1}{i\hbar}[A_g^r \mathbf{I}\cdot\mathbf{S}, \rho^r] + \sum_j R_{ex}^{rj}(\phi^r(1+4\left\langle \mathbf{S}^j\right\rangle\cdot\mathbf{S}) - \rho^r) - R_{sd}^r(\rho^r - \phi^r) \tag{2.302}$$

$$\begin{aligned}\frac{d\rho^d}{dt} = &\frac{1}{i\hbar}[A_g^d \mathbf{I}\cdot\mathbf{S} - 2\mathscr{E}_p \mathbf{s}_p\cdot\mathbf{S}, \rho^d] + R_p(\phi^d(1+2\mathbf{s}_p\cdot\mathbf{S}) - \rho^d) \\ &+ \sum_j R_{ex}^{dj}(\phi^d(1+4\left\langle \mathbf{S}^j\right\rangle\cdot\mathbf{S}) - \rho^d) - R_{sd}^d(\rho^d - \phi^d)\end{aligned} \tag{2.303}$$

where $\mathscr{E}_p$ and R_p are as defined in (2.269) and (2.237). $R_{ex}^{ij} = 1/T_{ex}^{ij}$ is as defined in (2.61), and by R_{sd}^i we mean here the sum of all electronic spin destruction rates for that alkali species. This would include spin destruction due to spin-axis collisions with other alkali atoms, spin-rotation collisions with noble/buffer gas molecules and spin-exchange collisions with noble gas atoms. We note that strictly speaking, if spin-exchange collisions with noble gas atoms are considered, there should be an additional term corresponding to the back polarization from noble-gas atoms (see (2.89)). However, since the equilibrium polarization of the alkali atoms tends to be more than 10 times larger compared to the noble gas polarization in our cells, the back polarization from the noble-gas atoms can typically be ignored. Multiplying both sides of the equations with $\mathbf{F}$ and taking the trace, we obtain for on resonant

pumping (so that $\mathscr{E}_p = 0$)

$$\begin{aligned}\frac{d\left\langle F_z^r\right\rangle}{dt} &= R_{ex}^{rd}(\left\langle S_z^d\right\rangle - \left\langle S_z^r\right\rangle) - R_{sd}^r \left\langle S_z^r\right\rangle \\ \frac{d\left\langle F_z^d\right\rangle}{dt} &= R_p\left(\frac{1}{2}s_z - \left\langle S_z^d\right\rangle\right) + R_{ex}^{dr}(\left\langle S_z^r\right\rangle - \left\langle S_z^d\right\rangle) - R_{sd}^d \left\langle S_z^d\right\rangle .\end{aligned} \tag{2.304}$$

The equilibrium polarization ($P \equiv \langle S\rangle / S$) for the two species is then

$$P^r = \frac{s_z}{1 + \frac{1}{R_p}\left(R_{sd}^d\left(1 + \frac{R_{sd}^r}{R_{ex}^{rd}}\right) + R_{sd}^r\frac{n_r}{n_d}\right) + \frac{R_{sd}^r}{R_{ex}^{rd}}} \tag{2.305}$$

$$P^d = \frac{R_p(R_{ex}^{rd} + R_{sd}^r)s_z}{R_{ex}^{dr}R_{sd}^r + R_{sd}^d(R_{ex}^{rd} + R_{sd}^r) + R_p(R_{ex}^{rd} + R_{sd}^r)}. \tag{2.306}$$

From (2.305), it is evident that the following two conditions are necessary in order to obtain high receiver alkali polarization:

$$\frac{R_{sd}^r}{R_{ex}^{rd}} \ll 1 \tag{2.307}$$

$$\frac{R_{sd}^d + R_{sd}^r\frac{n_r}{n_d}}{R_p} \ll 1, \tag{2.308}$$

where n_d, n_r are the number densities of the donor and receiver species respectively. These conditions basically state that the spin-exchange rate of the receiver with the donor species must be much larger compared to the spin-destruction rate of the receiver species; and the optical pumping rate of the donor species must be sufficiently large to polarize the atoms. If the first condition (2.307) is met, then (2.305),(2.306) reduces to

$$P_z^r = P_z^d = \frac{R_p s_z}{R_p + R_{sd}^d + R_{sd}^r\frac{n_r}{n_d}}, \tag{2.309}$$

which has led some in the literature to interpret that the alkali atoms acquires a new effective spin-destruction rate

$$\tilde{R}^r_{sd} \approx R^d_{sd} + R^r_{sd}\frac{n_r}{n_d}. \tag{2.310}$$

However, we contend here that this is the wrong interpretation. In particular, this "effective spin-destruction rate" does *not* give the correct the late-time pump or decay time constant and conversely, experimentally measuring the late-time pump or decay time constant of a hybrid pumped system to calculate the expected equilibrium polarization will yield the *wrong* answer. Before going on to show this, we note here that the equilibrium polarization is affected by R^d_{sd} and it is therefore best to use lighter alkali metals for the donor species since the lighter alkali metals have smaller spin-destruction cross-sections although R^d_{sd} is arguably less important at high n_r/n_d ratios where n_r/n_d will significantly amplify R^r_{sd} and potentially limit the maximum achievable polarization.

To understand our assertion why (2.310) should not be interpreted as an effective spin destruction rate for the alkali atoms, it is instructive to examine the time dependence of the homogeneous solution to the two coupled differential equations (2.304). To do so, we note that under sufficiently high spin-exchange rate so that the two alkali species are in spin-exchange equilibrium, $\langle F^i_z\rangle = \langle S^i_z\rangle\, Q(P^i)$, where Q is as defined in (2.133). Strictly speaking, Q is dependent on P and is hence time dependent. However, we note that Q does not typically vary too much over its entire range, especially for $I = 3/2$ where it only varies from 4 to 6, and we can therefore take it to be approximately constant in the limit as $\langle S\rangle$ is approaching its steady state value. In that case, we may write the coupled differential equations (2.304) as

$$\frac{d}{dt}\begin{pmatrix} P^r_z \\ P^d_z \end{pmatrix} = \begin{pmatrix} -\frac{1}{Q^r}(R^{rd}_{ex} + R^r_{sd}) & \frac{1}{Q^r}R^{rd}_{ex} \\ \frac{1}{Q^d}R^{dr}_{ex} & -\frac{1}{Q^d}(R^{dr}_{ex} + R^d_{sd} + R_p) \end{pmatrix}\begin{pmatrix} P^r_z \\ P^d_z \end{pmatrix} + \begin{pmatrix} 0 \\ \frac{1}{Q^d}R_p s_z \end{pmatrix}, \tag{2.311}$$

which has a homogeneous solution of the form

$$\mathbf{P}(t) = \mathbf{P}_+ e^{\lambda_+ t} + \mathbf{P}_- e^{\lambda_- t}, \tag{2.312}$$

where $\lambda_\pm$ are eigenvalues of the matrix in (2.311) and $\mathbf{P}_\pm$ are some constant 2D vectors. The eigenvalues are

$$\lambda_\pm = -\frac{Q^r(R_{ex}^{dr} + R_p + R_{sd}^d) + Q^d(R_{ex}^{rd} + R_{sd}^r) \pm \sqrt{C(R_{ex}^{dr}, R_{ex}^{rd}, R_{sd}^d, R_{sd}^r, R_p)}}{2Q^rQ^d}, \tag{2.313}$$

where C is

$$\begin{aligned} C = (Q^r R_{ex}^{dr} + Q^d R_{ex}^{rd})^2 \Bigg[1 + \frac{2(Q_r R_{ex}^{dr} - Q_d R_{ex}^{rd})}{(Q^r R_{ex}^{dr} + Q^d R_{ex}^{rd})^2}(Q^r R_{sd}^d + Q^r R_p - Q^d R_{sd}^r) \\ + \frac{1}{(Q^r R_{ex}^{dr} + Q^d R_{ex}^{rd})^2}\mathcal{O}(R_p, R_{sd}^d, R_{sd}^r)\Bigg]. \end{aligned} \tag{2.314}$$

In the limit of fast spin-exchange, the last term in the the square bracket can be dropped and the second term is less than 1, which allows us to expand $\sqrt{C}$ as

$$\sqrt{C} \approx Q^r R_{ex}^{dr} + Q^d R_{ex}^{rd} + \alpha(Q^r R_{sd}^d + Q^r R_p - Q^d R_{sd}^r), \tag{2.315}$$

where we have for convenience defined α as

$$\alpha \equiv \frac{Q_d R_{ex}^{rd} - Q_r R_{ex}^{dr}}{Q^r R_{ex}^{dr} + Q^d R_{ex}^{rd}} = \frac{Q_d n_d - Q_r n_r}{Q_r n_r + Q_d n_d}. \tag{2.316}$$

Evidently, the λ_+ solution damps extremely quickly and the relevant eigenvalue we are interested in is therefore

$$\lambda_- = \frac{1}{T_1^{pump}} \approx -\left[\frac{R_p}{2Q^d}(1+\alpha) + \frac{R_{sd}^r}{2Q^r}(1-\alpha) + \frac{R_{sd}^d}{2Q^d}(1+\alpha)\right]. \tag{2.317}$$

It is now clear why (2.310) should not be interpreted as an "effective spin destruction rate": the denominator of (2.309) looks nothing like (2.317) and will give a wrong decay/pump up late-time time constant. Rather, (2.317) suggests that the hybrid pumped system acquires a new effective pumping and spin-destruction rate given by

$$\tilde{R}_p = \frac{R_p}{2Q^d}(1+\alpha) \tag{2.318}$$

$$\tilde{R}^e_{sd} = \frac{R^r_{sd}}{2Q^r}(1-\alpha) + \frac{R^d_{sd}}{2Q^d}(1+\alpha), \tag{2.319}$$

which will give the correct time dependence and an "effective" mean photon spin

$$\tilde{s}_z = s_z \frac{R_p}{\tilde{R}_p} \frac{\tilde{R}_p + \tilde{R}^e_{sd}}{R_p + R^d_{sd} + R^r_{sd}\dfrac{n_r}{n_d}}, \tag{2.320}$$

which will give the correct equilibrium polarization. Substituting (2.318), (2.319) and (2.316) into (2.320) however, we find that

$$\tilde{s}_z = s_z \frac{n_d R_p + n_d R^d_{sd} + n_r R^r_{sd}}{n_d R_p + n_d R^d_{sd} + n_r R^r_{sd}} = s_z, \tag{2.321}$$

so that the hybrid pumped system can be neatly described by just the effective pumping and spin-destruction rate given by (2.318) and (2.319).

Using these effective pumping and spin-destruction rates, we may model the electron polarization of the hybrid pumped system in the limit of fast spin-exchange as

$$\frac{dP^e_z}{dt} = \tilde{R}_p\left(s_z - P^e_z\right) - \tilde{R}^e_{sd} P^e_z. \tag{2.322}$$

It is also interesting to consider the case where $Q^r = Q^d$, which corresponds to the case when both the donor and receiver species have the same nuclear spin. In that

case, the correction factor α simply reduces to

$$\alpha = \frac{n_d - n_r}{n_d + n_r}, \tag{2.323}$$

and the effective rates (after pulling out an overall $1/Q$ factor) and mean photon spin simplify to give

$$\tilde{R}_p = R_p \frac{1}{1 + \frac{n_r}{n_d}} \tag{2.324}$$

$$\tilde{R}^e_{sd} = \frac{n_r R^r_{sd} + n_d R^d_{sd}}{n_d + n_r} \tag{2.325}$$

so that the effective rate equation (2.322) now becomes

$$\frac{dP^e_z}{dt} = \frac{\tilde{R}_p}{Q}(s_z - P^e_z) - \frac{\tilde{R}^e_{sd}}{Q} P^e_z, \tag{2.326}$$

with the effective rates $\tilde{R}_p$ and $\tilde{R}^e_{sd}$ now given by (2.324) and (2.325) respectively.

We have numerically verified that (2.322) is indeed the correct effective differential equation to describe the coupled differential equations (2.311). Numerically solving the two coupled differential equations (2.311) yields the curves on the left of Figure 2.4, which shows that in the limit of high spin-exchange, the polarizations of P^r and P^d are, unsurprisingly, effectively the same. On the right of Figure 2.4, we show the solution (green dash-dot) of the effective electron polarization given by (2.322), which agrees with the full solution to an excellent approximation. On the other hand, the solution of a naive effective equation with just a modified spin destruction rate without any changes to the pumping rate yields the red dotted curve, which gives the correct equilibrium polarization but the wrong time dependence. Practically, this means that a measured late-time decay time constant should be interpreted not as a measure of (2.310) but of (2.319).

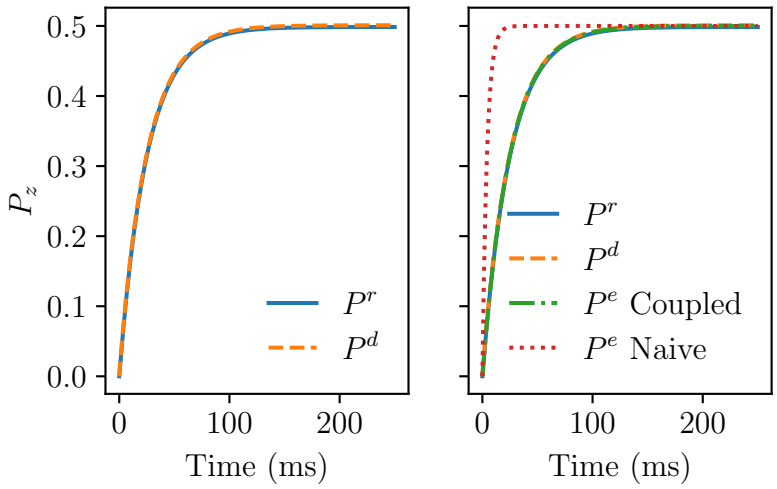

Figure 2.4: Effective dynamics of hybrid pumping.

Unfortunately, it is not easy to use (2.319) to predict the correct steady state polarization since one does not *a priori* know R^r_{sd} or R^d_{sd}. We note here that it is important to include the correction factor α to obtain good agreement between the effective differential equation (2.322) and the full coupled differential equations (2.311). This is especially true for large n_r/n_d ratios (which is typically the case) and/or large difference in Q^r and Q^d, which will increase the magnitude of α. Lastly, we note that (2.322) does not explicitly include in the slowing down factors since those are absorbed into the new effective rate constants. For different Q^r and Q^d (i.e. the receiver and donor alkali species have different nuclear spins), different rate constants are modified differently and it is hence not possible to pull out an overall slowing down factor. The results in Figure 2.4 were obtained with $Q^r = 5$ and $Q^d = 10$ (roughly corresponding to K and Rb) and demonstrate that (2.322) can accurately take into account the different slowing down factors of the two alkali species.

It is also instructive to consider how well the effective coupled rate equation (2.322), and the coupled Bloch equations (2.311), derived from taking $\mathrm{Tr}[\rho\mathbf{F}]$ of the relevant density matrix equations (2.302),(2.303) and assuming spin tempera-

ture equilibrium, compares to calculations using the density matrix equations (2.302) and (2.303). We first consider the case of using ^{85}Rb as the lean donor species and K as the optically thick receiver species with a density of $n_r = 1 \times 10^{14}$ cm^{-3} at a temperature of 192 °C. We nominally set $R^d_{sd} = 200$ /s and $R^r_{sd} = 100$ /s and consider a density ratio of $n_r/n_d = 10$. Spin-exchange rates were calculated per (2.61) using the cross-sections given in Table 2.1. Since there are no measurements of the ^{85}Rb-K spin-exchange cross-section, we have simply taken the average of the spin-exchange cross-section between ^{85}Rb-^{85}Rb and K-K, which are, in any case, only different from each other by $\approx 25\%$. Tuning R_p with (2.309) so as to obtain a equilibrium polarization of 50%, we obtain the results shown in Figure 2.5, which shows that for these parameters, the effective coupled rate equation as well as the coupled Bloch equations agree with the density matrix equations remarkably well, especially since ^{85}Rb has a different nuclear spin from K and hence different slowing down factors. For the effective rate and coupled Bloch equations, we have approximated $Q^r \approx 5$ and $Q^d \approx 10$ in this case.

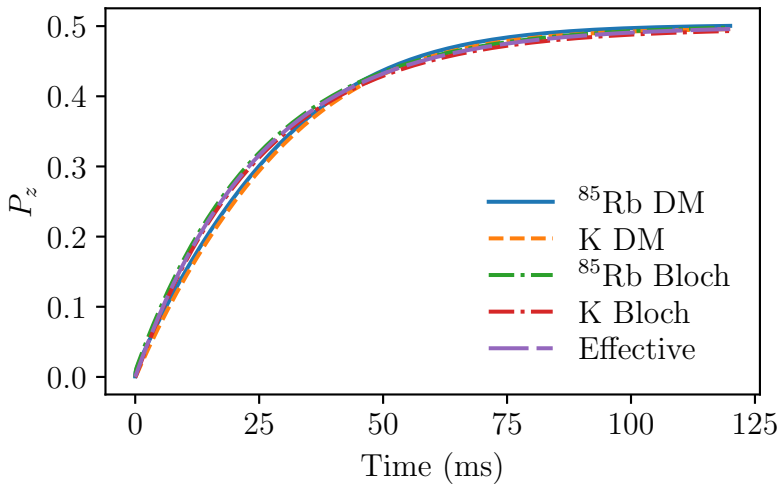

Figure 2.5: Agreement of effective and coupled Bloch equations with density matrix simulations at $n_r/n_d = 10$.

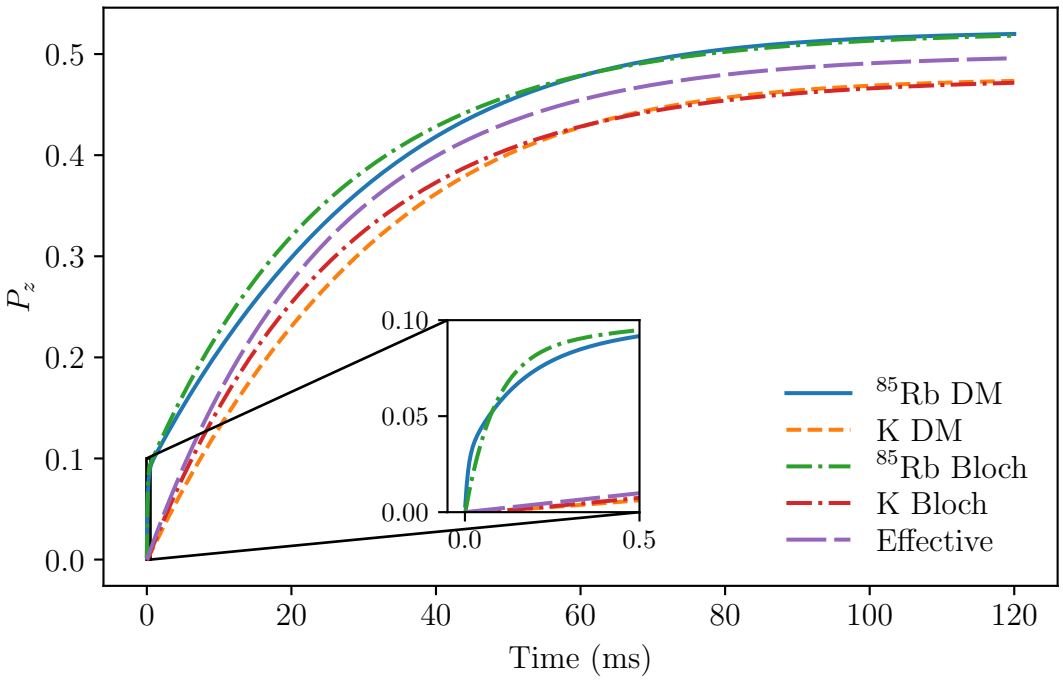

Figure 2.6: Break down of effective and coupled Bloch equations at $n_r/n_d = 100$.

Nevertheless, this nice agreement begins to break down as we further increase the density ratio n_r/n_d. Figure 2.6 shows the results of the same calculations when n_r/n_d is increased by an order of magnitude to 100. In this case, we see that the two species are no longer in spin-temperature equilibrium with each other with the donor ^{85}Rb being polarized more than the receiver K species. Interestingly enough, the coupled Bloch equations still agree reasonably well with their respective density matrix equations while the effective equation gives an average value in between the ^{85}Rb and K polarization. In particular, we note that the coupled Bloch equation for ^{85}Rb tracks the density matrix calculations relatively well at the scale of Figure 2.6 even during the initial period (see inset of Figure 2.6) where it rises sharply due to the high pumping rate required to polarize the vapor to $\sim 50\%$ polarization. This is somewhat surprising given that the derivation of the Bloch equation assumes that the vapor is in spin-temperature equilibrium and ^{85}Rb is likely to not be in spin-

temperature equilibrium with itself at early times when there is strong pumping from the laser.

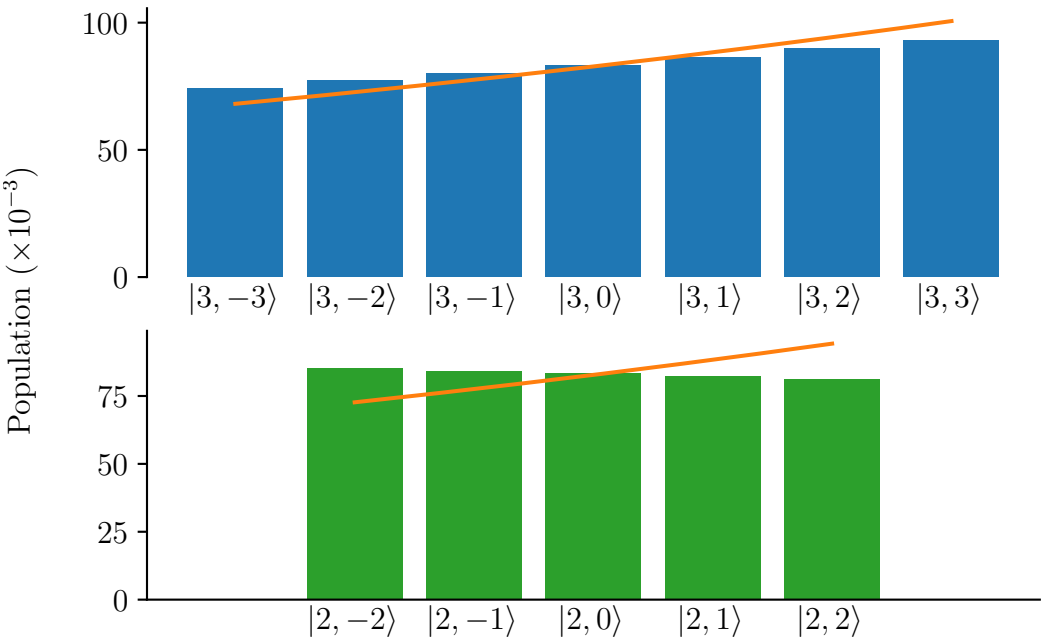

Figure 2.7: Population distribution of ^{85}Rb under intense pumping.

To determine if ^{85}Rb is in spin-temperature equilibrium with itself, we may plot out its population levels and check if it matches the levels predicted by (2.105) given its current value of $\langle \mathbf{S} \rangle$. Figure 2.7 shows the population levels of ^{85}Rb from the calculation in Figure 2.6 20 μs after the pump beam turns on. The blue and green boxes show the population in the $F = 3$ and $F = 2$ states respectively while the orange curves give the expected population levels that the vapor would be expected to have from (2.105) given its current value of $\langle \mathbf{S} \rangle$ if it was in spin-temperature equilibrium. Evidently, the vapor is not in spin-temperature equilibrium at early times.

However, at later times when more atoms become polarized and the pumping slows down, the vapor does regain spin temperature equilibrium with itself as Figure 2.8, which displays the population levels of ^{85}Rb at 10 ms after the onset of the pump

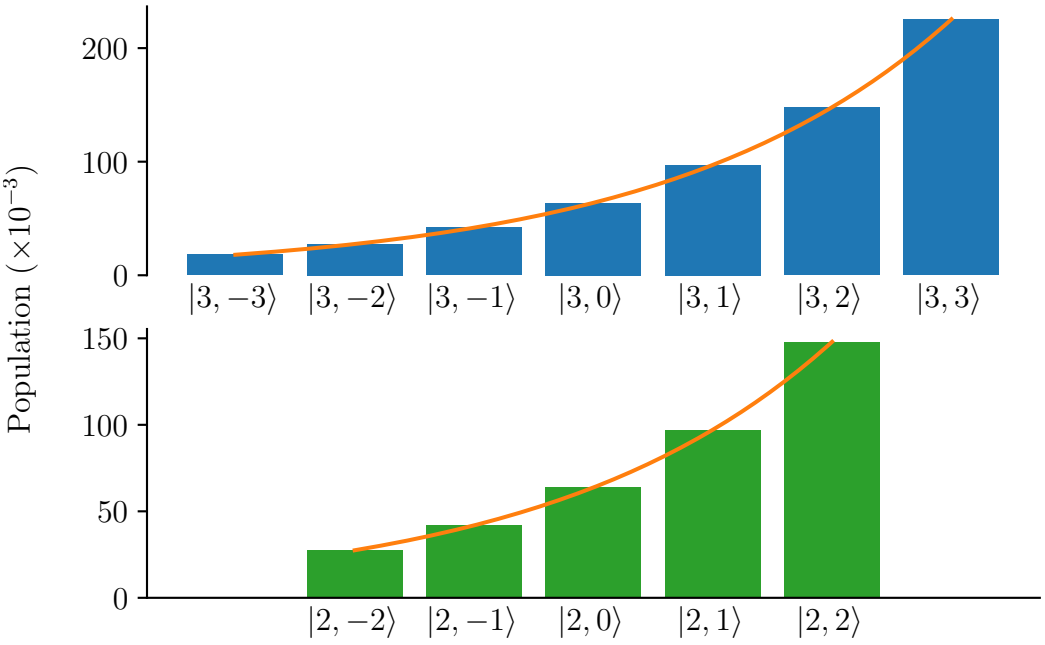

Figure 2.8: Population distribution of ^{85}Rb at later times.

beam, shows. We note that K remained in spin temperature equilibrium with itself throughout the entire time but is unable to come to spin temperature equilibrium with ^{85}Rb since n_d is simply too small due to the large n_r/n_d density ratio (i.e. condition (2.307) is no longer fulfilled). Of course, this problem can in theory be circumvented by going to higher temperatures so that both n_r and n_d become bigger[23] but in practice, there is an upper limit to the maximum operating temperature (around 220 °C) the glass cell can tolerate before the alkali attacks and discolors it.

For hybrid pumping to work as desired in our case, we would also like the donor species to be optically thin (OD$<$ 1), which gives the third and last condition for hybrid pumping to be effective:

$$n_d < \frac{1}{\sigma_d L}, \tag{2.327}$$

[23]We note that the two alkali species do come back into spin temperature equilibrium as expected if the simulations are repeated with all the same parameters except that $n_r = 1 \times 10^{15}$ cm^{-3} is an order of magnitude larger than before.

where σ_d is the absorption cross-section of the donor species (for linearly polarized light) as defined in (2.243) and L is the length of the cell.

If we assume $s_z \approx 1$ for circularly polarized pumping light and sufficiently rapid spin-exchange with the donor species so that the equilibrium polarization of the receiver species as a function of the pumping rate $\tilde{R}_p(z)$ is approximately

$$P^r(z) = \frac{\tilde{R}_p(z)}{\tilde{R}_p(z) + \tilde{R}^e_{sd}}, \tag{2.328}$$

where $\tilde{R}_p$ and $\tilde{R}^e_{sd}$ are as defined in (2.324) and (2.325) respectively, then we may solve for $\tilde{R}_p(z)$ and $P^r(z)$ by noting that from (2.232), (2.234) and (2.237),

$$\frac{d\tilde{R}_p}{dz} = -n_d\sigma_d\tilde{R}_p(z)(1 - P^r) = -n_d\sigma_d\tilde{R}_p(z)\frac{\tilde{R}^r_{sd}}{\tilde{R}_p(z) + \tilde{R}^r_{sd}}. \tag{2.329}$$

This solution to this differential equation is

$$\tilde{R}_p(z) = \tilde{R}^r_{sd} W\left(\frac{\tilde{R}_p(0)}{\tilde{R}^r_{sd}} e^{-n_d\sigma_d z + \tilde{R}_p(0)/\tilde{R}^r_{sd}}\right), \tag{2.330}$$

where W is here the Lambert-W function [151] and $\tilde{R}_p(0)$ is the initial (effective) pumping rate (for unpolarized atoms). Substituting this back in (2.328) yields the polarization as a function of z. We note that σ_d and n_d are here the absorption cross-section (for linearly polarized light) and number density of the donor species, even though the polarization P^r is the polarization of the receiver species. Figure 2.9 shows the polarization distribution across a 1 cm cell with and without hybrid pumping. In the calculation leading to Figure 2.9 we have used similar parameters as in our simulations above with $n_r = 10^{14}$ cm^{-3} and $R^r_{sd} = 100$ /s, $R^d_{sd} = 200$ /s. The absorption cross-section for unpolarized atoms can be calculated using (2.243) and the collisional broadened linewidths can be calculated using (4.16) and the rates in Table 4.1 for Rb and K in He. For the calculation leading to Figure 2.9, we have

assumed a He number density of 10 amagats and have let K to be the optically thick receiver species while Rb was chosen to be the lean donor species.

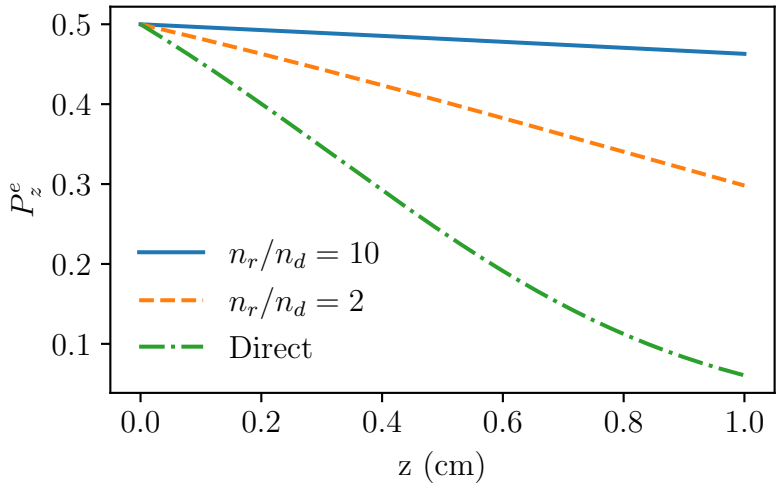

Figure 2.9: Polarization distribution with and without hybrid pumping over a 1 cm cell.

As Figure 2.9 shows, having a density ratio $n_r/n_d = 10$ can have a fairly dramatic effect, especially at a relatively high receiver number density of 10^{14} cm^{-3}. Compared to direct optical pumping, hybrid pumping gives a more uniform polarization gradient mainly by having smaller values of n.

2.8 Other Relaxation Processes

Besides collisional processes like spin-rotation and spin-axis collisions that randomize the spin orientation of polarized alkali atoms, there are a few other non-collisional relaxation mechanisms that affect spin polarized atoms. These mechanisms can be broadly classified into relaxation processes due to the walls of the cell and inhomogeneous magnetic fields. Wall collisions can be significant for both alkali and noble gas spin relaxation but inhomogeneous fields is mostly only significant for noble gas

depolarization. In this section, we briefly discuss these two relaxation mechanisms as they pertain to alkali and noble gas atoms.

2.8.1 Inhomogeneous magnetic fields

Inhomogeneous magnetic fields can cause faster relaxation of both the longitudinal and transverse components of the atoms' spin polarization. During operation of the co-magnetometer, we typically apply a homogeneous bias $\mathbf{B}_0 = B_0\hat{z}$ field to cancel out the net sum of the noble gas and alkali's magnetization. However, imperfections in the field coils as well as remnant magnetic fields from the innermost ferrite shield can give rise to a small, spatially varying magnetic field $\mathbf{B}_1(\mathbf{r})$ on top of a homogeneous field. Although $\mathbf{B}$ field inhomogeneity can in principle relax both the alkali and noble gas spins, the relaxation of the alkali atoms due to other collisional processes is far larger and hence, relaxation due to inhomogeneous $\mathbf{B}$ fields are typically negligible for alkali atoms. On the other hand, inhomogeneous $\mathbf{B}$ fields are a significant cause of spin relaxation in noble gas atoms since they are, by virtue of their nuclear spins' isolation from the environment, much less affected by collisions. Indeed, self-relaxation due to $\mathbf{B}$ field gradients produced by the noble gas' own magnetization is frequently what limits the noble gas' equilibrium polarization in our co-magnetometer cells [152].

The way in which transverse inhomogeneous fields result in longitudinal relaxation of the noble gas' spin depends, as noted in [153], on the ratio of two characteristic time scales: the time scale of precession in the homogeneous field $\mathbf{B}_0$ and a diffusion time scale. Intuitively, the precession time scale, which is a proxy of the strength of the homogeneous field, determines the strength of the inhomogeneity while the diffusion time scale is a proxy for how much of the inhomogeneity an atom actually experiences. Consider a ^{3}He atom with nucleus spin $K = 1/2$ moving through a region with inhomogeneous $\mathbf{B}$ fields. Its ground state Hamiltonian in between collisions is

simply [73]

$$H = -\frac{\mu_K}{K}\mathbf{K}\cdot\mathbf{B}, \tag{2.331}$$

where μ_K is its magnetic dipole moment. If at $t = 0$ we choose our z-axis to lie along the atom's local magnetic field and rotate our x, y-axes such that the atom's velocity vector lies in the z-y plane, then we may write that after a small time interval δt, the atom experiences a $\theta \approx B_y/B_z$ rotation of the $\mathbf{B}$ field. Suppose now that we rotate our coordinate system such that the z-axis is always along the local magnetic field. Evidently, the rotation must be about the x axis with an angular velocity

$$\omega = \frac{1}{B_z}\frac{\partial B_y}{\partial y}v_y, \tag{2.332}$$

where v_y is the velocity of the atom in the y direction and the appropriate rotation operator is $R(t) = e^{-i\omega t K_x}$. The transformed Hamiltonian $\tilde{H}$ can be read off from writing

$$\begin{aligned}\tilde{H}R\left|\psi\right\rangle = i\hbar\frac{d}{dt}R\left|\psi\right\rangle &= i\hbar\left(-i\omega K_x R\left|\psi\right\rangle + \frac{1}{i\hbar}RH\left|\psi\right\rangle\right)\\ &= \underbrace{\left(\omega\hbar K_x + RHR^{-1}\right)}_{\tilde{H}}R\left|\psi\right\rangle,\end{aligned} \tag{2.333}$$

to give

$$\begin{aligned}\tilde{H} &= -\frac{\mu_K}{K}\mathbf{B}_{\text{eff}}\cdot\mathbf{K} + RHR^{-1}\\ &= -\frac{\mu_K}{K}\left(\mathbf{B}_{\text{eff}}\cdot\mathbf{K} + e^{-i\omega t S_x}K_z B_z e^{i\omega t S_x}\right)\\ &= -\frac{\mu_K}{K}\left(\mathbf{B}_{\text{eff}}\cdot\mathbf{K} + K_z B_z\cos\omega t + K_y B_z\sin\omega t\right)\\ &\approx -\frac{\mu_K}{K}\left(\mathbf{B}_{\text{eff}}\cdot\mathbf{K} + K_z B_z\right),\end{aligned} \tag{2.334}$$

where we have used (A.51) in going from the second to third line and have made the assumption in the last line that the time t before the atom undergoes a collision with another atom is so short that the angle $\omega t \ll 1$. $\mathbf{B}_{\text{eff}}$ is here defined as

$$\mathbf{B}_{\text{eff}} \equiv -\frac{K\hbar}{\mu_K}\frac{1}{B_z}\frac{\partial B_y}{\partial y}v_y\hat{\mathbf{x}}. \tag{2.335}$$

Rapid collisions with other atoms result in a random walk of the velocity vector v_y, which in turns cause $\mathbf{B}_{\text{eff}}$ to fluctuate rapidly in both magnitude and direction, since following our prescription above, the x-y axes have to be rotated after each collision so that the the velocity vector is in the z-y plane. However, this fluctuating transverse effective magnetic field can cause transitions between the m_K states, which depolarizes the atom's nuclear spin polarization. By treating $\mathbf{B}_{\text{eff}}$ as a random stationary function of time, the longitudinal relaxation rate due to inhomogeneous $\mathbf{B}$ fields may be computed to give [154]

$$\frac{1}{T_1} = D\frac{|\boldsymbol{\nabla}B_x|^2 + |\boldsymbol{\nabla}B_y|^2}{B_z^2}, \tag{2.336}$$

where we have followed in [153] in dropping a $(1+\Omega_0^2\tau_c^2)^{-1}$ term that takes into account the Larmor precession of the spins about B_z during the time interval τ_c in between collisions with other atoms since as noted above, τ_c is extremely short in our high pressure cell and this factor is essential unity in our case. We note that (2.336) can also be derived using a classical random walk calculation [155].

Whereas inhomogeneity in the transverse components of the $\mathbf{B}$ field causes longitudinal relaxation, inhomogeneity in the longitudinal component of the $\mathbf{B}$ field results in enhanced transverse relaxation of the noble gas' polarization. This is not difficult to understand since inhomogeneity in B_z causes atoms in different parts of the cell to precess at slightly different rates, which will cause the precessing macroscopic polarization to rapidly decohere. Although the co-magnetometer's sensitivity depends

on the alkali atoms' T_2 coherence time, it does not depend on the noble gas' T_2; and while inhomogeneity in B_z can in principle affect the relaxation of the alkali atoms this tends, as we have noted above, to be a small contribution compared to other collisional processes. Consequently, we are typically more concerned with inhomogeneity of the transverse components of $\mathbf{B}$, which could prevent us from effectively pumping the noble gas' nuclear spins.

2.8.2 Diffusion and wall relaxation

Alkali atoms

Besides losing polarization to collisions and motion through magnetic gradients in the bulk, spin polarized atoms can also lose their polarization when they get adsorbed to the walls of the glass cell. Once adsorbed to the walls of the cell, atoms can "hop" along the surface and are subject to a smorgasbord of fields and interactions from the atoms of the wall that can depolarize their spin polarization. The dwell time of the atom on the surface of the glass depends on the adsorption energy, which was measured to be 0.71 eV for Na atoms on bare Pyrex glass [156] and estimated to be around 1 eV for gehlenite glass in [157], corresponding to sticking times of 82 and 300 μs respectively. The long amount of time (compared to a binary collision of duration ~ 1 ps) an atom spends on the surface of a bare glass wall should in theory result in complete depolarization of the alkali's spin polarization (both nuclear and electronic) and this is typically assumed in the literature [73], although we note that some have measured a depolarization of 50% for adsorbed alkali atoms [158]. Nevertheless, bare glass walls are generally considered strongly depolarizing at the least and can be a major hindrance to effectively polarizing the atoms, especially for smaller cells that have a higher surface area to volume ratio.

There are two main strategies for reducing the detrimental effects of wall collisions. The first is to coat the cell walls with a coating that prevents the alkali atoms from

adsorbing onto the bare glass walls. These coatings, which typically contain a long hydrocarbon chain, have lower polarizabilities and adsorption energies, which not only reduces the chance that an adsorbed alkali atom will be depolarized due to local **E**/**B** fields, but also decreases the time that an absorbed atom will spend on the coating. Indeed, it can take up to 10^4 collisions with a paraffin coating to depolarize an alkali atom [159]. However, with the exception of octadecyltrichlorosilane (OTS), which has been demonstrated to operate at temperatures up to 170 °C [160], most coatings can only be operated at relatively low temperatures ($\sim<$ 100 °C), which is too low for our purposes since we require a dense alkali vapor to spin polarize the noble gas atoms through spin-exchange collisions. Consequently, we do not employ coated cells in SMILE.

Rather, we rely on the high noble gas pressure in our cells to broaden the absorption cross-section of the alkali atoms, which reduces the amount of optical power absorbed by the layer of un-polarized atoms close to the walls of the cell. This is similar in effect to detuning the frequency of the pump laser except that it does not result in an unwanted vector light shift for the atoms. We note that contrary to what is sometimes claimed in the literature, the presence of noble/buffer gas does *not* help (for constant pump laser intensity) defeat wall relaxation by decreasing the size of the boundary layer of un-polarized atoms, which is mostly independent of noble/buffer gas pressure. To understand why this is the case, we note that from (2.304)

$$\frac{d\left\langle F_z\right\rangle}{dt} = R_p\left(\frac{1}{2}s_z - \left\langle S_z\right\rangle\right) - R_{sd}\left\langle S_z\right\rangle,$$

where we have for simplicity restricted ourselves to only considering the direct optical pumping of one alkali species and have accordingly dropped the spin-exchange term with the receiver species. Since the alkali atoms are in spin-exchange equilibrium, we have from (2.113) and (2.134) that $\left\langle F_z\right\rangle = (1+\epsilon(I,\beta))\left\langle S_z\right\rangle = Q(I,P)\left\langle S_z\right\rangle$. Although

the slowing down factor $Q(I,P)$ is in reality time-dependent due to its dependence on the polarization P, we note that it typically has a relatively small range and may be approximated as roughly constant. For example, for $I = 3/2$, Q varies between 4 and 6 for the entire range of P and may crudely be approximated as ~ 5. If we make this assumption, then we may write (2.337) as

$$\frac{dP}{dt} = \frac{R_p}{Q}(s_z - P) - \frac{R_{sd}}{Q}P, \tag{2.337}$$

where we have replaced $\langle S_z \rangle$ with the polarization $P = \langle S_z \rangle / S$. As written P is only a function of t but if we allow it to have spatial dependence and include in a diffusion term, we obtain

$$\frac{\partial P}{\partial t} = D\frac{\partial^2 P}{\partial z^2} + \frac{R_p}{Q}(s_z - P) - \frac{R_{sd}}{Q}P, \tag{2.338}$$

where D here is the diffusion constant of the alkali atom in the buffer gas. At steady state, the polarization distribution of the alkali atoms obey the second-order differential equation

$$\frac{d^2 P}{dz^2} = \frac{R_p + R_{sd}}{QD}P - \frac{R_p}{QD}s_z. \tag{2.339}$$

We may obtain a characteristic length λ_D over which the polarization rises from zero (we assume completely depolarizing walls) to its bulk value for an optically thin cell where R_p is mostly constant throughout the cell[24]. Indeed, if we assume that R_p is constant, then (2.339) has the simple general solution

$$P(z) = -\frac{R_p}{R_p + R_{sd}}e^{-z/\lambda_D} + \frac{R_p}{R_p + R_{sd}}, \tag{2.340}$$

where the characteristic length λ_D is

$$\lambda_D = \sqrt{\frac{QD}{R_p + R_{sd}}}. \tag{2.341}$$

[24]See section 2.7.4 for a treatment where R_p is not assumed to be constant.

We note that the diffusion constant D at temperature T scales as

$$D = D_0 \left(\frac{T}{T_0}\right)^{3/2} \frac{p_0}{p}, \tag{2.342}$$

where D_0 is the diffusion constant measured at a reference temperature and pressure T_0,p_0, and p is the pressure of the buffer gas at temperature T_0. Evidently then, D is inversely proportional to the buffer gas pressure p (at the reference temperature T_0). On the other hand, R_p on resonance is from (2.237)

$$R_p = I\frac{r_e f_{osc} c}{h\nu}\frac{1}{\Gamma_{tot}} = I\frac{r_e f_{osc} c}{h\nu}\frac{1}{\alpha p}, \tag{2.343}$$

where α is the pressure broadening rate and p is the buffer gas pressure. Consequently, R_p is also inversely proportional to the buffer gas pressure p. For experimental conditions where $R_p \gg R_{sd}$, this means that $\lambda_D \approx \sqrt{QD/R_p}$, which is then independent of the buffer gas pressure p since R_p and D are both inversely proportional to p. In the case of an optically thick vapor, this analysis is of course not quite correct since R_p will vary considerably and the solution to (2.339) is not exponential. Also, if R_p is tuned (by changing the laser intensity) to equal R_{sd}, as is typically the case in a continuously pumped co-magnetometer, then the relation $\lambda_D \approx \sqrt{QD/R_p}$ is also not completely accurate. Nevertheless, the basic argument is still valid since the boundary layer will generally be proportional to the diffusion constant but inversely proportional to the pumping rate and since both of these quantities are inversely proportional to the buffer gas pressure, the size of the boundary layer is therefore mostly independent of the buffer gas pressure. Evidently then, increasing the noble/buffer gas pressure will not significantly decrease the size of the boundary layer of unpolarized atoms, or in other words, the flux of alkali polarization to the walls is independent of buffer gas pressure. Yet, as mentioned above and in [68], having a high pressure noble/buffer gas pressure helps to decrease the laser power lost to

the boundary layer by broadening the atoms' absorption cross-section, which allows more laser power to reach the bulk of the cell where atoms are less affected by wall collisions.

Although λ_D cannot be decreased by increasing the buffer gas pressure, we note that it can be decreased by increasing the laser intensity. Indeed, it has been observed that at low pump intensities on resonance, there is a dip in the bulk polarization of the alkali atoms due to significant loss of laser power in the relatively large boundary layer. However, when the laser intensity is increased sufficiently, this dip disappears due to a decreased boundary layer [68].

Table 2.6 below lists the measured diffusion constants for various alkali-noble/buffer gas pairs at one atmospheric pressure. We note that most of the references below do not specify the isotopic content of the alkali/buffer/noble gas atoms used and we therefore assume that these elements were present in natural abundance in those works. While [161] did not find a significant difference in the diffusion constants of ^{85}Rb versus ^{87}Rb, we remark that they did find a significant difference between ^{3}He and ^{4}He and measured a ratio $D(\text{Rb-}^3\text{He})/D(\text{Rb-}^4\text{He}) = 1.25 \pm 0.1$.

Species	D_0 (cm^2/s)	Temperature (°C)	Reference
K-He	0.35 ± 0.3	0	[162]
K-Ne	0.19 ± 0.02	0	[162]
Rb-^{3}He	0.53 ± 0.09	27	[161]
Rb-^{4}He	0.42 ± 0.06	27	[161]
Rb-Ne	0.16	27	[163]
Rb-N_2	0.159 ± 0.004	60	[164]

Table 2.6: Measured diffusion constants of various alkali-noble/buffer gas pairs at 1 atm.

Noble gas

Noble gas atoms, like alkali atoms, can adsorb on the surface of the glass cell walls. However, studies of wall relaxation of ^{3}He on glass (Pyrex and quartz) surfaces in

the absence of alkali atoms have indicated that adsorption related relaxation is only dominant at low temperatures below 130 K. At higher temperatures, the dominant relaxation is through a*b*sorption into the glass walls [165]. Further investigation of the absorption related relaxation (in the absence of alkali atoms) above 130 K suggest that it is mainly due to the ^{3}He atoms encountering inhomogeneous **B** fields from ferromagnetic impurities as they diffuse through the glass [166]. As discussed in section 2.8.1, these magnetic gradients will in general depolarize the spins of the atoms. This relaxation mechanism can however be suppressed by choosing to use a relatively impermeable glass such as the GE180 aluminosilicate glass used for SMILE's cells [165]. Moreover, it appears that the presence of alkali metals in the cell greatly reduces absorption related relaxation, presumably by adsorbing onto the surface of the glass walls and forming a barrier between ^{3}He and the walls [165].

Nevertheless, for cell walls that do contain alkali atoms, there remains a mysterious and, as far as this author is aware, currently unknown wall relaxation mechanism that is strongly dependent on temperature [167]. This mysterious relaxation has been termed the "X" factor. Measurements of the X-factor on many different cells show that it is more variable in smaller cells, which have a higher surface area to volume ratio, than in larger cells [99, 168–170]. This is consistent with the belief that the X-factor is indeed some form of wall relaxation [121].

Besides the X-factor mentioned above, it is possible for noble gas atoms to exhibit significantly enhanced longitudinal spin relaxation after the cells they are in are exposed to strong **B** fields. It was reported in [171] that exposure of glass cells containing alkali and ^{3}He atoms to a 10 kGs field for $\approx$ 30 s was sufficient to consistently increase the wall relaxation of these cells by 2 to 20 times. It appears likely that this so-called "T_1 hysteresis" effect is due to the magnetization of ferromagnetic impurities on or close to the surface of the glass walls by the 10 kGs field since the original relaxation rates can be reliably restored by degaussing the cell. We note [172] later

reported that a 30 Gs **B** field was sufficient to observe the onset of T_1 hysteresis and a similar effect observed in [152] was estimated to have been caused by exposure to a **B** field of at most 10 Gs. Although rare, this author has also observed instances of this happening. We discuss some of the precautions we took to prevent such unwanted cell magnetization later in section 4.1.1.

2.9 Noble Gas Evolution

We have so far almost exclusively focused our discussion on alkali atoms since they are what we experimentally interact with via our pump and probe lasers. Moreover, the alkali atoms are somewhat more complicated due to the hyperfine coupling and the easy accessibility of their electronic spin permits a great many possible interactions. Noble gas atoms, by virtue of their closed electronic shells, are far more inert. This is especially true for ^{3}He with nuclear spin $K = 1/2$ since its nucleus has no higher multipole moments and is only susceptible to dipole-dipole interactions. Moreover, due to its low atomic number, it has relatively weak internal electric fields, which makes it less susceptible to spin relaxation due to spin-rotation collisions with other ^{3}He atoms in the bulk. Indeed, absent any **B** field inhomogeneity, the dominant spin relaxation process in the bulk for ^{3}He has been experimentally shown [173] to be due to the magnetic dipolar interaction between two ^{3}He atoms

$$V = \left(\frac{\mu_K}{K}\right)^2 + \frac{1}{r^3}\left(\mathbf{K}_1 \cdot \mathbf{K}_2 - \frac{3(\mathbf{K}_1 \cdot \mathbf{r})(\mathbf{K}_2 \cdot \mathbf{r})}{r^2}\right), \tag{2.344}$$

where $\mathbf{K}_i$ is the nuclear spin of the i^{th} atom, μ_K is the magnetic dipole moment of the nucleus and $\mathbf{r}$ is the relative displacement vector separating the two atoms. It can be shown, after integrating over all possible collisions, that (2.344) leads, at 23

°C, to a relaxation rate of [173]

$$\frac{1}{T_{sd}^n} = R_{sd}^n = \frac{n_b}{744} \quad 1/\text{hr}, \tag{2.345}$$

where n_b is the number density of the noble gas in amagats. In our co-magnetometer cells however, we rarely, as noted in section 2.8.1, reach this low relaxation limit since we are frequently limited by $\mathbf{B}$ field inhomogeneity caused by the ^{3}He's own magnetization in an aspheric cell.

Although we are primarily interested in ^{3}He in our experiment to constrain anomalous spin-mass interactions, we note here that in other noble gases, different bulk relaxation mechanisms dominate. For example, in ^{129}Xe, even though it like ^{3}He has no nuclear quadrupole moment owing to its spin $K = 1/2$ nucleus, yet because it is a heavy element and has a significant internal electric field, its bulk relaxation is proportional to its density and is dominated by spin-rotation collisions with other ^{129}Xe atoms [174, 175]. On the other hand, for noble gases with nuclear spins $K \geq 3/2$ that have non-zero nuclear quadrupole moment such as ^{131}Xe and ^{21}Ne, their bulk relaxations are limited by the interaction of their quadrupole moments with induced electric fields during a collision [95, 176].

In between collisions, the spin of the noble gas atom evolves under the simple spin Hamiltonian

$$H_g^n = -\frac{\mu_K}{K}\mathbf{K} \cdot (\mathbf{B} + \boldsymbol{\beta}_n)\,, \tag{2.346}$$

where we have explicitly included any possible nucleon coupling anomalous field $\boldsymbol{\beta}_n$. Analogous to (2.20), after transforming into a rotating frame with angular velocity $\boldsymbol{\Omega}$ we obtain

$$\tilde{H}_g^n \approx \hbar\boldsymbol{\Omega} \cdot \mathbf{K} - \frac{\mu_K}{K}\mathbf{K} \cdot (\mathbf{B} + \boldsymbol{\beta}_n)\,. \tag{2.347}$$

The density matrix for a spin-1/2 system can be easily written down as [73, 74]

$$\rho^n = \frac{1}{2} + 2\langle \mathbf{K} \rangle \cdot \mathbf{K}, \tag{2.348}$$

which is analogous to (2.33) with $\phi \to 1/2$, $\mathbf{\Theta} \to 2\langle \mathbf{K} \rangle$ and $\mathbf{S} \to \mathbf{K}$. As in (2.29), the density matrix of the noble gas atom evolves according to the Liouville equation in between collisions

$$\frac{d\rho_g^n}{dt} = \frac{1}{i\hbar}[\tilde{H}_g^n, \rho_n]. \tag{2.349}$$

For spin $K = 1/2$[25] noble gas, we may easily obtain the time-evolution of its density matrix under spin-exchange collisions with alkali atoms of species a by performing the replacements $\phi \to 1/2$, $\rho \to 1/2 + 2\langle \mathbf{K} \rangle \cdot \mathbf{K}$ and $\mathbf{K} \leftrightarrow \mathbf{S}^a$ in (2.78) to obtain

$$\frac{d_{se}^{na}}{dt} = \frac{2}{T_{se}^{na}}(\langle \mathbf{S}^a \rangle - \langle \mathbf{K} \rangle) \cdot \mathbf{K} + \frac{1}{i\hbar}[\delta\mathscr{E}_{se}^{na}, \rho], \tag{2.350}$$

where the frequency shift operator $\delta\mathscr{E}_{se}^{na}$ is now

$$\mathscr{E}_{se}^{na} = n_a \frac{8\pi g_s \mu_B \mu_K}{3K} \kappa_0 \langle \mathbf{S}^a \rangle \cdot \mathbf{K}, \tag{2.351}$$

and n_a is the number density of species a alkali atoms. The spin-exchange rate in this case is

$$R_{se}^{na} = \frac{1}{T_{se}^{na}} = n_a \langle \sigma_{se} \overline{v} \rangle, \tag{2.352}$$

where n_a is the density of alkali atoms in species a and $\langle \sigma_{se} \overline{v} \rangle$ is the same rate-constant as in (2.80). Since there is no electronic spin in a noble gas atom, all spin-destruction processes (including dipole-dipole, wall and $\mathbf{B}$ field inhomogeneity) can all be lumped into one overall spin destruction rate R_{sd}^n that causes the density matrix to relax as

$$\frac{d\rho_{sd}^n}{dt} = -2R_{sd}^n \langle \mathbf{K} \rangle \cdot \mathbf{K}. \tag{2.353}$$

[25] For the case of $K \neq 3/2$, the interested reader may refer to [75] for more details.

For hybrid pumping with a dense receiver (r) alkali species and lean donor (d) alkali species, the evolution of the ensemble averaged noble gas spin $\langle \mathbf{K} \rangle$ is therefore

$$\begin{aligned}\frac{d\langle \mathbf{K} \rangle}{dt} &= \mathrm{Tr}\left[\frac{d\rho_g^n}{dt}\mathbf{K}\right] + \mathrm{Tr}\left[\frac{d\rho_{se}^n}{dt}\mathbf{K}\right] + \mathrm{Tr}\left[\frac{d\rho_{sd}^n}{dt}\mathbf{K}\right] \\ &= \gamma_n\left(\mathbf{B} + \boldsymbol{\beta}_n + \frac{\boldsymbol{\Omega}}{\gamma_n}\right) \times \langle \mathbf{K} \rangle + R_{se}^{nr}(\langle \mathbf{S}^r \rangle - \langle \mathbf{K} \rangle) + \lambda M_e^r \mathbf{P}_e^r \times \gamma_n \langle \mathbf{K} \rangle \\ &\quad + R_{se}^{nd}(\langle \mathbf{S}^d \rangle - \langle \mathbf{K} \rangle) + \lambda M_e^d \mathbf{P}_e^d \times \gamma_n \langle \mathbf{K} \rangle - R_{sd}^n \langle \mathbf{K} \rangle, \end{aligned} \tag{2.354}$$

where the traces can be evaluated analogously as in (2.130), (2.89) and (2.98). $\gamma_n \equiv -\mu_K/(K\hbar)$ is here the gyromagnetic ratio of the nucleus and λ is as defined in (2.87). M_e^a, which is the maximum possible magnetization from species a alkali atoms, is simply[26]

$$M_e^a \equiv n_a \mu_B, \tag{2.355}$$

where n_a is the number density of alkali atoms, μ_B is the Bohr magneton and we have made the approximation $g_s \langle \mathbf{S} \rangle \approx \langle \mathbf{S} \rangle / S \equiv \mathbf{P}_e$. We may simplify (2.354) by noting that by design, $n_r \gg n_d$ and therefore $R_{se}^{nr} \gg R_{se}^{nd}$ and $M_e^r \gg M_e^d$. In that case, dividing (2.354) by $K = 1/2$, adding a diffusion term and re-arranging, we obtain the time-evolution of the noble gas polarization $\mathbf{P}^n \equiv \langle \mathbf{K} \rangle / K$

$$\frac{\partial \mathbf{P}^n}{\partial t} \approx D^n \nabla^2 \mathbf{P}^n + \gamma_n\left(\mathbf{B} + \lambda M_e^r \mathbf{P}^r + \boldsymbol{\beta}_n + \frac{\boldsymbol{\Omega}}{\gamma_n}\right) \times \mathbf{P}^n + R_{se}^{nr}\mathbf{P}^r - R_{tot}^n \mathbf{P}^n, \tag{2.356}$$

where D^n is noble gas' self-diffusion constant and we have defined $R_{tot}^n = R_{se}^{nr} + R_{se}^{nd} + R_{sd}^n \approx R_{se}^{nr} + R_{sd}^n$ for convenience.

[26] We note that the definition of M_e in [152] has what we believe is an erroneous additional factor of g_s there, which will in general give computational results that are off by a factor of 2. As we note in the main text, the g_s factor should be absorbed into the $\mathbf{P}_e$ term. [177] and [178] defines it as we do too and we note that this definition makes it symmetrical with the definition of M_n in (2.88).

2.10 Macroscopic Spin Dynamics

In the preceding sections of this chapter, we discussed various collisional and light-atom interactions that affect the alkali atoms. We now bring together these myriad effects and write down the evolution of the alkali and noble gas atoms under all processes relevant to co-magnetometer operation. Since we employ hybrid pumping, there are actually 3 spin species that we are concerned with rather than the usual 2 in more traditional co-magnetometer implementations. (2.356) already gives us the evolution of the noble gas' macroscopic spin polarization and we may obtain analogous equations for the alkalis' spin polarizations. As in section 2.7.4, we shall label the lean, optically pumped alkali species as d (for donor) and the denser, optically thick species as r (for receiver). The density matrix of these two species evolve as

$$\begin{aligned}\frac{\partial \rho^r}{\partial t} = D^r \nabla^2 \rho^r + \frac{1}{i\hbar}[\tilde{H}^r + \delta\mathscr{E}_{se} - \mathscr{E}_m \mathbf{q}_m \cdot \mathbf{S}, \rho^r] + R_m(\phi^r(1 + \mathbf{q}_m \cdot \mathbf{S}) - \rho^r) \\ + R^r_{sd}(\phi^r - \rho^r) + R^r_{se}(\phi^r(1 + 4\langle \mathbf{K} \rangle \cdot \mathbf{S}) - \rho^r) \\ + \sum_j R^{rj}_{ex}(\phi^r(1 + 4\langle \mathbf{S}^j \rangle \cdot \mathbf{S}) - \rho^r)\end{aligned} \tag{2.357}$$

$$\begin{aligned}\frac{\partial \rho^d}{\partial t} = D^d \nabla^2 \rho^d + \frac{1}{i\hbar}[\tilde{H}^d + \delta\mathscr{E}_{se} - \mathscr{E}_p \mathbf{q}_p \cdot \mathbf{S}, \rho^d] + R_p(\phi^d(1 + \mathbf{q}_p \cdot \mathbf{S}) - \rho^d) \\ + R^d_{sd}(\phi^d - \rho^d) + R^d_{se}(\phi^d(1 + 4\langle \mathbf{K} \rangle \cdot \mathbf{S}) - \rho^d) \\ + \sum_j R^{dj}_{ex}(\phi^d(1 + 4\langle \mathbf{S}^d \rangle \cdot \mathbf{S}) - \rho^d),\end{aligned} \tag{2.358}$$

where the first terms represent diffusion and the second terms account for the evolution of the (rotating-frame) ground state Hamiltonian $\tilde{H}$ (2.20) together with the frequency-shift operator due to spin-exchange collisions with noble gas atoms (2.79) and the frequency-shift operator due to optical pumping from the pump/probe beam (2.297). Notice that the receiver only sees the probe beam (labeled m) while the

donor species only sees the pump beam (labeled p). The third terms represent the pumping effects of the probe and pump beam (2.297), and in the fifth term, which models the effect of spin-destruction collisions, we have lumped together the rates for spin-rotation (2.96) and spin-axis collisions (2.100) together to form a combined spin-destruction rate R_{sd}. Finally, the last two terms account for spin-exchange collisions with noble gas atoms (2.78) and alkali atoms (2.59). We note that in the last term, which represents spin-exchange with other alkali atoms, the sum over j includes both alkali species.

From (2.130), (2.301), (2.89), (2.98) and (2.73), we can see that the ensemble averaged total angular momentum $\langle \mathbf{F} \rangle$ of the two species above evolves as

$$\begin{aligned}\frac{\partial \langle \mathbf{F}^r \rangle}{\partial t} = D^r \nabla^2 \langle \mathbf{F}^r \rangle + \gamma_e \left(\mathbf{B} + \lambda M_n \mathbf{P}^n + \mathbf{L}_m + \boldsymbol{\beta}_e \right) \times \langle \mathbf{S}^r \rangle + R_m \left(\frac{\mathbf{q}_m}{4} - \langle \mathbf{S}^r \rangle \right) \\ + R_{se}^r \left(\langle \mathbf{K} \rangle - \langle \mathbf{S}^r \rangle \right) + R_{ex}^{rd} \left(\langle \mathbf{S}^d \rangle - \langle \mathbf{S}^r \rangle \right) - R_{sd}^r \langle \mathbf{S}^r \rangle + \boldsymbol{\Omega} \times \langle \mathbf{F}^r \rangle \end{aligned} \tag{2.359}$$

$$\begin{aligned}\frac{\partial \langle \mathbf{F}^d \rangle}{\partial t} = D^d \nabla^2 \langle \mathbf{F}^d \rangle + \gamma_e \left(\mathbf{B} + \lambda M_n \mathbf{P}^n + \mathbf{L}_p + \boldsymbol{\beta}_e \right) \times \langle \mathbf{S}^d \rangle + R_p \left(\frac{\mathbf{q}_p}{4} - \langle \mathbf{S}^d \rangle \right) \\ + R_{se}^d \left(\langle \mathbf{K} \rangle - \langle \mathbf{S}^d \rangle \right) + R_{ex}^{dr} \left(\langle \mathbf{S}^r \rangle - \langle \mathbf{S}^d \rangle \right) - R_{sd}^d \langle \mathbf{S}^d \rangle + \boldsymbol{\Omega} \times \langle \mathbf{F}^d \rangle . \end{aligned} \tag{2.360}$$

(2.359) and (2.360) as written above follow directly (albeit after some computation) from (2.357) and (2.358). However, they are not extremely useful in their current form since we have $\langle \mathbf{F} \rangle$ on the l.h.s but $\langle \mathbf{S} \rangle$ on the r.h.s. We note that while we certainly could have computed the time evolution of $\langle \mathbf{S} \rangle$ from (2.357) and (2.358) instead of $\langle \mathbf{F} \rangle$, it would not make much sense to do so since $\langle \mathbf{S} \rangle$ is not (even approximately) conserved due to the hyperfine interaction at low $\mathbf{B}$ fields. Nevertheless, if we assume that the spin-exchange rate is much faster than any other rate so that we are in spin-temperature equilibrium, we may like in section 2.5, approximate $\langle \mathbf{F} \rangle \approx \langle \mathbf{S} \rangle Q(P)$ for small transverse excitations of $\langle \mathbf{F} \rangle$. $Q(P)$ is here the polarization $P = |\langle \mathbf{S} \rangle| / S$

dependent slowing down factor defined in (2.133). Consequently, $Q(P)$ is also strictly speaking time-dependent. However, we note that $Q(P)$ does not vary too much over its entire range, especially for small I. Indeed, for $I = 3/2$, it only varies from 4 to 6 over its entire range. Moreover, if the bulk of the polarization P is from a relatively constant longitudinal component and we are mostly only concerned with small transverse excitations of $\mathbf{S}$, which is indeed frequently the case for the continuously pumped co-magnetometer, then $Q(P)$ will be accordingly relatively constant. In this case, we may approximate $Q(P(t)) \approx Q(P_0)$ where P_0 is the relatively constant longitudinal component of the electron polarization. For $\mathcal{D}_1$ pumping and probing where $\mathbf{q} = 2\mathbf{s}$ (see section 2.7.3), (2.359) and (2.360) then, under these approximations reduce to the Bloch equations

$$\begin{aligned}\frac{\partial \mathbf{P}^r}{\partial t} \approx D^r \nabla^2 \mathbf{P}^r + + \frac{\gamma_e}{Q^r(P_0^r)} \left(\mathbf{B} + \lambda M_n \mathbf{P}^n + \mathbf{L}_m + \boldsymbol{\beta}_e + \frac{Q^r(P_0^r)\boldsymbol{\Omega}}{\gamma_e} \right) \times \mathbf{P}^r \\ + \frac{1}{Q^r(P_0^r)} \left(R_m \mathbf{s}_m + R_{se}^r \mathbf{P}^n + R_{ex}^{rd} \left(\mathbf{P}^d - \mathbf{P}^r \right) - R_{tot}^r \mathbf{P}^r \right) \end{aligned} \tag{2.361}$$

and

$$\begin{aligned}\frac{\partial \mathbf{P}^d}{\partial t} \approx D^d \nabla^2 \mathbf{P}^d + + \frac{\gamma_e}{Q^d(P_0^d)} \left(\mathbf{B} + \lambda M_n \mathbf{P}^n + \mathbf{L}_p + \boldsymbol{\beta}_e + \frac{Q^d(P_0^d)\boldsymbol{\Omega}}{\gamma_e} \right) \times \mathbf{P}^d \\ + \frac{1}{Q^d(P_0^d)} \left(R_p \mathbf{s}_p + R_{se}^d \mathbf{P}^n + R_{ex}^{dr} \left(\mathbf{P}^r - \mathbf{P}^d \right) - R_{tot}^d \mathbf{P}^d \right), \end{aligned} \tag{2.362}$$

where we have for convenience defined $R_{tot}^r \equiv R_m + R_{se}^r + R_{sd}^r$ and $R_{tot}^d \equiv R_p + R_{se}^d + R_{sd}^d$.

Chapter 3

Co-magnetometer Theory

As alluded to in the previous chapter, an alkali-noble gas co-magnetometer vapor cell consist of alkali and noble gas atoms co-located within the same volume. In chapter 4 we shall describe an experimental search for anomalous spin-mass couplings between two 250 kg Pb source masses and spin-polarized atoms in a K-^{3}He co-magnetometer. Although not immediately obvious, a K-^{3}He co-magnetometer has numerous advantages that make it an attractive platform for studying such tiny hypothetical magnetic-like interactions.

Firstly, when a bias magnetic "compensation field" is applied to cancel out the sum of the alkali and noble-gas magnetization, the co-magnetometer exhibits a suppressed response to ordinary magnetic fields while retaining sensitivity to anomalous magnetic-like fields [179]. This is extremely desirable since it enables us to better suppress magnetic systematic effects that would otherwise mask the presence of a magnetic-like anomalous spin-mass coupling. Although magnetic systematic effects can also be reduced by enclosing the co-magnetometer cell with magnetic shields, these shields produce their own magnetic noise due to Johnson currents and an inherent suppression to magnetic fields is therefore necessary to overcome this source of magnetic noise.

Secondly, at the "compensation point" when the compensation field cancels out the sum of the alkali and noble-gas magnetization, the alkali vapor sees a small magnetic field that is equal to its own magnetization. For a K vapor, this magnetic field is typically of the order of 10 μGs for K. At our operating density of 10^{14} cm^{-3}, this implies that the alkali vapor is in the SERF regime where transverse relaxation due to spin-exchange collisions is eliminated, which greatly improves the sensitivity of the co-magnetometer. Indeed, alkali magnetometers operating in the SERF regime can exceed the sensitivity of cryogenic superconducting quantum interference devices (SQUIDs) [180] and alkali-noble gas co-magnetometers inherit this same sensitivity to anomalous magnetic-like fields.

Thirdly, the dynamics of both spin species are strongly coupled and highly damped in the vicinity of the compensation point, which is useful since it means that unwanted transients that accidentally excite the spins quickly die away. This is a particularly useful feature in allowing us to quickly find the correct compensation field by executing a series of quick quasi-static $\mathbf{B}$ field modulations. A series of such automated routines have been developed in [177] and they allow us to easily keep the bias $\mathbf{B}$ field tuned correctly despite drifts in the ^{3}He's magnetization during long periods of operation.

Lastly, compared to the more traditional dual noble gas species co-magnetometers [181–183], an alkali-noble gas co-magnetometer is advantageous in that the easily accessible energy levels of the alkali atoms allows us to read out the projection of their spins directly via Faraday rotation of a linearly polarized probe laser beam that is tuned off the alkali's $\mathcal{D}_1$ line. This is inherently more efficient than simply using external inductive coils to measure changes in the magnetic field caused by the spins since the magnetic field of a simple dipole falls off as $1/r^3$ and higher multipoles falls off even faster.

In this chapter, we describe these useful properties of the alkali-noble gas co-magnetometer in further detail. We begin with the alkali and noble gas Bloch equations in (2.361),(2.362) and (2.356).

As written, these are actually 9 non-linear coupled differential equations which is not easily tractable. However, we can simplify these coupled partial differential equations considerably by first restricting ourselves to the behavior of the system in the bulk where the diffusion terms can be neglected. Secondly, we can further simplify the now 9 coupled ordinary differential equations (ODEs) by realizing that we are mainly interested in small transverse excitation of the spins about a relatively constant longitudinal polarization. We can therefore decouple the longitudinal components from the transverse components by separately solving for the steady state longitudinal polarizations and then substituting $P_z^i(t)$ with these constants. The steady state longitudinal polarization for the two alkali species is from (2.309) approximately[1] given by

$$P_z^r = P_0^r = P_0^e = \frac{R_p s_z^p}{R_p + R_{se}^d + R_{sd}^d + \frac{n_r}{n_d}(R_m + R_{se}^r + R_{sd}^r)}, \tag{3.1}$$

and the steady state noble gas longitudinal polarization is then from (2.356)

$$P_z^n = P_0^n = \frac{R_{se}^{nr} P_0^r}{R_{tot}^n}, \tag{3.2}$$

where P_0^r is the steady state longitudinal polarization of the alkali. Decoupling the longitudinal polarizations leaves us with 6 real ODEs but we can further reduce this number by realizing that the due to the extremely fast spin-exchange between the two alkali species, they are much more strongly coupled to each other than to the noble gas. Furthermore, as is evident from (2.361) and (2.362), spin-exchange collisions between the 2 species drives the polarization of both species into an equilibrium and

[1]The equations there do not take into account the back polarization from the noble gas but as noted there, this is not too big of a correction.

so we expect to be able to treat the two tightly coupled species as one effective species that evolves with some effective rate constants with the noble gas and pump/probe beams. In section 2.7.4, we demonstrated that we can reduce the two coupled differential equations of the receiver and donor alkali's longitudinal polarization into one effective differential equation that describes the coupled system. We seek to do the same here with the alkalis' transverse polarizations and to then couple that effective differential equation with the noble gas' differential equation. Before we begin, we note that it is convenient to describe the transverse components of a general 2D vector $\mathbf{A} = A_x\hat{\mathbf{x}} + A_y\hat{\mathbf{y}}$ by mapping it to the complex plane so that $A_x + iA_y \to A_\perp$. Applying this transformation allows us to deal with 3 complex coupled ODEs instead of 6 real ODEs and in this notation, the transverse components of (2.361) and (2.362) can, without the diffusion term and ignoring the coupling from $P_\perp^n$ which is much smaller compared to the spin-exchange between $P_\perp^r$ and $P_\perp^d$, be written as

$$\frac{d}{dt}\begin{pmatrix} P_\perp^r \\ P_\perp^d \end{pmatrix} = \begin{pmatrix} (-R_{ex}^{rd} - R_{tot}^r + i\gamma_e B_{ze}^r)/Q^r & R_{ex}^{rd}/Q^r \\ R_{ex}^{dr}/Q^d & (-R_{ex}^{dr} - R_{tot}^d + i\gamma_e B_{ze}^d)/Q^d \end{pmatrix}\begin{pmatrix} P_\perp^r \\ P_\perp^d \end{pmatrix} + \begin{pmatrix} (R_m s_\perp^m - i\gamma_e P_0^r B_{\perp e}^r)/Q^r \\ (R_p s_\perp^p - i\gamma_e P_0^d B_{\perp e}^d)/Q^d \end{pmatrix}, \tag{3.3}$$

where we have for convenience here defined

$$B_{ze}^r \equiv B_z + \lambda M_n P_0^n + L_z^m + \beta_z^e + \frac{Q^r\Omega_z}{\gamma_e} \tag{3.4}$$

$$B_{ze}^d \equiv B_z + \lambda M_n P_0^n + L_z^p + \beta_z^e + \frac{Q^d\Omega_z}{\gamma_e} \tag{3.5}$$

$$B_{\perp e}^r \equiv B_\perp + \beta_\perp^e + L_\perp^m + \frac{Q^r\Omega_\perp}{\gamma_e} \tag{3.6}$$

$$B_{\perp e}^d \equiv B_\perp + \beta_\perp^e + L_\perp^p + \frac{Q^d\Omega_\perp}{\gamma_e}, \tag{3.7}$$

and P_0^n is the steady steady noble gas longitudinal polarization (3.2) and R_{tot}^d, R_{tot}^r are as defined in (2.361) and (2.362). As before, the homogeneous solution to this

coupled differential equation is

$$\mathbf{P}(t) = \mathbf{P}_+ e^{\omega_+ t} + \mathbf{P}_- e^{\omega_- t}, \tag{3.8}$$

where $\mathbf{P}_\pm$ and $\omega_\pm$ are some constant eigenvectors and eigenvalues of the matrix in (3.3). The eigenvalues are

$$\omega_\pm = -\frac{Q^r(R^{dr}_{ex} + R^d_{tot}) + Q^d(R^{rd}_{ex} + R^r_{tot}) - i\gamma_e(Q^d B^r_{ze} + Q^r B^d_{ze}) \pm \sqrt{C}}{2Q^d Q^r}, \tag{3.9}$$

where $C = C(R^{dr}_{ex}, R^{rd}_{ex}, R^d_{tot}, R^r_{tot}, B^d_{ze}, B^r_{ze})$ here is a complicated complex expression. Using the same strategy as in section 2.7.4 however, we may expand $\sqrt{C}$ in powers of $(Q^r R^{dr}_{ex} + Q^d R^{rd}_{ex})^{-1}$. As before, the ω_+ solution damps extremely quickly and we are interested in the ω_- eigenvalue which, after expanding $\sqrt{C}$, can be approximated as

$$\begin{aligned}\omega_- \approx -\frac{1}{2}\Bigg[&\frac{R^d_{tot}}{Q^d}(1+\alpha) + \frac{R^r_{tot}}{Q^r}(1-\alpha) \\ &-i\gamma_e\left(\frac{B^d_{ze}}{Q^d}\left(1 - \frac{\epsilon}{Q^d} + \frac{\delta}{Q^r}\right) + \frac{B^r_{ze}}{Q^r}\left(1 + \frac{\epsilon}{Q^d} - \frac{\delta}{Q^r}\right)\right)\Bigg],\end{aligned} \tag{3.10}$$

where α is as defined in (2.316) and ϵ, δ are

$$\epsilon \equiv \frac{Q^d Q^r R^{dr}_{ex}}{Q^r R^{dr}_{ex} + Q^d R^{rd}_{ex}} \tag{3.11}$$

$$\delta \equiv \frac{Q^d Q^r R^{rd}_{ex}}{Q^r R^{dr}_{ex} + Q^d R^{rd}_{ex}}. \tag{3.12}$$

Substituting $B^d_z e$, B^r_{ze} and the various rates in R^d_{tot} and R^r_{tot} into (3.10), it is easy to see by analogy from section 2.7.4 that the effective differential equation we seek is

$$\begin{aligned}\frac{d\mathbf{P}^e}{dt} = \gamma_e\left(\tilde{\mathbf{B}} + \lambda M_n \tilde{\mathbf{P}}^n + \tilde{\boldsymbol{\beta}}^e + \tilde{\mathbf{L}}^p + \tilde{\mathbf{L}}^m + \frac{\boldsymbol{\Omega}}{\gamma_e}\right) \times \mathbf{P}^e + \tilde{R}_p(\mathbf{s}^p - \mathbf{P}^e) + \tilde{R}_m(\mathbf{s}^m - \mathbf{P}^e) \\ + R^{en}_{se}(\mathbf{P}^n - \mathbf{P}^e) - R^e_{sd}\mathbf{P}^e,\end{aligned} \tag{3.13}$$

where the effective rates are

$$\tilde{R}_p = \frac{R_p}{2Q^d}(1+\alpha) \qquad R^{en}_{se} = \frac{R^d_{se}}{2Q^d}(1+\alpha) + \frac{R^r_{se}}{2Q^r}(1-\alpha)$$
$$\tilde{R}_m = \frac{R_m}{2Q^r}(1-\alpha) \qquad R^e_{sd} = \frac{R^d_{sd}}{2Q^d}(1+\alpha) + \frac{R^r_{sd}}{2Q^r}(1-\alpha), \tag{3.14}$$

and the effective fields are

$$\tilde{\mathbf{L}}^p = \mathbf{L}^p\left(\frac{1}{Q_d} + \frac{\delta}{Q_d Q_r} - \frac{\epsilon}{Q_d^2}\right) \qquad \tilde{\mathbf{L}}^m = \mathbf{L}^m\left(\frac{1}{Q_r} - \frac{\delta}{Q_r^2} + \frac{\epsilon}{Q_d Q_r}\right), \tag{3.15}$$

$$\tilde{\mathbf{B}} = \eta\mathbf{B} \quad , \quad \tilde{\boldsymbol{\beta}}^e = \eta\boldsymbol{\beta}^e \quad , \quad \tilde{\mathbf{P}}^n = \eta\mathbf{P}^n, \tag{3.16}$$

with η being defined as

$$\eta \equiv \frac{Q_d^2(Q_r - \delta) - Q_r^2\epsilon + Q_d Q_r(Q_r + \delta + \epsilon)}{2Q_d^2 Q_r^2}. \tag{3.17}$$

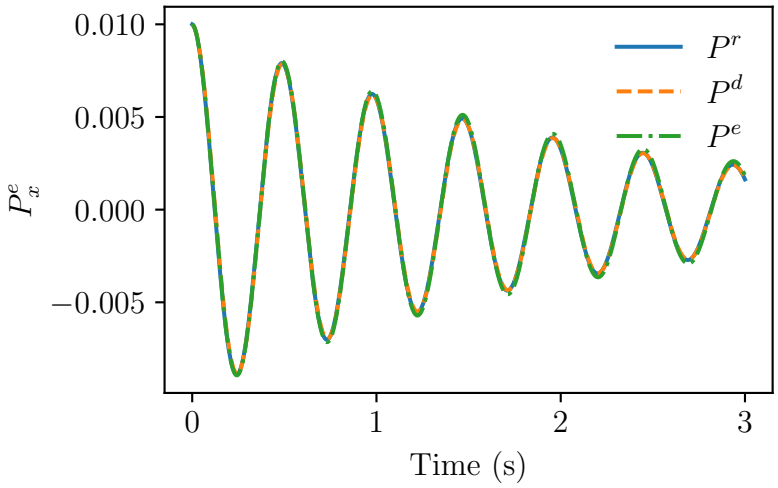

Figure 3.1: Effective dynamics of alkalis in hybrid pumped co-magngetometer.

We note that the effective pumping $\tilde{R}_p$ and spin-destruction rates R^e_{sd} are identical to what we found earlier in section 2.7.4 ((2.318) and (2.319)) so that we can write

(3.13) as a true 3-D vector equation. As in section 2.7.4, we have numerically verified that (3.13) with the effective rates and fields listed above, is indeed the correct effective differential equation to use. The solid blue and orange dashed lines in Figure 3.1 are the x-component of the receiver and donor alkali's polarization obtained from numerically solving the full 9 coupled ODEs (2.361), (2.362) and (2.356) in response to an excitation. Once again, we see that in the limit of high spin-exchange, the electronic polarization of the receiver and donor alkali species precess together in lock step. This tightly coupled system can be well described by the effective differential equation (3.13), which when coupled with the noble gas' differential equation (2.356), yields the green dash-dot curve in Figure 3.1 in response to the same excitation that closely approximates the solution from the full 9 coupled ODEs.

The effective differential equation (3.13) does not contain any explicit slowing down factors since these have been absorbed into the effective fields and rates to allow for (3.13) to account for the case when $Q_r \neq Q_d$. Indeed, the simulation in Figure 3.1 was performed for $Q_r = 5$ and $Q_d = 10$, which demonstrates that (3.13) is capable of accounting for two different slowing down factors in the two alkali species. However, the use of these effective fields is problematic when working analytically with the noble gas' differential equation since the effective $\tilde{\mathbf{B}}$ in the alkali's ODE is in that case not the same as the $\mathbf{B}$ in the noble gas' ODE. In the work of this thesis, we use K and ^{87}Rb, which both have nuclear spin $I = 3/2$ and their slowing down factors are therefore the same. With this simplification of $Q_r = Q_d$, we note that η reduces to $1/Q$ and similarly, an overall factor of $1/Q$ can be pulled out from all of the effective rates and from $\tilde{\mathbf{L}}^p, \tilde{\mathbf{L}}^m$. Moreover, the correction factors reduce in this case to

$$\alpha = \frac{n_d - n_r}{n_d + n_r} \quad , \quad \epsilon = \frac{Q n_r}{n_r + n_d} \quad , \quad \delta = \frac{Q n_d}{n_r + n_d}, \tag{3.18}$$

and we may re-write (3.13) as

$$\frac{d\mathbf{P}^e}{dt} = \frac{\gamma_e}{Q}\left(\mathbf{B} + \lambda M_n \mathbf{P}^n + \boldsymbol{\beta}^e + \tilde{\mathbf{L}}^p + \tilde{\mathbf{L}}^m + \frac{Q\boldsymbol{\Omega}}{\gamma_e}\right) \times \mathbf{P}^e + \frac{\tilde{R}_p(\mathbf{s}^p - \mathbf{P}^e) + \tilde{R}_m(\mathbf{s}^m - \mathbf{P}^e)}{Q} + \frac{R_{se}^{en}(\mathbf{P}^n - \mathbf{P}^e) - R_{sd}^e \mathbf{P}^e}{Q}, \tag{3.19}$$

where $\mathbf{B}$, $\mathbf{P}^n$, and $\boldsymbol{\Omega}$ are now the ordinary fields. The light-shifts still have a correction and are

$$\tilde{\mathbf{L}}^p = \mathbf{L}^p \frac{2}{1 + \frac{n_r}{n_d}} \qquad \tilde{\mathbf{L}}^m = \mathbf{L}^m \frac{2}{1 + \frac{n_d}{n_r}}, \tag{3.20}$$

and similarly, the effective rates are now

$$\begin{aligned} \tilde{R}_p &= \frac{R_p}{1 + \frac{n_r}{n_d}} & R_{se}^{en} &= \frac{n_d R_{se}^d + n_r R_{se}^r}{n_d + n_r} \\ \tilde{R}_m &= \frac{R_m}{1 + \frac{n_d}{n_r}} & R_{sd}^e &= \frac{n_d R_{sd}^d + n_r R_{sd}^r}{n_d + n_r}. \end{aligned} \tag{3.21}$$

For notational brevity, we shall drop the tildes from now on but it should be understood that when we write $\mathbf{L}^p, \mathbf{L}^m$, we actually mean the effective fields $\tilde{\mathbf{L}}^p, \tilde{\mathbf{L}}^m$ given in (3.20) unless otherwise specified. Similarly, from now on when we write $R_p, R_m, R_{se}^{en}, R_{sd}^e$ we shall mean $\tilde{R}_p, \tilde{R}_m, R_{se}^{en}, R_{sd}^e$ as defined in (3.21). Also, we note that mathematically, $\boldsymbol{\beta}^e$, $\mathbf{L}^p$ and $\mathbf{L}^m$ (we mean the effective light-shifts here) have the same effect since they all appear in the cross product with $\mathbf{P}^e$ but do not appear anywhere else in either the alkali's ODE or the noble gas' ODE. Consequently, it makes sense to define $\mathbf{b} \equiv \boldsymbol{\beta}^e + \mathbf{L}^p + \mathbf{L}^m$ as a convenient place holder for the three otherwise physically distinct fields. Also, we shall introduce a total electronic relaxation rate $R_{tot}^e = R_p + R_m + R_{se}^{en} + R_{sd}^e$ (again, all of the rates here should be understood as referring to the effective rates) so that we may finally write the effective coupled

ODEs for the hybrid pumped alkali-noble gas co-magnetometer as

$$\begin{aligned}\frac{d\mathbf{P}^e}{dt} &= \frac{\gamma_e}{Q}\left(\mathbf{B} + \lambda M_n \mathbf{P}^n + \mathbf{b} + \frac{Q\boldsymbol{\Omega}}{\gamma_e}\right) \times \mathbf{P}^e + \frac{1}{Q}\left[R_p \mathbf{s}^p + R_m \mathbf{s}^m + R_{se}^{en}\mathbf{P}^n - R_{tot}^e \mathbf{P}^e\right] \\ \frac{d\mathbf{P}^n}{dt} &= \gamma_n \left(\mathbf{B} + \lambda M_e^r \mathbf{P}^e + \boldsymbol{\beta}_n + \frac{\boldsymbol{\Omega}}{\gamma_n}\right) \times \mathbf{P}^n + R_{se}^{nr}\mathbf{P}^e - R_{tot}^n \mathbf{P}^n. \end{aligned} \tag{3.22}$$

Decoupling the longitudinal component as before, the transverse components evolve as

$$\begin{aligned}\frac{d}{dt}\begin{pmatrix} P_\perp^e \\ P_\perp^n \end{pmatrix} = &\begin{pmatrix} (-R_{tot}^e + i\gamma_e B_{ze}^e)/Q & (R_{se}^{en} - i\gamma_e \lambda M_n P_0^e)/Q \\ R_{se}^{nr} - i\gamma_n \lambda M_e^r P_0^n & -R_{tot}^n + i\gamma_n B_{ze}^n \end{pmatrix}\begin{pmatrix} P_\perp^e \\ P_\perp^n \end{pmatrix} \\ &+ \begin{pmatrix} (R_m s_\perp^m + R_p s_\perp^p - i\gamma_e B_{\perp e}^e P_0^e)/Q \\ -i\gamma_n B_{\perp e}^n P_0^n \end{pmatrix}, \end{aligned} \tag{3.23}$$

where we have for convenience defined

$$B_{ze}^e \equiv B_n + B_z + b_z + \frac{Q\Omega_z}{\gamma_e} \quad , \quad B_{ze}^n \equiv B_e + B_z + \beta_z^n + \frac{\Omega_z}{\gamma_n} \tag{3.24}$$

$$B_{\perp e}^e \equiv B_\perp + b_\perp + \frac{Q\Omega_\perp}{\gamma_e} \quad , \quad B_{\perp e}^n \equiv B_\perp + \beta_\perp^n + \frac{\Omega_\perp}{\gamma_n} \tag{3.25}$$

$$B_e \equiv \lambda M_e^r P_0^e \quad , \quad B_n \equiv \lambda M_n P_0^n, \tag{3.26}$$

and P_0^e and P_0^n are the steady state longitudinal alkali and noble gas polarization from (3.1)[2] and (3.2) respectively.

3.1 Steady State Behavior

We asserted at the start of this chapter that the co-magnetometer retains first order sensitivity to anomalous magnetic-like fields while having a suppressed response to ordinary magnetic field at the compensation point where a bias magnetic field cancels out the sum of the alkali and noble-gas magnetization. In this section, we show that

[2]We note that the rates in (3.1) are the actual rates and *not* the effective rates defined in (3.14).

this is indeed the case and we provide an expression for the co-magnetometer's signal at the compensation point. Since we measure the orientation of the alkali's spins by detecting the optical rotation of a linearly polarized off-resonant probe beam, we are primarily sensitive to the projection of the alkali's electronic polarization along the x-axis. Our signal is therefore proportional to P_x^e and we may find its steady state behavior by setting the l.h.s of (3.23) to zero and solving for the real part of $P_\perp^e$. Although this is analytically tractable, solving for $\mathbb{R}\mathrm{e}[P_\perp^e]$ yields a great many term that complicates the analysis. We therefore begin by noting that in the off-diagonal terms of the matrix in (3.23), the alkali-noble gas spin-exchange rates R_{se}^{en} and R_{se}^{nr} are much slower compared to the frequency $\gamma_e \lambda M_n P_0^e$ and $\gamma_n \lambda M_e^r P_0^n$. Consequently, we may approximate the off-diagonal terms to be purely imaginary. Similarly, since R_{tot}^n is much smaller in magnitude compared to $\gamma_n B_{ze}^n$, we may drop the $-R_{tot}^n$ in (3.23). (3.23) then reduces to

$$\frac{d}{dt}\begin{pmatrix} P_\perp^e \\ P_\perp^n \end{pmatrix} = \begin{pmatrix} (-R_{tot}^e + i\gamma_e B_{ze}^e)/Q & -i\gamma_e \lambda M_n P_0^e/Q \\ -i\gamma_n \lambda M_e^r P_0^n & i\gamma_n B_{ze}^n \end{pmatrix}\begin{pmatrix} P_\perp^e \\ P_\perp^n \end{pmatrix} + \begin{pmatrix} (R_m s_\perp^m + R_p s_\perp^p - i\gamma_e B_{\perp e}^e P_0^e)/Q \\ -i\gamma_n B_{\perp e}^n P_0^n \end{pmatrix}. \tag{3.27}$$

Since we pump along the longitudinal z direction, the spins of the atoms are nominally aligned along B_z and we therefore expect that there will automatically be no first order response to changes in B_z since a B_z field is unable to produce a torque on the spins. On the other hand, transverse B_y and B_x fields will in general cause the spins to project onto the x-axis and we therefore wish to find a B_z such that the co-magnetometer's first order sensitivity to B_y and B_x vanishes. Mathematically, we desire to find B_z such that

$$\frac{\partial}{\partial B_x}\mathbb{R}\mathrm{e}[P_\perp^e] = \frac{\partial}{\partial B_y}\mathbb{R}\mathrm{e}[P_\perp^e] = 0. \tag{3.28}$$

Differentiating $\mathbb{R}\mathrm{e}[P_\perp^e]$ w.r.t. B_x, setting it to zero and solving for B_z yields three distinct values of B_z while repeating the same procedure for B_y gives two distinct answers. Conveniently however, there is a common value of B_z such that the first order sensitivity to B_x *and* B_y vanishes:

$$B_z = -B_e - B_n - \beta_z^n + \frac{\Omega_z}{\gamma_n}. \tag{3.29}$$

As first pointed out in [178], the compensation point does technically depend on Ω_z, but since that is nominally zero, we may ignore it. We note here that theoretically it also depends on β_z^n, a neutron-coupling anomalous field although this quantity is also nominally zero and we do not, in any case, have control over that quantity. Experimentally, unless the entire experiment is set up on a rotating platform as in [152], we also have no control over Ω_z and consequently, we shall for practical reasons, take the compensation point B_c to be $B_c = -B_e - B_n$. We note that B_e and B_n are the effective magnetization that the noble gas and alkali atoms see respectively so that at the compensation point each species effectively sees a magnetic field that is equal in magnitude to its own effective magnetization to the other species.

Armed with this definition of the compensation point, we may derive the steady state behavior of the co-magnetometer at the compensation point. Since we remain interested in deviations of B_z away from the compensation point, we shall set $B_z \to -B_n - B_e + B_z$ so that B_z now represents small deviations away from the compensation point B_c. Despite the simplifications made, there is still a great many terms in the steady state solution to (3.27). Consequently, we shall for the sake of brevity only write down the first order[3] terms as well as the leading order $\mathbf{B}$ field[4] terms since that is a quantity that we can easily control experimentally and is therefore a quantity

[3]By first order we mean here terms that only contain one small experimental parameter. Since B_z has been re-defined as deviations away from the compensation point, we shall consider it to be small. Essentially, all the fields and Ω/γ_n will be considered small.

[4]We mean here terms that *only* contain $\mathbf{B}$ field terms i.e. we do not include mixed terms including one B field term and other non magnetic terms.

of interest. Given these qualifications, the steady state solution to (3.27) at the compensation point is

$$P_x^e = \frac{P_0^e \gamma_e R_{tot}^e}{{R_{tot}^e}^2 + \gamma_e^2 (B_z + \beta_z^e + L_z^p + L_z^m)^2} \times \left[\beta_y^n - \beta_y^e - L_y^p - L_y^m - \frac{R_m s_x^m}{P_0^e \gamma_e} - \frac{R_p s_x^p}{P_0^e \gamma_e} + \left(\frac{1}{\gamma_n} - \frac{Q}{\gamma_e} \right) \Omega_y + \frac{B_y B_z}{B_n} + \frac{\gamma_e B_x B_z^2}{B_n R_{tot}^e} \right]. \tag{3.30}$$

As expected, at the compensation point, there is no first order sensitivity to any magnetic fields. Nevertheless, as asserted, the co-magnetometer retains first order sensitivity to the anomalous fields β_y^n and β_y^e in the y-direction, thus making it a good platform on which to search for anomalous magnetic-like interactions. We concede, however, that although the co-magnetometer does not have any first order sensitivity to magnetic fields, it does possess first-order sensitivity to various other quantities such as light-shifts, rotation and pump/probe misalignment. Of these effects, pump/probe misalignments are the most significant since there is nominally no beam traveling in the y-direction and no rotation of the apparatus about the y-axis. Indeed, as we show in section 4.2.6, the co-magnetometer noise is dominated by pump and probe beam noise, although we note that the probe beam noise in that case is an optical rotation noise that is not related to the R_m term in (3.30). We note that the leading order **B** field term comes in as a second order $B_y B_z$ term that is suppressed by a factor B_n ($\sim 3 - 5$ mGs) while the leading order B_x term comes in as third order $B_x B_z^2$ term that is suppressed by a factor of B_n and $R_{tot}^e/\gamma_e \sim 200$ μGs.

3.2 Sensitivity to Anomalous Fields

The fundamental sensitivity of an atomic magnetometer (and co-magnetometer) depends on contributions from both the photon shot noise and the spin-projection noise [184, 185]. In general, it can also depend on light-shift induced noise but in our geometry, this contribution can in principle be dropped by ensuring the orthogonality of the pump and probe beam [184]. The magnetic field sensitivity due to spin-projection noise is typically given as in (2.117) while the contribution from photon shot noise scales as $1/\sqrt{N}$, where N is the number of incoming photons. In the ideal case where the co-magnetometer's sensitivity is not limited by technical noise (such as optical rotation noise due to beam motion through inhomogeneous optical components), it is desirable to improve the magnetic field sensitivity by detuning the probe beam and increasing the number of probing photons [186] (without introducing additional significant relaxation or technical noise from the laser). In this section however, we shall be mainly interested in comparing the optimum sensitivity of a directly pumped co-magnetometer versus a hybrid pumped co-magnetometer for a given probe power and consequently, when we write "optimum sensitivity" we shall mean optimum sensitivity at a given probe power.

The pre-factor on the r.h.s of (3.30) determines the sensitivity of the co-magnetometer to anomalous fields for a given probe power. If B_z, L_z^p, L_z^m are all zeroed (and ignoring the anomalous β_z^e term), then the pre-factor reduces to $P_0^e\gamma_e/R_{tot}^e$. In a directly pumped co-magnetometer, $R_{tot}^e = R_p + R_m + R_{se}^{en} + R_{sd}^e$ and the steady state longitudinal polarization P_0^e is

$$P_0^e = \frac{R_p s_z^p}{R_p + R_m + R_{se}^{en} + R_{sd}^e} = \frac{R_p s_z^p}{R_p + R_{np}} = \frac{R_p s_z^p}{R_{tot}^e}, \tag{3.31}$$

where we have defined $R_{np} \equiv R_m + R_{se}^{en} + R_{sd}^e$ so that the maximum of P_0^e/R_{tot}^e occurs when

$$R_p = R_m + R_{se}^{en} + R_{sd}^e = R_{np}, \tag{3.32}$$

and the optimum sensitivity for a directly pumped co-magnetometer is therefore achieved at an alkali polarization of $s_z^p/2$ or 50% for $s_z^p = 1$ circularly polarized pumping light.

In the case of the hybrid co-magnetometer, the steady state longitudinal alkali polarization P_0^e is from (3.1)

$$P_0^e = \frac{R_p s_z^p}{R_p + R_{se}^d + R_{sd}^d + \dfrac{n_r}{n_d}(R_m + R_{se}^r + R_{sd}^r)}, \tag{3.33}$$

and R_{tot}^e is actually

$$\tilde{R}_{tot}^e = \frac{1}{2}(R_p(1+\alpha) + R_m(1-\alpha) + R_{se}^d(1+\alpha) + R_{se}^r(1-\alpha) + R_{sd}^d(1+\alpha) + R_{sd}^r(1-\alpha)), \tag{3.34}$$

where all the rates on the r.h.s are all the original rates here[5] and α is as defined in (2.316). In this case, $P_0^e/\tilde{R}_{tot}^e$ is maximized when R_p is

$$\begin{aligned} R_p = \frac{1}{\sqrt{Q_d}} &\sqrt{R_{sd}^d + R_{se}^d + \frac{n_r}{n_d}(R_m + R_{sd}^r + R_{se}^r)} \\ &\times \sqrt{Q_d(R_{sd}^d + R_{se}^d) + \frac{n_r}{n_d} Q_r (R_m + R_{sd}^r + R_{se}^r)}. \end{aligned} \tag{3.35}$$

For the case of $Q_r = Q_d$, this reduces to

$$R_p = R_{sd}^d + R_{se}^d + \frac{n_r}{n_d}(R_m + R_{se}^r + R_{sd}^r), \tag{3.36}$$

[5]To avoid confusion, we will in this section explicitly place a tilde over rates that are supposed to be effective rates.

so that the equilibrium polarization at optimum sensitivity is from (3.33) also, as in the case of the CW co-magnetometer, 50% for perfectly circularly polarized pumping light. The expression in the general case where $Q_r \neq Q_d$ is somewhat more complicated but can be simplified in the limit that n_r/n_d is sufficiently large so that

$$R_{sd}^d + R_{se}^d \ll \frac{n_r}{n_d}(R_m + R_{sd}^r + R_{se}^r). \tag{3.37}$$

In that case, (3.35) simplifies to

$$R_p \approx \frac{n_r}{n_d}\sqrt{\frac{Q_r}{Q_d}}(R_m + R_{se}^r + R_{sd}^r), \tag{3.38}$$

and the equilibrium polarization at optimum sensitivity, under the approximation (3.37) is therefore from (3.33)

$$\begin{aligned} P_0^e &= \frac{s_z^p}{1 + \dfrac{1}{R_p}\dfrac{n_r}{n_d}(R_m + R_{se}^r + R_{se}^r)} \\ &\approx \frac{s_z^p}{1 + \sqrt{\dfrac{Q_d}{Q_r}}}, \end{aligned} \tag{3.39}$$

where we have substituted (3.38) for R_p in the second line. Evidently, if $Q_r = Q_d$, we recover the exact result (without resorting to (3.37)) that the equilibrium polarization at optimum sensitivity is 50% for $s_z^p = 1$. However, in the case where $Q_r \neq Q_d$ and for sufficiently large n_r/n_d ratios so that (3.37) holds, we see that the equilibrium polarization at optimum sensitivity can be higher than 50% if $\sqrt{Q_d/Q_r} < 1$, or equivalently, if $Q_d < Q_r$. A higher alkali equilibrium polarization at optimum sensitivity will lead to a higher equilibrium noble gas polarization as well, which all other things being equal, is desirable since that leads to higher suppression of ordinary magnetic fields at the compensation point (see (3.30)).

It is also interesting to compare the hybrid pumped co-magnetometer's optimum sensitivity with its directly pumped counterpart. From (3.31) and (3.32), the optimum sensitivity of the directly pumped co-magnetometer scales as

$$\frac{P_0^e}{R_{tot}^e} = \frac{R_{np}s_z^p}{R_{np}+R_{np}}\frac{1}{R_{np}+R_{np}} = \frac{s_z^p}{4R_{np}}. \tag{3.40}$$

Intuitively, the optimum sensitivity of the directly pumped co-magnetometer improves as the relaxation rates decreases. For the case of the hybrid pumped co-magnetometer with $Q_r = Q_d$, the optimum sensitivity of the hybrid co-magnetometer can be shown from (3.33),(3.34) and (3.36) to scale as

$$\frac{P_0^e}{\tilde{R}_{tot}^e} = \frac{(n_d+n_r)s_z^p}{4\left[n_d(R_{se}^d+R_{sd}^d)+n_r(R_m+R_{se}^r+R_{sd}^r)\right]}. \tag{3.41}$$

To compare this with the directly pumped co-magnetometer in the best of circumstances, we may take the limit that $R_{np}^d \equiv R_{se}^d + R_{sd}^d \to 0$, which then gives us

$$\lim_{R_{np}^d\to 0}\frac{P_0^e}{\tilde{R}_{tot}^e} = \frac{s_z^p}{4\dfrac{n_r}{n_d+n_r}R_{np}^r}, \tag{3.42}$$

where $R_{np}^r \equiv R_m + R_{se}^r + R_{sd}^r$. For large n_r/n_d ratios, $n_r/(n_d+n_r) \approx 1$ so that in this case, the hybrid co-magnetometer's optimum sensitivity scales in the same way as the directly pumped co-magnetometer (3.40). On the hand, in the limit where $R_{np}^d \to 0$, (3.42) suggests that the hybrid co-magnetometer's sensitivity might for $Q_r = Q_d$ scale better than the directly pumped co-magnetometer for smaller n_r/n_d ratios. Nevertheless, we note that this somewhat defeats the purpose of hybrid pumping and is likely to not be accurate since R_{np}^d's contribution to (3.42) will become significant in that case. Indeed, we note that taking the limit $R_{np}^d \to 0$ to obtain (3.42) from (3.41) has the same effect as applying the condition(3.37) to (3.41), or in other words,

taking the limit $R^d_{np} \to 0$ to obtain (3.42) is similar to making the approximation that $n_r/n_d \gg 1$, which is inconsistent with smaller n_r/n_d ratios.

For the more general case where $Q_r \neq Q_d$, the expression for $P^e_0/\tilde{R}^e_{tot}$ is somewhat complicated but can be simplified as before for sufficiently large n_r/n_d ratios so that

$$R^d_{se} + R^d_{se} \ll \frac{n_r}{n_d}\left(\frac{Q_r}{Q_d} + \sqrt{\frac{Q_r}{Q_d}}\right)(R_m + R^r_{se} + R^r_{sd}), \tag{3.43}$$

and

$$Q_d \ll \frac{n_r}{n_d} Q_r, \tag{3.44}$$

in addition to (3.37) holds. For such large n_r/n_d ratios, $P^e_0/\tilde{R}^e_{tot}$ for $Q_r \neq Q_d$ can then be written as

$$\frac{P^e_0}{\tilde{R}^e_{tot}} \approx \frac{s^p_z}{\left(1 + \sqrt{\frac{Q_d}{Q_r}}\right)^2 R^r_{np}}. \tag{3.45}$$

As before, we note that for large n_r/n_d ratios and for $Q_r = Q_d$, the sensitivity of the hybrid co-magnetometer scales like the directly pumped co-magnetometer (3.40). However, for $\sqrt{Q_d/Q_r} < 1$ or equivalently, for $Q_d < Q_r$, the hybrid co-magnetometer's sensitivity can actually scale slightly better than the directly pumped co-magnetometer for sufficiently large n_r/n_d ratios.

We may therefore conclude that for large n_r/n_d ratios, having $Q_d < Q_r$ can, all other things being equal, be beneficial in allowing for a higher equilibrium noble gas polarization and a more advantageous sensitivity scaling (for the same probe power) compared to the directly pumped co-magnetometer. However, we note that this supposed advantage might not be easy to achieve in practice since a larger Q_r tend to translate experimentally into using a heavier alkali atom as the optically thick receiver species and the heavier alkali atoms have in general higher relaxation rates compared to their lighter counterparts so that the additional relaxation will likely more than offset the advantage of having $Q_d < Q_r$.

3.3 Suppression of Low Frequency Magnetic Fields

Besides having no first order sensitivity to magnetic fields at steady state, the co-magnetometer also suppresses slow changes to the magnetic field at the compensation point. To observe this, we may solve for $P_x^e(t)$ in the presence of a transverse oscillating $\mathbf{B}$ field from (3.27). Since we are primarily interested in the behavior of the co-magnetometer to oscillating $\mathbf{B}$ fields, we set $s_\perp^m = s_\perp^p = 0$ and $\boldsymbol{\beta}^n = \mathbf{b} = \boldsymbol{\Omega} = 0$ so that (3.27) becomes

$$\frac{d}{dt}\begin{pmatrix} P_\perp^e \\ P_\perp^n \end{pmatrix} = \begin{pmatrix} (-R_{tot}^e + i\gamma_e(B_n + B_z))/Q & -i\gamma_e\lambda M_n P_0^e/Q \\ -i\gamma_n\lambda M_e^r P_0^n & i\gamma_n(B_e + B_z) \end{pmatrix}\begin{pmatrix} P_\perp^e \\ P_\perp^n \end{pmatrix} + \begin{pmatrix} -i\gamma_e B_\perp P_0^e/Q \\ -i\gamma_n B_\perp P_0^n \end{pmatrix}. \tag{3.46}$$

The oscillating $B_\perp$ source term may be written as

$$B_\perp(t) \equiv B_x(t) + iB_y(t) = \frac{B_0}{2}(e^{i\omega t} + e^{-i\omega t}) = B_0 \cos\,\omega t, \tag{3.47}$$

where in general $B_0 \in \mathbb{C}$ but $B_x(t), B_y(t), \omega \in \mathbb{R}$. We expect that the solution will also have an oscillating form given by the ansatz

$$\begin{aligned} P_\perp^e(t) &\equiv P_x^e(t) + iP_y^e(t) = P_+^e e^{i\omega t} + P_-^e e^{-i\omega t} \\ P_\perp^n(t) &\equiv P_x^n(t) + iP_y^n(t) = P_+^n e^{i\omega t} + P_-^n e^{-i\omega t}, \end{aligned} \tag{3.48}$$

where $P_\pm^e, P_\pm^n \in \mathbb{C}$ are some unknown amplitudes to be solved and $P_{x,y}^e, P_{x,y}^n, \omega \in \mathbb{R}$. Substituting the source term (3.47) and ansatz (3.48) into the differential equations (3.46), and making use of the orthogonality of $e^{\pm i\omega t}$, we may solve for $P_\pm^e$ and $P_\pm^n$ at the compensation point where $B_z = -B_n - B_e$. From (3.48), the signal of the

co-magnetometer that is proportional to $P_x^e(t)$ is given by

$$P_x^e(t) = (\mathbb{R}\mathrm{e}[P_+^e] + \mathbb{R}\mathrm{e}[P_-^e])\cos\omega t + (\mathbb{I}\mathrm{m}[P_-^e] - \mathbb{I}\mathrm{m}[P_+^e])\sin\omega t. \tag{3.49}$$

We note that R_{tot}^e is of order $\sim$ 100 Hz so that for sufficiently slow changing $\mathbf{B}$ fields such that $\omega \ll \gamma_n B_n \sim \mathcal{O}(10)$ Hz, $\omega \ll \gamma_n B_n \ll R_{tot}^e$. We therefore expand denominators in $P_\pm^e$ to first order in $\omega/(\gamma_n B_n)$ and obtain for a slow B_x modulation,

$$\begin{aligned} P_x^e(t) \approx \frac{P_0^e\gamma_e}{R_{tot}^e}\left(\frac{\omega}{\gamma_n B_n} - \frac{2\omega^3}{\gamma_n^3 B_n^3}\right) B_0 \sin\omega t \\ - \frac{P_0^e\gamma_e}{R_{tot}^e}\left(\frac{Q\omega^2}{\gamma_n B_n R_{tot}^e} + \frac{\gamma_e B_e \omega^2}{\gamma_n^2 B_n^2 R_{tot}^e} - \frac{2Q\omega^4}{\gamma_n^3 B_n^3 R_{tot}^e}\right) B_0 \cos\omega t. \end{aligned} \tag{3.50}$$

As discussed in section 3.2, the pre-factor $P_0^e\gamma_e/R_{tot}^e$ serves as an overall scale factor that defines the sensitivity of the co-magnetometer to anomalous magnetic-like fields. Consequently, we see that the leading response to a slow changing B_x field is an out-of-phase term that is suppressed by a factor of $\omega/(\gamma_n B_n)$. Similarly, for a slow modulation of B_y, we obtain the result

$$P_x^e(t) \approx -\frac{P_0^e\gamma_e}{R_{tot}^e}\left(\frac{\omega}{\gamma_n B_n}\right)^2 B_0\cos\omega t - \frac{P_0^e\gamma_e}{R_{tot}^e}\left(\frac{2\gamma_e B_e\omega^3}{\gamma_n^3 B_n^3 R_{tot}^e} + \frac{Q\omega^3}{\gamma_n^2 B_n^2 R_{tot}^e}\right) B_0 \sin\omega t. \tag{3.51}$$

Evidently, the co-magnetometer suppresses slow changes to the B_y field even more strongly than it does to B_x since the leading term in this case comes in as an in-phase 2nd order term that is suppressed by a factor of $[\omega/(\gamma_n B_n)]^2$. We conclude this section by remarking that in theory, the co-magnetometer should exhibit no response to changes in B_z if everything is perfectly aligned. Experimentally however, there is typically some small response to changes in B_z, which indicates the presence of small misalignments.

3.4 Strongly Damped Dynamics

The co-magnetometer exhibits striking dynamics as a function of the longitudinal field B_z. At high B_z such that $B_z \gg B_n \gg B_e$, the signal of the co-magnetometer is weakly damped and has an effective gyromagnetic ratio of the noble gas species. However, at the compensation point, the co-magnetometer's signal is strongly damped and it has an effective gyromagnetic ratio that has been measured to approach that of the alkali's [179]. We may obtain information on the dynamics of the co-magnetometer's signal by solving for the homogeneous solution of (3.46), where we have for convenience set $s^m_\perp = s^p_\perp = 0$ and $\boldsymbol{\beta}^n = \mathbf{b} = \boldsymbol{\Omega} = 0$ as in the previous section. The homogeneous solution of (3.46) has the form

$$\mathbf{P}(t) = \mathbf{P}_+ e^{\lambda_+ t} + \mathbf{P}_- e^{\lambda_- t}, \tag{3.52}$$

where $\lambda_\pm$ are the eigenvalues of the matrix in (3.46), which can be solved to give

$$\lambda_\pm = \frac{-R^e_{tot} + i\gamma_e B^e_{ze} + iQ\gamma_n B^n_{ze} \pm \sqrt{F(B^e_{ze}, B^n_{ze})}}{2Q}, \tag{3.53}$$

with $B^e_{ze} = B_n + B_z$, $B^n_{ze} = B_e + B_z$, and F is here defined as

$$F = -(iR^e_{tot} + \gamma_e B^e_{ze} + Q\gamma_n B^n_{ze})^2 + 4Q\gamma_n(iB^n_{ze}R^e_{tot} + \gamma_e B^e_{ze} B^n_{ze} - \gamma_e B_n B_e). \tag{3.54}$$

For maximal damping of the longer lived solution corresponding to the eigenvalue λ_+, we would like to find a B_z such that $\mathbb{R}\mathrm{e}[\sqrt{F}]$ is minimal. In general, the square root of any complex number $z = x + iy$ can be written as

$$\sqrt{z} = \pm\sqrt{\frac{x + \sqrt{x^2+y^2}}{2}}\left(1 + i\frac{\sqrt{x^2+y^2} - x}{y}\right), \tag{3.55}$$

where $x, y \in \mathbb{R}$. The condition for maximal damping is therefore

$$\frac{d}{dB_z}\,\mathbb{R}\mathrm{e}[\sqrt{F}] = \frac{d}{dB_z}\left(\frac{\sqrt{\mathbb{R}\mathrm{e}[F] + \sqrt{\mathbb{R}\mathrm{e}[F]^2 + \mathbb{I}\mathrm{m}[F]^2}}}{\sqrt{2}}\right) = 0, \tag{3.56}$$

from which we obtain

$$B_z = \frac{-B_n\gamma_e + B_eQ\gamma_n}{\gamma_e\left(1 - \dfrac{Q\gamma_n}{\gamma_e}\right)} \approx -B_n + B_eQ\frac{\gamma_n}{\gamma_e} \approx -B_n, \tag{3.57}$$

where we have dropped the $Q\gamma_n/\gamma_e$ factors since Q is typically of order 10 and γ_n is typically three orders of magnitude smaller than γ_e. Consequently, we see that the co-magnetometer's signal is maximally damped at $B_z \approx -B_n$. As defined in section 3.1, the compensation point B_c where the co-magnetometer's first order sensitivity to B_x and B_y field vanishes is $B_c = -B_n - B_e$. Although the compensation point does not exactly coincide with the B_z required for maximum damping of the co-magnetometer's signal, we note that in practice, these two values are quite close to each other since for a K-^{3}He co-magnetometer, $B_e \sim 10$ μGs. Accordingly, by a happy coincidence, the co-magnetometer's signal is strongly damped near the compensation point although it still retains good sensitivity to anomalous magnetic-like fields. As we discuss in greater detail later, this is a very convenient feature of the co-magnetometer since it allows us to quickly run quasi-static $\mathbf{B}$ field modulations to automatically tune the compensation point condition.

At high B_z fields such that $B_z \gg B_n \gg B_e$, one can also show using (3.54) and (3.55) that $\sqrt{F}$ reduces approximately to

$$\sqrt{F} \approx R^e_{tot} + iB_z(Q\gamma_n - \gamma_e), \tag{3.58}$$

and λ_+ is consequently

$$\begin{aligned}\lambda_+ &= \frac{-R^e_{tot} + i\gamma_e B^e_{ze} + iQ\gamma_n B^n_{ze} + \sqrt{F(B^e_{ze}, B^n_{ze})}}{2Q} \\ &\approx \frac{-R^e_{tot} + i\gamma_e B_z + iQ\gamma_n B_z + \sqrt{F(B^e_{ze}, B^n_{ze})}}{2Q} \approx i\gamma_n B_z. \end{aligned} \tag{3.59}$$

Similarly, we have for λ_- at high B_z

$$\lambda_- \approx \frac{-R^e_{tot} + i\gamma_e B_z + iQ\gamma_n B_z - \sqrt{F(B^e_{ze}, B^n_{ze})}}{2Q} \approx -\frac{R^e_{tot}}{Q} + i\frac{\gamma_e B_z}{Q}. \tag{3.60}$$

Evidently, at high B_z field, the alkali and noble gas polarization decouple from each other and there are two distinct oscillation frequencies with two distinct damping rates[6]. In that case, the λ_- eigenmode clearly corresponds to the uncoupled alkali's (transverse) polarization while the λ_+ mode corresponds to that of the noble gas. As B_z approaches the compensation point, the noble gas' λ_+ mode experiences *maximal* damping as $\sqrt{F}$ reaches a minimum while the alkali's λ_- mode simultaneously experiences *minimal* damping although the result is far more dramatic for the noble gas since it has such a long uncoupled transverse relaxation time. Physically, at the compensation point, each spin species see a real magnetic field that is of the same magnitude as its own effective magnetization to the other species, which roughly compensates for the significant difference in the alkali and noble gas' gyromagnetic ratio so that at the compensation point, the resonance frequency of each spin species approach each other. The convergence of these frequencies mean that the two species can interact strongly with each other and helps give rise to the strongly coupled dynamics at the compensation point.

[6] We note that in general there should be a small but non-zero real damping term in (3.59). However, since we have neglected that term in (3.46), (3.59) is purely imaginary.

3.5 Zeroing of Fields

The strongly damped dynamics of the co-magnetometer near the compensation point allows us to implement a series of quasi-static **B** field modulations that can automatically (through a LabVIEW program) tune the **B** fields to render the co-magnetometer insensitive at first order to various experimental parameters. Of these experimental parameters, B_z, which depends on the ^{3}He magnetization, is most susceptible to long term drifts and it is consequently convenient to have a procedure that is capable of keeping the co-magnetometer at the compensation point ($B_z = 0$) during long periods of operation. A set of such automated zeroing routines were devised in [177] and we give here a quick description of the zeroing routines used in this work to minimize the co-magnetometer's response to changes in B_y and B_z fields.

Since the co-magnetometer exhibits strong damping close to the compensation point, it quickly returns to the steady state behavior described in (3.30) after a transient change in an experimental parameter. We can therefore use (3.30) to come up with a scheme for zeroing the co-magnetometer's sensitivity to various parameters.

Zeroing of B_z

For example, from (3.30), the co-magnetometer depends on B_z at second order with the term

$$P_x^e = \frac{P_0^e \gamma_e R_{tot}^e}{{R_{tot}^e}^2 + \gamma_e^2 (B_z + \beta_z^e + L_z^p + L_z^m)^2} \frac{B_y B_z}{B_n}. \tag{3.61}$$

We note that β_z^e, L_z^p and L_z^m are all nominally zero since L_z^p is zero on resonance and the probe beam is nominally along the x. Therefore, if B_z is sufficiently close to zero so that the second term in the denominator can be neglected, the co-magnetometer's second order dependence on B_z becomes

$$P_x^e = \frac{P_0^e \gamma_e}{R_{tot}^e} \frac{B_y B_z}{B_n}. \tag{3.62}$$

For a sufficiently small ΔB_y modulation leading to a change ΔP_x^e of the signal, we may approximate the ratio $\Delta P_x^e/\Delta B_y$ as a partial derivative w.r.t B_y and we therefore have

$$\frac{\Delta P_x^e}{\Delta B_y} \approx \frac{\partial P_x^e}{\partial B_y} = \frac{P_x^e \gamma_e}{R_{tot}^e}\frac{B_z}{B_n}. \tag{3.63}$$

We may then zero B_z by adjusting B_z to minimize the change in P_x^e due to a fixed ΔB_y modulation. Experimentally, the $\mathbf{B}$ field modulation applied is a smoothed square wave of the form [177]

$$B_i(t) = B_0 \tanh(s \sin(\omega t)), \tag{3.64}$$

where s is a dimensionless parameter used to control the sharpness of the transition. We note that in reality there are other (mixed) second order terms that also depend linearly on B_y and so this procedure does not exactly zero B_z. However, what it *does* accomplish is to minimize the co-magnetometer's response to small changes in B_y, which is what we desire experimentally. As mentioned earlier, for this procedure to work, B_z has to be relatively close to zero. Practically, we note that this is most easily accomplished by exciting a transient and varying B_z to maximize the damping since as discussed in section 3.4, the co-magnetometer's signal is maximally damped close the compensation point.

Zeroing of B_y

After B_z has been nominally zeroed, we may then zero B_y using the same procedure as we used to zero B_z but with the roles of the fields reversed. From (3.30), the leading order dependence of P_x^e on B_y is $\propto B_y B_z/B_n$ and consequently, for a small modulation ΔB_z, we may write

$$\frac{\Delta P_x^e}{\Delta B_z} \approx \frac{\partial P_x^e}{\partial B_z} = \frac{P_x^e \gamma_e}{R_{tot}^e}\frac{B_y}{B_n}, \tag{3.65}$$

so that as above, we may zero B_y by adjusting B_y to minimize the change in P_x^e due to a fixed ΔB_z modulation. The careful reader might have realized that there is in (3.30) a third order dependence of P_x^e on B_z through the $B_x B_z^2$ term and consequently, the change ΔP_x^e due to a ΔB_z modulation is not exactly given by (3.65). However, we note that the $B_x B_z^2$ term is suppressed by an additional factor of R_{tot}^e/γ_e and besides, its contribution to ΔP_x^e can be mitigated by making a symmetric modulation of B_z about $B_z = 0$. As before, we note that strictly speaking there are other terms that also depend linearly on B_z so this procedure doesn't exactly zero B_y and is more accurately understood as one which minimizes the co-magnetometer's response to linear changes in B_z. Indeed, the co-magnetometer has a surprising number of (mixed) second-order terms that depend on B_z at steady state including light-shift terms in both the x and y directions. Practically speaking, if there is a considerable light-shift term due to the probe beam in the x direction, B_y will be adjusted to compensate for that light-shift and will not be exactly zeroed with this procedure.

Zeroing of B_x

Similarly, after B_y and B_z have been "zeroed" using the procedures above, we may attempt to "zero" B_x. With B_y and B_z nominally zeroed, the change in P_x^e due to an asymmetric modulation of B_z away from $B_z = 0$ is

$$\Delta P_x^e = \frac{P_x^e \gamma_e}{R_{tot}^e} \frac{\gamma_e B_x}{B_n R_{tot}^e} (\Delta B_z)^2, \tag{3.66}$$

and we may zero B_x by adjusting B_x to minimize the co-magnetometer's response to $(\Delta B_z)^2$. We note that this zeroing procedure does depend on B_z and B_y being relatively well zeroed and it can be therefore somewhat less reliable compared to the other two procedures. In particular, as we noted above, the procedure to "zero" B_y can in practice leave B_y with a significant offset if there is considerable light-shift from

the probe beam, which will in turn cause this zeroing procedure to fail. In theory, a perfectly linearly polarized probe beam should cause no light-shift but birefringence in optical components can give it a slight elliptical polarization that contributes to a light-shift in the x direction. This can however be sometimes partially compensated by rotating a $\lambda/4$ wave plate or a glass stress plate in the path of the probe beam. Besides failing due to an improperly zeroed B_y, this procedure can also fail due to an improperly zeroed B_z field. This is most frequently due to drifting noble gas polarization and can be compensated by using a B_z modulation that is bigger in size compared to the drift of the noble gas' magnetization during the procedure. As before, this procedure of "zeroing" B_x can also be thought of as minimizing the co-magnetometer's response to $(\Delta B_z)^2$.

3.6 Co-magnetometer Calibration

As discussed in section 3.1, the co-magnetometer's signal, which consists of the x projection of the alkali's electronic polarization, is sensitive to anomalous magnetic-like fields at the compensation point. Experimentally however, we measure a voltage V that is proportional to P_x^e and hence the anomalous field. We would therefore like to find a calibration constant C such that $\beta = CV$, where β here is some anomalous field. Mathematically, we may from (3.30) write our measured voltage V due to the anomalous field β as

$$V = \kappa P_x^e = \kappa \frac{P_0^e \gamma_e}{R_{tot}^e} \beta, \tag{3.67}$$

where κ is some optical and electronic gain factor and we are here assuming that the fields have been zeroed so that $B_z \gamma_e \ll R_{tot}^e$. Evidently, the calibration factor we seek is thus

$$C = \frac{1}{\kappa} \frac{R_{tot}^e}{P_0^e \gamma_e}. \tag{3.68}$$

As discussed in section 3.5, close to the compensation point, small modulations ΔB_y will cause the measured signal to change as

$$\Delta V = \kappa \frac{P_0^e \gamma_e}{R_{tot}^e} \frac{B_z}{B_n} \Delta B_y. \tag{3.69}$$

If we measure ΔV at two different values of B_z, we may then obtain the desired calibration constant C as

$$C = \frac{1}{\kappa} \frac{R_{tot}^e}{P_0^e \gamma_e} = \frac{\Delta B_y}{B_n} \frac{B_{z,2} - B_{z,1}}{\Delta V_2 - \Delta V_1}. \tag{3.70}$$

We note that $B_n \approx B_c$ and B_c is known since it is just the applied longitudinal B field needed to zero B_z, where by B_z we here mean deviations away from the compensation point. The calibration constant can therefore be easily obtained while performing the B_z zeroing procedure described in section 3.5.

Alternatively, the calibration constant may also be measured using a low frequency B_x modulation due to [152]. From (3.50), the co-magnetometer's first order out of phase response to a slow B_x modulation is

$$V(t) \approx \kappa \frac{P_0^e \gamma_e}{R_{tot}^e} \frac{\omega}{\gamma_n B_n} B_0 \sin \omega t = \frac{1}{C} \frac{\omega}{\gamma_n B_n} B_0 \sin \omega t. \tag{3.71}$$

Since ω, γ_n, B_n and B_0 are all known, we may also obtain the calibration constant C by measuring the co-magnetometer's response to a slow B_x modulation and using this relation. These two calibration methods typically agree to within $10 - 20$ %. We note that in [152] it is argued that the discrepancy is due to alkali polarization gradients in the z direction, which systematically decreases the $\Delta V_2 - \Delta V_1$ term in the denominator of (3.70). Measurements of the earth's rotation in [152] indicated that the slow B_x modulation calibration is the more accurate of the two methods. Consequently, we use the calibration constant obtained from a slow B_x modulation

as the definitive calibration in this work. This calibration was also independently verified by physically inducing a rotation along the y-axis (by floating the optical table and slowing lifting one end of it) and measuring Ω_y (using a tiltmeter) and the co-magnetometer's signal simultaneously.

Chapter 4

Spin Mass Interaction Limiting Experiment (SMILE)

The K-^{3}He co-magnetometer described in the previous chapters possesses high sensitivity to anomalous fields but has a suppressed response to ordinary magnetic fields, which makes it particularly well suited to investigate tiny anomalous spin mass interactions that are typically obscured by ordinary magnetic interactions. In this chapter, we present an experiment designed to find or constrain these interactions using a K-^{3}He co-magnetometer and two large Pb source masses. We discuss the design and setup of both the co-magnetometer and source masses before moving on to characterizations of the co-magnetometer. Studies of various systematic effects and our efforts to mitigate them will also be discussed. Finally, data analysis of both the signal and systematics will be presented, culminating in the derivation of new constraints on $g_p^n g_s^N$, the product of the axion's pseudoscalar coupling to neutrons with its scalar coupling to nucleons, that represent an order of magnitude improvement over previous results [49, 50]. These results are currently the most stringent laboratory constrains of $g_p^n g_s^N$ for axions with masses between $\sim 10^{-6} - 10^{-8}$ eV [187]. Similarly, new limits

on $g_p^e g_s^N$, the product of the axion's pseudoscalar coupling to electrons with its scalar coupling to nucleons, will also be presented.

4.1 Experimental Setup

Figure 4.1 shows a schematic of SMILE along with the pump and probe optical setups. We note that for illustrative clarity, we have displayed the pump optics (on the bottom right of Figure 4.1) as though it was further away from the cell (along the x axis in the figure's coordinate system which is specified at the top right of the figure) than the probe optics immediately above it in the figure. In reality, the probe optics is mounted vertically (along the figure's specified z axis) on top of the pump optics so that both sets of optics are enclosed by the same polycarbonate enclosure (denoted by dashed lines in Figure 4.1) as illustrated by the bottom left insert (note the different coordinate system of the insert that is specified at the bottom left of the insert).

The experimental setup of SMILE can be divided into two independent systems: 1) a co-magnetometer system including the co-magnetometer cell, oven/stem heaters, magnetic shields, vacuum chamber, pump and probe optics, and 2) a source mass system including the two Pb weight stacks, the mechanical frame that guides the motion of the weights and all things related to the motor/reduction gear system necessary to move the weights. We begin this section by first discussing the co-magnetometer setup before moving on to describe the source masses.

4.1.1 Cell

At the very heart of SMILE is a hand blown spherical aluminosilicate GE180 glass cell that contains the alkali and noble gas atoms. GE180 was used as the glass of choice since it resists discoloration by the alkali atoms at our operating temperature

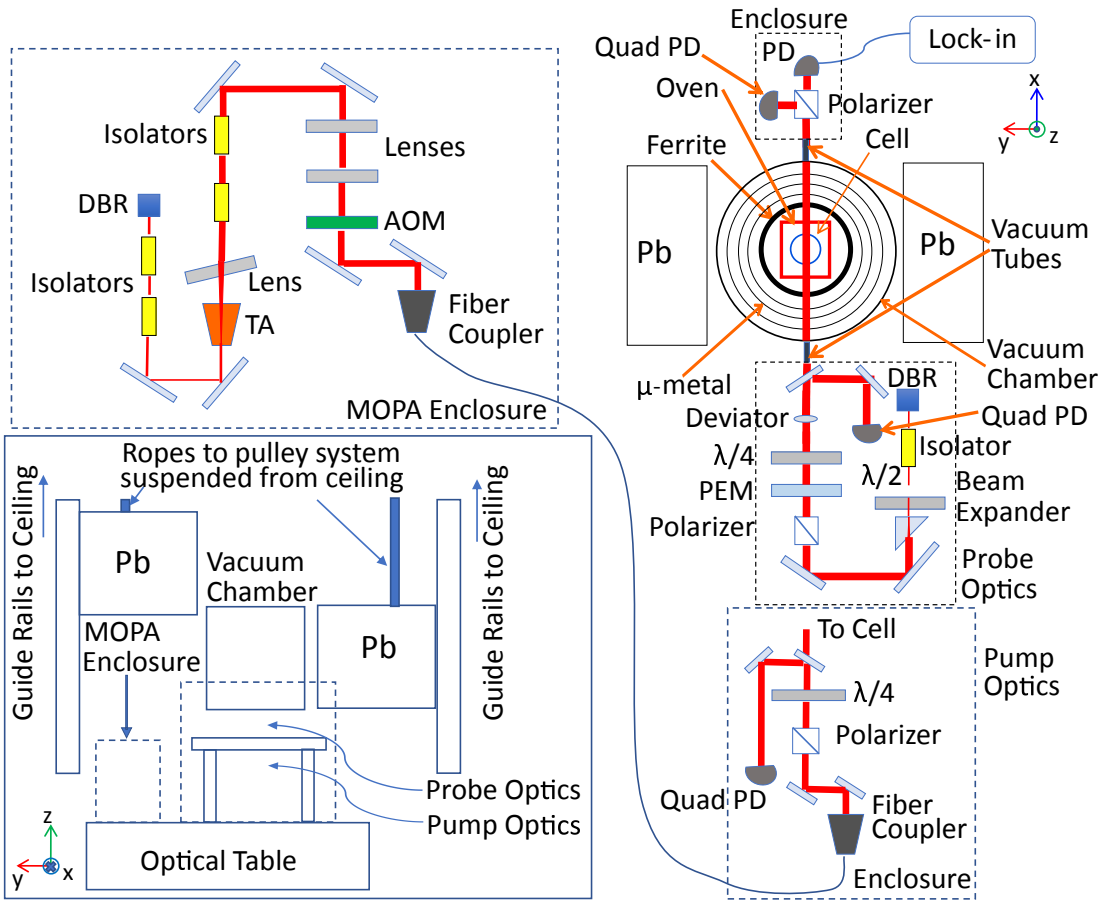

Figure 4.1: Probe and pump optical setup of SMILE in the x-y plane. Bottom left insert: Experimental schematic in the y-z plane.

of ~ 200 °C [188] and is less porous to ^{3}He atoms [189] as compared to other common glass such as Pyrex. The spherical shape is required to obtain high ^{3}He polarization since the dominant mode of relaxation for the ^{3}He spins is self-relaxation due to $\mathbf{B}$ field gradients generated by its own magnetization, which is eliminated in the case of an exactly spherical cell. Happily enough, a sphere is also the most natural glass shape to blow and is the ideal theoretical shape to withstand internal pressure [190].

As described in more detail in section 4.2.3, measurements of the alkali polarization within our initial glass cells indicated that it was advantageous to use as large (in diameter) a cell as possible. In our case, the diameter of the cell was limited by the size of the holes in the magnetic shields though which the cell has to be inserted into, which is about 15 mm. The manufacture of these cells begins with our esteemed

glassblower Mike Souza blowing spherical cells from GE180 tubes to our specified dimensions. We then check the dimensions and optical quality of each cell by shining a collimated visible laser through the spherical part of the cell and observing the amount of divergence caused by the sphere, which essentially acts as a weakly diverging lens[1]. Shining a visible laser through the cell also allows us to spot "bubbles" or "streaks" of inhomogeneity within the glass. In addition to checking the optical divergence through the cell, we also visually inspect the sphericity of the cell's interior by immersing it in mineral oil, which allows us to peer into the cell's interior since mineral oil has a refractive index that is similar to glass.

Cells that are not rejected due to their optical quality and asphericity then move on to the next stage of cell manufacture where they are baked to 700 °C and then cooled in a relatively zero **B** field environment. This is a step that was not typically done but was performed for the SMILE cells as a way to potentially de-magnetize magnetic impurities within the glass by heating them past their Curie temperature and then cooling them in a zero field environment. Although rare, we have observed instances of extremely fast relaxation of the ^{3}He spins due to strong local magnetic field gradients that are indicative of magnetized impurities near the surface of the glass walls (see section 2.8.2 for more details). The efficacy of this procedure is uncertain since we did not perform a systematic study to evaluate it but since adopting this step, we have not encountered a magnetized cell. In the event that a cell does become magnetized however, it may be de-gaussed by subjecting it to an oscillating magnetic field that increases in magnitude before slowing returning back to zero although we note that the success of this procedure depends on the coercivity of the magnetic impurity and the magnitude of the de-gaussing field.

[1]The amount of divergence is a function of the thickness of the glass walls. In general, we want the thinnest possible (least divergence) cell that is capable of withstanding $\sim$ 15 atm of internal pressure at our operating temperature of around 200 °C. That a spherical glass cell with wall thickness of $\sim$ 0.5 mm can withstand that amount of pressure never ceases to amaze this author.

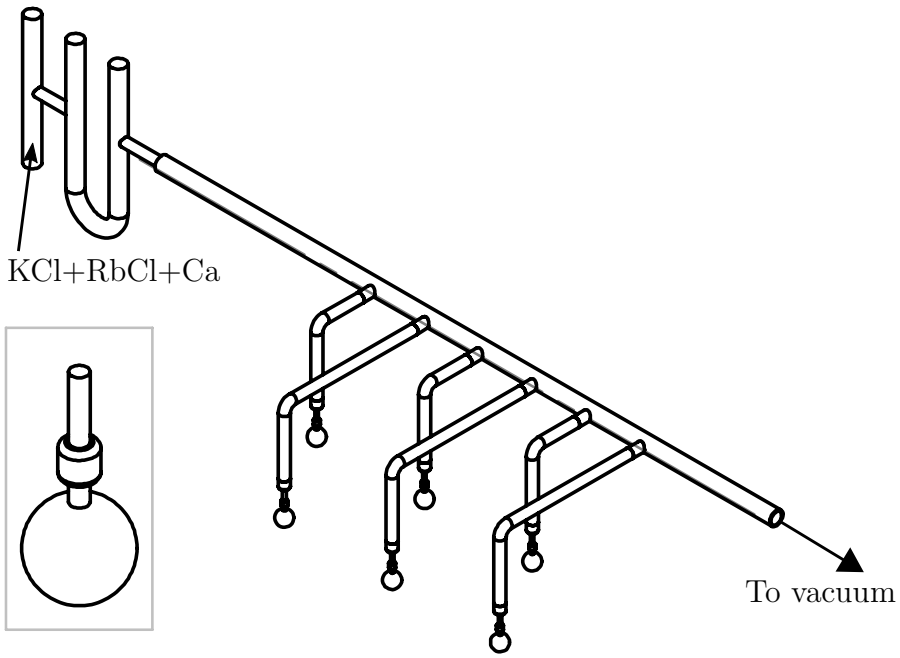

Figure 4.2: Diagram of a typical cell string. Insert: Schematic diagram of a SMILE cell.

After the cells are done baking in a zero field environment, they are handed back to the glassblower who connects them to a glass cell "string", a schematic of which is shown in Figure 4.2, that is then connected to a vacuum system and evacuated. Before sealing off the glass cell string, Ca granules along with the correct proportion of KCl and ^{87}RbCl[2] is added to the end of the string as indicated in Figure 4.2. In SMILE, we employ hybrid optical pumping (described in greater detail in an earlier section) where a dense, optically thick K vapor is spin polarized via spin-exchange collisions with an optically thin ^{87}Rb vapor. To accomplish this discrepancy in partial vapor pressure at the operating temperature, small amounts of ^{87}RbCl is added to KCl so as to achieve a ^{87}Rb:K ratio of about 0.002.

The evacuated cell string is then baked at a moderately high temperature $\sim 300\,^{\circ}$C for about a week to allow impurities on the surface of the glass to outgas, after which K and ^{87}Rb may be liberated by reacting the KCl and ^{87}RbCl salts with the Ca granules using a low temperature flame. Once liberated, the resulting alkali vapor can then be

[2]In early testing, we had used CsCl but it was found that Cs's higher spin relaxation rate was causing K to also have more spin relaxation (since they are both in spin temperature equilibrium). Consequently, the decision was made to switch to ^{87}Rb.

chased through the 'U'-tube (see Figure 4.2) (which serves to trap Ca particles) into each individual cell with the flame. The final step of the cell manufacture process is to fill each individual cell with the appropriate buffer gases and to "pull" each of them off the cell string by melting the glass stem by which they are connected to the cell string with a high temperature flame. If done correctly, the melted glass forms a seal that traps the alkali atoms and buffer gases within the cell without exposing them to atmosphere.

To selectively fill each cell with the correct amount of buffer gas, we first fill the entire cell string with the appropriate gas and then submerge an individual cell in a cryogenic dewar filled with liquid ^{4}He[3]. In the case of the N_2 buffer gas, which is added to quench excited alkali atoms (see section 2.7.2), all of the N_2 previously in the cell string freezes in the cell that is submerged in liquid ^{4}He. This may be verified by checking that the pressure in the cell string goes to zero (or more accurately the baseline vacuum pressure). Once all of the N_2 gas has frozen in the cell, the cell string is then filled with ^{3}He by expanding it from a known initial pressure and volume. Although ^{3}He does not freeze like N_2 at this temperature, it does get concentrated within the cold cell, which may be estimated by measuring the discrepancy of the pressure in the cell string from its expected value after the expansion of ^{3}He into it. Once sufficient ^{3}He is estimated to be within the cell, the cell is "pulled-off" the cell string by melting the stem that connects it to the cell string with a high temperature flame. This is a somewhat delicate process that involves heating the stem up to $\sim$ 1500 °C while simultaneously keeping most of the cell a few centimeters below at $\sim$ -268 °C[4]. As the stem beings to melt, the cell will begin to drop so the dewar has to be simultaneously lowered while the stem is melted to ensure that the flame can continue to heat the stem. Due to stresses that develop within the glass during

[3]We note here that cells in Figure 4.2 are staggered and spaced apart to provide sufficient clearance so that only one cell will be submerged in the dewar at any one time.

[4]This author is always amazed at how glass can withstand such abuses.

this process, it is important to anneal (with a lower temperature flame) the stem in between melting it. An improperly annealed stem will tend to crack once the cell returns to room temperature and is subjected to an internal pressure of $\sim$ 10 atm. Indeed, the stem is the weakest part of the cell and is almost always the point of failure in failed cells. We note here that it is somewhat important for the stem to have a small initial diameter (this needs to be specified to the glassblower) of $\sim$ 2 - 3 mm because thinner stems have less thermal mass and tend to anneal better. Once the cells are all pulled off, the surviving cells are then stress-tested by placing them in an oven and heating them to slightly above our operating temperature of 200 °C for a day to weed out bad cells.

We note that the cell manufacture process outlined above means that the cells will inevitably have a stem that will cause them to deviate from perfect sphericity, which as mentioned above, would be detrimental to the relaxation rate of ^{3}He. To correct for this, the alkali droplet in the cell is typically chased with a hot air gun into the neck to plug it. This entails melting the alkali droplet (with the hot air) and tapping the droplet into the correct position. This author has found it easiest to hold the stem of the cell with a glove (for thermal insulation) and getting the droplet to move by tapping his hand (not the cell!) on a lab bench. The position of this droplet may be controlled by keeping the bulb and stem of the cell at different temperatures during co-magnetometer operation and creating a pressure gradient between the two regions. For this to work with a reasonable temperature gradient, the volume of the stem should not be much smaller than the volume of the bulb, which is why cells used in SMILE have an additional cylindrical bulb in their stems (see insert of Figure 4.2). Initially, we overestimated the size of this cylindrical bulb, which led to the droplet moving too easily due to temperature fluctuations. This was later corrected for and the diameter of this cylindrical bulb is around 4mm.

Figure 4.3: Comparison of a SMILE (right) cell with a more 'conventional' spherical cell (left).

Figure 4.3 shows a SMILE cell on the right in contrast to a "usual" spherical co-magnetometer cell. We note that the SMILE cell is larger and that it has the aforementioned cylindrical bulb with an alkali droplet placed right at the neck to plug the stem.

4.1.2 Oven

The main oven that heats up the spherical bulb of the co-magnetometer cell is made out of a 1"×1"×1" boron nitride cube, which possesses high thermal conductivity and is non-magnetic. Optical access for the probe beam is provided by a drilled through-hole from one side to another while another orthogonal through-hole provides access for the pump beam and cell. Within the coil form (the structure supporting the magnetic field coils) inside the innermost ferrite shield, the oven sits in a square lip that has been cut into a rectangular G-7[5] plate that has tapped holes on its sides for 4 PEEK screws to hold onto the oven as it sits inside the lip. Meanwhile, the G-7

[5]We use G-7 here since it has a maximum continuous operating temperature of 220 °C.

plate is itself secured to the lid of the coil form by means of appropriate spacers and PEEK screws.

Rather than using twisted resistive wires for heating, thick film heater panels, which can have their resistive traces printed much closer to each other than a pair of wires can be twisted together, were used instead since the close proximity of the traces ensures good cancellation of the **B** field they produce at the position of the co-magnetometer cell. Each 0.25"×1" panel has two solder pads at one end of its long side that allows external wires to be connected to it. High temperature solder (rated to above 220 °C) was used to form the solder joints to ensure that the joints did not fail during operation. Similarly, the heater panels were soldered to magnet wires since they have high temperature tolerance and thin insulation, which allows us to twist them together tightly to reduce the net **B** field they produce within the co-magnetometer cell.

Despite the use of high temperature solder however, we found that the solder joints were not reliable and were prone to failing. In particular, we have, by measuring the resistance of the heater panels, observed one too many instance in which some heater panels would fail at a low temperature but become operable again at higher temperature or vice versa[6], which suggests that the solder joints are only making electrical connections intermittently. We believe that this is due to repeated thermal cycling and unequal thermal expansion coefficients between the solder pad and solder, which stresses the joint until it eventually fails. Also, since the solder pads are on the ends of the heater panel, there is not much mechanical support and strain relief for the wires. We have mitigated these problems by soldering and securing the wires in a way depicted in Figure 4.4. Rather than soldering the wires away from the heater panel, we instead solder them so that they initially run towards the other end, which allows us to provide some mechanical support to them by bonding them to the panel

[6]These panels will eventually fail altogether so this is just the first sign of trouble.

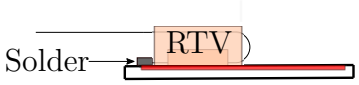

Figure 4.4: Recommended way to connect thick film heater panels.

with (Dow Corning 736) high temperature Room-Temperature-Vulcanizing (RTV) silicone that is rated to 260 °C. After a short distance, the (twisted) wires are bent 180° back so that they run away from the panel again. A second application of RTV on top of the first secures the wire in this configuration, which helps to reduce stress on the solder joint even when the wires are tugged on the other end. We have found this method of connecting the wires to the heater panels to be fairly robust. Also, we note that it is helpful to use solder flux in the soldering process since the high temperature involved in soldering the high temperature solder causes rapid oxidation that is detrimental to the quality of the solder joint.

Initially, the heaters were inserted into slits that were cut into the boron nitride oven and bonded together with a high temperature, high thermal conductivity aluminum nitride based potting adhesive (Aremco's Ceramacast^{TM} 675-N). Unfortunately, since some of these heaters failed and were difficult to remove from the slits without damaging the oven (boron nitride is a rather soft material), additional heaters were added to the sides of the oven to compensate for the loss of power. A combination of aluminum nitride and RTV[7] holds these additional heater panels in place. This added bulk however, has the unintended effect of causing the oven to not sit as intended in the square lip of the G-7 rectangular plate, making it somewhat less rigidly held by the PEEK screws. The heater panels are connected in parallel and have an effective series resistance of 30 Ω.

It is typical after long periods of continuous operation for alkali vapor to condense on the coldest part of the cell. Ideally, the stem should be the coldest part of the

[7]Aluminum nitride does not bond too well with boron nitride so it's important to use some RTV as well since we don't the heater panels falling off the oven during operation.

cell but unfortunately, this is not always the case in practice. In particular, the parts of the cell along the laser beams are often most likely to see condensation since they also, by virtue of the holes made in the oven to provide for the optical access, lose the most amount of heat via black-body radiation to the exterior of the oven. Annoyingly enough, these are also the areas of the cell where condensation is most detrimental since it reduces optical transmission through the cell. This problem is especially severe for small ovens where the optical access is close to the cell since that increases the solid angle through which black body radiation can escape.

Rather than using a larger oven with thermal shields (which increases power requirements) to help prevent condensation, we decided to use GaP covered windows as a means of preventing condensation on the cells [191]. A combination of GaP and glass was used since GaP has high thermal conductivity and is transparent at the probe wavelength of 795 nm. However, since GaP's transparency to infrared radiation also allows a good fraction of black body radiation from within the oven to escape, it is paired with a glass substrate that is less transparent to infrared radiation above 795 nm. The windows in SMILE were expertly made by Nezih Dural and featured a polished circular Pyrex substrate with a slightly smaller (in diameter) thin GaP wafer attached on top of it by carefully placing RTV around the edges of the wafer and the top surface of the Pyrex. RTV was used since it is flexible even after curing and would allow for mismatchs in the thermal expansion coefficients of Pyrex and GaP. The window is then placed into a circular depression cut into the oven and a second layer of aluminum nitride potting adhesive is added on top of the RTV and oven to secure the window to the oven. We note that although GaP is transparent to infrared radiation, it has a high refractive index of 3.2 at those frequencies and there is consequently large reflective losses at its interface with air/vacuum. It is therefore crucial to apply an appropriate anti-reflection coating on its surface to reduce these losses. The quality of these coatings can vary from one supplier to another. For SMILE, we

had two high quality coating with a transmission of 99% or higher and a lower quality coating with a transmission of 86%. The two wafers that had transmissions of over 99% were used for the probe windows while the one with lower transmission was used for the pump window since obtaining a good probe beam transmission is somewhat more crucial to obtaining a good sensitivity[8]. We note that the coatings which had transmissions of over 99% did not cover the entire area of the wafer and so there is a somewhat small (centered) circular area in the wafer that the probe beam has to go through in order to obtain high transmission.

A MP108FD power amplifier chip supplies the oven's heaters with AC currents at 120 kHz, which is well above the bandwidth of the co-magnetometer. Blocking capacitors on both the input and output of the amplifier ensure that only AC currents are passed to the oven heaters while temperature sensing of the oven is accomplished by a Honeywell 112-105PAJ-B01 1 MΩ (at room temperature) platinum-iridium thermistor that is buried with thermally conductive aluminium nitride cement inside a drilled hole of the boron nitride oven. It is desirable to use a high resistance thermistor to reduce the sensing current, which could potentially generate a bias DC magnetic field at the position of the cell. Similarly, platinum-iridium was chosen as the material of choice since it is non-magnetic. The thermistor is connected via a four-wire configuration to a CryoCon 32B controller that sends in a 10 μA DC excitation current. Since the CryoCon controller is unable to measure a thermistor with a 1 MΩ resistor, we added a 249 kΩ resistor in parallel to it and entered a custom calibration curve into the controller. The analog output of the controller is sent to an AN633AN multiplier that multiplies it with a reference 120 kHz signal from a function generator, which then goes into the input of the MP108FD power amplifier. To prevent a current overload that might accidentally destroy the oven's panel heaters, a resistor divider

[8]Essentially, every probe photon that passes through the cell carries a measurement of the atoms' spin but it also contributes to the relaxation of the atoms so it is desirable to "make every single photon count" by collecting all of them into the detector.

before the amplifier ensures that a full-scale output from the controller would only causes a maximum voltage output of 86 $V_{pk\text{-}pk}$[9].

4.1.3 Stem heater and cell mount

During operation, the co-magnetometer cell is surrounded by an oven, an innermost ferrite magnetic shield and three additional μ-metal shields within the vacuum chamber. In theory, the co-magnetometer cell can be placed within the oven by opening each layer of shielding progressively, fixing the cell in position, and then closing back each layer of shielding. However, this is a *major* hassle and is especially tricky in SMILE where there is not much access to the inside of the vacuum chamber due to the proximity of the weights. To make inserting/removing a cell easier, a cell mount, made mostly out of a PEEK tube that is vacuum sealed at one end by an O-ring, holds on to the cell on the other end with an on-axis boron nitride stem heater. This allows us to insert the cell from outside the vacuum chamber through a series of holes in the magnetic shields to its proper position within the oven without the hassle of opening the vacuum chamber and magnetic shields. Moreover, it also allows us to independently control the temperature of the stem and spherical bulb of the cell by independently controlling the temperature of the stem and oven heater respectively[10]. Wires from the boron nitride stem heater run inside the PEEK tube and may be accessed through a home-made vacuum feed-through at the end the tube. PEEK was chosen as the material of choice here since it is non-magnetic and can withstand a continuous operating temperature of 260 °C.

The stem heater, for reasons elaborated above in our discussion of the oven in section 4.1.2, comprises of a boron nitride piece that has been machined with two

[9] We note that this is actually close to the maximum voltage output of the amplifier since the amplifier is powered by ± 50 V DC power supplies.

[10] We assume that the temperature of the spherical bulb of the cell is mainly given by the temperature of the oven and that the temperature of the stem of the cell is primarily given by the temperature of the stem cell heater.

slots for two thick film panel heaters. These heating panels are connected in parallel and have an effective series resistance of 58 Ω. Temperature sensing, like the oven, is accomplished with a Honeywell 112-105PAJ-B01 1 MΩ (at room temperature) platinum-iridium thermistor that is positioned and read-out in a similar fashion as that of the oven's thermistor described in section 4.1.2. Since the CryoCon 32B temperature controller has two independent control loops, the oven and stem heater's temperature can be independently controlled with one controller that puts out two separate analog control voltages. The stem's panel heaters are, like the oven's panel heaters, driven by amplified AC currents from the same 120 kHz reference signal to avoid any strange interference effects. This is accomplished by multiplying the stem's analog control voltage from the controller with the same 120 kHz reference signal using another AN633AN multiplier and sending it to a home-built push-pull amplifier. In principle, a similar MP108FD power amplifier as that used for the oven may be used here as well. However, to save on unnecessary labor, an existing home-built push-pull amplifier was used instead. Unlike a MP108FD power amplifier, the push-pull amplifier is is unable to drive a load with high resistance. Consequently, the output of the push-pull amplifier is sent to to a step-up transformer that then drives the heater panels. To prevent the stem heater panels from burning out due to an accidental current overload, an appropriate winding ratio for the transformer was chosen so that the maximum output voltage across a 58 Ω resistor is less than 86 $V_{pk\text{-}pk}$. We note that use of the transformer ensures the stem's heater panels are always AC-coupled.

As noted in section 4.1.1, the position of the alkali droplet is chased via a hot air gun into the neck of the cell before insertion into the vacuum chamber and is subject to change once the temperature rises above the alkali's melting point. To ensure that the liquid droplet remains in roughly the same position during the heat up to operating temperature, we have found that it is crucial to ensure (for SMILE

cells) that the oven is always roughly 12 °C hotter than the stem heater once the alkali has melted. Operationally, we have found that this is most easily accomplished by first establishing the appropriate temperature difference while the temperatures are still below the alkali's melting point and then ramping both the oven and stem heater's temperature up to their operating temperatures at the same rate using the CryoCon's ramp control mode. We typically use a ramp rate of 1 °C/min. It is sometimes necessary to fine tune the PID parameters to ensure that the ramp is closely followed by both control loops. A LabVIEW program that allows us to read and control both control loops on the CryoCon controller via GPIB was written to help with the monitoring and controlling of the oven and stem heater's temperatures.

4.1.4 Magnetic shields and vacuum chamber

To have avoided detection thus far, any anomalous spin-mass interactions must of necessity be much smaller than a magnetic interaction. Consequently, it is crucial to shield the co-magnetometer cell from random and systematic magnetic interactions if SMILE is to stand a chance at detecting a tiny anomalous spin-mass interaction. Moreover, for the co-magnetometer to achieve high sensitivity, it needs to be in the SERF regime, which requires the alkali atoms to be in a relatively low $\mathbf{B}$ field environment[11]. Accordingly, magnetic shielding is also required to shield the atoms from Earth's magnetic field. Magnetic shielding of a volume is typically accomplished by the use of high permeability material, such as μ-metal, to divert external $\mathbf{B}$ fields around the shielded volume [192]. Although μ-metal possesses extremely high permeability, the magnetic noise within their enclosed volume is typically limited to $1-10$ $\mathrm{fT}/\sqrt{\mathrm{Hz}}$ due to inherent Johnson currents within the material [180, 193]. A shielding system that only incorporates μ-metals would therefore subject the co-magnetometer

[11] More precisely, to be in the SERF regime, the precession frequency of the atoms in the $\mathbf{B}$ field should be much smaller than the rate of spin-exchange collisions (which is proportional to the alkali density). At typical number densities of $\sim 10^{13} - 10^{14}$ cm^{-3} alkali atoms, this means that $\mathbf{B}$ must be much less than Earth's magnetic field.

to a magnetic noise floor at that level. However, this problem can be mitigated by using high resistivity magnetic material such as ferrite, which has considerably smaller intrinsic Johnson currents and therefore lower magnetic noise [194]. In SMILE, we employ 3 outer μ-metal shields but the innermost shield is made out of a ferrite material.

Magnetic shielding in the case of SMILE is complicated by the need for electrical and optical access (i.e. holes in the shields) to the shielded volume and the competing requirement that the weights be placed as closed as possible to the co-magnetometer cell, which reduces the space available for magnetic shielding[12]. There is consequently a trade-off between the amount of magnetic shielding available and the sensitivity of the experiment to anomalous spin-mass interactions. Fortunately, the optimum air-gap between two layers of finite length cylindrical shields is significantly smaller compared to two layers of infinitely long cylindrical shields [195], which implies that it is possible to have a compact set of shields that does not overly sacrifice either magnetic shielding or sensitivity to anomalous spin mass interactions. Furthermore, the presence of holes within the shields can be mitigated by increasing the air gap between the shields [196] although this does has the effect of increasing the overall volume of the shields to the detriment of SMILE's sensitivity to anomalous spin-mass interactions.

For simple geometries such as infinitely long cylindrical shields, there are exact analytical formulas that give the transverse shielding factors of the shields. Infinitely long cylindrical shields do not, of course, exist but there are nevertheless approximate analytical formulas that give the radial and transverse shielding factors of multi-layer cylindrical magnetic shields [197, 198]. To optimize the dimensions of the shields, we used these analytical formulas as a starting point and then used the commer-

[12]We note that this is because the strength of the spin-mass interaction falls off exponentially with the distance of the weights to the cell for an axion-like particle with non-zero mass.

cially available Ansoft Maxwell[13] finite-element package to numerically calculate the shielding factor at the position of the co-magnetometer's cell for various shielding geometries. Assuming that the co-magnetometer will have at least an inherent factor of 10 suppression at DC (see section 4.2.4), our goal was to have a total magnetic suppression of at least 1×10^8 so that a 1 μGs external field will be suppressed to only 1 aT in the co-magnetometer.

For practical purposes, we attempted to achieve the target suppression factor within the radius of a standard vacuum flange so that the vacuum chamber, consisting simply of two vacuum flanges and an appropriately sized cylindrical tube, can be made out of mostly standard off-the-shelf components. It turns out we were able to, including the inherent suppression from the co-magnetometer, exceed our suppression target while still having the outermost μ-metal shield fit within a standard ISO-200 (metric) K-style vacuum flange since the final simulated suppression of all our shields was 1.3×10^8 and 3.6×10^7 in the radial and axial directions respectively.

In SMILE, the cylindrical vacuum chamber and magnetic shields were positioned so that their longitudinal axes were parallel to the vertical. Figure 4.5 shows a (rotated) schematic diagram of the 3 outer μ-metal shields as well as the inner ferrite shield. The beige rectangular blocks and cylindrical disk in Figure 4.5 are Delrin spacers that determine the vertical spacing between the vacuum chamber and magnetic shields while the four 3/8" diameter green G-10 rods that fit through holes in the bottom end cap of each μ-metal shield provides horizontal alignment between the chamber and shields. The green G-10 rods are threaded on either end and are screwed into the bottom vacuum flange. We note that the G-10 rods do not go through holes in the bottom end cap of the ferrite but rather, the ferrite sits snugly in the middle of all 4 G-10 rods. Good mechanical (and ideally magnetic) contact between the

[13]Ansoft Maxwell was used since we already had a license for it back then. We note that there is a highly capable general open-source FEM package in Python (FEniCS) that would be able to do the job equally well. Indeed, this author has found FEniCS to be quite useful in simulating various non-uniformities and diffusion within a co-magnetometer cell.

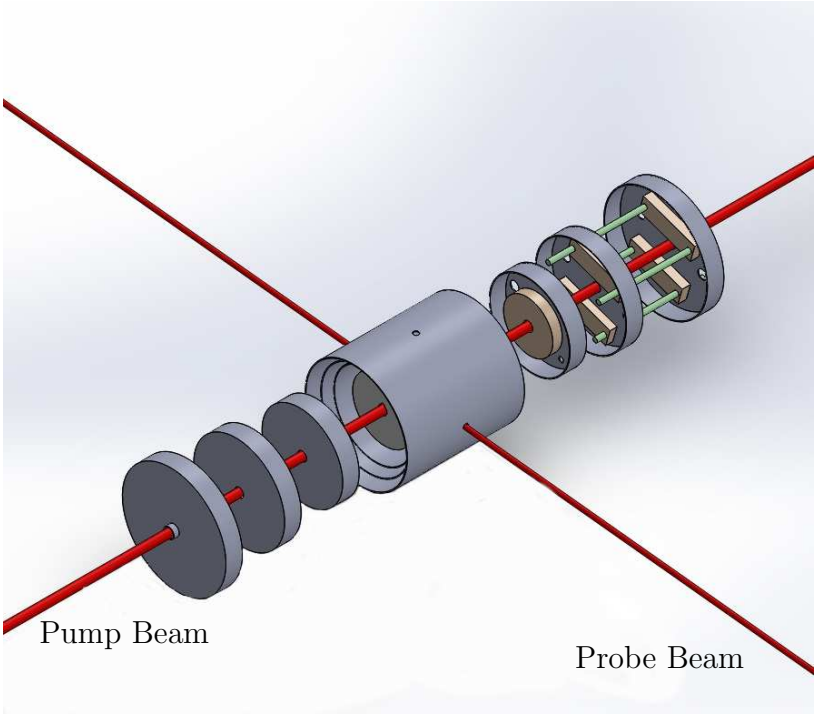

Figure 4.5: Exploded view of magnetic shields.

polished ferrite's end caps and body is accomplished by screwing four brass nuts into the threaded top of the four G-10 rods that then press down gently on the ferrite's top lid. To ensure good mechanical/magnetic contact between the μ-metal end caps and cylindrical bodies, the μ-metal end caps were fabricated to tightly enclose the bodies of the μ-metal shields[14]. Due however to this tight tolerance, it is necessary to secure the bodies of the shields to the vacuum chamber so that the top end caps can be separately removed. This is accomplished by having two G-10 screws fit through two holes, located orthogonal to the holes for the probe beam (see Figure 4.5) in the sides of the shields, and screwed into a threaded blind hole in the vacuum chamber.

Electrical wires and cooling water for the ferrite[15] are brought through two larger 18 mm holes at the bottom of each μ-metal bottom end cap. Wires that carry larger currents such as the wires for the oven's heaters and the de-gaussing wires are

[14]We note that this is not possible with ferrites since they are considerably more brittle.

[15]The cooling water is to ensure that the ferrite, which is closest to the oven, does not get too hot. For the ferrite to be an effective magnetic shield, it has to be in a ferromagnetic phase.

all brought up through one hole while wires for the all the magnetic field coils are brought up through the other hole to minimize electrical cross-talk between them. These wires are connected to electrical feed-throughs located in the bottom ISO-200 vacuum flange, through two Fischer connectors. To further reduce electrical cross-talk, the oven and de-gaussing wires are fed through a 4-pin DEE 103 A053-130 hermetic Fischer panel receptacle located on one side of the bottom vacuum flange while all magnetic field coil wires are fed through a 12-pin DEE 103 A062-130 hermetic Fischer panel receptacle located on the other side of the flange. Connections to these receptacles on the air side of the flange is accomplished by a Fischer 4-pin S 103 A053-130 and 12-pin S 103 A062-130 plug. To de-gauss the shields, the de-gaussing wires have to go through the top end caps of all the μ-metal shields, which is a little tricky to accomplish since there is only one (axial) hole in each top end cap that is already being used by the cell mount to insert the cell. Nevertheless, the de-gaussing connection through the top end caps of the μ-metal shields can be made by placing a thin cylindrical conducting shell within the axial hole of the top end caps which extends through all 3 μ-metal shields. Care was taken to insulate the shell with Kapton tape so as to avoid current flowing through the shields themselves. To complete the de-gaussing circuit, the top flange of the vacuum chamber has additional electrical feed-throughs that allow de-gaussing currents flowing in from the bottom of the vacuum chamber to exit via the top.

4.1.5 Probe setup

In SMILE, we search for anomalous spin-mass interactions by measuring the spin orientations of spin-polarized atoms while modulating the position of two large nearby source masses that should, for non-zero anomalous spin-mass coupling, cause the spin orientation of the atoms to be correlated with the position of the masses. To measure the spin orientation of the atoms, we send a linearly polarized off resonance probe

beam through the cell, which according to (2.226) will undergo optical rotation due projections of the atoms' spin along its direction of travel.

A detailed schematic of SMILE's probe beam optical setup is presented in Figure 4.1 and we elaborate further on it in this section. As depicted in Figure 4.1, the 11 mW, 769.53 nm (blue detuned from K's $\mathcal{D}_1$ line) probe beam is supplied by a single-mode Photodigm distributed Bragg reflector (DBR) laser that comes packaged together with a thermo-electric cooler (TEC) in a TO-8 can package. To shield the laser from electromagnetic interference from the motor (see section 4.5.1 for more discussion), the laser is mounted inside a rectangular aluminum box that is grounded via the laser cable; electrical insulation of the laser, its mount and the aluminum box from the optical table is accomplished with a ceramic spacer. An additional circuit inside the box filters the laser current using inductors (protected with flyback diodes) and capacitors. To further mitigate electromagnetic noise, the shields on the TEC/laser cables were all appropriately connected so that they are only grounded at one end and do not form any ground loops. The laser and its attendant optics are all mounted on a Thorlabs PBH11102 breadboard and enclosed with a large polycarbonate enclosure to minimize convective air currents that are detrimental to the probe beam's optical rotation noise (see section 4.2.6 for more details).

An optical isolator right outside the laser isolates the laser from stray incoming reflections that might otherwise cause instability in its lasing mode. After the passing through the isolator, the probe beam passes through a $\lambda/2$ wave-plate and is reflected off two mirrors that direct it towards the cell. Since reflections off the mirror surfaces can, due to their different reflectivities for s and p polarized light, potentially mess up the light's linear polarization, the light's polarization is cleaned up with a Glan-Taylor linear polarizer after the mirrors. The probe beam then travels through a Hinds photo-elastic modulator (PEM) and $\lambda/4$ wave-plate that together modulates the light's plane of polarization at 50 kHz. After the $\lambda/4$ wave-plate, the beam is

transmitted through a deviator, which consists of a fixed and translating lens in a refractive index matching liquid that together allow for inline steering of the beam. Finally, before entering a vacuum tube and leaving the polycarbonate enclosure, a beam sampler picks off a tiny fraction of the beam and sends it to a quadrant photo-diode for position and intensity monitoring.

After leaving the initial enclosure, the probe beam enters the vacuum tube and travels through the oven and cell in the vacuum chamber. A collimation lens right outside the vacuum chamber's window slow down the divergence of the laser beam (the cell acts as a weakly diverging lens) and directs it into another vacuum tube that ends in a second polycarbonate enclosure where the polarization of the light is analyzed by a crossed Glan-Taylor linear polarizer. A photo-diode measures the power of the transmitted beam while rejected light from the polarizer is directed into another quadrant photo-diode for further position and intensity monitoring.

Detection electronics

To achieve high optical rotation sensitivity, we employ a narrow bandwidth lock-in technique that greatly reduces our sensitivity to environmental noise at frequencies other than multiples of the lock-in reference frequency. Physically, this is accomplished by carrying the desired optical rotation signal on top of a 50 kHz optical rotation modulation that is then demodulated later with a lock-in amplifier. As mentioned above, the 50 kHz modulation is achieved with a combination of a PEM and $\lambda/4$ wave-plate. For this to work, the retardation axis of the PEM should be oriented 45° with respect to the light's polarization while the fast-axis of the $\lambda/4$ wave-plate ought to be aligned with the initial polarization of the light. To see this, we note that we may, using the formalism of Jones calculus, describe the (vertically) linearly

polarized probe beam as

$$\mathbf{E}_i = \begin{pmatrix} 0 \\ 1 \end{pmatrix} E_0 e^{i(kz-\omega t)} \rightarrow \begin{pmatrix} 0 \\ 1 \end{pmatrix} E_0, \tag{4.1}$$

where we have dropped the overall phase factor since it is the same for both the x and y components. We note that the $\exp(i(kz - \omega t))$ phase convention means that a retardation is given by a positive argument so that a $\lambda/4$ wave-plate with its fast-axis aligned to the vertical (slow-axis aligned to the horizontal) may be represented as

$$\Lambda = \begin{pmatrix} e^{i\pi/2} & 0 \\ 0 & 1 \end{pmatrix}. \tag{4.2}$$

In general, the axes of the optical components will be misaligned from the initial polarization of the light, which we may use to define our axes so that (4.1) will always hold. These misalignments may be accounted for by introducing the rotation operator in 2D

$$R(\theta) = \begin{pmatrix} \cos\theta & -\sin\theta \\ \sin\theta & \cos\theta \end{pmatrix}, \tag{4.3}$$

and recalling that the rotation for any operator O is given by $\tilde{O} = R(\theta)OR^{-1}(\theta)$. The effect of the PEM, which applies a time-varying retardation $\delta(t) = A\cos\omega_m t$ along its retardation axis is therefore

$$M = R(\theta_m + \pi/4) \begin{pmatrix} e^{i\delta(t)} & 0 \\ 0 & 1 \end{pmatrix} R^{-1}(\theta_m + \pi/4), \tag{4.4}$$

where θ_m is some arbitrary misalignment. Similarly, the effect of the $\lambda/4$ wave-plate and final polarizer can then, including arbitrary misalignments, be respectively given

by the operators

$$\Lambda = R(\theta_l) \begin{pmatrix} e^{i\pi/2} & 0 \\ 0 & 1 \end{pmatrix} R^{-1}(\theta_l), \tag{4.5}$$

$$\Pi = R(\theta_\pi) \begin{pmatrix} 1 & 0 \\ 0 & 0 \end{pmatrix} R^{-1}(\theta_\pi). \tag{4.6}$$

In the absence of misalignments, the polarization vector of the light after passing through the PEM and $\lambda/4$ wave-plate is then

$$\mathbf{E}_f = \Lambda \cdot M \cdot \mathbf{E}_i = \frac{E_0}{2} \begin{pmatrix} i\left(-1 + e^{i\delta}\right) \\ 1 + e^{i\delta} \end{pmatrix} = E_0\, e^{i\delta/2} \begin{pmatrix} \sin \delta(t)/2 \\ \cos \delta(t)/2 \end{pmatrix}, \tag{4.7}$$

so that the net effect of the PEM and $\lambda/4$ wave-plate is to rotate the linearly polarized light's plane of polarization by a time varying angle $\delta(t)/2$ with respect to the vertical at the modulation frequency ω_m of the PEM. According to (2.226), a non-zero projection of the alkali atoms' spin in the direction of the linearly polarized, off resonant probe beam rotates the beam's polarization. Consequently, the effect of the atoms may be simply represented by $R(\theta_s)$ and the transmitted **E**-field through the final polarizer is therefore

$$\mathbf{E}_t = \Pi \cdot R(\theta_s) \cdot \Lambda \cdot M \cdot \mathbf{E}_i. \tag{4.8}$$

For small PEM modulation amplitude and misalignment angles so that $\delta, \theta_m, \theta_l, \theta_\pi \ll 1$, the (time-averaged) transmitted power is given to first order in the angles by

$$\begin{aligned} P &= \frac{1}{2}\mathbf{E}^* \cdot \mathbf{E} \approx \frac{E_0^2}{8}\delta^2 + \frac{E_0^2}{2}\delta(\theta_l - \theta_\pi + \theta_s) + C \\ &= P_0 \frac{A^2}{8}\cos(2\omega_m t) + P_0 A \cos(\omega_m t)(\theta_l - \theta_\pi + \theta_s) + C + P_0 \frac{A^2}{2}, \end{aligned} \tag{4.9}$$

where we have used C in the first line to represent terms that are independent of the time varying modulation amplitude δ, and have used $P_0 \equiv E_0^2/2$ in the second

line to represent the power of the initial beam. From (4.9) we see that to first order, the measured transmitted power contains time-varying modulations at the first and second harmonic of the PEM's modulation frequency. Moreover, the amplitude of the first harmonic is proportional to θ_s, the optical rotation due to the atoms, and to θ_l, θ_π, the misalignment angles of the $\lambda/4$ wave-plate and final polarizer respectively. Evidently, our signal is contained in the amplitude of the first harmonic of the transmitted power. Furthermore, it is obvious that we may easily calibrate our optical rotation signal by simply rotating either the $\lambda/4$ wave-plate or final polarizer by a known amount and measuring the change in the amplitude of the first harmonic. Lastly, we note that since the second harmonic of the transmitted power is proportional to P_0 but not to any angles, it is a good proxy for measuring the initial power of the probe beam.

Before moving on, we note that in principle, the modulation of the probe beam's plane of polarization can also be accomplished by a Faraday modulator consisting of a transparent material with a large Verdet constant (such as terbium gallium garnet) surrounded by a coil driven with AC currents. Indeed, one such device was used early on in SMILE but was replaced by the PEM/$\lambda/4$ wave-plate combination because a Faraday modulator required significant currents for generating the necessary magnetic fields, which in turn heated the air surrounding it and created convection currents. As discussed in more detail in section 4.2.6, these air currents are detrimental to the probe beam's optical rotation noise. Moreover, due again to the large currents involved, it is difficult to modulate the beam's polarization by more than a few kHz using a Faraday modulator, whereas the PEM's mechanical resonance is at a much higher 50 kHz frequency where there is typically less environmental noise.

We measure the transmitted power (4.9) with a photo-diode that is reverse biased with a 9V battery to ensure it operates in the photo-current mode with low capacitance and high bandwidth. A home-built 2 stage photo-diode amplifier consisting of

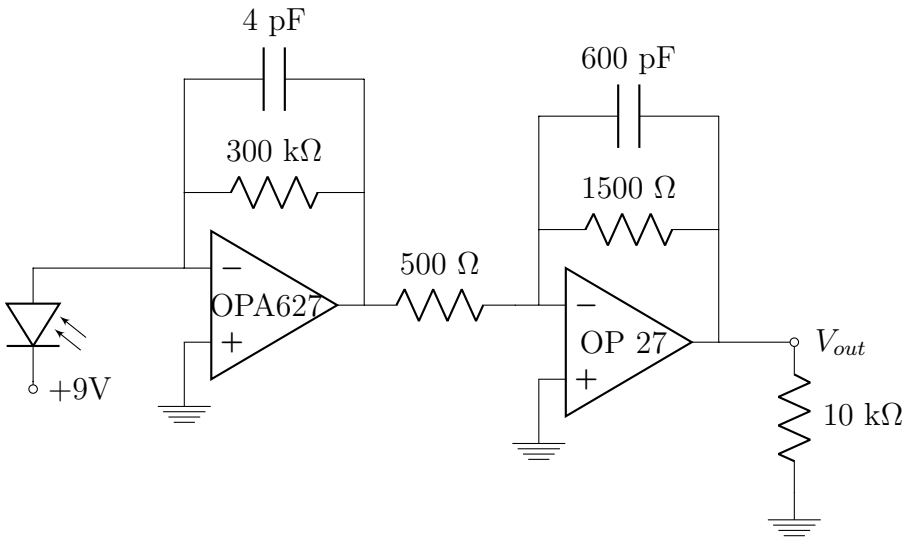

Figure 4.6: Circuit diagram of probe beam's photo-diode amplifier.

a transimpedance amplifier coupled to an inverting amplifier turns the photo-current into a voltage that is then sent to a SRS 830 lock-in amplifier for de-modulation. Figure 4.6 shows the circuit schematic (for brevity, power supply bypassing capacitors are not shown). We note that to reduce additional stray capacitance, the amplifier is mounted together with the photo-diode and is connected to the photo-diode by just one BNC connector. To prevent making a ground loop, the photo-diode amplifier is powered from a floating 15 V DC power supply that is then grounded via the shell of the BNC cable to the lock-in amplifier, which as depicted in Figure 4.6, is connected to ground via a 10 kΩ resistor[16]. Similarly, ceramic spacers help to electrically insulate the photo-diode and its amplifier from the grounded optical table. It's important to not leave the photo-diode case floating since it would then serve as an antenna that could pick up environmental noise and re-broadcast it into the diode's circuitry. Consequently, we tie it to the +9V supplied by the battery that reverse biases the photo-diode. Since we only need a bandwidth of 100 kHz (second harmonic of the PEM's modulation frequency), the amplifiers in Figure 4.6 rolls off their gain after 133 kHz.

[16]This corresponds to the "floating" ground option on the SRS 830 lock-in amplifier.

Optical alignment

Good optical alignment of the probe beam is important for various reasons. Firstly, to achieve optimum sensitivity, we need to attempt to collect all the photons that went through the cell since these photons have already contributed (at a small level) to the relaxation of the atoms and should not be "wasted". It is therefore evident that good alignment between the initial beam, cell, and final photo-diode is important. Secondly, good optical alignment is important to minimizing polarization noise in the probe beam due to the spherical nature of the cell. As discussed and illustrated in [177], the probe beam's polarization can undergo optical rotation due to different reflectivities for s and p polarized light across the curved surface of the cell. Motion of the beam across the curved surface of the cell can therefore translate into unwanted optical rotation noise. However, this effect can be minimized by ensuring that the beam passes through the center of this cell (historically called the "sweet spot") where this effect, to first order, disappears [177].

In [177], it was shown using the ABCDEF formalism [199] that an appropriately chosen fixed and translating lens pair, placed at the correct distance apart from each other and the cell, can help to keep the beam's position on the cell fixed while allowing its angle to be changed (with a deviator or mirror before the lens pair). This should, in theory, minimize changes to the beam's position on the cell, and furthermore, in [177, 178], active feedback using a piezo mirror and a quadrant photo-diode (placed at the equivalent position of the cell) was also employed to reduce beam motion on the cell. During an early stage of SMILE, a similar optical setup was employed. However, we did not find a substantial reduction in the probe noise because as further discussed in Figure 4.19 and section 4.2.6, most of the additional (above the photon shot-noise level) noise is due to optical rotation caused by beam motion through vacuum windows with inhomogeneous birefringence.

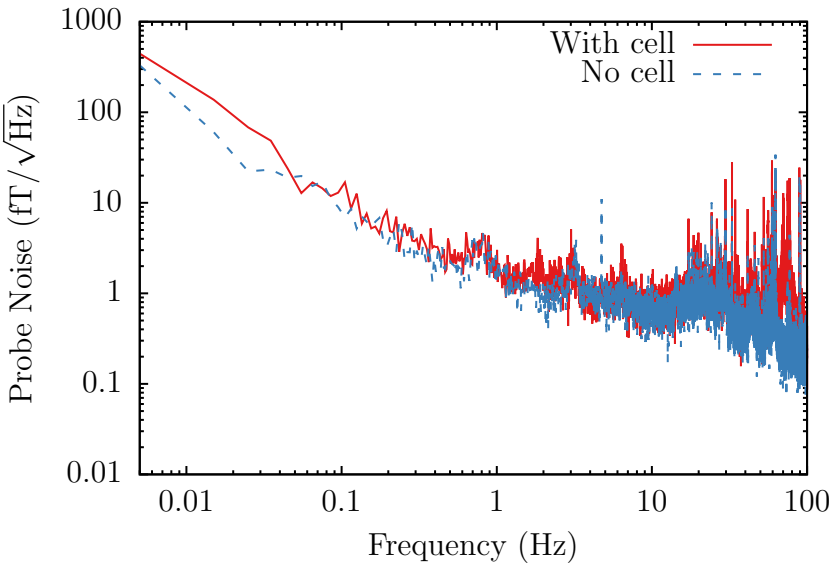

Figure 4.7: Measured probe noise with and without cell.

Indeed, as Figure 4.7 demonstrates, when the probe beam is properly aligned (without using the scheme in [177]), there is no appreciable difference in the probe noise with or without the cell inserted, which indicates that optical rotation due to beam motion through the cell is negligible in SMILE. On the other hand, significantly lower probe noise can be obtained by removing the vacuum windows (see Figure 4.19). Consequently, we eventually favored the simpler probe optical setup depicted in Figure 4.1 rather than the more elaborate setups of [177, 178]. This author has found that it is typically sufficient to align the probe laser to the cell using the old-fashioned technique of first aligning two irises on the breadboard to the cell (with a clear line of sight to the bread board on the other side) and then aligning the probe laser beam to the irises. Usually, this rough alignment is enough to get the beam in close proximity to the "sweet-spot", which can then be found by modulating the position of the beam and attempting to minimize the response (from the lock-in) while changing the equilibrium position of the probe beam on the cell.

4.1.6 Pump setup

As alluded to in section 2.7, the thermal spin polarization of our alkali atoms is woefully insufficient for use in an experiment designed to constrain anomalous spin-mass interactions. Consequently, the atoms have to be spin polarized via circularly polarized resonant light. In SMILE however, we employ, as mentioned in section 4.1.1, a hybrid pumping technique where we spin polarize an optically thin ^{87}Rb vapor that then spin polarizes an optically dense K vapor via spin-exchange collisions. The use of this technique allows us to produce a more uniform alkali polarization since most of the pumping light is able to propagate through the cell without significant attenuation from the optically thin ^{87}Rb vapor. However, on the flip side, since the ^{87}Rb vapor is optically thin, most of the pump light is not absorbed in the vapor and is "wasted" after it exits the cell. Consequently, hybrid pumping requires significantly more laser power compared to a direct optical pumping scheme. Further adding to the power requirement woes is the fact that the pump beam is, for reasons explained more fully in section 4.2.6, sent through an acoustic-optic modulator (AOM) and coupled into a single mode polarization-maintaining fiber (PMF), which results in a significant loss of power due to less than ideal coupling efficiencies.

To meet the power demands of SMILE, we use a 3W 795 nm tapered amplifier (TA) from m2k (now DILAS) to amplify light from a single-mode 795 nm Photodigm DBR seed laser in a master-oscillator power amplifier (MOPA) setup. The tapered structure of the amplifier enables high output power (by decreasing the optical power density at the output facet that could otherwise cause catastrophic optical damage) while still maintaining the narrow linewidth of the seed laser. As discussed in greater detail in section 4.2.6, the TA, which generates significant heat requires water cooling and tends to produce convection currents that causes unwanted beam deflections. Consequently, for this and other reasons detailed in section 4.2.6, the TA is housed in a separate polycarbonate enclosure from the probe beam optics (see Figure 4.1)

and is then coupled into that enclosure through a single mode PMF. Although the PMF decouples the output beam's position stability from convection currents in the TA's enclosure and ensures a nice Gaussian beam profile, its output intensity can still vary significantly since beam deflections and other environmental noise in the TA's enclosure will affect the fiber's coupling efficiency and hence output intensity. To stabilize the output fiber's intensity, we therefore sample the output beam and send it to a quadrant photo-diode where its measured intensity is used in tandem with an AOM placed before the input fiber coupler to control the laser power coupling into the fiber. Nominally, the beam coupling into the fiber is aligned with the zeroth order diffraction mode of the AOM. However, during operation we deliberately waste some laser power by applying a RF voltage to the AOM, which causes some of the laser beam to diffract into the first order mode that does not couple into the fiber. This then allows us to stabilize the PMF's output intensity by controlling the total input power into the fiber with the AOM that can either send more or less light into the zeroth order diffraction mode that is coupling into the fiber. Although it may seem easier to control the fiber's output intensity by directly controlling the amplifier's current, we note the output power of a TA does not always vary linearly with laser current and "kinks" in the output power have been known to form at high current densities [200], which makes stabilizing the output intensity by varying the laser current tricky. We have observed these "kinks" and have therefore decided to implement the intensity feedback with an AOM instead. The use of a PMF together with a intensity feedback did help to greatly reduce noise from the pump beam (see section 4.2.6). Nevertheless, this particular implementation of the pump beam has its own pitfalls and challenges that we further discuss below.

Firstly, since we need the pump beam to be circularly polarized, it is essential for the optical fiber to preserve the linear polarization of the input beam so that upon its exit from the fiber, we can convert it to a circular polarization by means of a $\lambda/4$

wave-plate. A PMF nominally preserves the linear polarization of the input beam but for it to work well, the polarization angle of the input beam has to match one of two polarization modes within the fiber that has been specifically designed to have a large refractive index differential. Otherwise, both polarization modes will be excited and the large refractive index differential will in general produce elliptically polarized light that is sensitive to mechanical stress and temperature fluctuations. Although a linear polarizer at the fiber's output cleans up the output beam's polarization, this is still undesirable because it leads to erratic swings of the transmitted power that makes it difficult for the AOM to stabilize the (linearly polarized) output power. Indeed, if the polarization angle of the input beam is not matched to the polarization axes of the fiber, gently touching the fiber will cause a slow but significant fluctuation of the output power (after a linear polarizer) due to the heating from a human finger.

To align the input polarization of the laser to the fiber's axes, we note that the optical rotation at the output depends on the phase difference accumulated in the two polarization modes of the fiber. Since the phase accumulated in one mode by traveling through length l of the fiber is simply $kl = 2\pi nf/cl$, the phase difference between the two modes is just

$$\Delta\phi = \frac{2\pi f l \Delta n}{c}, \tag{4.10}$$

where Δn is the refractive index difference between the 2 modes, which is typically ~ 0.0001. (4.10) suggests a relatively simple way to tune the input polarization angle. According to (4.10), a frequency modulation of just 8 GHz will result in a phase difference of about 1° in a 1 m long fiber. Considering that the Photodigm DBR lasers have a frequency/temperature transfer function of $\sim$ 30 GHz/°C, it is relatively easy to observe an appreciable modulation in the phase difference, which translates into a power modulation after a linear polarizer, by modulating the seed

laser's temperature. The polarization angle of the input beam can then be tuned by rotating a $\lambda/2$ wave-plate placed in front of the input fiber coupler to minimize the transmission fluctuations of the output beam through a linear polarizer while the seed laser's temperature is modulated. We note however, that this process needs to be iterated a number of times since it is possible that the output polarization has, during the tuning process, rotated orthogonal to the final polarizer. Consequently, the linear polarizer should be rotated to maximize the transmission through it and the process repeated to ensure that the minimum indeed corresponds to an aligned input polarization.

Besides taking care to align the polarization of the input beam into the PMF, it is also important to have a reasonably good coupling efficiency into the single-mode PMF to meet the pump power requirements of SMILE. To obtain high coupling efficiency, the input beam should be Gaussian and have roughly the right size, which will allow the focusing lens of the fiber coupler to focus the incoming beam into the tiny core of the fiber. However, due to filamentation processes [201] within the amplifier chip, the output beam's intensity profile from the TA is not exactly Gaussian and the beam is not quite diffraction limited. Furthermore, due to the highly asymmetric dimensions of the TA's output facet, the emerging beam is highly astigmatic, which is detrimental to its coupling efficiency to the PMF since it means that the focusing lens can only correctly focus one aspect of the incoming beam into the fiber. The astigmatism of the TA's output can be partially corrected by carefully selecting the focal lengths of both the initial aspheric and secondary cylindrical lens used to (respectively) collimate the fast and slow divergence axes of the output beam. Nevertheless, since it is not possible to fully correct for this, an additional cylindrical telescope (before the AOM in Figure 4.1) has to be employed to provide finer control of the beam's aspect ratio at the input fiber coupler. With these aids, we were able to achieve a coupling efficiency of around 35%, which is by no means impressive but par

for the course with tapered amplifiers [202] (although we note that somewhat higher efficiencies are possible [203]). We note that the beam profile of the TA changes with amplifier current and therefore, final adjustments ought to be performed at the intended operating current.

Similar to the probe laser, both the pump DBR seed laser and TA are all electrically insulated from the grounded optical table by means of ceramic spacers. Their cases are both grounded via their laser cables and care was taken to ensure that the shields of the laser and TEC cables are appropriately tied so that there are no ground loops. The DBR laser is isolated from the TA with two optical isolaters[17], and the TA is itself isolated from stray reflections with another two optical isolators. We use a single mode PMF with angled-polished contacts (APC)[18] to ensure that most of the reflected beam that does not get coupled into the fiber is reflected off at an angle and does not return to the TA. As elaborated in section 4.2.6, there is by design minimal optics on the output side of the fiber. After exiting the fiber, the light is directed by two mirrors to exit the polycarbonate enclosure through a vacuum tube and it eventually hits a 45° mirror under the vacuum chamber that reflects it up into the cell. Before the beam leaves the enclosure, a linear polarizer cleans up the polarization of the light after the mirrors and a $\lambda/4$ wave-plate then creates the necessary circular polarization. As mentioned above, a beam sampler also samples the pump beam and sends it into quadrant photo-diode at an equivalent position as the cell for position and power monitoring/feedback.

We conclude this section by remarking that in SMILE, the alignment of the probe and pump beam into the vacuum chamber is somewhat more complicated since both the probe and pump laser have to exit the same enclosure at fixed holes. Since it is not possible to easily align the pump optics once it is enclosed by the polycarbonate

[17] We note that for amplification to occur, the output of the DBR laser has to be co-linear with the spontaneous emission of the TA, which means that without the isolators, the TA's spontaneous emission will be directly entering the DBR's laser cavity which can lead to unwelcome feedback.

[18] Similarly, the fiber coupler is designed to mate with APC fibers.

enclosure, we drilled two 0.75" diameter holes in a strip of aluminum to mimic the position of the optical access holes in the enclosure and used that as a guide on the optical table to ensure that the probe and pump laser will indeed exit the enclosure cleanly without clipping on any surfaces. The horizontal alignment of the enclosure is determined by the orientation of the fixed 45° degree mirror under the vacuum chamber that usually reflects the pump beam up into the cell. This author has found it easiest to determine this horizontal alignment by sending in the pump light from the reverse direction (i.e. from the top of the vacuum chamber when the cell is not in place) using a custom made fiber mount attached to the vacuum chamber that centers it to the oven and sends it straight down to the 45° mirror below, which then reflects it towards the aluminum strip that can then be moved to mark the correct horizontal alignment of the enclosure. With the position of the enclosure marked, the path of the pump beam can then be further marked with another two irises and the pump beam (traveling towards the vacuum chamber) can now be aligned to be co-linear with these irises and the hole in the aluminum strip. Similarly, the probe optics should be adjusted to ensure that the probe beam will exit through the center of its hole in the aluminum strip.

4.1.7 Source masses

In SMILE, we search for anomalous spin-mass interactions between two 250 kg Pb source masses, comprised of multiple lead bricks with an overall dimension of 30 cm $\times$ 36 cm $\times$ 20 cm, and spin polarized atoms in a K-^{3}He co-magnetometer vapor cell. The masses are situated along the sensitive y-axis of the co-magnetometer (see Figure 4.1) and the faces of the bricks are located approximately 14 cm away from the vapor cell. Since the spin-mass interaction falls off exponentially for a finite mass axion, it is advantageous to use a dense material that will maximize the number of

interacting nucleons in close proximity to the spin polarized atoms. Pb ended up being the material of choice since it is dense, non-magnetic and readily available.

To eliminate spurious signals not related to the source masses, we would like to correlate the co-magnetometer's signal with the change in the spin-mass interaction due to (1.35). This can be accomplished by correlating the co-magnetometer's signal in between reversals of the mass' position since the spin-mass interaction is, according to (1.35), directional with respect to the position of the mass (relative to the spins of the atoms). In principle, this reversal of the mass' position can be accomplished with just one source mass. For example, an apparatus can be constructed to rotate a single mass about the co-magnetometer's cell but this approach can potentially introduce additional systematic effects related to the position of the mass since the mechanical load in the laboratory due to the mass would be markedly different in between each mass position reversal. To alleviate this problem, we chose to use two source masses that are alternately raised and lowered from the ceiling of the laboratory. Attaching the masses to the ceiling reduces its mechanical coupling to the co-magnetometer (on the ground) while the scheme of alternately raising and lowering the masses ensures that the load on the ceiling is identical during the data collection period between each mass position reversal. Although such a scheme eliminates possible systematic effects stemming from the load of the masses on the room, the presence of the second source mass does reduce the (possible) energy shift due to anomalous spin-mass interactions. The distance over which to raise and lower the masses is therefore dictated by how much reduction in energy shift one is willing to tolerate. For an axion mass of 20 cm and the dimensions of our system, our calculations indicate that our final raising/lowering distance of 50 cm will result in less than 5% decrease in energy shift, which was deemed by us to be acceptable.

Since the signal of the continuously pumped K-^{3}He co-magnetometer is a DC signal that is susceptible to drifts, it is desirable to operate at as high of a frequency

as possible. The operating frequency of SMILE is, in theory, limited by how fast the mechanical apparatus is capable of moving the two source masses, and therefore pushing the maximum operating frequency of SMILE higher translates into designing a system capable of moving the masses as quickly as possible. Although we eventually ran SMILE at a slower frequency, the mechanical apparatus was initially designed to move the weights over 50 cm in about 1 s. To do so, we attached the two weights to each other via two Amsteel Blue fiber ropes that each go over a set of nylon pulleys and are coiled around a central aluminum driveshaft that is rotated by a 4 kW Yaskawa SGMG-44A servo motor coupled to a 5:1 Wittenstein Alpha SP 140S-MC1-5-1K1 planetary reduction gear (see Figure 4.9). By attaching the weights to each other, each weight serves as a counter-weight for the other so that the motor does not have to work against gravity in lifting the weights but only has to overcome friction and inertia. To prevent the weights from swinging excessively during motion, each weight stack has 8 delrin rollers that slides up and down a 90° aluminum angle guide rail. The guide rails are suspended from a support structure mounted to the ceiling and is braced at the bottom by cross-bars that connect them to each other without touching the optical table or any other component on it. Additional side braces also help to secure the guide rails to the sides of the room (see Figure 4.8).

We note that since systematic magnetic interactions was another major concern during the design of the source masses, the apparatus was made, as much as possible, out of non-magnetic materials. For example, we used non-magnetic fiber ropes instead of steel cables, nylon pulleys instead of steel pulleys, delrin rollers instead of steel ball bearings and almost all of the support structure was made out of aluminum. In cases where strength or galling was a concern, brass was used. Nevertheless, when strength was of utmost concern, such as when mounting the structure to the ceiling, standard steel fasteners were used. However, we note that these steel fasteners are all located high above the co-magnetometer close to the ceiling, and in any case, their positions

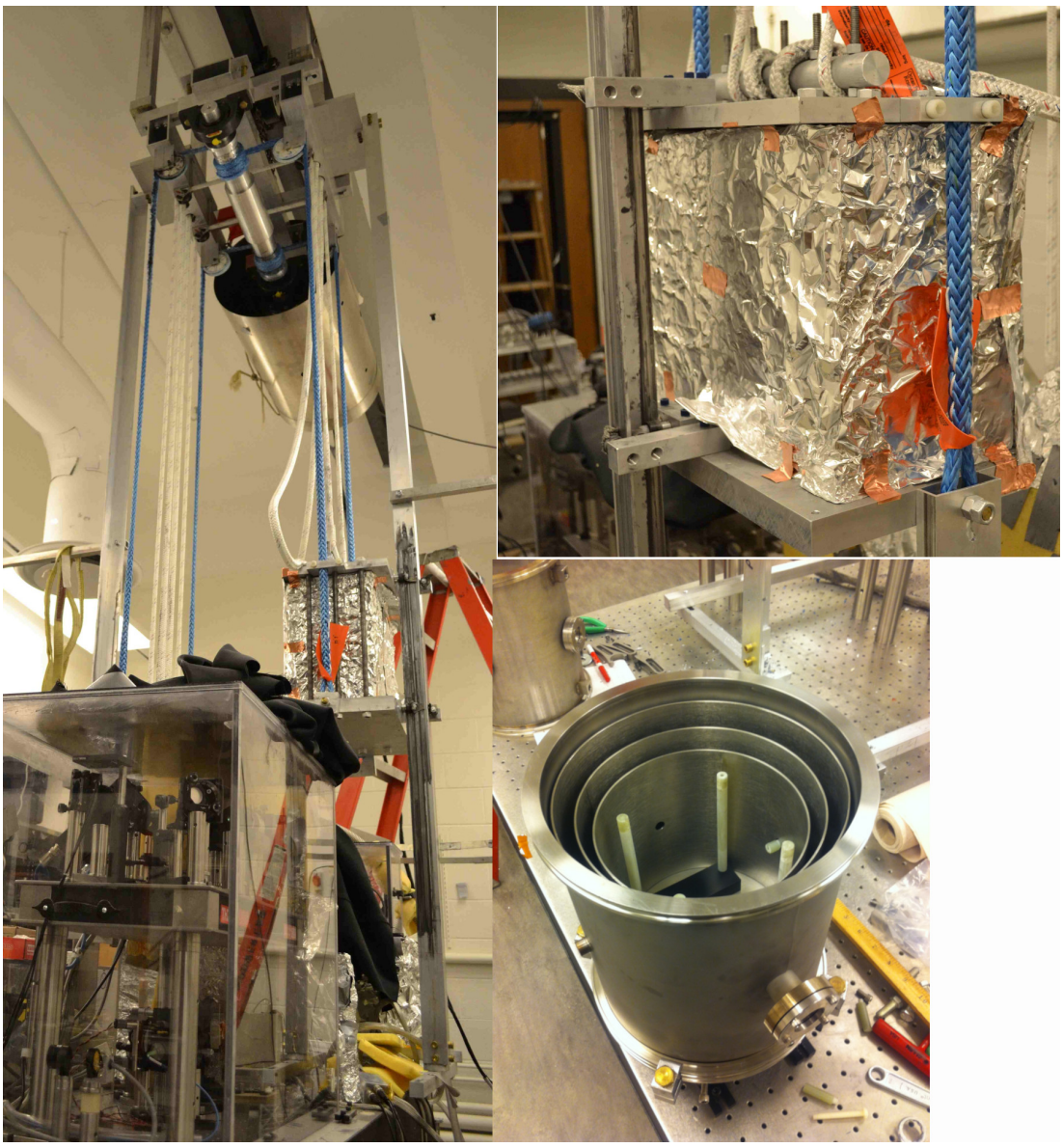

Figure 4.8: Picture of source masses suspended from ceiling (left), one of the weight stacks (top right), and an empty vacuum chamber with its μ-metal shields opened (bottom right).

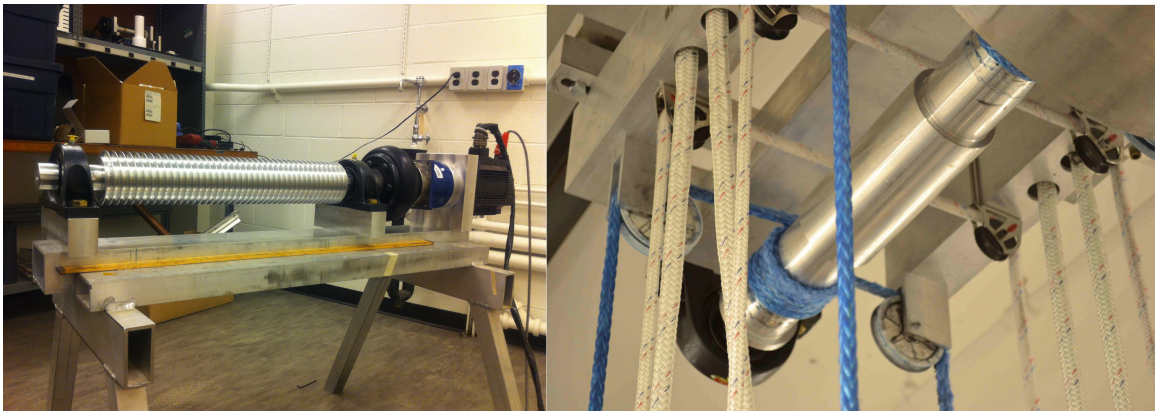

Figure 4.9: Picture of the old driveshaft coupled to the reduction gear/servo motor (left) and the new driveshaft as used in SMILE (right).

do not change under a position reversal of the weights so it is unlikely that they will contribute to a magnetic interaction that is correlated with the position of the weights. Moreover, we also designed the dimensions of the drive shaft to be such that the motor and reduction gear spin an integer number of revolutions[19] in moving the weights from one extremal position to another, which should reduce possible magnetic correlations due to the position of the motor/gear. We note however that the hysteresis of soft magnetic material within the motor/gear means that the **B** field they produce will not be exactly the same after every position reversal even though the motor/gear might indeed have returned to the same position. To counteract this and to further reduce the magnitude of the magnetic fields produced by the motor/gear, we also mounted a μ-metal shield over the motor and gear that is visible in Figure 4.8 (left).

One of the challenges of SMILE was ensuring the reliability of the ropes over long periods of operation. Since a run can easily have thousands of position reversals, the fiber ropes need to be able withstand considerable wear. Unfortunately, we found during initial runs of SMILE that the ropes wore out relatively quickly and we wound up replacing them multiple times during the course of the entire experiment. There were multiple reasons for this. Firstly, the initial driveshaft had grooves that were

[19] 10 for the motor and 2 for the reduction gear.

cut into it to guide the ropes as they wound and un-wound around the shaft since there were concerns initially that the ropes might either slide on top of each other or creep unpredictably up and down the shaft during operation. However, the edges of these grooves were too sharp and were responsible for much of the abrasion we observed in the ropes. Eventually, we replaced the grooved driveshaft with a smooth bore shaft that decreased the rate of wear on the ropes and in the end, it turns out that our initial concerns were unfounded; there was so much friction between the ropes and shaft that the ropes do not creep up and down the shaft but rather trace out predictable positions on the shaft as they repeatedly wind and unwind around it. Figure 4.9 shows both the old and new driveshaft.

Secondly, we initially used off-the-shelf mounted pulleys to lift the weights, which turned out to be problematic because there was insufficient side clearance between the mount and ropes that lead to the sides of the mount abrading the ropes. We note that under normal circumstances when the rope leaves the pulley in the plane of the pulley, the side clearances would have been sufficient. However, since the rope does not slide on top of itself but is rather winding/un-winding over fixed positions on the shaft, it is clear that the angle at which it leaves the pulley must change and consequently, there are times when the side clearances become insufficient and the rope abrades against the side of the mount. Furthermore, the initial pulleys we obtained were too small and contributed to bending wear of the ropes, since as the rope is bent, the outer fibers are stretched more and accordingly, more load is placed on them, which contributes to their premature wear. To correct for these problems, we eventually used stand alone larger nylon pulleys and machined our own pulley mounts to have sufficient clearance for the ropes throughout their entire range of motion[20]. These pulleys rotate around flanged and regular ball bearings (available

[20]Figure 4.9 (right) shows both the old and new pulleys. Notice that the Amsteel Blue ropes are attached to the larger, white nylon pulleys with a custom pulley mount whereas two of the thinner nylon ropes are attached to the older off-the-shelf pulley mounts. As discussed in section 4.1.8, these two nylon ropes serve as backup ropes to ensure that the weights are always connected to each other.

from McMaster-Carr) that are supported by a shoulder screw that also acts as the axis of rotation. To keep the flanged ball bearings from hitting the sides of the mount, thin shim metal washers are used to delicately fill the space in between the flange and the sides of the mount. Although this works relatively well, we note that this is somewhat unsatisfactory since the ball bearings do grind against the shim metal and will eventually wear them out. We note that McMaster-Carr now sells flanged ball bearings with extended inner rings that could eliminate this problem if an additional mechanism is provided for the mount to securely hold onto the extended inner ring. One possibility would be to tap one side of the mount and have a through-hole on the other side so that a screw can be used to slightly decrease the gap between the sides of the mount and thereby grip onto the extended inner ring securely.

4.1.8 Safety features and interlocks

It is evident that bad things can happen when 250 kg stacks of Pb bricks are constantly moving up and down a narrow space with plenty of sensitive equipment nearby but no human to supervise the automated dance. Besides concerns about systematic effects stemming from mechanical and magnetic couplings, safety was also an important early consideration during the design phase of the source masses. In particular, there was a very real danger of the Amsteel Blue ropes suddenly failing during motion, which will, barring any other intervention, result in the weights catastrophically crashing into the optical table below them. This concern has proven to be especially prescience since a severely abraded Amsteel Blue rope did partially fail during operation once but thankfully no one was hurt and nothing else was damaged.

Key to stopping the weights from crashing into the optical table below is to prevent them from free-falling. As mentioned in section 4.1.7, two Amsteel Blue fiber ropes attach both weights to each other so that they serve as counter-weights to each other. In the event that these ropes break however, it is important that the weights

are still connected to each other so that neither of them free-fall down towards the optical table. Consequently, as part of the safety design, there are two additional nylon ropes that attach the two weights together without coiling around the main driveshaft. During operation, the attachment point for these ropes are adjusted so that they are only under slight tension, which allows them to quickly provide the necessary tension to keep the two weights attached together should the Amsteel Blue ropes fail. We note that since these nylon ropes do not coil around the driveshaft and are under minimal tension during regular operation, they do not get abraded like the Amsteel Blue ropes. With a counter-weight attached, the weights do not accelerate down towards the optical table but if they were in motion before the Amsteel Blue ropes snapped, they would still have to be stopped. To stop the weights, two high stretch nylon ropes attached from the support structure above catch the weights if they fall below their usual limits. Since the ropes are fairly elastic, the weights are gradually slowed down and do not impart a huge impulse to the ropes or structure. These ropes have been sized to stop the weights in about 6". Figure 4.9 (right) shows these four additional safety ropes; the inner two are the thicker ones responsible for stopping the weights and the outer two that go over the pulleys are responsible for keeping the weights connected to each other.

Besides these physical safeguards, we employed additional monitoring to stop and abort all motor operation in the event of an impact of the weights with the optical table or vacuum chamber. To achieve this, we modified a wireless home alarm system to deactivate the motor upon receiving an "alarm" from one of its sensors that we have deployed on the optical table and vacuum chamber. The home alarm sensors are essentially vibration sensors that transmit an "alarm" signal to a receiver if they detect excessive vibration. Upon receipt of the alarm signal from a sensor, the system receiver opens[21] a normally closed switch (schematically depicted as S1

[21] We have schematically represented this as a traditional reed relay with the coil in Figure 4.10 producing the necessary magnetic field but we note that in reality, these relays are solid-state relays.

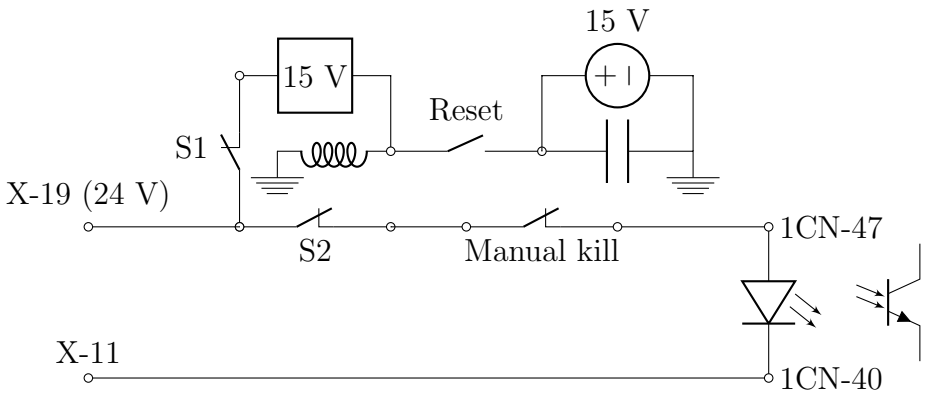

Figure 4.10: Diagram of motor's safety interlock circuit.

and S2 in Figure 4.10), which if opened, deactivates the motor *and* the receiver so that additional alarm signals will not change the state of the switch. This last step is unfortunately necessary because the alarm system receiver's circuitry is such that one cannot make the switch latch. Technically, the receiver only toggles the switch from one state to another upon receipt of a alarm signal from the sensor. Since we want to permanently (until a human figures out what is going on) deactivate the motor after an impact, this is undesirable for us. Consequently, we modified the circuit to latch by making the receiver also kill its own power (from a 15 V regulator powered from X-19 in Figure 4.10) upon receipt of an alarm signal. To reset the receiver, we have also added a "Reset" switch that is normally open but may be closed to restart the receiver after it trips. Upon restarting, the receiver closes the switches S1 and S2, after which the reset switch should be re-opened to ensure that the interlock works as intended.

We note that the safety interlock circuit in Figure 4.10 essentially works by disrupting the same circuit that the SMC-2000-1 controller does when it receives a text command, from the motor computer via an optically coupled DB-9 connection, to deactivate the motor. Essentially, for the amplifier to be activated, a photo-transistor (schematically represented by the LED/photo-transistor combination in Figure 4.10) in between the amplifier's 1CN-47/1CN-40 terminals has to be turned on. This is

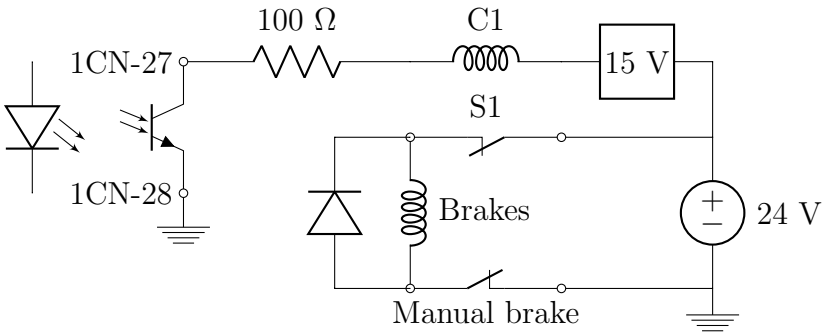

Figure 4.11: Diagram of motor's brake interlock circuit.

typically accomplished by connecting the X-19/X-11 terminals of the SMC-2000-1 to the 1CN-47/1CN-40 terminals on the amplifier respectively so that the amplifier may be turned on/off when the SMC-2000-1 sets X11 to 0 V (on) or 24 V (off). By disrupting the otherwise constant 24V supply from the X-19 terminal of the SMC-2000-1 controller, the safety interlock circuit is able to deactivate the amplifier using the same circuit as the SMC-2000-1 controller.

If the motor is deactivated while it is moving, it applies an emergency brake to the spinning rotor by deliberately shorting its coils, but what happens next depends on how the amplifier was programmed. In our case, we have programmed the amplifier to turn off a photo-transistor between its 1CN-27/1CN-28 terminals (schematically depicted as the LED/photo-transistor in Figure 4.11) once the motor has slowed down sufficiently, which we then use as part of a separate brake interlock circuit to engage the mechanical brakes of the motor. If the motor is deactivated while stationary, it does not apply an emergency brake but turns off the aforementioned photo-transistor before deactivating. Figure 4.11 shows a schematic of the brake interlock circuit. We note that when the photo-transistor is off, the coil C1 is de-energized and switch S1 opens, which de-energizes the brake coils and cause the mechanical brake to engage. As in the case of the safety interlock, there is also a manual switch that allows us to manually de-energize the brake coils and engage the brakes.

4.2 Co-magnetometer Characterization

In order to optimize the performance of the co-magnetometer, it is frequently necessary to characterize its properties. For example, the sensitivity of the co-magnetometer is dependent on both its alkali polarization and relaxation rates. Measurements of these numbers enable us to quantify how ideally the co-magnetometer is performing and can frequently suggest areas of improvement. In this section, we present techniques and measurements used to characterize the co-magnetometer.

4.2.1 Density measurement

The density of alkali atoms in the vapor cell is a quantity that is frequently needed in the calculation of many other parameters such as the spin polarization of the atoms and various other rates that appear in the Bloch equations. Its value may be estimated through empirical formulae such as (2.1) and (2.2) that relate the temperature of the vapor to the alkali density but since we only measure the temperature of the oven, the empirical formulae are only valid to the extent that the oven and cell are in thermal equilibrium. Besides, there is an inherent uncertainty about the accuracy of the empirical formulae and it is therefore frequently desirable to measure the density of the alkali vapor independently. In the sections below, I outline a few methods that has proven useful in the experimental measurement of the alkali density.

Optical absorption of linearly polarized light

As discussed in section 2.6.6, linearly polarized light with intensity $I(z)$ traveling through an alkali vapor is attenuated as

$$\frac{dI}{dz} = -n\sigma I, \tag{4.11}$$

where n is the number density of alkali atoms and σ is the absorption cross-section given by

$$\sigma = r_e f_{osc} c \frac{\Gamma_{tot}}{(\nu - \nu_0)^2 + (\Gamma_{tot})^2}, \tag{4.12}$$

where r_e here is the classical electron radius, f_{osc} is the oscillator strength, and ν, ν_0 and Γ_{tot} are the laser frequency, transition frequency and transition HWHM in non-angular units respectively. From (4.11), the intensity of a linearly polarized probe beam traveling through the vapor is

$$I(\nu, z) = I_0 \, e^{-n\sigma(\nu)z}, \tag{4.13}$$

where I_0 is the incident intensity of the beam. For an on-resonant beam with $\nu = \nu_0$, the equation above may be re-written as

$$n = -\frac{\Gamma_{tot}}{c r_e f_{osc} L} \log\left[\frac{I(\nu_0, L)}{I_0}\right], \tag{4.14}$$

thus allowing for a determination of the number density n given the length L of the vapor cell, the incident intensity I_0, and the transmitted on-resonant intensity $I(\nu_0, L)$. In practice, since $\sigma(\nu)$ is strongly peaked around the transition frequency ν_0, the incident intensity may be approximated as the transmitted intensity of a sufficiently detuned beam $I_0 \approx I(\nu_{off}, L)$ so that

$$n \approx -\frac{\Gamma_{tot}}{c r_e f_{osc} L} \log\left[\frac{I(\nu_0, L)}{I(\nu_{off}, L)}\right]. \tag{4.15}$$

Using the transmitted intensity of an off-resonant beam $I(\nu_{off}, L)$ is convenient since in reality, the on-resonance transmitted intensity $I(\nu_0, L)$ is also attenuated by scattering off optical components that is then canceled by dividing it with $I(\nu_{off}, L)$. We also note that since there is some variation of transmitted laser power as a function

of laser frequency[22], to obtain a clean absorption spectrum it is best to normalize the actual absorption spectrum with the measured transmitted intensity in the absence of any alkali atoms (i.e. when the cell is cold).

Experimentally, we only measure $I(\nu, L)$ so to obtain Γ_{tot} we need to fit (4.12) to $\log I(\omega, L)$, which from (4.13), is proportional to $\sigma(\omega)$. Figure 4.12 is a typical absorption spectrum from a high pressure co-magnetometer cell.

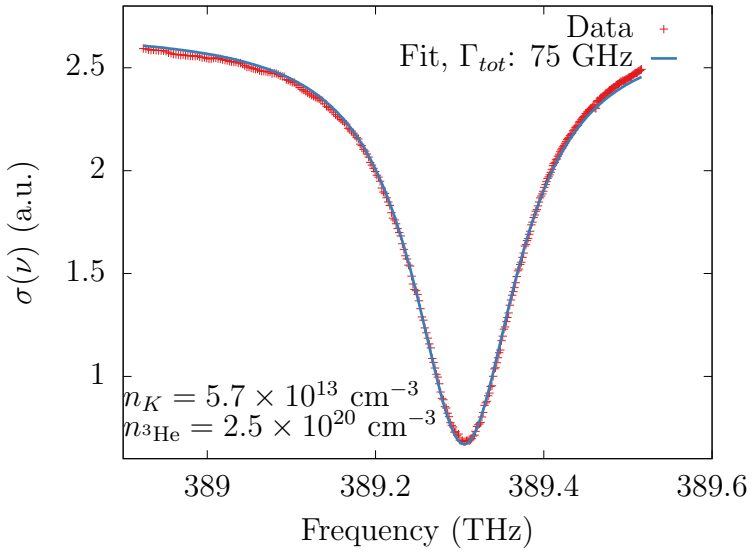

Figure 4.12: Typical absorption spectrum of a high pressure co-magnetometer cell. This was measured at an oven temperature of 184.6 °C.

Measuring Γ_{tot} not only gives us information about the alkali number density but it also tells us the number density of the noble gas species since Γ_{tot} in a high pressure co-magnetometer cell is dominated by pressure broadening from the noble gas. The pressure broadening rates of various noble gas species on alkali atoms have been experimentally measured and they allow us to extract the noble gas number density from the absorption spectrum of the alkali vapor.

As measured in [204], the FWHM $\Delta\nu$ of K and Rb's absorption spectrum broadens as a function of temperature T (in Kelvins) and number density n (in amagats) of

[22]This is due to at least two reasons. Firstly, the laser frequency of laser diodes is tuned by tuning their temperatures and there is variation of laser power with temperature. Secondly, there can be interferences due to some optical components that will be dependent on the laser frequency.

^{3}He as:

$$\Delta\nu = \alpha n \left(\frac{T}{353\ \mathrm{K}}\right)^{\epsilon} + \beta, \tag{4.16}$$

where α, ϵ and β are as given in Table 4.1 below. Using these numbers, we may calculate the number density of ^{3}He in a K-^{3}He co-magnetometer cell from an absorption spectrum of K, as was done in Figure 4.12.

Species	α (GHz/amg)	ϵ	β (GHz)	Reference
Rb $\mathcal{D}_1$	18.31 ± 0.07	0.26 ± 0.04	-0.19 ± 0.13	[204]
Rb $\mathcal{D}_2$	20.51 ± 0.08	0.39 ± 0.04	-0.35 ± 0.15	[204]
K $\mathcal{D}_1$	14.26 ± 0.09	0.44 ± 0.06	0.04 ± 0.11	[204]
K $\mathcal{D}_2$	19.59 ± 0.10	0.39 ± 0.05	0.11 ± 0.13	[204]

Table 4.1: Pressure broadening rates with ^{3}He for K and Rb.

4.2.2 Relaxation measurements

One of the crucial, fundamental quantities that determine the sensitivity of the co-magnetometer is the relaxation rate of the alkali atoms since the overall sensitivity of the co-magnetometer scales as P_z^e/R_{tot}^e, where $R_{tot}^e = R_{sd}^e + R_{se}^{en} + R_p + R_m$ is the sum of the spin-destruction, spin-exchange and pumping rates from both the pump (R_p) and probe (R_m) lasers[23]. The spin-destruction rate is itself a sum of the relaxation rates due to alkali-buffer gas spin-rotation collisions as well as alkali-alkali spin-axis collisions. In the absence of any transverse fields, the longitudinal alkali polarization from (3.22) evolves approximately as

$$\frac{dP_z^e}{dt} = \frac{1}{Q(P_0^e)}\left[R_p s_z^p + R_m s_z^m + R_{se}^{en} P_z^n - \left(R_p + R_m + R_{se}^{en} + R_{sd}^e\right) P_z^e\right]. \tag{4.17}$$

[23] In the context of the hybrid pumped co-magnetometer, these rates should all be viewed as the effective rates (see chapter 3).

At low (or zero) noble-gas polarization, which is easily accomplished experimentally by decreasing the pumping light intensity so that there is hardly any noble-gas polarization build up, the alkali atoms decay in the dark as

$$\frac{dP_z^e}{dt} = -\frac{1}{Q(P_0^e)}\left(R_m + R_{se}^{en} + R_{sd}^e\right) P_z^e. \tag{4.18}$$

Since the slowing down factor $Q(P_0^e)$ is not a constant, the solution to the equation above is, strictly speaking, not a simple exponential (see section 2.7.4 and 2.10). Nevertheless, at low alkali polarization, which may once again be accomplished by using weak pumping light or considering only the tail end of the decay, we may take the low polarization limit of $Q(P_0^e)$ and assume it is a constant. In that case, the decay of the alkali longitudinal polarization is simply

$$P_z^e(t) \approx P_0 e^{-\left(R_m + R_{se}^{en} + R_{sd}^e\right)t/Q} = P_0 e^{-t/T_1}, \tag{4.19}$$

so that measuring the time constant T_1 of the alkali longitudinal decay is a measure of the relaxation rates $R_{cm}^e = R_m + R_{se}^{en} + R_{sd}^e$. Experimentally, we measure the optical rotation of the linearly polarized off-resonant probe beam, which is only sensitive to P_x^e. Consequently, in order to see a decay, we need to tilt the longitudinal $\mathbf{B}$ field in the x-z plane by applying a sufficiently large B_x field. Also, since R_m must of necessity be non-zero during the measurements, we note that obtaining the collisional relaxation rates $R_{co}^e = R_{se}^{en} + R_{sd}^e$ from T_1 measurements require performing a few measurements at successively lower probe intensities so that the results can be extrapolated to zero probe intensity. Once R_{co}^e has been determined, R_m, the relaxation rate due to the probe beam at its operating intensity, may be determined by repeating the measurement with the probe beam at its operating intensity and taking the difference between the new relaxation rate $R_{cm}^e = R_m + R_{co}^e$ and R_{co}^e.

At low pumping intensity so that $Q(P_0^e)$ may be approximated with its low polarization limit during steady state, we may also measure R_p by measuring the pump-up time constant of the longitudinal alkali polarization. Since R_p is proportional to the pump power, we may express R_p (and by extension the other rates) as a function of the pump power by measuring R_p in the manner described above at given pump powers.

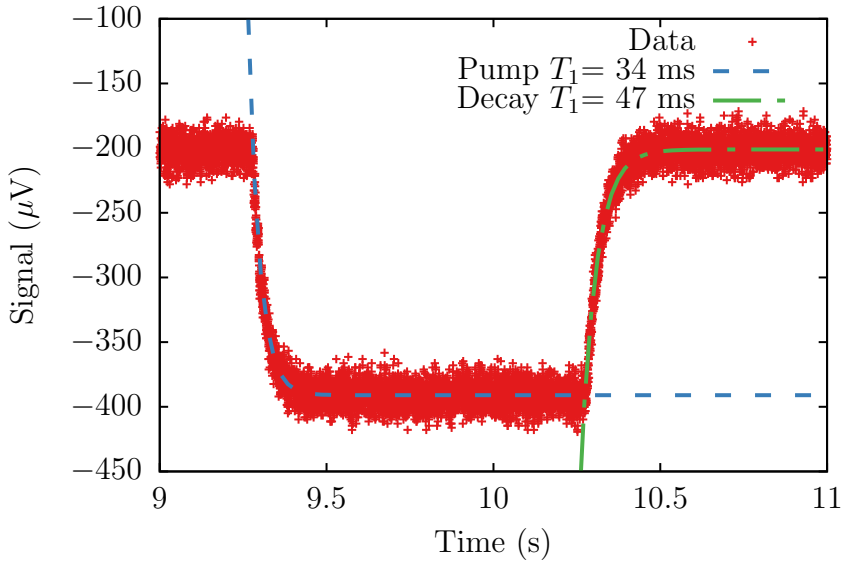

Figure 4.13: K T_1 measurement.

Figure 4.13 shows a measurement of the pump and decay time constants of the alkali atoms in the limit of low pump and probe intensities, which is evident in the relatively poor signal-to-noise ratio and the relatively small change in signal level when the pump is on/off. The blue dashed and green dash-dot lines are respectively fits to the signal when the pump beam is on and off. We note that in this case, the signal becomes more negative[24] when the pump beam is on. Experimentally, this is measured by tilting the longitudinal **B** field and modulating the pump laser amplifier

[24]This is arbitrary and depends on the projection of the **B** field and the x-axis.

with an appropriately smoothed[25] square wave while measuring the optical rotation of the probe beam.

4.2.3 Polarization measurement

For $Q_r = Q_d$, the hybrid continuously pumped co-magnetometer ideally achieves maximum sensitivity at an alkali polarization of 50% (see section 3.2) while the pulsed co-magnetometer[26] benefits from fully polarizing the alkali atoms with each laser pulse. Alkali polarization measurements are therefore important diagnostic tools. Here, we describe two common methods for measuring the alkali polarization in a continuously pumped co-magnetometer.

Optical rotation of linearly polarized light

A linearly polarized, off-resonant probe beam undergoes Faraday rotation when transversing through a vapor of polarized alkali atoms. From section 2.6.4, the magnitude of this rotation for a linearly polarized off-resonant probe beam traveling along the x-axis through a cell of length L is

$$\theta_{FR} = \frac{1}{2} n r_e c P_x^e L \left(f_{\mathcal{D}_1} \frac{\nu - \nu_{\mathcal{D}_1}}{\left(\nu - \nu_{\mathcal{D}_1}\right)^2 + \left(\Gamma_{tot}^{\mathcal{D}_1}\right)^2} - \frac{1}{2} f_{\mathcal{D}_2} \frac{\nu - \nu_{\mathcal{D}_2}}{\left(\nu - \nu_{\mathcal{D}_2}\right)^2 + \left(\Gamma_{tot}^{\mathcal{D}_2}\right)^2} \right), \quad (4.20)$$

where n is the number density of alkali atoms, r_e is the classical electron radius, c is the speed of light, P_x^e is the x-component of the alkali polarization, ν is the laser frequency and $\Gamma_{tot}^{\mathcal{D}_{1,2}}$ is the transition's HWHM in non-angular units. $f_{\mathcal{D}_1}$ and $f_{\mathcal{D}_2}$ are the oscillator strengths for the $\mathcal{D}_1$ and $\mathcal{D}_2$ transitions while $\nu_{\mathcal{D}_1}$ and $\nu_{\mathcal{D}_2}$ are the transition frequencies (in non-angular units) of those transitions. Experimentally,

[25] It needs to be sufficiently smooth for the PID loop on the laser controller to follow. An appropriately chosen RC filter is usually sufficient to do the job. Alternatively, if there is an AOM along the path of the pump beam, it can also be used to (more cleanly) modulate the pump beam intensity.

[26] To be described in chapter 5.

the alkali atoms are nominally polarized in the z direction and $P_x^e = 0$. To obtain a projection of $\mathbf{P}^e$ in the x-direction, we apply a sufficiently large $\mathbf{B}$ field in the x-z plane since for a sufficiently large $\mathbf{B}$ field, the spins of the alkali atoms are parallel to the field. In that case, $P_x^e = P^e \sin(\phi)$, where ϕ is the angle such that $\tan(\phi) = B_x/B_z$. Equation (4.20) may then be re-written as

$$P^e = \frac{2\theta_{FR}}{nr_e cL} \frac{\sqrt{B_x^2 + B_z^2}}{B_x} \frac{1}{f_{\mathcal{D}_1} D\left(\mathcal{D}_1\right) - \frac{1}{2} f_{\mathcal{D}_2} D\left(\mathcal{D}_2\right)}, \tag{4.21}$$

where we have, for convenience, made the definition

$$D(j) \equiv \frac{\nu - \nu_j}{\left(\nu - \nu_j\right)^2 + \left(\Gamma_{tot}^j\right)^2} \quad , \quad j = \mathcal{D}_1, \mathcal{D}_2. \tag{4.22}$$

The condition that the $\mathbf{B}$ field is sufficiently large may be verified by performing the polarization measurements at different values of ϕ and checking that the measured polarization is indeed the same. To use (4.20), we require a measurement of the Faraday rotation angle θ_{FR} in angular units. Since we typically measure that angle as a voltage output from the lock-in, using (4.20) also requires us to perform an optical calibration relating the voltage measured from the lock-in and actual amount of optical rotation of the light. Such an optical calibration may be easily performed by measuring the change in voltage from the lock-in's output as we change the angular orientation of the final polarizer in the probe setup. We note that this calibration depends both on the gain of the electronic detection circuit as well as the intensity of the probe beam.

The alkali polarization measured by this method is an ensemble average across the atoms in the path of the probe beam. This can be different from the average polarization across the entire volume of the cell. In the next sub-section, we present another measurement technique that allows one to measure the average alkali polarization over the cell.

Frequency shift of noble gas

At the compensation point, the dynamics of the alkali and noble gas spins are highly coupled and damped. However, far away from the compensation point, the spins of the alkali and noble gas atoms are decoupled and we can think of them as independent of each other (see section 3.4). Nevertheless, spin-exchange collisions between alkali and noble gas atoms will continue to cause the noble gas atoms to experience an effective, enhanced magnetic field

$$\mathbf{B}^e = \lambda M_e \mathbf{P}^e, \tag{4.23}$$

where λ and M_e are as defined from (2.87) and (2.355) respectively

$$\lambda = \frac{8\pi}{3}\kappa_0 \text{ (c.g.s)} = \frac{2}{3}\kappa_0 \text{ (S.I.)} \tag{4.24}$$

$$M_e = n_a \mu_B \text{ (c.g.s)} = n_a \mu_0 \mu_B \text{ (S.I)}, \tag{4.25}$$

with $\mathbf{P}_e$ as the alkali polarization so that λ is the geometric factor to obtain the magnetic field from a uniformly magnetized sphere with magnetization M_e due to fully polarized alkali atoms that is enhanced by the factor κ_0 which is given at the end of section 2.3.2. At sufficiently large $\mathbf{B}$ field (away from the compensation point) so that the noble gas spins are effectively decoupled from the alkali atoms, applying a tipping pulse will cause the noble gas spins to precess in the sum of the (ordinary) B_z and effective B_z^e fields at the (non-angular) rate

$$f = \frac{\gamma_n}{2\pi}\left(B_z + B_z^e\right). \tag{4.26}$$

The sign of P_z^e may be easily reversed by changing the polarity of the circularly polarized pumping light, which is experimentally accomplished by simply rotating a quarter-wave plate by 90°. The frequency shift of the noble gas precession due to

different polarities of the circularly polarized pumping light is therefore

$$\Delta f = \frac{\gamma_n}{2\pi} 2B_z^e = \frac{\gamma_n}{\pi} \lambda M^e P_z^e, \tag{4.27}$$

which may be re-written to give P_z^e as

$$\begin{aligned} P^e = \frac{\Delta f \pi}{\gamma_n \lambda M^e} &= \frac{3\pi \Delta f}{2\gamma_n \kappa_0 n_a \mu_0 \mu_B} \text{ (S.I)} \\ &= \frac{3\Delta f}{8\gamma_n \kappa_0 n_a \mu_B} \text{ (c.g.s).} \end{aligned} \tag{4.28}$$

We note that P^e as measured in this way is a measure of the volume averaged alkali polarization in the cell as opposed to a line-averaged polarization along the path of the probe beam when using the optical rotation method described in the previous section. Ideally, in a uniformly polarized cell, both methods should give the same result; conversely, discrepancy between the two methods is a measure of the polarization non-uniformity within the cell.

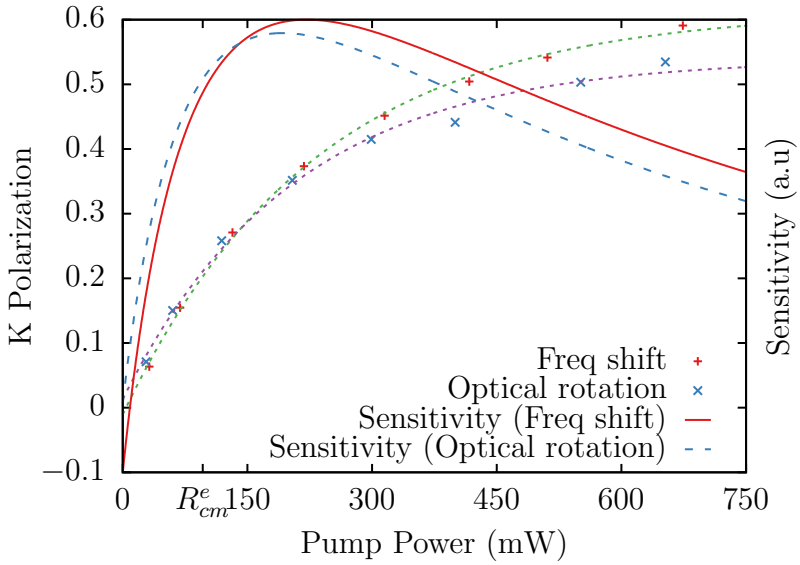

Figure 4.14: K polarization measurements as a function of pump power.

Figure 4.14 shows the measured K polarization (on the left axis) as a function of pumping power in a cell that is ~ 10 mm in diameter using the two methods described

above. Red '+' points denote measurements using the frequency shift method whereas blue 'x' points correspond to measurements using the optical rotation method. Green and purple dotted lines are exponential fits to the data points. By separately measuring the decay and pump-up time of the alkali atoms at a given pump power[27], we can measure R^e_{cm}, the rate of relaxation due to collisions and the probe beam, and set it at the appropriate place on the pump power axis. Since the sensitivity of the co-magnetometer is proportional to $P^e/(R_p + R^e_{cm})$, we may also plot (on the right axis) the sensitivity of the co-magnetometer as a function of pump power. The red solid line depicts the sensitivity of the co-magnetometer using polarization measurements from the frequency shift method while the blue dashed line shows the same but with polarization measurements from the optical rotation method.

In an ideal co-magnetometer, optimum sensitivity is achieved at $R_p = R^e_{cm}$ and at that pumping rate, $P^e_z = 0.5$ since the steady state longitudinal polarization is

$$P^e_z = \frac{R_p}{R_p + R^e_{cm}}. \tag{4.29}$$

However, to the extent that diffusion to the walls is significant and requires an additional term in the denominator of (4.29)[28], this relation will not hold. We note that in Figure 4.14 above, the optimum sensitivity occurs at an alkali polarization between 30 to 40%, indicating that loss of polarization due to alkali diffusion to the wall is not insignificant. As a result of this measurements, a new batch of larger cells (whose size were limited by the holes in the magnetic shields) were made to decrease the effects of diffusion.

[27] This will be further elaborated in a later section.

[28] We note that experimentally, R^e_{cm}, which is determined by the decay time of the alkali, does not include relaxation of the alkali atoms due to diffusion.

4.2.4 Magnetic suppression measurement

One of the attractive features of the co-magnetometer is that it possesses suppressed response to ordinary magnetic fields while retaining sensitivity to anomalous fields at the compensation point. We may experimentally measure the amount of "inherent" suppression by deliberately modulating the **B** field inside the innermost ferrite shield and measuring the normalized response of the co-magnetometer signal as a function of the frequency of the **B** field modulation. In general, the co-magnetometer's response to a sinusoidal modulation of a **B** field consists of both an in-phase amplitude X and an out-of-phase amplitude Y. Here we define the normalized magnetic field response as the ratio of the total calibrated (in magnetic field units) co-magnetometer response ($R = \sqrt{X^2 + Y^2}$) to the amplitude of the **B** field modulation. A normalized magnetic field response smaller than 1 will therefore imply that the co-magnetometer is suppressing changes to the **B** field.

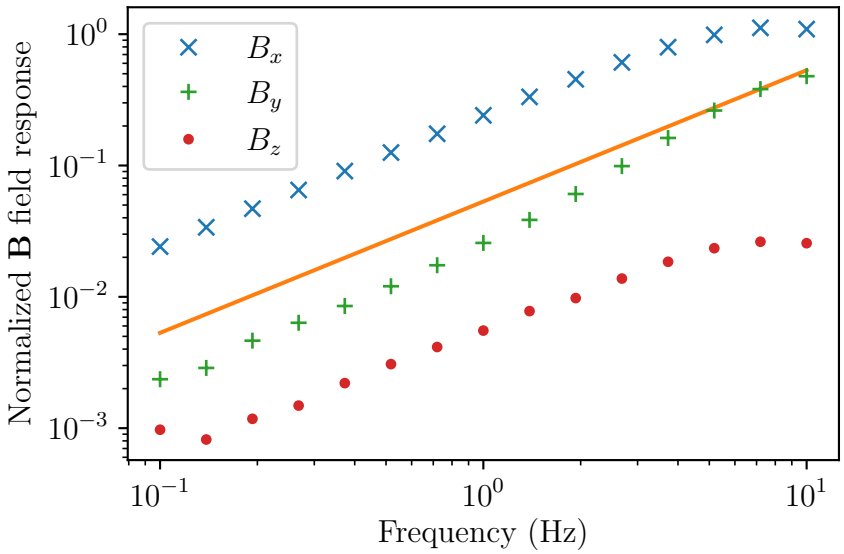

Figure 4.15: Measured co-magnetometer **B** field suppression.

Figure 4.15 shows the result of such a measurement for a ^{3}He compensation field of 5.8 mGs. The orange solid line is the theoretical response for a modulation in B_x if only the first-order contribution ($\omega/\gamma_n B_n$) to the co-magnetometer's response

is included. We note that as expected, the magnetic field suppression increases at lower frequencies but that the actual B_x response is larger than the first order limit since there are, in reality, higher-order contributions to the co-magnetometer's response. Indeed, if there was insignificant contributions from higher order terms, the co-magnetometer's response should be purely out-of-phase with the B_x modulation but experimentally, it was observed that there is a non-zero in-phase component to the co-magnetometer's response, indicating that higher-order contributions are not insignificant. We also note that in theory, the co-magnetometer should not exhibit any sensitivity to small changes in B_z since that is nominally orthogonal to the probe beam. The fact that the co-magnetometer does retain sensitivity to B_z is an indication of misalignment between the field coils and laser beams.

The measurement above measures the "inherent" magnetic field suppression of the co-magnetometer and does not take into account the suppression provided by multiple layers of external magnetic shields surrounding the co-magnetometer vapor cell. In this experiment, the co-magnetometer vapor cell is surrounded by a high resistivity ferrite shield, followed by three more layers of μ metal shields that together provide a simulated suppression of 1.3×10^8 and 3.6×10^7 in the radial and axial directions respectively. The total suppression of external magnetic fields may be measured by using a large coil around the apparatus to apply a known amount of magnetic field and measuring the corresponding co-magnetometer response.

Figure 4.16 shows an example of such a measurement. In this case, a large coil was placed around the apparatus to produce a magnetic field in the x direction, which as Figure 4.15 shows, has the worst amount of inherent suppression. Since the total magnetic suppression is expected to be extremely large ($\sim 10^8$) and the co-magnetometer's response is conversely extremely small, we periodically turn on/off the B_x magnetic field and then search for a correlation in the co-magnetometer signal after many periods. The data analysis used to extract out the signal's correlation

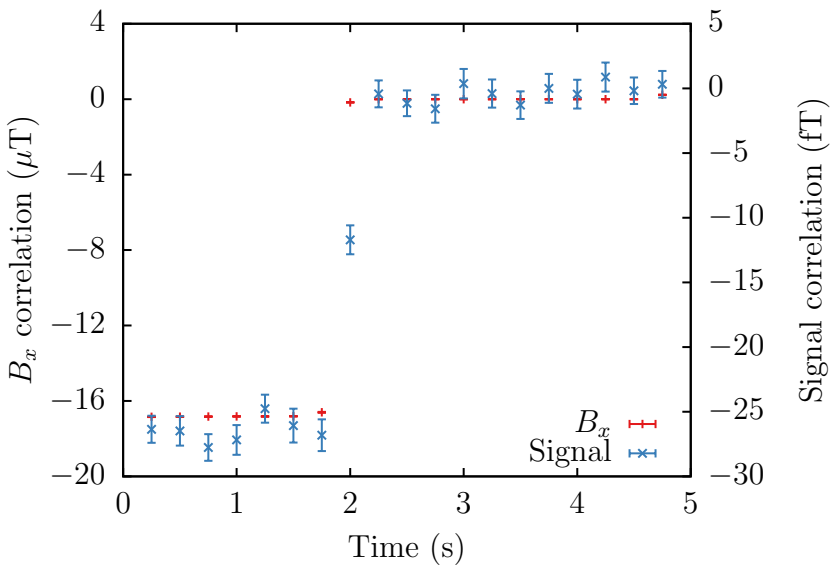

Figure 4.16: Measured total B_x suppression.

is exactly the same as in the actual experiment and is described in greater detail in section 4.4. In Figure 4.16 the applied magnetic field is simultaneously measured by a fluxgate and is subjected to the same data analysis for comparison with the signal's correlation in order to extract the total suppression of the experiment to external B_x fields. We note that the B_x correlation plotted on the left axis of Figure 4.16 is in units of μT while the signal's correlation plotted on the right axis is in units of fT. Computing the ratio of the measured B_x to signal's correlation during the first two second while the B_x field is on gives us a total measured suppression of 6.3×10^8 for external B_x fields. Total suppression in the other two components are expected to be even higher.

4.2.5 Mean photon spin

The mean photon spin $\mathbf{s}$ is a quantity that affects how well the incoming light is able to pump the atoms and it also determines the magnitude of the vector light-shift on the atoms. Its value may be experimentally measured by measuring the modulation of transmitted intensity through a polarizer as the polarizer is rotated 180°. Indeed,

we note that the electric field of a plane wave may be written as

$$\mathbf{E} = \mathbb{R}\mathrm{e}\left[\hat{\mathbf{e}} E_0 e^{-i\omega t}\right], \tag{4.30}$$

where the complex polarization vector $\hat{\mathbf{e}}$ is

$$\hat{\mathbf{e}} = \cos(\phi)\hat{\mathbf{x}} + i\,\sin(\phi)\hat{\mathbf{y}}, \tag{4.31}$$

so that the transmitted $\mathbf{E}$ field through a polarizer with polarization axis $\boldsymbol{\eta} = \cos(\theta)\hat{\mathbf{x}} + \sin(\theta)\hat{\mathbf{y}}$ is

$$E_t = \boldsymbol{\eta} \cdot \mathbf{E} = \cos(\theta)\cos(\phi)\cos(\omega t) + \sin(\theta)\sin(\phi)\sin(\omega t), \tag{4.32}$$

and the transmitted (time-averaged) intensity is therefore proportional to

$$\left\langle E_t^2 \right\rangle = \frac{1}{2}\left(\cos^2(\theta)\cos^2(\phi) + \sin^2(\theta)\sin^2(\phi)\right). \tag{4.33}$$

Since θ describes the polarization axis of the polarizer, we may without loss of generality restrict it to the range $\theta \in [0, \pi)$. It is then easy to show that (4.33) has two stationary points at $\theta = 0$ and $\theta = \pi/2$. Differentiating (4.33) twice at these points yield

$$\left.\frac{d^2\left\langle E_t^2\right\rangle}{d\,\theta^2}\right|_{\theta=0} = -\cos(2\phi) \tag{4.34}$$

$$\left.\frac{d^2\left\langle E_t^2\right\rangle}{d\,\theta^2}\right|_{\theta=\frac{\pi}{2}} = \cos(2\phi), \tag{4.35}$$

so that if $\theta = 0$ is a maxima, then $\theta = \pi/2$ is a minima or vice versa. We may define the modulation depth m as

$$m \equiv \frac{\max(I_t) - \min(I_t)}{\max(I_t)}, \tag{4.36}$$

where I_t is the transmitted intensity and $\max(I_t), \min(I_t)$ are the maximum/minimum transmitted intensity as the polarizer is rotated 180°. Without loss of generality, we may assume that $\cos(2\phi) > 0$[29], so that $\theta = 0$ is a local maximum. In that case, the modulation depth m becomes

$$m = \frac{\frac{1}{2}\left(\cos^2\phi - \sin^2\phi\right)}{\frac{1}{2}\cos^2\phi} = 1 - \tan^2\phi, \tag{4.37}$$

but since from (A.16) $\mathbf{s} \equiv \mathbf{e}^* \times \mathbf{e}/i = \sin(2\phi)\hat{\mathbf{z}}$, we have

$$s = 2\frac{\sqrt{1-m}}{2-m}. \tag{4.38}$$

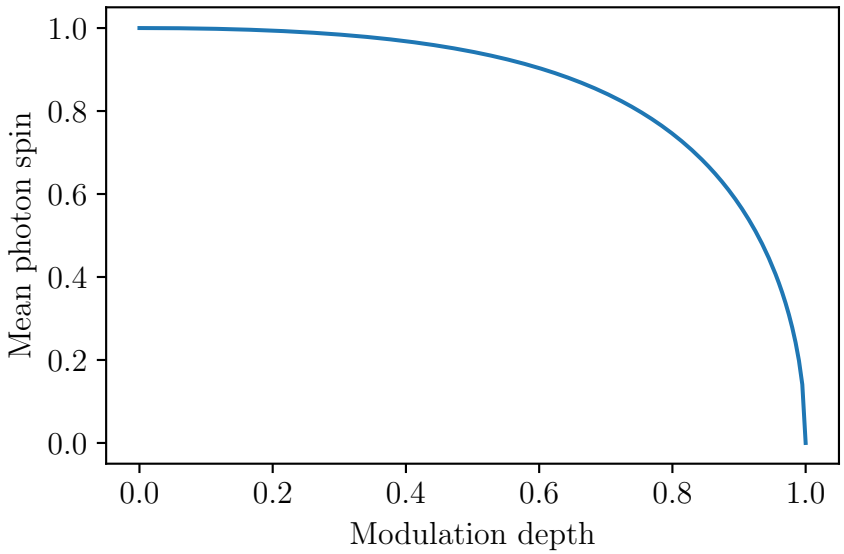

Figure 4.17: Mean photon spin as a function of modulation depth.

[29] If $\cos(2\phi) < 0$, we simply have a sign flip but since we're more interested in the magnitude of $\mathbf{s}$, this does not really matter.

Figure 4.17 above shows a plot of the magnitude of the mean photon spin s as a function of the modulation depth m as derived in (4.38). We note that s is non-linearly related to m. It is common to achieve a modulation depth of 0.5 or less, corresponding to a mean photon spin of ≈ 0.943 or higher. A modulation depth of 0.2 gives a mean photon spin of ≈ 0.994.

4.2.6 Co-magnetometer noise

An important part of any precision measurement is the identification and elimination of unwanted noise in the signal of interest. For the co-magnetometer, we may broadly divide its noise into three categories: a purely electronic component stemming from the detection electronics, optical noise from the probe laser, and of course, spin noise from the atoms. Figure 4.18 shows measurements of the electronic, probe (plus electronic), and full co-magnetometer (electronic+probe+spin) noise in effective magnetic field units. In the sub-sections below, we discuss this measurement of the co-magnetometer's noise, delineate various sources of noise contributing to each of the aforementioned components and describe steps we have taken to mitigate noise from these sources.

Electronic noise

Since we require the use of our detection electronics in any measurement, the electronic noise is in some sense the "baseline" noise. Practically speaking, we would like our overall noise to not be dominated by the "baseline" electronic noise. Since incoherent noise is summed in quadrature, it is typically sufficient to have the electronic noise a factor of 3 to 4 smaller than the optical noise. Experimentally, this is typically relatively easily accomplished by ensuring good optical transmission and detection of the probe beam while having sufficient gain in the electronic circuit so that the noise

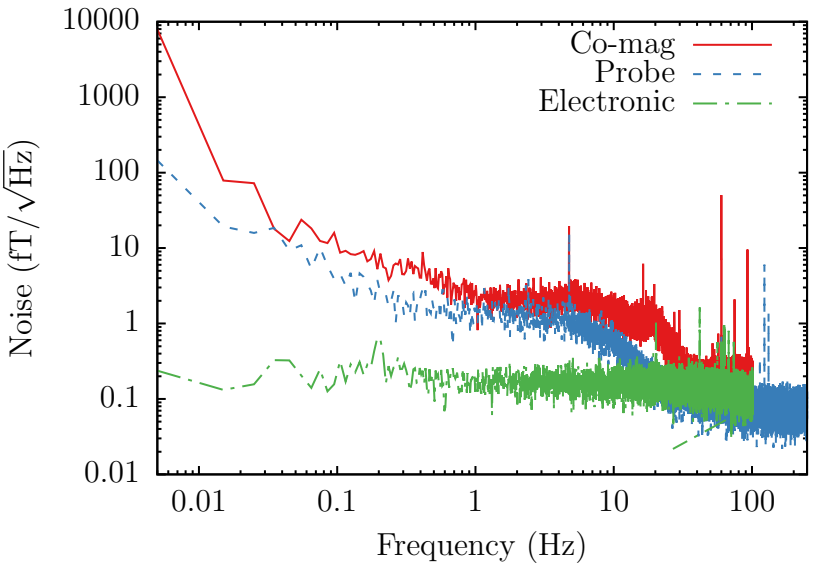

Figure 4.18: Measured effective magnetic noise of the co-magnetometer.

due to the probe beam's photon shot noise is 3 - 4 times larger than the electronic noise floor.

In SMILE, we measure the spin orientation of the alkali atoms via optical rotation of a linearly polarized off-resonant probe beam (see section 2.6.4). To measure this optical rotation, linearly polarized light from the probe beam is modulated at a carrier frequency of 50 kHz, sent through the co-magnetometer cell, and then analyzed by a linear polarizer and photo-diode. The photo-diode converts incoming photons into a photo-current that is then converted to a voltage with a home-built transimpedance amplifier and fed into a SRS 830 lock-in amplifier, which de-modulates the signal. Finally, a computer acquires the de-modulated signal in the form of an analog voltage from the lock-in amplifier using a National Instruments data acquisition card.

Electronic noise can therefore arise from the transimpedance amplifier circuit, the lock-in amplifier and the data acquisition card. We note that noise on the data acquisition card is typically limited by the card's bit noise and is rarely a limiting problem so that the major sources of electronic noise are from the transimpedance amplifier and lock-in amplifier. In SMILE, our electronic noise is limited by that

from the lock-in amplifier and lower electronic noise can be attained by using a higher gain setting on the lock-in amplifier but that results in its phase sensitive detectors overloading due to the large second harmonic component of the signal. In principle, this problem can be solved by either implementing a notch filter tuned to 100 kHz or by rolling off the gain from the transimpedance amplifier more sharply after 50 kHz. Nevertheless, these steps were not taken since our overall noise was not, as shown in Figure 4.18, dominated by the electronic noise.

Probe noise

The use of a linear polarizer and photo-diode to analyze the light's polarization means that the optical noise is sensitive to both the intensity and polarization noise in the laser beam. Due to the discrete nature of light, the intensity noise is always limited by the photon shot noise. Although, additional intensity noise due to fluctuations of the laser current is possible, in SMILE, the intensity noise is roughly limited by the photon shot noise, which may be estimated by knowing the transimpedance of the transimpedance amplifier circuit and measuring the power of the probe laser entering the photo-diode. Ideally, the total optical noise would just be limited to the white photon shot noise. However, as shown in Figure 4.18, the optical noise is in reality pink (i.e. has a strong 1/f dependence) with a corner frequency of ~ 0.5 Hz. We note that the roll off at around 10 Hz is due to the low-pass filter of the lock-in amplifier and that the flat region from ~ 0.5 to 10 Hz is consistent with noise due to white photon shot noise. Measurement of the total intensity noise by deliberately detuning the reference frequency of the lock-in away from 50 kHz yields a white noise spectrum, which indicates that the observed 1/f noise is due to polarization noise. We believe that this polarization noise is due mostly to beam motion through optical components with inhomogeneous birefringence that results in optical rotation of the light. More specifically, measurements indicate that the offending optical components are mostly

the windows on the vacuum chamber. Indeed, as Figure 4.19 demonstrates, there is a substantial reduction of the probe's 1/f noise when the vacuum windows are removed (green dash-dot line) as compared to when they are on (solid red and dashed blue). Furthermore, the measured probe noise can vary depending on how much each of the 4 screws holding the window in place is tightened. For example, in Figure 4.19, the solid red line corresponds to a measurement with the screws tightened and the dashed blue line corresponds to a measurement in which each screw has been "tuned" to reduce the probe noise. We note however, that it was not ultimately possible, to achieve the same low noise level with the windows on as without the windows.

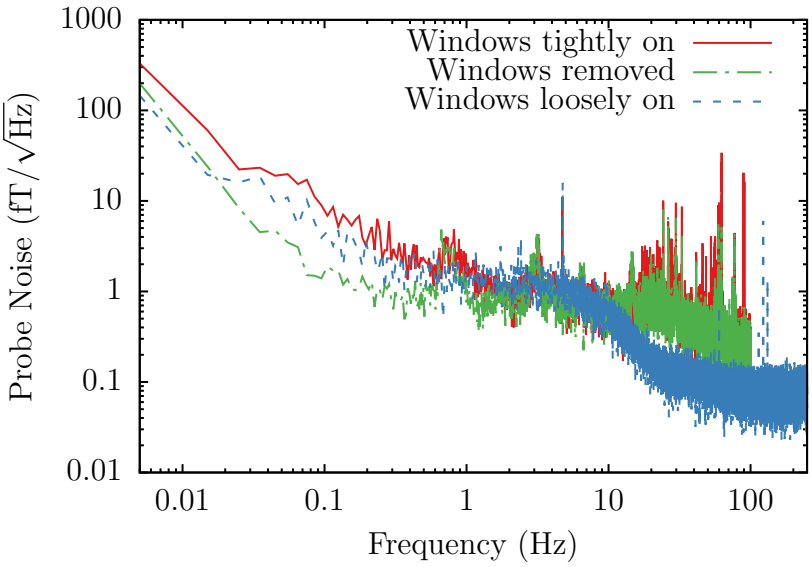

Figure 4.19: Measured noise from probe beam under different conditions.

The measurements in Figure 4.19 indicate that the source of the 1/f polarization noise is due to beam motion through optical components with inhomogenous birefringence. One way to reduce this noise is to reduce the inhomogeneity of the optical components such as by "tuning" the tightness of each screw. A parallel strategy would be to reduce the beam motion in the first place. A major source of beam pointing instability is due to convection air currents that result in air density and hence refractive index fluctuations that deflects the path of a laser beam. This can

be significantly reduced by enclosing the optics in polycabonate boxes and sending the laser into the vacuum can through vacuum tubes. We note here that some of the tubes in SMILE were accidentally broken/cracked during the course of the experiment so that they are no longer under vacuum but it appears that enclosing the air in that region is sufficient since we did not observe a significant increase in noise between using tubes filled with air versus using truly vacuum tubes. Indeed, the onset of convection in a volume with its length much larger than its height h and its top surface at a temperature ΔT cooler than its bottom surfaces can be predicted by calculating the dimensionless Rayleigh number, which is given by

$$\mathrm{Ra} = \frac{\rho h^3 g}{\eta \alpha} \beta \Delta T, \tag{4.39}$$

where g is the earth's gravitational acceleration and η, ρ, α and β are respectively here the viscosity, density, thermal diffusivity and thermal expansion coefficient of the fluid. If the Rayleigh number is above the critical value of ~ 1708 [205], convection rather than diffusion becomes the primary mode of energy transfer. Nominally, the temperature of the glass vacuum tube sitting in air should be the same everywhere but if we assume a temperature gradient of 0.01 °C, this gives us a Rayleigh number of ~ 1000, which is just under the critical value. However, a more conservative, larger temperature gradient of 0.1 °C will obviously be above the critical value. It is therefore likely that the cracked tubes did have some convection currents in them but they were likely not of a sufficiently big magnitude to adversely affect the noise. On the other hand, it is evident that plugging in the numbers for the polycarbonate boxes will yield a Rayleigh number many orders of magnitude above the critical value, which implies that convection is almost certainly still occurring within them[30].

[30]To make matters worse, we note that the bottom surface of the enclosure is the steel skin of the optical table whereas the top surface is a polycarbonate sheet and it's therefore quite likely that the two surfaces will have a temperature difference greater than 0.1 °C due to their vastly different thermal conductivities

Besides reducing convective air current, it is also possible to reduce beam motion due to convective air currents by replacing air with ^{4}He, since ^{4}He has a smaller refractive index compared to air, which makes their refractive index fluctuations due to convective currents smaller compared to air. However, since ^{4}He can rapidly leak out of the box, it is challenging to fill the box with sufficient amount of ^{4}He without causing additional mixing/movement of the air/^{4}He within the box, which would introduce additional noise. Despite multiple attempts to fill the boxes with ^{4}He with variable flow rates, we were unable to reduce the probe noise by filling the optical enclosures with ^{4}He. An alternative to filling the enclosure with ^{4}He is to place the optics entirely within a low vacuum as was done in [206], but this would entail a fairly major upgrade and was not done.

We note that the probe noise in Figure 4.18 is, despite our best effort, unfortunately worst compared to [178], which maintained a flat level of ~ 1 fT/$\sqrt{\text{Hz}}$ up till 0.1 Hz. We now suggest a few reasons for why this might be the case and point out possible improvements in the hopes that it'll prove useful for upgrades in the future.

Firstly, the measurements in Figure 4.19 suggest an easy path towards reducing the probe's 1/f noise: replacing the vacuum chamber's windows to glass that have very low stress-induced birefringence. In particular, some dense flint glass like SF57 are known to have extremely low stress optical co-efficients [207, 208] and have stress-induced birefringence that are two orders of magnitude smaller as compared to Pyrex or BK-7 [209]. If the measurements in Figure 4.19 are any indication, this change will likely bring the probe noise down to the level of the green dash-dot line in Figure 4.19, which we note, is not far from the probe noise level in [178] that also incidentally did not have to deal with stress-induced bireringence of vacuum windows since in that case, the co-magnetometer cell was not placed in a vacuum. Besides changing the vacuum windows, it is also possible that having a windowless oven with appropriately sized thermal shields (to prevent condensation of alkali atoms on the sides of the

cell facing the optical access ports) will be better than using an oven with gallium phosphide windows since stress on these windows due to thermal expansion might induce additional inhomogenous birefringence that will contribute to optical rotation noise from beam motion. Moreover, having a windowless oven will also increase the overall optical transmission of the probe beam, which will aid in improving the overall probe sensitivity.

Secondly, a parallel strategy would be to reduce the beam motion. Unfortunately, it is not always obvious what is causing the beam to move but a safe bet is to decrease the optical path length of the probe laser as much as possible. In SMILE, the placement of the optics is complicated by the presence of the weight stacks and care obviously needs to be taken to avoid the weights accidentally slamming into an optical breadboard. In this work, we mounted all of the probe optics on off-the shelf Thorlabs PBH11102 2'×1'×2.4" rectangular breadboards; all of the probe optics before the beam enters the vacuum chamber was mounted on one breadboard and all of the optics after the vacuum chamber was mounted on another breadboard. However, the use of these rectangular breadboards placed constraints on the enclosure surrounding the optics that are detrimental in a few ways. For example, since the breadboard was not sufficiently large to mount all of the optics and have an enclosure on top of it, the probe optics and the pump optics below them on the main optical table have to share the same enclosure that had to be made sufficiently large in order to enclose the entire PBH11102 breadboard comfortably (see Figure 4.1). The large size of the enclosure meant that it was not possible for it (and the breadboard) to approach too close to the vacuum chamber without hitting the weights, which increased the overall optical path length. Perhaps more importantly, the large volume of the enclosure significantly increases the Rayleigh number (we remark that from (4.39) it scales as the cube of the dimension), which implies that convection rather than diffusion is much more likely to be the dominant mode of heat transport, which can in turn adversely affect

beam pointing stability. We therefore believe that a custom breadboard with sufficient space for its own enclosure on top of it and possessing dimensions designed to conform around the vacuum chamber and weights would prove beneficial in reducing the probe noise. Moreover, in that scenario, increasing the height of the breadboard above the main optical table, which allows for the use of shorter optical posts and consequently a shorter enclosure, would probably also aid in further reducing convection. Currently, increasing the height of the breadboard is of no avail since the height of the enclosure, which sits on the main optical table, is determined by the height of the cell above the main optical table. We note that in [177, 178], the height of the optics and the enclosures surrounding them are all much shorter as compared to this work. In addition to helping keep convection down, having shorter optical posts is also advantageous in making the optics more mechanically stable.

Lastly, since (natural) convection is ultimately due to temperature gradients, it is possible that reducing temperature gradients by passively and/or actively stabilizing the air temperature around the experiment might be beneficial and in any case, as discussed later in sections 4.5.3 and 4.5.2, temperature gradients were discovered to have deleterious systematic effects so some sort of temperature stabilization will likely prove useful. We note that thermal instability in [177] was also an issue and that active/passive thermal stabilization was eventually employed.

Spin noise

Polarization noise in the probe beam can be due to purely optical effects as described above, or they can also stem from spin noise from alkali atoms that is then translated into an optical rotation/polarization noise in the probe beam. These two causes may be easily distinguished by either going to a high B_z field, which effectively "pins" the spins of the atoms to the field and suppresses any spin noise, or by cooling down the cell. Spin noise from the atoms are typically either due to magnetic noise within

the innermost ferrite shield or to noise from the pump beam that is polarizing the atoms' spin. Unfortunately, it is not always easy to directly differentiate between *these* two plausible causes, especially if both causes are affecting the atoms at a similar level. Nevertheless, in the case where one cause is dominant, it is possible to pinpoint the troublemaker. Essentially, this entails having a calibrated sensor that measures the noise of an experimental parameter that could be responsible for the observed spin noise. If the calibrated noise of the experimental parameter is much less than the observed spin noise, then it can be safely concluded that it is not the transgressor. The calibration of the sensor may be accomplished by applying an appropriate excitation and measuring the response of both the co-magnetometer and sensor's signal. For example, in the case of noise due to misalignments of the pump beam, a piezo mirror can be moved and the response from the co-magnetometer and a quadrant photo-diode measuring a sample of the pump beam can be simultaneously recorded to calibrate the quadrant photo-diode. Obviously, this method only works if the experimental parameter is easily measurable but unfortunately this is not always the case.

For example, magnetic noise within the innermost ferrite shield can come from Johnson currents within it, which is not easily measurable. This is particularly annoying since by design, the ferrite shield has a high resistivity, which translates to low Johnson currents and small magnetic noise. Therefore, it can be quite challenging to characterize its performance with an off-the-shelf commercial magnetometer. On the other hand, there are other sources that can contribute to the magnetic field noise within the ferrite that are more easily measurable such as the DC currents that are applied to the magnetic field coils and the AC currents that power the oven and stem heaters. The DC currents are most easily measured by measuring the voltage across as large a resistor as feasible (while still allowing the current/voltage source to supply the operating current) using a digital multimeter (DMM) with 6 or 7 digits precision.

Thanks to the co-magnetometer's suppression of magnetic fields (see section 4.2.4), the actual amount of real magnetic field required to cause noise at the 1 fT level is significantly larger, which allows a DMM with 6 to 7 digits precision to constrain possible magnetic field noise at the 1 fT level due to currents flowing across a resistor of a few or tens of kΩ. Similarly, the magnitude of the AC currents flowing into the oven/stem heaters can be measured by measuring the voltage across the heaters and de-modulating it with a lock-in amplifier. Our measurements of the noise from the currents in the coils and the oven/stem heaters were insufficient to explain the spin noise observed in Figure 4.18. However, as Figure 4.20 shows, initial measurements of the calibrated noise due to the pump beam were large enough to explain the spin noise in Figure 4.18.

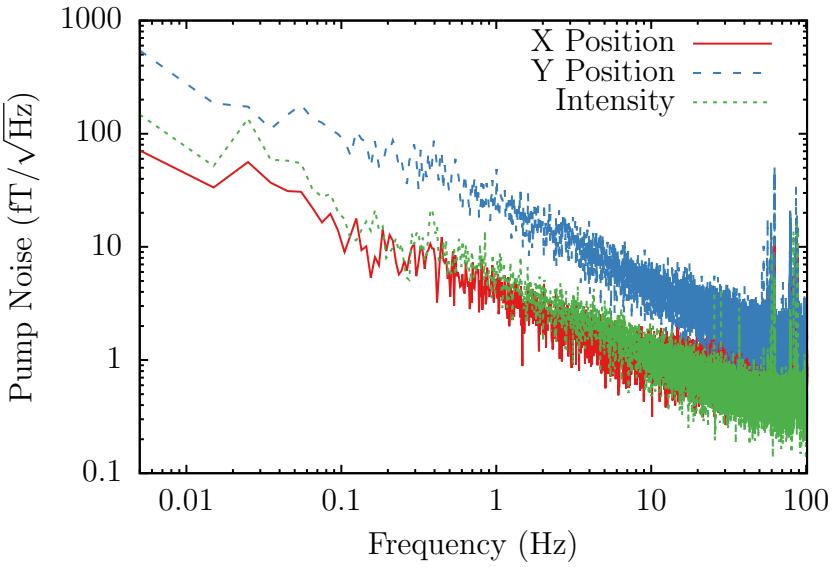

Figure 4.20: Measured calibrated noise from pump position detector.

The large (effective) magnetic noise measured by the pump quadrant photo-diode in Figure 4.20 led to a complete revamp of the pump optics. Previously, when the data in Figure 4.20 was taken, the pump seed laser, tapered amplifier (TA) and all other pump optics was located underneath the probe optics in the same enclosure. Amplified light from the TA was then directed through a vacuum tube to a 45° deg

mirror underneath the vacuum chamber that reflected it up into the cell without any form of filtering and/or feedback. We now believe that this arrangement was undesirable for multiple reasons.

Firstly, the output of the tapered amplifier is prone to undergo filamentation due to non-linear light-matter interactions within the amplifier chip at high current densities [201], which translates to a time varying spatial intensity profile that will in turn lead to polarization noise across the cell. Secondly, even though the tapered amplifier is mostly cooled through a water-cooled heat-exchanger, it still inevitably causes convection currents whether through heating or cooling (due to the incoming cold water), which deflect the laser beam and results in polarization noise of the atoms, since to a good approximation, the atoms are polarized along the direction of the pump laser beam at the compensation point. Moreover, the relatively long optical path from the pump seed laser to the cell allows for considerable beam deflections.

To address these issues, we decided to move the pump seed laser and TA into a separate section of the optical table with its own enclosure. Amplified light there is then coupled into a single-mode polarization maintaining fiber (PMF) whose output is located inside the original enclosure close to the entrance of the vacuum tube to minimize the optical path length of the beam after it exits the fiber. A beam sampler picks off a fraction of the beam before it enters the vacuum tube and sends it to a quadrant photo-diode, which monitors the beam's position and intensity. The measured intensity of the sampled fiber's output is then fed back to an acoustic-optic modulator (AOM) placed before the input of the fiber to stabilize the output intensity of the fiber. In this way, the spatial profile of the pump beam is fixed by the single-mode fiber and its output intensity is controlled and stabilized via active feedback. Furthermore, the effective optical path length is decreased in this setup, which will also help to mitigate polarization noise due to beam motion.

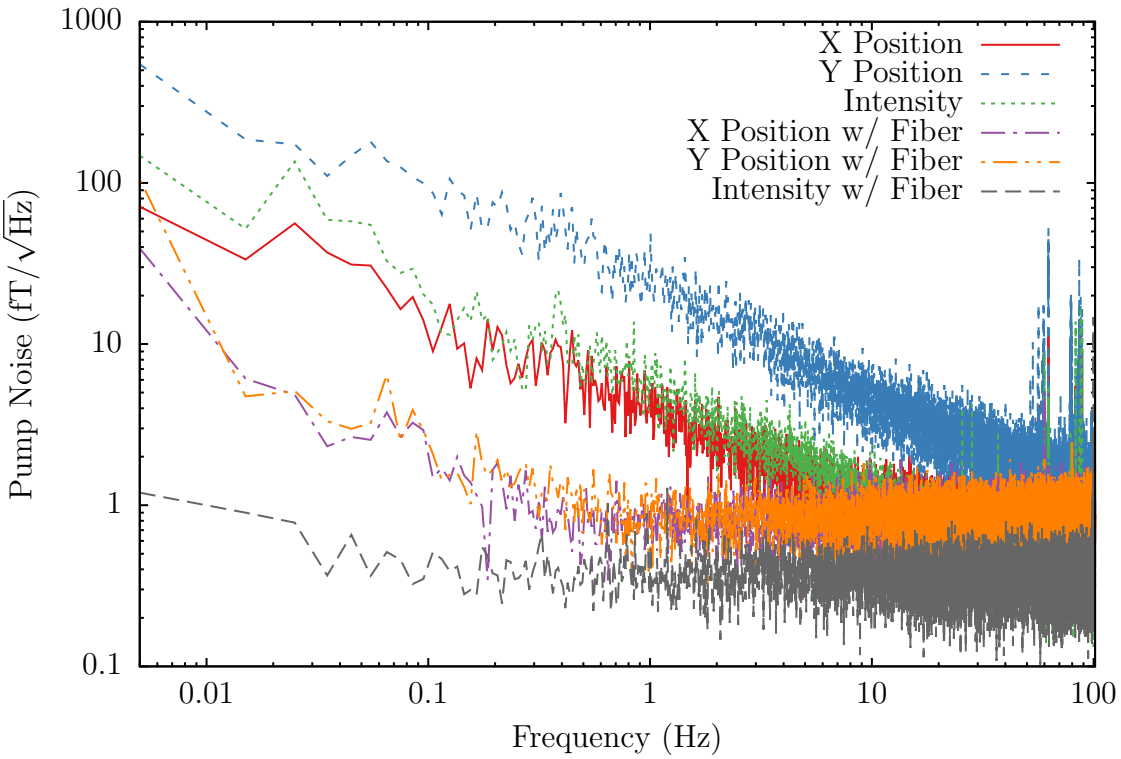

Figure 4.21: Pump noise after fiber upgrade.

Figure 4.21 demonstrates the significant improvement in pump noise after the upgrades were performed. Comparing the improved probe[31] and pump noise in Figure 4.19 and 4.21, we believe that the total co-magnetometer noise in Figure 4.18 is mostly a sum of the improved probe and pump noise which are both contributing to the total noise at roughly the same level. Consequently, both the pump and probe noise have to be improved in order to see further significant improvement of the total co-magnetometer noise. We have suggested several strategies to further improve the probe noise in the section above and we believe that some of the same strategies will also aid in further reducing the pump noise. In particular, we believe that the residual 1/f noise in the pump's position is due to convective air currents and can be further reduced by re-designing the way the vacuum chamber is mounted on the main optical table so that there is sufficient access under the vacuum cham-

[31]The "improved probe noise" here refers to the dashed blue 'Windows loosely on' plot in Figure 4.19, which is the same plot labeled 'Probe' in Figure 4.18.

ber to move the output of the fiber directly (or almost directly) under the vacuum chamber. This would significantly reduce the path length of the beam after its exit from the fiber and minimize polarization noise due to the pump beam's motion. A even better (albeit slightly more ambitious) strategy would be to use a cage system attached from the vacuum chamber's window port to hold lens tubes that contain the output of the fiber and other necessary optical components including a $\lambda/4$ wave plate and polarizer. The alignment of the beam should in principle be guaranteed by the mechanical placement of the cage system and the cage/lens tube system ensures minimal volume and temperature gradient for convection to occur within the path of the pump beam. We note however, that this configuration might make it somewhat more tricky to sample the pump beam and to direct that sample into a quadrant photo-diode, although it is not impossible if there is sufficient access at the bottom of the vacuum chamber.

4.3 Experimental Procedure

Running SMILE, which involves simultaneously measuring a sensitive co-magnetometer and a host of other sensors while modulating the positions of two ~ 250 kg Pb weights centimeters away for long periods of time without active human supervision and only partial one-way communication between the weights and co-magnetometer, requires some sophistication that we elaborate here in this section.

Before we get into the details, we sketch out the basic sequence of events in a SMILE data run. Data from the co-magnetometer and various other sensors are gathered in regular records of 312 s during which the position of the weights are modulated and after which the co-magnetometer performs an automated zeroing routine to ensure that all fields remain well zeroed. After the zeroing is completed, the cycle repeats. Since the spin-mass interaction is directional with respect to the position of

the weights, reversing the position of the weights should reverse the sign of the interaction, which translates to a reversal in the orientation of the spins and a concomitant reversal in the co-magnetometer's signal. This modulation scheme therefore allows us to search for tiny anomalous spin-mass interactions by looking for correlations between the signal and the position of the weights.

In order to minimize any possible (non-anomalous) correlation between the position of the weights and the co-magnetometer, it is desirable to separate the control of each on different computers. Accordingly, we have a "motor computer" that is dedicated to controlling and recording the position of the weights and another "co-magnetometer computer" that is dedicated to controlling the co-magnetometer and measuring its signal together with all other diagnostic sensors. There is only unidirectional communication from the co-magnetometer computer to the motor computer using LabVIEW's Network Streams, in which the co-magnetometer computer sends a single boolean value that instructs the motor computer to execute a fixed predetermined number of position reversals and to save data associated with this motion into file. An odd number (31) of reversals is chosen so that each 312 seconds data record begins with the weights in an opposite orientation from the preceding record. Since the co-magnetometer computer simply sends a single boolean value, it is blind to the number of reversals or the position of the weights. The motor moves the weights in 5 seconds and waits for another 5 seconds before reversing the positions of the weights. Data from the last 2 seconds of the wait time was used to search for correlations with the position of the weights. We note that the length of the data acquisition record on the co-magnetometer computer must be appropriately set so that the motor finishes all of its position reversals before data acquisition ceases on the co-magnetometer computer[32]. Time stamps (in sidereal days since 12:00 PM January

[32]We also note that since the trigger is sent from the co-magnetometer computer to the motor computer, the co-magnetometer computer has already started acquiring data before the weights move.

1st 2000[33]) of both the co-magnetometer and motor's data allow us to later verify that this is indeed the case. For the time stamps on both computers to be meaningful, the clocks of both computers must be synchronized to a reference clock. This is separately accomplished in both the co-magnetometer and motor computer by their respective LabVIEW programs that synchronizes their computers' clocks before/after each 312s data record to a NIST time server using the Network Time Protocol (NTP), which by taking into account the round-trip delay, is accurate to a few ms.

Experimentally, a SMILE data run always involve first running the co-magnetometer computer's LabVIEW program to zero out the magnetic fields and to ensure that the co-magnetometer is running smoothly under conditions that are optimal. Once optimal conditions have been established, various experimental settings on the co-magnetometer's computer should be checked. Firstly, multiple options related to data acquisition should be set accordingly. In this experiment, we utilize 3 NI-DAQ cards for simultaneous acquisition and generation of analog signals. The 3 PCI cards are synchronized via a Real-Time System Integration (RTSI) ribbon cable and can acquire/generate signals that are all hardware synchronized with each other. To accomplish this, a low-level LabVIEW sub-VI used in previous experiments to synchronize two cards was generalized to allow for the synchronization of an arbitrary number of PCI cards, along with numerable other features such as the ability to trigger (with a set delay if desired) on an external signal or to export a start trigger TTL signal. All of the synchronization is invisibly handled by the sub-VI but the user has to set a few parameters in the experiment's preference file[34] such as the sampling rate, the (global virtual) channels to acquire data from, and of course, the names of the files that the data would be saved to.

[33] This was chosen for historical reasons.

[34] This is saved in a LabVIEW binary file that comes along with a dedicated LabVIEW program, inherited and modified from previous experiments, to allow for its modification.

In principle, each different DAQ card can acquire data at a separate rate[35] (a high frequency time-base is synchronized between them, which can then be separately divided down to achieve the desired sampling rate) but since this is unnecessary for our purposes, a "global" sampling rate is set for all three cards in the preference file. We typically sample data at a rate of 200 Hz. Since we collect data over days and weeks continuously for over 30 channels, the size of the data files can rapidly swell. Consequently, we average and down sample the acquired data before saving them. Traditionally, data from each DAQ card is saved into a separate binary file with its own down sampled rate and we have followed this convention. Unlike previous experiments however, we have centralized the data acquisition settings in the preferences file to allow for an arbitrary number of devices to be used. The user now specifies, for each device, the global virtual channels (with physical channels on the same device) to acquire, the precision to save the data in, the appropriate calibration (if any), the down sampled rate for that device and a filename suffix. Raw binary data file names have a "SMILE" prefix, followed by a sidereal day identifier and a device suffix. To keep the I/O of the data files fast, they are typically kept below a GB, after which a new data file is created. A sidereal day identifier, which is essentially a time stamp of when the data file was created, differentiates between files containing data from the same device. New data files for all devices can be easily created by pushing a button in the main co-magnetometer LabVIEW program. Besides these parameters, the length of the data taking record[36] and the exact zeroing sequence after each data taking record must also be set in the aforementioned file.

[35] However, we note that individual analog input channels on a single DAQ card must all acquire data at the same rate since there is only one analog input sample clock per M/S series NI-DAQ card.

[36] As mentioned above, this has to be longer than the time it takes for the motor to complete its pre-determined number of position reversals.

Besides acquiring data from various DAQ cards, we also acquire data from two additional Keithley digital multi-meters that have a resolution of 6 - 7 digits[37], which we typically use to measure quantities such as currents flowing into the magnetic field coils. Unlike previous experiments, data acquisition is all centralized in one LabVIEW VI[38] that acquires data from all the DAQ cards as well as peripheral devices such as the Keithley multi-meters. Since it is not possible to synchronize the onboard clocks of the DAQ cards with the Keithley multi-meters, the multi-meters are programmed (through the LabVIEW VI) to acquire samples over a fixed interval[39] on receiving a trigger signal from the DAQ cards. This interval must be appropriately set in the data acquisition VI so that the weights complete all their position reversals before the Keithley multi-meters stop recording. All other parameters relevant to the operation of the multi-meters may be set in the data acquisition VI and the user may specify which physical terminal on the DAQ card to export the trigger signal to. Data acquired by the multi-meters are stored on onboard buffers that are then transferred to the co-magnetometer computer after acquisition has completed. Given a specified resolution (and hence sampling rate), there is therefore a finite interval that the multi-meters can acquire data for before running out of memory.

Once these parameters on the co-magnetometer's computer has been set, the motor has to next be configured on the motor computer. The Yaskawa SGMG-44A servo motor used to move the weights is powered by a servo amplifier that is in turn controlled by a Yaskawa SMC-2000-1 motion controller that can be programmed by a computer via a serial interface. This serial interface is connected to the motor computer through an optically isolated DB-9 interface that allows for electrical isolation between the motor circuitry and the computers, which are both connected to

[37] We note that a typical $\pm$ 10 V 16-bit NI-DAQ card only has a voltage resolution of 0.3 mV whereas these DMMs can measure at the level of a μV.

[38] This makes it easier to maintain the code.

[39] We note that the sampling rate is dependent on the resolution requested since the meter performs some averaging in order to obtain the requested resolution. The number of samples acquired is therefore dependent on both the specified resolution and interval.

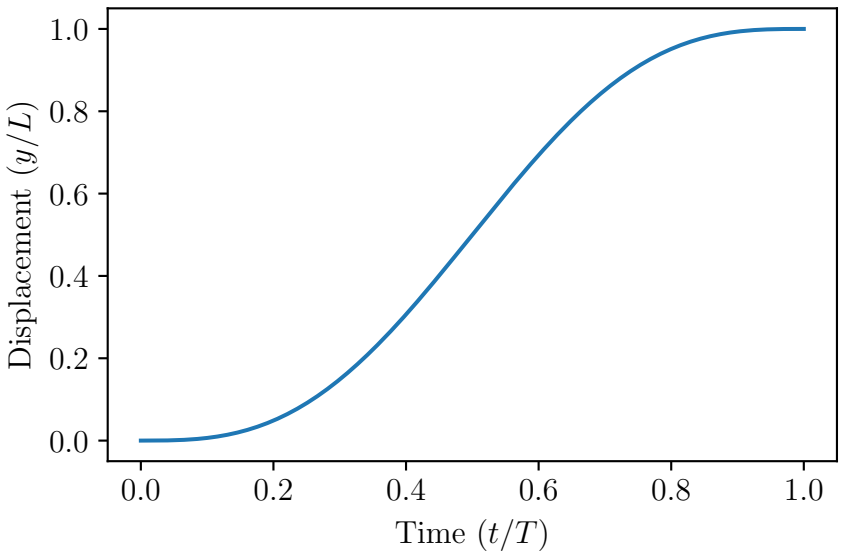

Figure 4.22: Pb weight stack's displacement as a function of time.

the same uninterruptible power supply (UPS). In order to smoothly move the weights from one extremal position to another, we upload a custom profile to the SMC-2000-1 controller so that the linear acceleration of the weights starts and ends at zero. More precisely, the desired acceleration of the weights is

$$a(t) = A_0 \sin\left(\frac{2\pi}{T}t\right), \qquad 0 \leq t \leq T \tag{4.40}$$

where T is the time for the motion to complete so that given a total displacement L traveled in time T, A_0 is given by

$$A_0 = \frac{2L\pi}{T^2}. \tag{4.41}$$

The linear displacement from integrating (4.40) twice (with A_0 as given above) is

$$y(t) = L\left(\frac{t}{T} - \frac{1}{2\pi}\sin\left(\frac{2\pi}{T}t\right)\right), \tag{4.42}$$

which as Fig 4.22 shows, changes smoothly from one extremal position to another.

To set up the motor for running SMILE, a contour profile derived from (4.42) has to be uploaded to the SMC-2000-1 given the total (angular) displacement[40] and the time to complete the motion. In addition to these two parameters, the user also has to specify the time step for the contour profile and the sampling rate for recording various quantities such as the actual position, error and torque during the motion, which are limited by the amount of memory on the SMC-2000-1. With these quantities specified, the user may upload the contour profile to the SMC-2000-1 with the push of a single button from the motor computer's LabVIEW program. Since the dimensions of the system was designed such that the motor rotates 10 revolutions between each extremal position, the total angular displacement is typically 3600°, while T was chosen to be 5 seconds although the motor can, in principle, move the weights to their extremal positions in about a second. Before starting a SMILE data run, the number of position reversals, the wait time after each position reversal[41] and the appropriate sidereal day identifier[42] also needs to be entered.

Once the contour profile has been uploaded, the weights need to be moved to their initial positions to await the trigger signal from the co-magnetometer computer. However, for safety reasons, a software over-travel safety limit has to first be programatically activated in the LabVIEW program. Since the over-travel is defined relative to the motor's current position, the safety limit should be activated with the weights at equal height above the optical table before the motor is rotated 1800° to bring them to their initial extremal positions to await the trigger signal. Finally, a switch in the program should be flipped to enable contour motion and the motor turned off. Upon receipt of a "trigger" command from the co-magnetometer computer, the motor computer's LabVIEW program checks to ensure that: 1) the safety limits have been

[40]The LabVIEW program performs the necessary conversions required so that the SMC-2000-1 gets displacements in units of encoder counts.

[41]We note that these two quantities, together with the time to complete the move has to be appropriately set in light of the data taking interval on the co-magnetometer's computer.

[42]This should match the sidereal day identifier on the co-magnetometer computer.

engaged, 2) the weights are in their initial position and 3) that contour motion has been enabled, before telling the SMC-2000-1 to execute it's pre-programmed contour. The motor LabVIEW VI tracks the position of the weights and depending on their positions, tells the SMC-2000-1 to either execute a "forward" or "rearward" contour.

As part of an additional layer of safety to prevent unintentional movement of the weights, a push button on the co-magnetometer computer's data acquisition VI has to be pushed in order for the co-magnetometer computer to send out a trigger signal to the motor computer. Lastly, a network stream connection needs to be established between the two computers, which may be accomplished from the co-magnetometer computer's main LabVIEW VI. A (LabVIEW front panel) LED on each computer lights up if the connection was successful (otherwise, one might try again or restart the motor computer's VI). A SMILE data run can now begin by pushing a button on the co-magnetometer computer to start the experiment. If everything works normally, the user then turns off the lights in the room and exits it. Despite the use of black-out fabric to cover the optical boxes, SMILE ran under the cover of darkness because changes in ambient light due to the positions of the weights can result in photodiode signals being correlated with the position of the weights.

Since the spin-mass interaction is directional with respect to the direction of the spins, its sign should be reversed upon the reversal of the atoms' spins. Conversely, spurious effects that do not couple to the atoms' spins (such as optical effects) retain the same sign under such a reversal, which may be accomplished by switching the polarity of the pumping light and the direction of the bias magnetic field. In a co-magnetometer, the polarity of the pumping light is fixed by the direction of the bias field so that only two, $B+$ and $B-$, configurations are possible. We ran SMILE in both configurations in order to cancel out any spurious effects that do not couple to the spins of the atoms.

4.4 Data Analysis

As discussed in section 4.3, the raw data from SMILE is saved in binary files that is then analyzed later for correlations with the position of the weights. Time-stamped raw data from the co-magnetometer's signal as well as a host of other diagnostic sensors are recorded by the co-magnetometer computer while position and torque data from the motor is recorded by the SMC-2000-1 and then transmitted to the motor computer after each position reversal of the weights[43]. Upon receipt of the data from the SMC-2000-1, the motor computer time-stamps it with the appropriate value so that data from the motor can be compared with data recorded by the co-magnetometer computer. Comparison of the two data sets allow us to look for correlations in the signal after the weights have fully come to a rest in their extremal positions (instead of while they are in motion, although we shall also frequently look for correlations during the motion to understand the source of various systematic effects). In the sections below, we discuss the methods we used to analyze the data from SMILE. Data analysis in this section was performed using Octave.

4.4.1 String analysis

Since we are looking for a correlation in the signal due to a binary change in the position of the weights, one simple way of determining the correlation is to simply take the difference of the co-magnetometer's signal when the weights are in opposite orientation and dividing that difference by two. Although this is a valid way of performing the analysis, it is susceptible to drifts in the signal. Instead, we employ a string analysis that was first introduced in the context of a search for a neutron electric dipole moment [210]. The basic idea is to the note that the signal $y(t)$ is a

[43] We note that in addition to the amount of memory on the SMC-2000-1, the wait time also limits the amount of data the SMC-2000-1 should save during each position reversal since the SMC-2000-1 has to finish sending the data before the wait time expires otherwise the actual wait time will be longer than that which was specified.

function of a spin-mass term $A(t)$ that flips sign after each position reversal of the weights, and a drift term that may be expressed as a polynomial (as a function of time) of arbitrary degree. More specifically, we can write $y(t)$ as

$$y(t) = A(t) + \sum_{n=0}^{M} C_n t^n, \tag{4.43}$$

where C_n are unknown co-efficients of the the drift polynomial of degree M. Now suppose that the weights reverse positions at regular intervals Δt and that we measure $y(t)$ at regular intervals of Δt so that $y_i = y(i\,\Delta t), \quad i = 0, 1, 2, 3, \ldots$ and $a = A(0)$. Then we may write the i^{th} measurement of y as

$$y_i = (-1)^i a + \sum_{n=0}^{M} C_n (\Delta t)^n i^n. \tag{4.44}$$

This implies that if we make m measurements of y, we would have a system of m equations that would allow us to cancel out $m-1$ drift terms, or equivalently, a drift polynomial of degree $m-2$. The price to pay for this is that we only obtain one measurement of a for every m measurements of y. We define a measurement of a from m measurements of y as a m point string. If we define a_j as the j^{th} measurement of a from $\{y_j, \ldots, y_{j+m-1}\}$ measurements of y, then we may write that for a m-point string,

$$y_{j+i} = (-1)^{i+j} a_j + \sum_{n=0}^{m-2} c_n i^n, \quad i \in [0, m-1] \cap \mathbb{Z}, \tag{4.45}$$

where we have defined $c_n \equiv C_n (\Delta t)^n$ for convenience. Since the coefficients c_n are unknown, we hope to find m constants B_i, $i = 0, \ldots, m-1$ such that

$$\sum_{i=0}^{m-1} \sum_{n=0}^{m-2} B_i c_n i^n = \sum_{n=0}^{m-2} c_n \sum_{i=0}^{m-1} B_i i^n = 0. \tag{4.46}$$

The constants B_i may be obtained by considering the binomial expansion of $(1+x)^{m-1}$

$$(1+x)^{m-1} = \sum_{i=0}^{m-1} \binom{m-1}{i} x^i, \tag{4.47}$$

which implies that

$$\left(x\frac{d}{dx}\right)^n (1+x)^{m-1} = \sum_{i=0}^{m-1} \binom{m-1}{i} i^n x^i. \tag{4.48}$$

For $n \in [0, m-1] \cap \mathbb{Z}$, all the terms on the l.h.s contain the term (1+x), which means that

$$\left(x\frac{d}{dx}\right)^n (1+x)^{m-1}\Big|_{x=-1} = 0 = \sum_{i=0}^{m-1} \underbrace{\binom{m-1}{i}(-1)^i}_{B_i} i^n, \tag{4.49}$$

where we have explicitly identified the coefficient B_i in the last equality after comparison with (4.46). Multiplying (4.45) by B_i, summing and re-arranging, we obtain

$$a_j = \frac{(-1)^j}{2^{m-1}} \sum_{i=0}^{m-1} (-1)^i \binom{m-1}{i} y_{i+j}, \tag{4.50}$$

for the j^{th} measurement of a m point string. If the uncertainty of each measurement y_i is δy_i, then by standard error propagation[44], the uncertainty of a_j is

$$\delta a_j = \frac{1}{2^{m-1}} \sqrt{\sum_{i=0}^{m-1} \binom{m-1}{i}^2 (\delta y_{i+j})^2}. \tag{4.51}$$

We note that each individual a_j is a measurement of the correlation of the signal with the position of the weights. Given N measurements of a_j, each with an uncertainty δa_j, we may compute their weighted average $\overline{a}$ and the uncertainty of that average, which would give us a best estimate on the correlation of the signal with the position of the weights. In general, the weighted average of any set of N independent

[44] We assume that each y_i measurement is independent of each other.

measurements $\{x_1, \ldots, x_N\}$ is [211]

$$\overline{x} = \frac{\sum_{i=1}^{N} w_i x_i}{\sum_{i=1}^{N} w_i}, \tag{4.52}$$

where the weights w_i are given by $w_i = 1/(\delta x_i)^2$, and the uncertainty of $\overline{x}$ is

$$\delta\overline{x} = \frac{1}{\sqrt{\sum_{i=1}^{N} w_i}} = \frac{1}{\sqrt{\sum_{i=1}^{N} \frac{1}{(\delta x_i)^2}}}. \tag{4.53}$$

In the case where the uncertainty of each measurement δx_i is the same, i.e. $\delta x_i = \delta x$ $\forall\ i$, then (4.53) reduces to

$$\delta\overline{x} = \frac{\delta x}{\sqrt{N}}, \tag{4.54}$$

so that making N independent measurements of the same quantity decreases the uncertainty of their mean by $\sqrt{N}$. However, since a m-point string a_j is defined as the j^{th} measurement of a from m measurements of y, $\{y_j, \ldots, y_{j+m-1}\}$, the strings a_j and a_{j+1} will in general consist of $m-1$ overlapping y measurements. Consequently, each a_j is not an independent measurement of a and the uncertainty of the mean $\delta\overline{a}$ from (4.53) has to be modified by a correction factor f_0.

As argued in [152], the grouping of m measurements of y into a m point string cancels out a systematic bias but the final statistical uncertainty of the measurement of the correlation should be the same as in the naive case where each correlation measurement b_j is simply $b_j = (y_{2j-1} - y_{2j})/2$ since we are ultimately looking at the same set of data. For simplicity, we consider the case where there are N measurements of y, $y_1, \ldots, y_N$, where $N \in 2\mathbb{N}$. In this case, we have for the naive case

$$\delta b_j = \frac{1}{2}\sqrt{(\delta y_{2j-1})^2 + (\delta y_{2j})^2}, \tag{4.55}$$

and consequently,

$$\delta\overline{b} = \frac{1}{\sqrt{\sum_{i=1}^{N} \frac{1}{(\delta b_i)^2}}} = \frac{1}{\sqrt{\sum_{j=1}^{N/2} \frac{4}{(\delta y_{2j-1})^2 + (\delta y_{2j})^2}}} \approx \frac{\delta y}{\sqrt{N}}, \tag{4.56}$$

where we have in the last step made the approximation that the uncertainty for each y_i measurement is the same and is given by δy.

In contrast, substituting (4.51) into (4.53), we obtain that for a m-point string, the uncertainty of the weighted average $\delta\overline{a}$ is

$$\delta\overline{a} = \frac{1}{\sum_{j=1}^{N-m+1} 4^{m-1} \frac{1}{\sum_{i=0}^{m-1} \binom{m-1}{i}^2 (\delta y_{i+j})^2}} \approx \frac{\delta y}{\sqrt{\beta}\sqrt{N-m+1}}, \tag{4.57}$$

where we have again made the approximation that the uncertainty for each y_i is δy in the last step, and β is, using the Chu-Vandermonde's identity,

$$\beta = 4^{m-1} \frac{1}{\sum_{i=0}^{m-1} \binom{m-1}{i}^2} = 4^{m-1} \frac{1}{\binom{2(m-1)}{m-1}} = 4^{m-1} \frac{(m-1)!\,(m-1)!}{(2m-2)!}. \tag{4.58}$$

From the argument above, we require a correction factor f_0 such that $\delta\overline{a}\, f_0 = \delta\overline{b}$. Evidently then, for a m-point string, the correction factor f_0 is

$$f_0 = 2^{m-1} \sqrt{\frac{N-m+1}{N}} \sqrt{\frac{(m-1)!\,(m-1)!}{(2m-2)!}}, \tag{4.59}$$

where N here is the total number of y measurements.

Given N measurements y_i, each with uncertainty δy_i for $i = 1, \ldots, N$, we can then form $N - m + 1$ m-point strings that are each given by (4.50) and with an uncertainty that is given by (4.51). The best estimate of the correlation with respect to the position of the weights from those N measurements of y is the weighted average of the $N - m + 1$ strings, $\overline{a}$, given by (4.52) (with $x \to a$) and with an uncertainty $\delta\overline{a}$ that is given by (4.53) (with $x \to a$) multiplied by the correction factor f_0 from

(4.59). Despite the use of strings to remove background drifts however, a non-zero background typically remains, which often leads to an underestimation of uncertainties. To compensate for this, the uncertainty in the weighted average $\delta\overline{a}$ is therefore further scaled by the square root of the reduced chi-square $\tilde{\chi}^2$ of the strings.

In general, for a set of N measurements $\{x_1, \ldots, x_N\}$ where the expected value is given by the weighted average $\overline{x}$, we may define $\tilde{\chi}^2 = \chi^2/d = \chi^2/(N-1)$ as[45]

$$\tilde{\chi}^2 = \frac{1}{N-1}\sum_{j=1}^{N}\left(\frac{x_j - \overline{x}}{\delta x_j}\right)^2. \tag{4.60}$$

Accordingly, the $\tilde{\chi}^2$ for $N-m+1$ m-point strings from N measurements of y is

$$\tilde{\chi}^2 = \frac{1}{N-m}\sum_{j=1}^{N-m+1}\left(\frac{a_j - \overline{a}}{\delta a_j}\right)^2, \tag{4.61}$$

and the final, corrected uncertainty $\delta\overline{a}$ is

$$\delta\overline{a} = \frac{f_0\sqrt{\tilde{\chi}^2}}{\sqrt{\sum_{j=1}^{N-m+1}\frac{1}{(\delta a_j)^2}}}, \tag{4.62}$$

where $\tilde{\chi}^2$ is as (4.61) and f_0 is as (4.59).

In the analysis of SMILE, we mostly work with 3-point strings since higher-order strings did not significantly improve the end result. For convenience, we explicitly list here the relevant equations for 3-point strings:

$$a_j = \frac{(-1)^j}{4}(y_j - 2y_{j+1} + y_{j+2}) \tag{4.63}$$

$$\delta a_j = \frac{1}{4}\sqrt{(\delta y_j)^2 + 4(\delta y_{j+1})^2 + (\delta y_{j+2})^2} \tag{4.64}$$

$$f_0 = \sqrt{\frac{N-2}{N}}\frac{4}{\sqrt{6}}. \tag{4.65}$$

[45] We note that the degree of freedom d is $d = N-1$ since calculating $\overline{x}$ gives us one constraint.

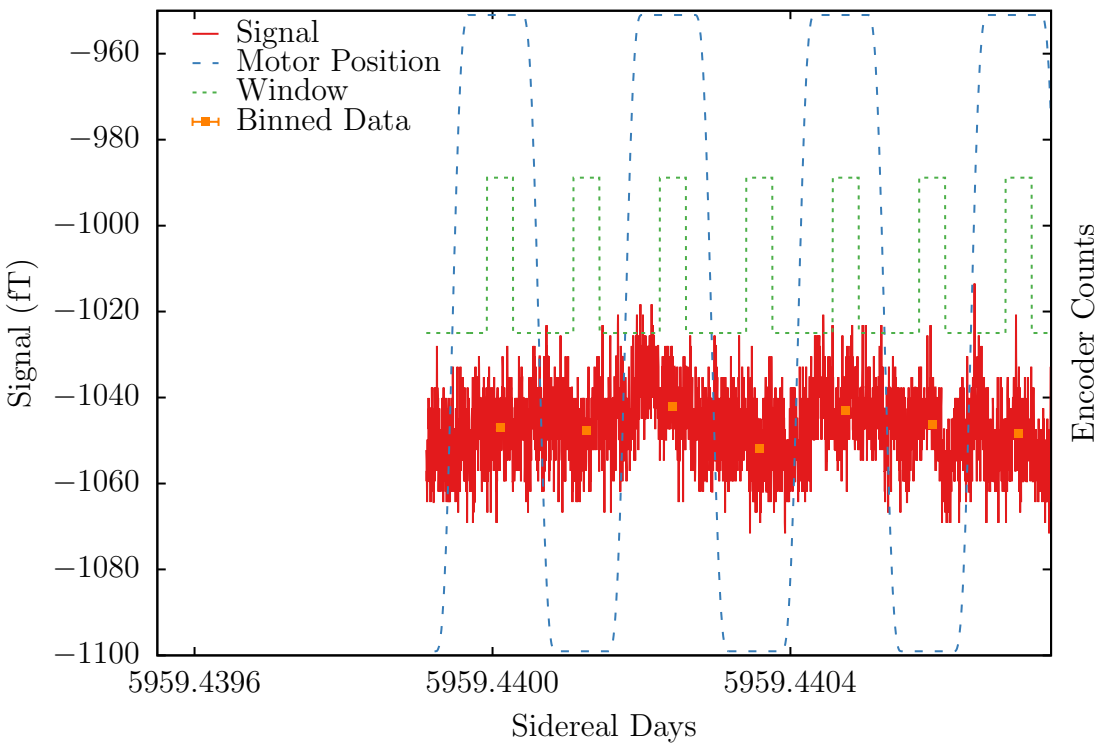

Figure 4.23: Representative experimental sequence.

Experimentally, we measure the co-magnetometer's signal continuously and obtain each y_i measurement by windowing the data appropriately during the analysis. Figure 4.23 shows the co-magnetometer's signal of a typical data run, calibrated in magnetic units and plotted on the left axis. Also plotted in Figure 4.23 is the motor's position, plotted on the right axis, and the window used to obtain each y_i measurement. We note that the motor position alternates between two binary levels corresponding to the two extremal positions of the weights. By design, when the motor position is at one of these extremal positions, one weight stack is close to the co-magnetometer while the other is far away and vice versa when the motor moves to its other extremal position. Each y_i measurement, labeled "binned data" (orange filled boxes) in Figure 4.23, is formed by averaging the co-magnetometer's signal within the data window. We estimate the uncertainty of each y_i measurement as the standard deviation of the points within that data window, divided by the square root of the number of points

within the window[46]. After obtaining these y_i measurements, 3-point strings are generated as described above. Once the strings have been generated, one can average the strings within each record (defined as the 312 s of data taking in between each automated zeroing of the magnetic fields) to obtain the best estimate of the correlation from each record before further combining all of these estimates in a single data file (which we will call a data run) to get a best estimate of the correlation from a data run. Since the intermediate step is somewhat superfluous, we do not perform the average at the level of a single record but directly calculate the best estimate from all the strings in a single data file using the procedure outlined above. Estimates of the correlation from multiple runs (including runs with different polarity of the pumping light/bias magnetic field) are then combined to derive the final result for SMILE.

4.4.2 Time resolved correlations and fluctuations

The procedure described in the section above gives us the correlation of the signal (from the co-magnetometer or any other sensor) with the position of the weights at a particular point in the motor's period. For example, in Figure 4.23, the strings formed from the "binned data" (denoted by the orange filled squares) are a measure of the co-magnetometer's signal correlation with the position of the weights at the end of the motor's period when the weights have come to a rest at their extremal positions. In the final analysis for SMILE, that is what we are primarily interested in since we are searching for a correlation of the signal with the extremal position of the weights where one weight stack is close to the co-magnetometer while the other has been removed far away. However, we are frequently interested in studying the correlation of signals, from both the co-magnetometer and other sensors, as a function of the time during the motor's period to better understand how the motion/position

[46]We assume that each measurement by the DAQ is an independent measurement and estimate the uncertainty of each individual measurement by the standard deviation of all the measurements in the data window.

of the weights affects the experiment. This may be easily accomplished by simply translating the data window and repeating the string analysis outlined above for y_i measurements made at different points within the motor's period.

Figure 4.24 shows the result of such an analysis for both the co-magnetometer's signal (plotted on the left axis) and the measured external **B** field just vertically above the co-magnetometer (plotted on the right axis) for one of SMILE's data run. As described in section 4.3, the motor moves for 5 seconds and then waits for 5 seconds. It is interesting to observe that during the middle of the motor's motion ($\sim$ 2.5 s), there is a large, noticeable peak correlation of the external **B** fields (primarily B_y and B_z) of the order of tens of nT that dies away after the motor comes to a rest. As is consistent with the measured suppression of the co-magnetometer to external **B** fields however, the co-magnetometer's signal does not register any correlation at the level of 0.1 fT.

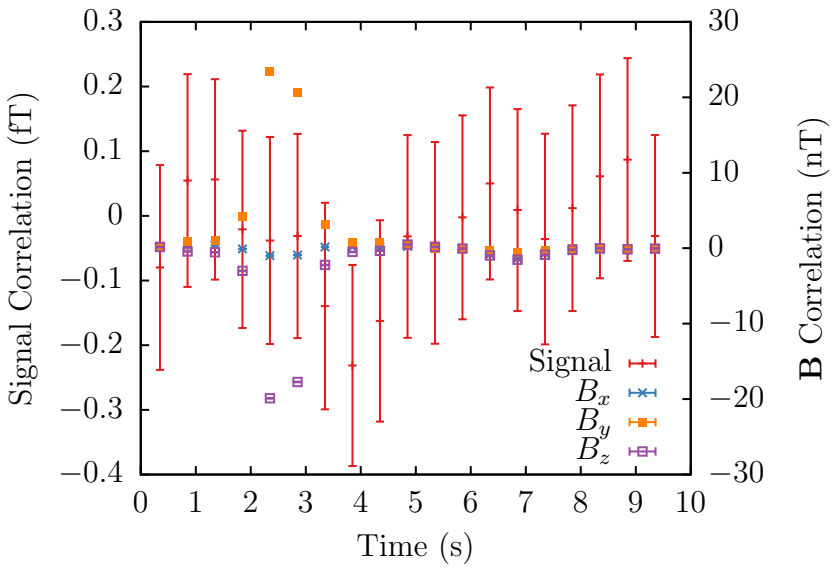

Figure 4.24: Time resolved correlations of the signal and external **B** field.

Translating the data window as described above allows one to study the correlation of any signal with the position of the weights as a function of the motor's period over an entire data run. This analysis is particularly good at picking out tiny but consistent

correlations that faithfully repeat themselves over every motor period but they can average out intermittent fluctuations that affect the signal only occasionally. Such transient events can remain undetected using the methods described above while still adversely affecting the experiment and it is therefore imperative for us to search for such events using other methods. Clearly, any such methods will require that we do not average over the entire data file since we would lose all temporal resolution in that case. Besides, since we are looking for transient events, averaging over long times where the event does not occur will further wash out the effect of a transient. On the other hand, without any averaging at all, we would have a limited ability to detect small events.

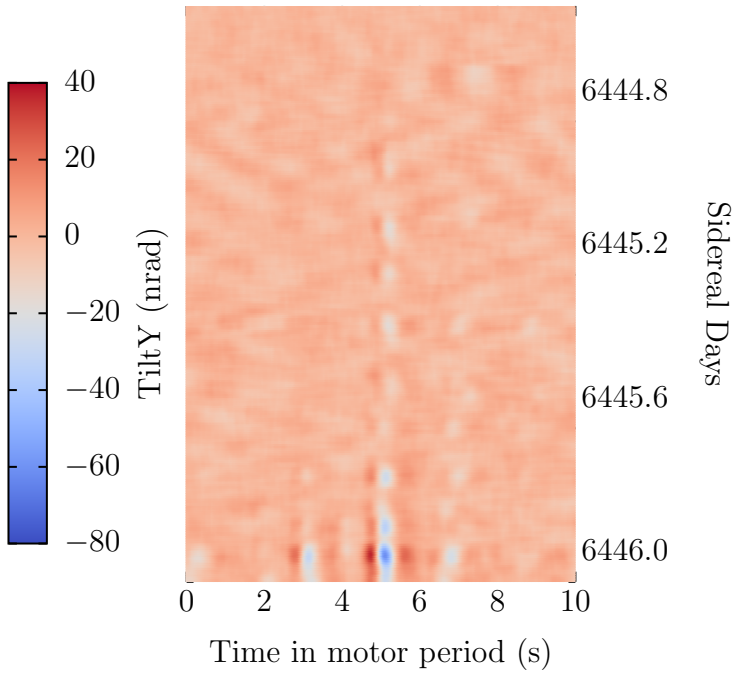

Figure 4.25: Averaged fluctuations of the optical's table tilt.

A compromise can be made by realizing that there are two relevant time scales involved: the motor period (typically 10 s) and the much longer time scale of a data run (typically over a few days). It is therefore reasonable to expect that there may be

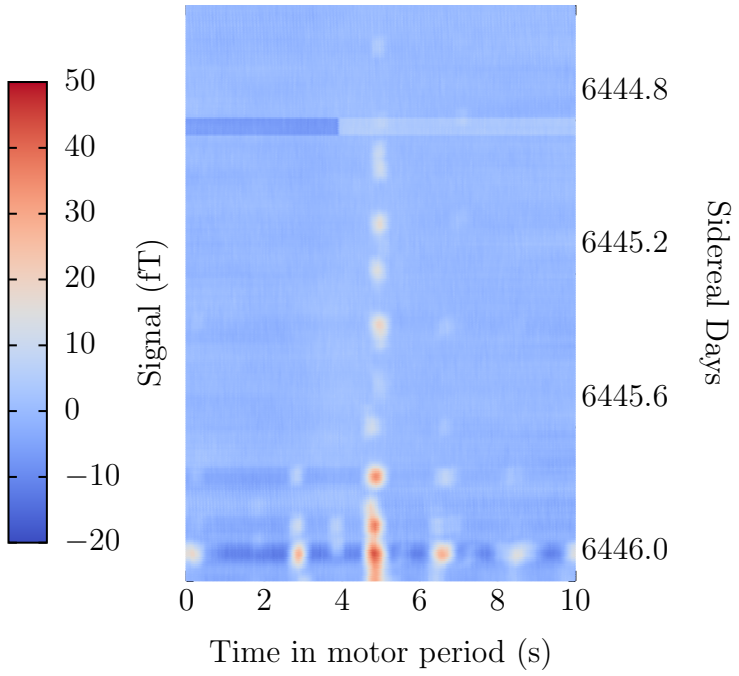

Figure 4.26: Averaged fluctuations of the co-magnetometer's signal corresponding to Fig 4.25.

events that are transient with respect to a data run but are yet long compared to a single motor period so that they persist over the duration of a few motor periods. Our resolution to such events may then be increased by applying, for each measurement in a motor period, a moving average over an adjustable number of motor periods. This yields an average measurement of a signal, as a function of time within a motor period, that is short compared to the duration of a data run that can then be plotted as a function of time on the time scale of a data run to check for events that are transient with respect to a data run but short compared to a motor period. However, since the signal of any sensor is bound to drift significantly over the time scale of a data run, such a "global" plot will not be very instructive unless that drift is corrected. Since we are primarily interested in transients that are a result of the motion of the weights, one way to subtract this drift is to subtract the mean value of the averaged signal described above over a motor period. The result will therefore be an averaged (over

a few motor periods) fluctuation of the signal from its local background as a function of time within a motor period that can then be plotted as a function of time on the larger time scale of a data run. This technique therefore allows for the detection of events that are transient with respect to a data run but long compared to a single motor period.

Figures 4.25 and 4.26 show the result of applying this analysis on the signal from a tiltmeter mounted on the optical table and the co-magnetometer. We note that data in both these plots are taken simultaneously from the same run and that the data presented cover the same time range from $\sim$ sidereal days 6444.8 to 6446.0 (time flows vertically downward on these plots). We see that from sidereal days 6444.8 onward, the signal begins to exhibit an anomalous fluctuation at 5 s in the motor period, which corresponds to end of the weights' motion. Although less obvious, a similar pattern can be seen in the data from the y-axis of the tiltmeter. This similarity grows in time until it becomes extremely obvious by (sidereal day) 6446.0 that the two are related. It turns out that the weights have in this run started to very slightly (note that we are measuring the tilt in nrads) touch a plate mounted on the optical table that was supporting the vacuum chamber. The early discovery of this problem through an analysis of the data allowed us to prematurely terminate the run and prevented a catastrophic accident of having the weights slam into the optical table.

4.5 Systematic Effects

Systematic effects are perhaps the bane of any precision measurement since they are difficult to distinguish from an actual signature of the phenomenon under investigation. To mitigate systematic effects, SMILE was performed with the spin polarizations of the atoms oriented in opposite directions, which helps us to cancel out systematic effects that are symmetric with respect to the polarity[47] of the spins since

[47] We mean by polarity here whether or not the spins are (nominally) in the $+$ or $-$ z direction.

a true spin-mass interaction is asymmetric to the spins' polarity. Nevertheless, there remains a large class of interactions that cannot be canceled out in this way. Indeed, any interaction with the spins that result from a dot product with the spins in the Hamiltonian (e.g. $\mathbf{B} \cdot \mathbf{S}$) are asymmetric with respect to the polarity of the spins and will not be canceled out by running SMILE with both polarities. Consequently, it is necessary to understand, reduce and quantify this class of systematic effects to ensure that it does not corrupt the result of the experiment. In the sub-sections below, we delineate some of the more troublesome effects that we have discovered in the course of this experiment and describe the steps that we have taken to mitigate them. Since many of these effects are small, it is frequently necessary to use the data analysis techniques described in section 4.4 to measure and study them.

4.5.1 Electromagnetic interference

Given the large measured suppression of the experiment to external magnetic fields described in section 4.2.4, it was with some surprise that initial operation of SMILE revealed that the servo motor used to move the Pb weight stacks was capable of significantly affecting the co-magnetometer's signal. For example, turning on the servo motor would cause a DC shift in the co-magnetometer's signal and cause spikes to appear in the previously quiet signal. It was known from previous testing of the servo motor that it produces a DC magnetic field at the location of the co-magnetometer when turned on but the measured magnitude of it was far too small to explain the DC shift observed in the signal given the experiment's suppression of external magnetic fields.

Low-pass filters

The cause of the DC shift was eventually traced to an innocuously looking home-built filter box taken over from previous experiments that we were using to filter the

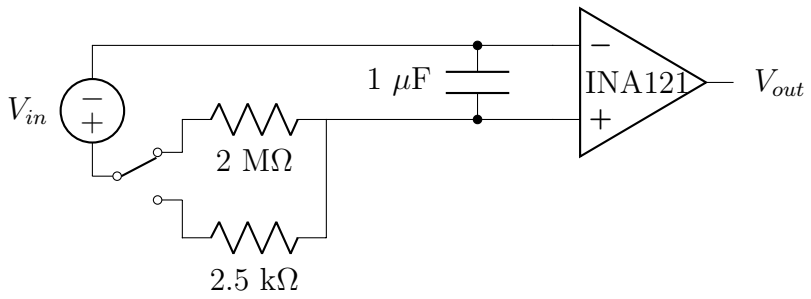

Figure 4.27: Original circuit for the **B** field coils utilizing an instrumentation amplifier.

currents going into the magnetic field coils of the co-magnetometer. Since we operate at low magnetic fields, it is typically sufficient to supply 10 mA or less to the coils, which can be supplied directly from the analog output of our NI-DAQ cards with a suitable resistor placed in series with the coils. However, since the voltage from the DAQ card can be susceptible to noise, the analog output voltage from the DAQ card is instead fed into the aforementioned filter box, which essentially consist of a voltage buffer that also serves as a low-pass filter, the output of which is then connected in series to an appropriately chosen resistor before going into the coils. Schematically, the original circuit diagram for the old filter box are as shown in Figure 4.27. Note that INA121 is an instrumentation amplifier rather than an op-amp. Its external gain can be set by a single external resistor (not shown) from values between 1 to 10000. A gain of 1 is used in Figure 4.27.

V_{in} in Figure 4.27 can be the voltage of any of the four analog outputs typically used to control the magnetic fields inside the co-magnetometer. Since B_x and B_y are nominally zero, they have considerably less dynamic range compared to B_z, which has to compensate for the noble gas' magnetization. Consequently, it suffices to have one analog output voltage each to control the currents in the B_x and B_y coils. Accordingly, after filtering, V_{out} in Figure 4.27 for the B_x and B_y outputs are then directly connected in series to an appropriately sized resistor followed by the coils. On the other hand, two analog outputs are usually used to control the B_z current due to its larger dynamic range. After filtering, V_c and V_f, the filtered outputs from

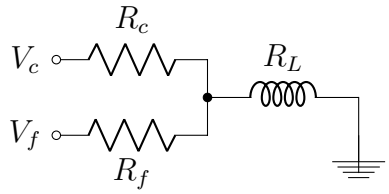

Figure 4.28: B_z coil circuit.

Fig 4.27 are combined as in Figure 4.28, where the current in the coils I_L is given by

$$I_L = \left[1 + \frac{R_L}{R_c} + \frac{R_L}{R_f}\right]^{-1} \left(\frac{V_c}{R_c} + \frac{V_f}{R_f}\right) \approx \left(\frac{V_c}{R_c} + \frac{V_f}{R_f}\right), \tag{4.66}$$

so that for $R_c, R_f >> R_L$, the current I_L is approximately the sum of the currents in the R_c and R_f resistors. Since R_L, the resistance of the coil, is typically only a few ohms, and $R_c \sim 200\Omega, R_f \sim 40\,k\Omega$, this approximation is quite good.

We note here that the SPDT switch in Figure 4.27 allows us to have a filter with two different time constants. During operation of the co-magnetometer, the SPDT switch is connected to the 2 MΩ resistor as shown in Figure 4.27 to give a low cut-off frequency. However, during zeroing of the co-magnetometer when we need to change the magnetic fields quickly, the SPDT switch connects with the 1.4 kΩ resistor instead. Experimentally, the SPDT switch is a mechanical relay that is controlled (after buffering) by another voltage analog output from the computer. INA121 was the instrumentation amplifier of choice due to its low noise and low input bias current[48], which allows for the use of the large 2 MΩ resistor without causing too much of an output voltage offset.

Although this circuit design worked sufficiently well in previous experiments, it has a significant flaw that would prove to be problematic in this experiment. Indeed, the filter as implemented has poor common-mode rejection ratio (CMRR) since the impedance that the inverting and non-inverting terminal see is vastly different. Moreover, as is typical of FET-input amplifiers, the INA121 has protective diodes on its

[48]The INA121 uses FET input-amplifiers, which have extremely small bias currents.

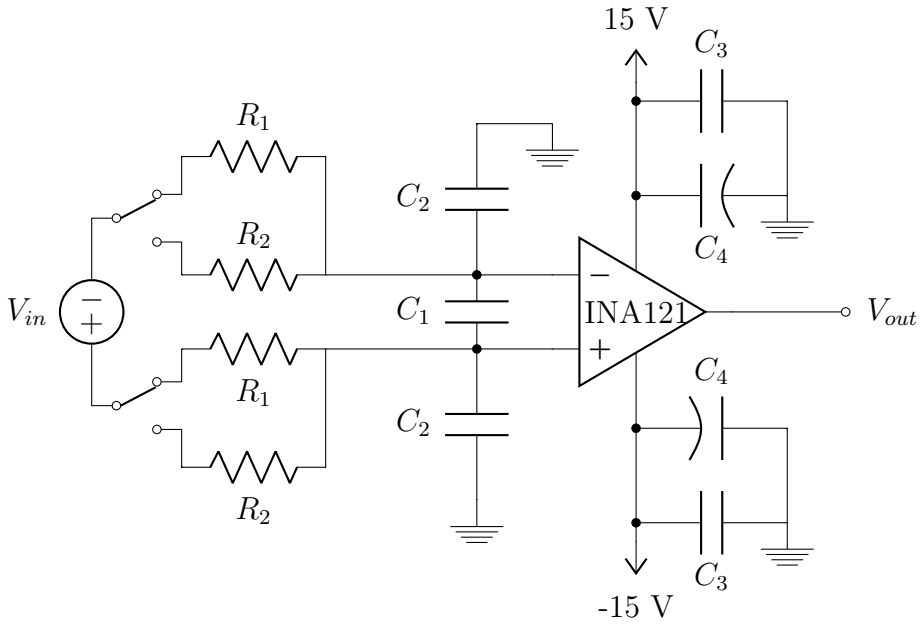

Figure 4.29: Ideal circuit for **B** field coils.

inputs that can inadvertently rectify high frequency noise on its input into a DC signal. Due to the use of switching power supplies, the motor's servo amplifier produces high frequency switching noise when turned on that is then rectified by the protective diodes in the INA121 input terminals to give a constant DC output voltage offset, which then translated into a DC shift in the magnetic field and a corresponding DC shift in the co-magnetometer's signal. One way to add (low-pass) filtering with an instrumentation amplifier like the INA121 while still retaining high CMRR is shown in Figure 4.29.

In Figure 4.29, the two SPDT switches are controlled by the same analog output voltage. Consequently, they both switch at the same time, which ensures that the impedance seen by both the inverting and non-inverting terminal of the INA121 is always the same. Moreover, this circuit design balances the input voltage offset caused by the input bias currents so that in theory, resistors larger than 2 MΩ can also be used. Capacitor C_1 in between the input terminals filters out common-mode noise while capacitors C_2 on each input rejects high frequency differential noise. Power

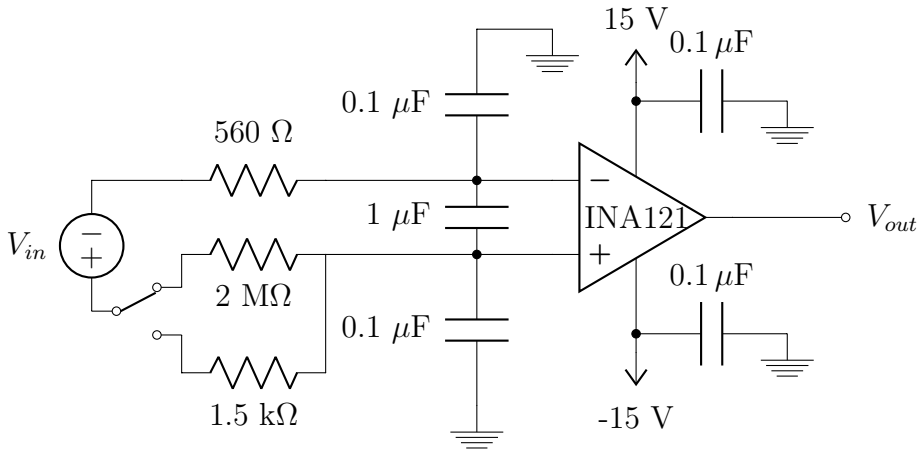

Figure 4.30: Actual filter and buffer circuit for the magnetic field coils.

bypassing capacitors C_3 and C_4 placed near the power pins also help filter out noise from the power lines. We note that the $f_{-3\text{dB}}$ frequency for this filter is somewhat different from the simpler filter in Figure 4.27. Indeed, it is not difficult to show by applying Kirchoff's laws and performing some algebra that the magnitude of the voltage V_{C_1} across the capacitor C_1 is[49]

$$|V_{C_1}| = \frac{V_{in}}{\sqrt{1 + \omega^2 R_1^2 \left(C_2 + 2C_1\right)^2}}, \tag{4.67}$$

so that the cut-off frequency is

$$f_{-3\text{dB}} = \frac{1}{2\pi R_1 \left(C_2 + 2C_1\right)}. \tag{4.68}$$

Although the circuit in Figure 4.29 would be ideal, it would require twice the number of SPDT switches and resistors on the circuit board, which the existing board could not accommodate. Even though building an entirely new filter circuit was not difficult, it was moderately laborious and time consuming. Consequently, we settled for a compromise that worked sufficiently well. The actual circuit used in the experiment is shown in Figure 4.30.

[49] We assume an ideal amplifier and that the SPDT switches are connected to the R_1 resistors.

We note that in the actual circuit, a single resistor of 560 Ω is[50] placed on the inverting input instead of having another SPDT switch and the corresponding 2 MΩ/1.5 kΩ resistor due to spatial constraints on the board. Also, only one (ceramic) power bypassing capacitor is used closed to the pins (there are two larger electrolytic capacitors that filter the shared power line for all the chips) due again to spatial constraints.

Analog inputs

In addition to affecting the low-pass filters in the magnetic field circuits, the high frequency switching noise from the motor's amplifier can also couple to the data acquisition systems and cause additional noise in the data. To mitigate this, passive low-pass filters similar to that depicted in Figure 4.29 were added in the electronic breakout box before the National Instrument programmable gain amplifier (NI-PGIA)[51] to filter out any noise picked up by the cables. Since these data acquisition (DAQ) cards have only one NI-PGIA, they are unable to perform truly simultaneous measurements of different analog inputs. Rather, they use a multiplexer to quickly connect the PGIA to different analog input channels. The cross-talk from one physical channel to another is therefore dependent on the sampling rate and the settling time after each switch by the multiplexer. Since the passive low-pass filters effectively increases the source impedance[52], it is crucial to choose a resistor that does not drastically increase the source impedance to the detriment of the settling time in between each physical channel (and by extension, the amount of cross-talk between distinct physical channels). A filter with the resistor/capacitor values in Figure 4.31 was used in

[50] This value was chosen by trial and error to provide sufficient impedance on the inverting terminal so that there was no visible change in offset when the filter is turned on/off while the motor amplifier is turned on.

[51] We use National Instruments M and S series data acquisition cards for data acquisition. Analog inputs to these cards are all fed to a NI-PGIA before being digitized.

[52] We note that this will not be a problem if active filters are used. However, building active filters for the over 30+ channels used in this experiment is prohibitively time consuming. In the end, the passive filters, chosen appropriately, work sufficiently well.

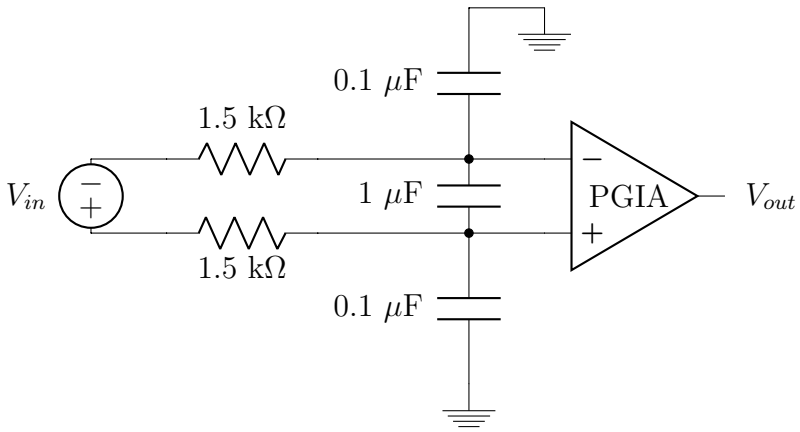

Figure 4.31: Low-pass filter used before NI-PGIA.

this experiment, which have a $f_{-3\text{dB}} \approx 50$ Hz. We note that as in the case of the INA121, it is important to retain high CMRR by employing a balanced filter. Since we typically sample at 200 Hz, the filters in Figure 4.31 also act as anti-aliasing filters.

Ground loops

By Faraday's law of induction, a changing magnetic flux through a loop of wire induces a voltage along the length of the wire that is proportional to both the rate of change of magnetic field and the area of the loop. This is frequently a source of much annoyance when the "loop" is formed by ground connections between different equipment since high frequency magnetic noise, which is not easily shielded, can then induce voltage differences on a supposedly common "ground" line that changes over time. Twisted wire pairs and co-axial cables reduce this coupling by minimizing the relevant loop area but the area covered by an inadvertent ground loop can be quite significant and it is therefore important to avoid such loops by making ground connections carefully. Physically, this implies that each equipment should only be grounded via one source.

In this experiment, the optical table is grounded via a single braid that is screwed down onto the table on one end and connected to the building ground on the other end. Equipment placed on the optical table can therefore be grounded either via their power cables (which is preferable) or by electrical contact with the table. Many

unintentional ground loop connections are formed when an equipment is grounded both by its power cable and its contact with the optical table. For example, the Hinds photoelastic modulator (PEM) optical head is grounded via its connection to the electronic head. However, it can also be grounded via electrical contact with the optical table through the optical post used to support it on the optical table. To avoid this problem, Kapton tape was used to carefully isolate it from the table. Other prominent equipment that are susceptible to this problem include lasers, photo-diodes and quadrant photo-diodes. For all of these equipment, a one inch ceramic spacer was used to electrically isolate them from the optical table. The Edwards vacuum gauge measuring the vacuum pressure inside the vacuum chamber was another source of such a ground loop connection since it is grounded both by virtue of its electrical contact with the optical table through the vacuum chamber and its own power cable. Since the vacuum pressure is a relatively unimportant measurement for us once the vacuum chamber has been pumped down, we simply disconnect the vacuum gauge's power cable during the experiment to eliminate the ground loop associated with it. We have also found that the Jewell Instruments tiltmeter used in this experiment can have a ~ 4 MΩ connection to the optical table through its legs when it is turned on that can be mitigated by placing Kapton tape on its legs.

Ground loop connections can also be formed in a data acquisition channel if the reference line is grounded at both the source/sensor and at one input of the acquisition instrumentation amplifier. To eliminate such loops, the reference line should be grounded at either the source or at the input of the acquisition instrumentation amplifier[53]. Since we typically use differential analog inputs on our NI-DAQ cards to acquire analog voltages (which means that the reference line is not grounded at the input of the NI instrumentation amplifier), this implies that most sources should be grounded on their end. The exception to this is the signal photodiode since its output

[53]We note that the reference line should not be left floating since in that case, it may float beyond the amplifier's rails.

does not go directly to the NI-DAQ card but is first sent to a SRS 830 DSP lock-in amplifier for demodulation. The SRS 830 DSP lock-in amplifier's input configuration ties the shell of the input cable to ground either via a 10 Ω (ground option) or a 10 kΩ (float option) resistor. Accordingly, the signal photodiode's reference should be left floating on its end to avoid a ground loop.

Accidental ground loop connections may also be formed by electrical contact between copper braids, which are typically used to provide extra shielding for sensitive cables, and another electrically grounded surface. Ideally, these braids should be covered with either electrical or Kapton tape to ensure that no such accidental electrical contact can occur.

During our campaign to remove all ground loops from the experiment, we also uncovered an unexpected ground loop connection involving the motor, which should be nominally grounded only via its power cable from the servo motor amplifier. However, unbeknownst to us (initially), the support frame to which it is attached and that is suspended from the ceiling was also separately grounded even though it had no contact, electrical or otherwise, with any objects below. Evidently, one (or more) of the eight 5/8" bolts that suspend the entire structure from the ceiling is in contact with a rebar rod in the reinforced concrete ceiling, which is tied to earth ground. Since the motor and reduction gear are only supported via an adapter plate that is held by screws from the aluminum support structure, to break this ground loop it should, in theory, be sufficient to break this electrical connection. However, there was an additional sneaky electrical connection because the rubber shaft coupler, which couples the gear to the aluminum drive shaft, turns out to also be conductive. Consequently, to break up this insidious ground loop we had to not only use electrical tape to insulate the rubber from the aluminum driveshaft, but we also had to insulate

the adapter plate from the aluminum support structure by placing thin insulating washers between them[54].

Additional shielding

To further suppress the effects of the motor amplifier's electromagnetic interference, sensitive cables were equipped with clamp-on ferrite beads to reject high-frequency common-mode noise and they are shielded with additional tinned copper braids. We note here that for these braids (or any other conductor used for this purpose) to provide shielding, they *must* be grounded on one and only one end. If the braid is left floating, it simply acts as an antenna that can re-radiate and couple more noise into the wires it was supposed to shield. If the braid is grounded on two ends, it forms a ground loop and can cause the same problem. For co-axial cables without an additional separate shield, it is crucial that the shell is grounded (i.e. the signal is referenced to ground) to prevent excessive (and strange) noise/interference. However, this is rarely a problem since most analog inputs have to (as explained above) be grounded. Analog outputs are also typically referenced to ground so in most cases, this is not an issue. However, there are instances when the analog outputs are *not* referenced to ground and this can lead to unexpected problems.

For example, the NI S series DAQ card used in this experiment (PCI-6154) has isolated analog outputs, which means that the shell of the co-axial cable can now be floating if it is also not tied down to ground on the other end. Indeed, this was exactly what happened when the four analog outputs from the isolated PCI-6154 card were used to control the magnetic field coils. As described above, these analog outputs were each connected to the differential inputs of a INA121 instrumentation amplifier for filtering and buffering. However, since the differential inputs of the

[54]It might perhaps seem easier to simply ground the motor/gear via the ceiling structure and to break the ground connection between the motor and the amplifier. However, it was important to directly ground the motor with the amplifier and not doing so can lead to wrong voltage differences and increased noise, which we observed.

INA121 were not tied down to ground, the shell of all four co-axial cables from the isolated PCI-6154 card was inadvertently left floating, which led for a while to very bizarre, bewildering and amusing behavior. For example, electrostatic charge accumulated on the human body (for example by standing up from a chair) can allow a human dancing near the entrance of the laboratory (away from any other equipment) to affect the co-magnetometer's signal as charge on the human body shift the potential of the shell of the co-axial cables, which then result in a (small but measurable) shift in the currents to the magnetic field coils that is then translated to a measurable change in the co-magnetometer's signal. We have confirmed the electrostatic origin of this spooky action at a distance by checking that the effect disappears as soon as the human grounds himself and reappears after the human charges himself by, for instance, rubbing on a piece of plastic[55].

In addition to shielding critical wires, electromagnetic interference from the motor's amplifier was also mitigated at the source by placing the entire amplifier in a μ-metal shield that was also grounded to minimize any high frequency switching noise emanating from the amplifier itself. Nevertheless, the cable running from the amplifier to the servo motor is still capable of radiating high frequency noise. A three-phase reactor was installed on the output wires (within the μ-metal shield) to mitigate this effect and a noise filter was also installed on the inputs to the amplifier to reduce any noise coupling back into the wall power supplies. Finally, all motor related circuitry was separated from the rest of the experiment; the computer that communicates with the motor controller does so through an optically isolated DB-9 interface.

[55]The night this effect was discovered was probably this author's most amusing night in the dungeons of Jadwin since it seemed for a while as though he possessed a truly supernatural ability to change the current in a wire by the mere movement of his body.

4.5.2 Mechanical contact and vibration

During the course of SMILE, many diagnostic sensors were deployed in the hopes of detecting systematic effects that the motion/position of the weights may have on various experimental and environmental parameters, which might in turn induce a systematic effect on the actual co-magnetometer's signal. For example, there was concern that the position of the vacuum chamber might shift ever so slightly due to either the motion and/or position of the weights. Consequently, Omega's LD701 series non-contact inductive linear displacement sensors were employed to measure the position of the vacuum chamber. It was quickly discovered during early test runs of SMILE that these sensors were measuring a large systematic effect with respect to the position of the weights.

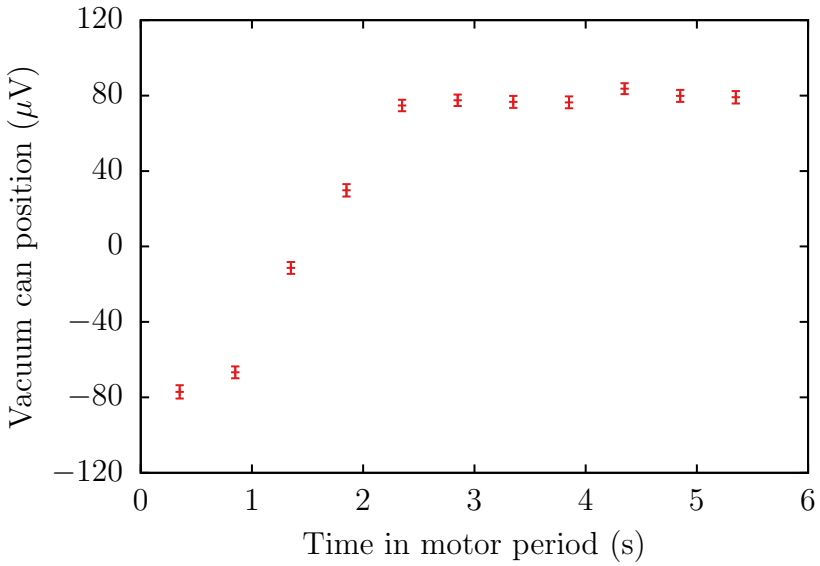

Figure 4.32: Correlation measurements from a LD703 non-contact displacement sensor at a motor period of 6 s.

Figure 4.32 shows the correlation of the vacuum can's position as a function of the time within a motor period, as analyzed using the procedure outlined in section 4.4.2. During this early phase of testing, we were using a different motor period of 6 s in which the weights completed their motion in 3 s and waited for 3 s before reversing

their positions. At first sight, the data in Figure 4.32 seems to be indicating that the vacuum chamber's position was very strongly correlated with the position of weights. Based on the manufacturer's calibration, a correlation of 80 μV would correspond to a position correlation of roughly 20 nm, which is small enough to be believable. However, the cause of this movement seems mysterious since analysis of data from a tiltmeter mounted on the optical table using the methods described in section 4.4.2, which has proven capable (see Figure 4.25) of detecting even slight mechanical contact between the weights and optical table (or parts thereof), yielded null results implying that there was never any mechanical contact between the weights and the vacuum chamber.

Even though the mechanical load on the ceiling of the room is by design nominally the same when the weights are at rest, it is perhaps plausible that to the extent that the cancellation is imperfect, the position of the weights could still result in a slight tilt of the optical table. Nevertheless, an overall tilt of the optical table cannot explain the result in Figure 4.32 since to the degree that the LD701 detector and the vacuum chamber are both rigidly mounted to the optical table, a overall tilt of the table does not cause a relative change in position between the vacuum chamber and the LD701 detector. And in any case, the size of the position correlation in Figure 4.32 would (naively and discounting the fact that both the detector and vacuum chamber are in fact rigidly mounted on the optical table) have required a tilt correlation of $\sim$ 20 nrad, which was not detected.

A plain interpretation of the result in Figure 4.32 would suggest that the position of the weights are somehow capable of warping either the mount holding the LD701 detector or the supports of the vacuum can. The aforementioned tiltmeter is in some sense a vibration sensor but it has a low bandwidth (around 1 - 2 Hz), which might obscure higher frequency mechanical noise that could potentially indicate some kind of mechanical coupling between the weights and objects on the optical table. Therefore,

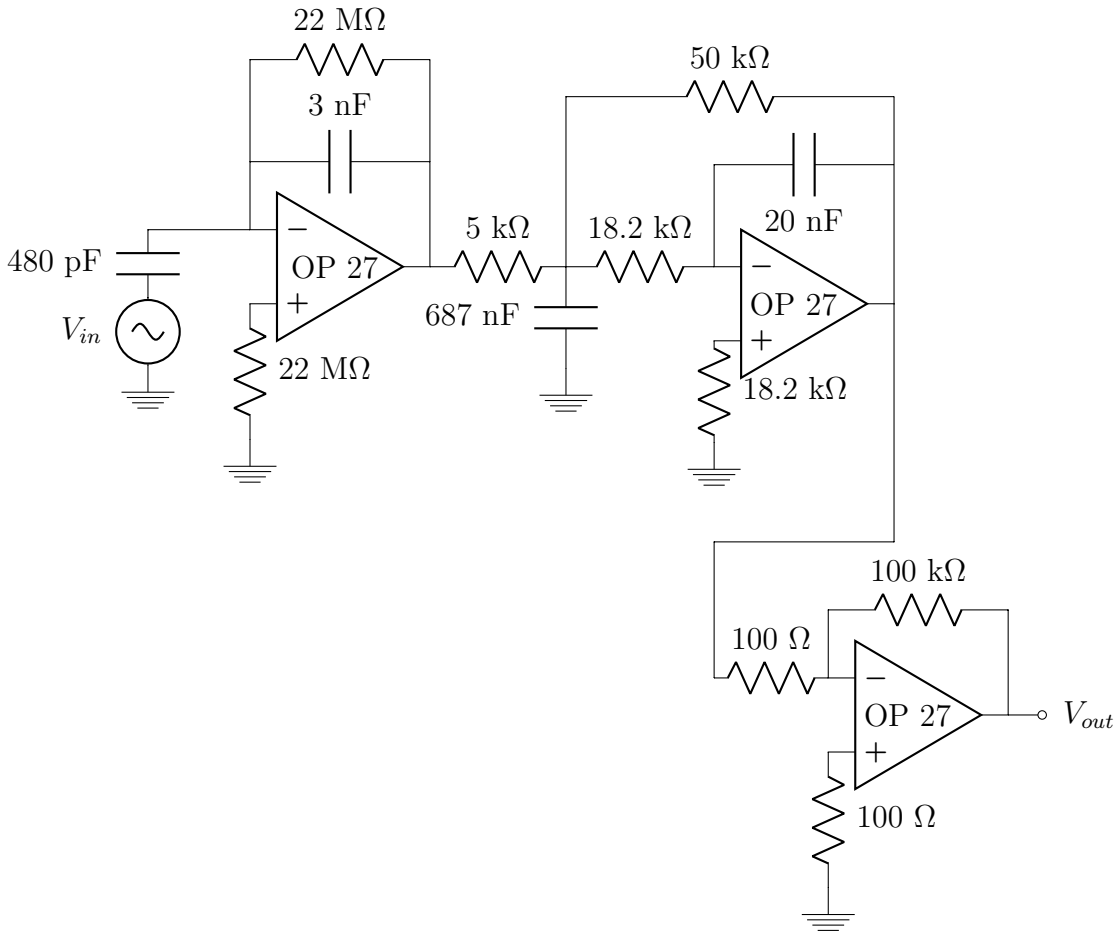

Figure 4.33: Circuit diagram for vibration sensor.

to further investigate the magnitude of any possible mechanical coupling between the weights and the table, we devised an inexpensive home-built vibration sensor built around a cantilever piezo film to mount on the optical table.

We used a LDT0 series cantilever piezo film with an added mass at its end for increased sensitivity. The film has a quoted mechanical resonant frequency at 90 Hz with $f_{+3\text{dB}} \sim 45$ Hz, and a capacitance of 480 pF. Figure 4.33 shows the electronic circuit[56] that was employed to read out the charge build-up on the film as a result of it flexing due to motion/vibration. In Figure 4.33, the piezo film is modeled as an oscillating voltage source in series with a 480 pF capacitor on the left, which is

[56]For the sake of brevity, power bypassing capacitors for all of the op-amps are not shown here.

then connected to a charge amplifier[57]. The output of the charge amplifier is then fed to a 2nd order Butterworth low-pass filter with a gain of 10 and a corner frequency of $f_{-3\text{dB}} \sim 45$ Hz that was chosen to roughly match the $f_{+3\text{dB}}$ of the piezo film's mechanical resonance. Finally, the output of the Butterworth filter is passed into an inverting voltage follower with a gain of 1000 for further amplification.

We tested the vibration sensor to ensure that it was functioning as expected. Unsurprisingly, the vibration sensor excelled at detecting higher frequency mechanical noise but was considerably less sensitive compared to the tiltmeter in measuring slow tilts. Consequently, a sharp knock of the table with a hard, metallic object would produce a signal in the vibration sensor but not in the tiltmeter whereas a knock with a softer object like a human hand would produce a signal noticeable on the tiltmeter but less so in the vibration sensor. We took additional data with the vibration sensor but data from the vibration sensor also did not indicate anything unusual when the weights are in motion and it was ultimately unable to explain the results in Figure 4.32.

It turns out that the large correlation observed in Figure 4.32 was a "dirty" effect that has to do with the LD701's principle of operation. As mentioned earlier, the LD701s are inductive linear displacement sensors, which means that they measure distance to a metal target by measuring the damping (back e.m.f) of a time-changing magnetic field that a coil inside it produces. In the ideal case, there ought to be no additional damping of the magnetic field besides that from the target but in the real world, the presence of other metals in the LD701's vicinity could contribute to a false signal. This is particularly problematic in our case since even though the weight stacks are arguably considerably further away from the sensor compared to the vacuum chamber, it is nevertheless conceivable that some of the damping the sensor

[57]We note that the 22 MΩ resistor connected to the inverting input is necessary since a finite input bias current at that terminal will otherwise eventually saturate the capacitors. The 22 MΩ resistor at the non-inverting input is there for balancing.

measures is attributable to the weight stacks, which implies that the sensor would directly measure a signal that is correlated to the position of the weights through this unintended coupling. To test this hypothesis, we shielded the sensor from the weights by mounting and enclosing the sensor in a metallic box so that only its front, which faces the vacuum chamber, is exposed. Copper tape between the mounting box and the vacuum chamber further shield the sensor from the presence of the weights and turned out to be an important additional piece of shielding. The result was dramatic.

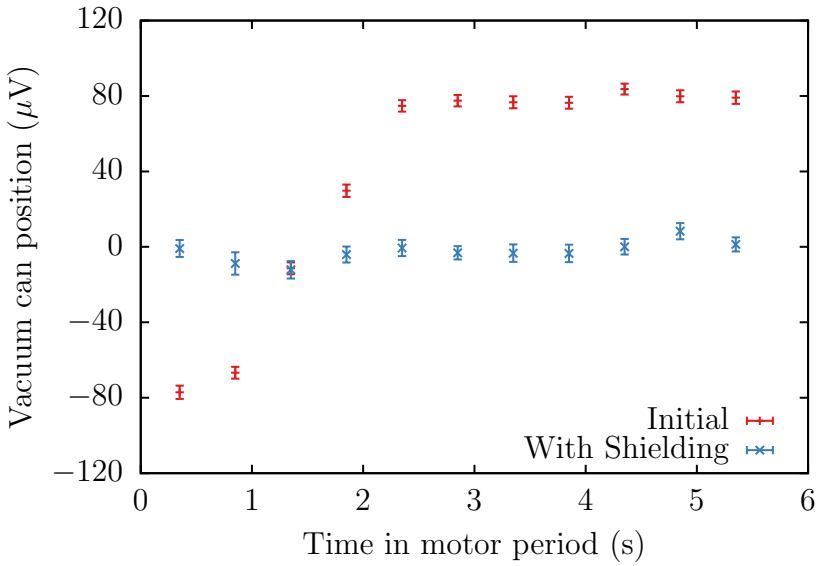

Figure 4.34: Effect of shielding on LD703 non-contact inductive displacement sensors.

Figure 4.34 shows the reduction in measured correlation after the implementation of the aforementioned shielding. Clearly, the electromagnetic shielding of the LD701s described above was successful in mitigating the false correlation first depicted in Figure 4.32. However, we soon became aware of another correlation in the distance measurements of the LD701 after we increased the motor period from 6 seconds to 10 seconds.

Figure 4.35 shows the magnitude and time-dependence of this new correlation in the measurements of the LD701 sensor. We note that in Figure 4.35, the motor moves the weights in 5 seconds and waits for an additional 5 seconds before reversing

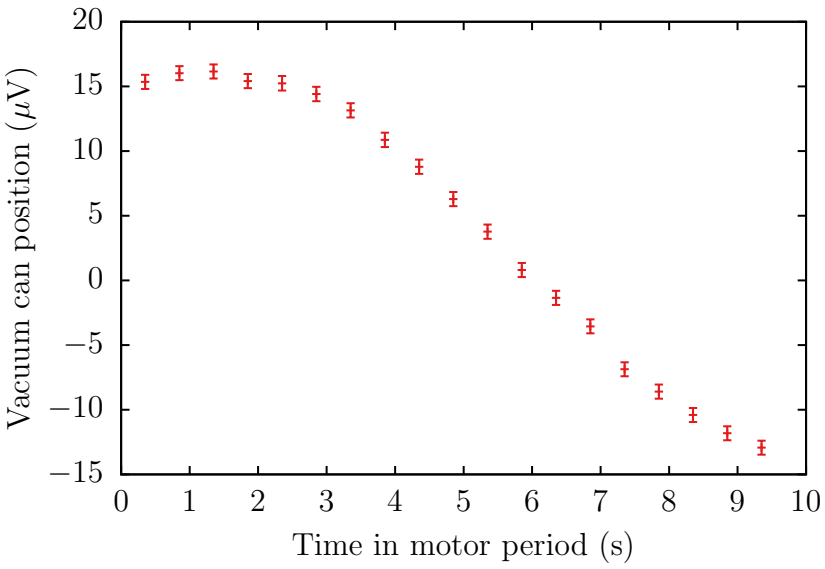

Figure 4.35: Correlation measurements from a shielded LD703 non-contact displacement sensor at a motor period of 10 s

the positions of the weights. Evidently, the time dependence depicted in Figure 4.35 is quite distinct from that shown in Figure 4.32. Indeed, in Figure 4.32, the time dependence of the correlation closely tracks the position of the weights, which is consistent with the fact that the correlation originates, albeit in an unintentional way, from the aluminum plates supporting the Pb weights. On the other hand, the correlation depicted in Figure 4.35 does not track the position of the weights since it continues to change long after the weights have come to a rest at 5 seconds. Together with its reduced magnitude at 15 μV instead of 80 μV, this suggests that the correlation shown in Figure 4.35 has a different physical origin and is not due to the sensor unintentionally measuring the position of the weights.

In fact, the time dependence of this new correlation closely resembles the time dependence of a correlation that appeared in the home-built vibration sensor described above. As Figure 4.36 shows, the correlation from the vibration sensor has a similarly long time constant that continues to change long after the motor has stopped at 5 seconds. We note here that although the vibration sensor was designed to have a higher bandwidth compared to the tiltmeter, the analysis used to produce Figure 4.36

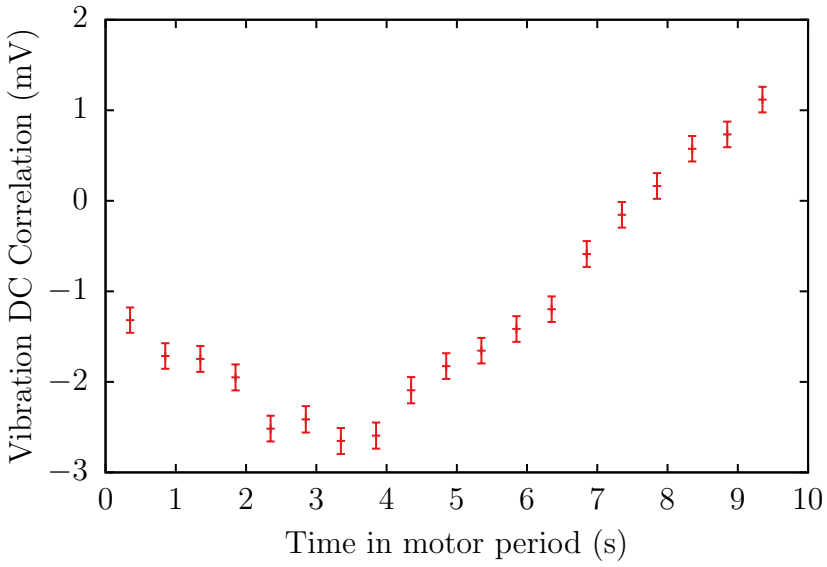

Figure 4.36: Correlation measurements of vibration sensor's DC offset.

effectively averages (see discussion in section 4.4.2) out the ac part of the vibration sensor's signal so that we should understand the result in Figure 4.36 as the correlation in the DC offset of the vibration sensor's signal. The DC offset of the piezo film can be due to a mechanical force but the slow time dependence depicted in Figure 4.36 makes this possibility unlikely. Rather, the slow time dependence suggests a thermal origin for the correlation, which the vibration sensor is particularly sensitive to due to its high electronic gain.

To test if the correlation in Figure 4.36 is thermal in nature, we taped foam insulation on top of the aluminum box housing the electronics of the vibration sensor and acquired additional data. As Figure 4.37 demonstrates, there was a significant decrease in the correlation of the vibration sensor's DC level after application of the foam insulation indicating that the cause of the correlation in Figure 4.36 is indeed thermal in nature.

This suggests that the correlation of the LD701 displacement measurements is also of thermal origin. Consequently, we started to cover as much of the vacuum chamber with foam insulation as was feasible given spatial constrains.

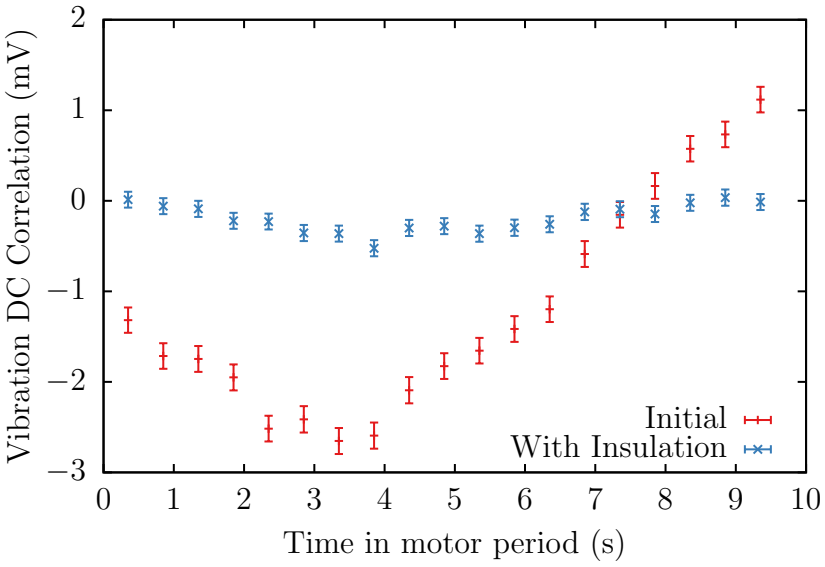

Figure 4.37: Effect of thermal insulation on vibration sensor's correlation.

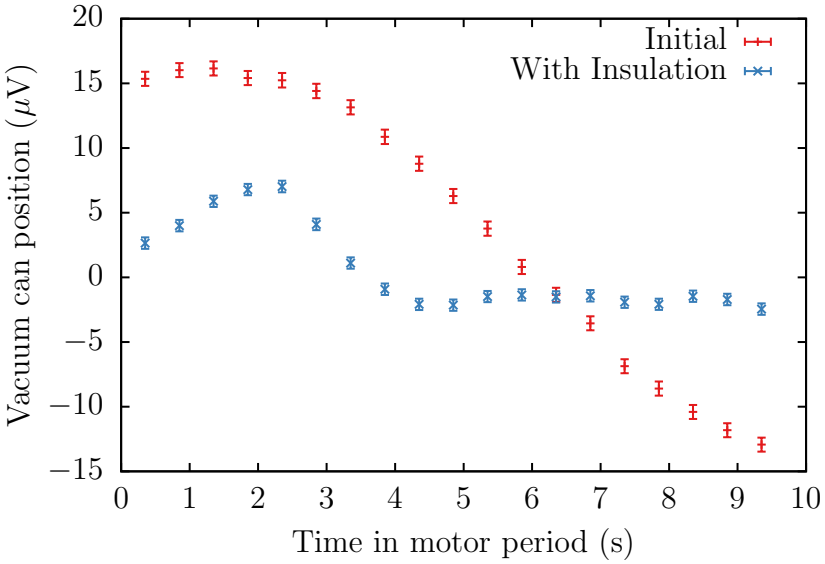

Figure 4.38: Effect of thermal insulation on vacuum chamber.

Figure 4.38 shows how applying thermal insulation to the vacuum chamber affects the measured correlation of the LD701 non-contact displacement sensor. We note that the decrease in correlation is not as dramatic as in Figure 4.37 or in Figure 4.34. Furthermore, a careful look at the measurements after 5 seconds reveal a small but non-zero correlation that persists after the weights have come to a rest. The residual correlation is $\sim 2\mu$V, which translates into a displacement correlation of about 0.5

nm. As we shall discuss in greater detail in the following section, we have measured a 1 m°C correlation in temperature difference between the two sides of the vacuum chamber facing the weight stacks. Given a fractional linear expansion co-efficient of 23.1×10^{-6} per °C for aluminum [66], a displacement correlation of 0.5 nm due to thermal expansion then seems quite plausible since an aluminum sheet with 25 mm in linear dimensions would expand by ~ 0.5 nm given an increase of 1 m°C. Also, we note that the correlation shown in Figure 4.38 does not cross zero in the middle of the motor's motion (at 2.5 seconds) as it does in Figure 4.32 (at 1.5 seconds), which suggests that this remaining systematic effect is of a different physical origin and is not due to the sensor measuring the position of the weights through an inductive coupling. We therefore believe that the remaining systematic effect observed at the end of the weights' motion in Figure 4.38 is a real physical effect and is due to imperfect thermal insulation of the vacuum chamber since there was insufficient clearance to apply any thermal insulation to the sides of the vacuum chamber facing the weight stacks[58], where they are arguably most needed.

Since we were unable to completely remove this systematic effect, we sought to quantify it by calibrating the co-magnetometer's response to a slight displacement of the vacuum chamber. This calibration was accomplished by pushing on the vacuum chamber with a spring and measuring the signal of both the co-magnetometer and the LD701 non-contact displacement sensor. The magnitude of this systematic effect can then be constrained by measuring the actual displacement of the chamber during the experiment.

[58] We note that this lack of clearance was intentional in the design of SMILE since it was desirable to have the weights as close to the co-magnetometer as experimentally feasible given constrains such as magnetic shielding.

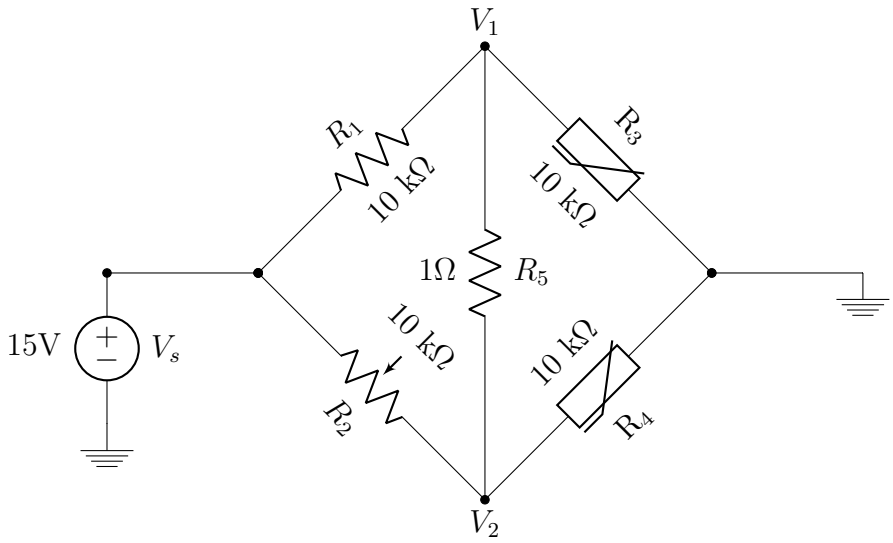

Figure 4.39: Circuit diagram of vacuum can temperature sensors.

4.5.3 Temperature gradient

As discussed in the previous section, placing foam insulation around the vacuum chamber aided in reducing the correlation of its position with the position of the weights as measured by the LD701 non-contact linear displacement sensors. This strongly suggests that the origin of the vacuum chamber's motion is due to a temperature difference between different sides of it. To investigate this further, we placed two 10 kΩ RTD on either side of the vacuum can facing the weight stacks. Since the effect is expected to be small, we utilized the Wheatstone bridge circuit in Figure 4.39 to eliminate common mode drifts and noise between either RTD.

To account for variations in resistances, the circuit in Figure 4.39 was tuned by placing the two RTDs, R_3 and R_4, together in a cup of melting ice. The potentiometer R_2 was then tuned to zero out the voltage difference $V_1 - V_2$. During the experiment, V_1, V_2 and $V_1 - V_2$ were measured. It is easy to show that given V_1 and V_2, the resistance R_3 and R_4 are

$$R_3 = -\frac{R_1 R_5 V_1}{R_1 (V_1 - V_2) - R_5 (V_s - V_1)}$$
$$R_4 = \frac{R_2 R_5 V_2}{R_2 (V_1 - V_2) + R_5 (V_s - V_2)}. \tag{4.69}$$

The nominal values of the R_1, R_2, R_5 and V_s are shown in Figure 4.39. A rough calibration to temperature units may be accomplished using the nominal values of the components and equations (4.69), and taking the temperature coefficient of resistance of the platinum RTDs to be $\alpha = 0.00385\ \Omega/\Omega/°\mathrm{C}$ (the ASTM standard).

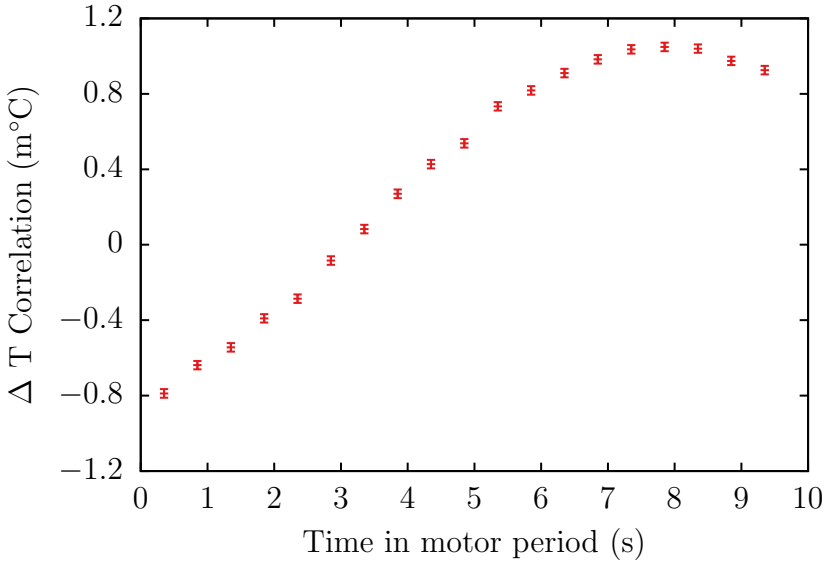

Figure 4.40: Measured correlation of temperature difference between the two sides of the vacuum chamber.

Figure 4.40 shows the measured correlation in the temperature difference between the two sides of the vacuum chamber facing the weight stacks. We note that it has a long time constant like the correlation of the vacuum chamber's position in Figure 4.35. Also, it has a magnitude of about 1 m°C, which as argued in the preceding section, is sufficient to explain a positional shift of the vacuum chamber by 0.5 nm due to thermal expansion. There could be various causes for this correlated temperature gradient to develop including differential cooling from the motion of the air when

the weights are moved and/or decreased volume of air that restricts heat loss via convection on one side of the vacuum chamber when one weight is close to it, and/or changes in black body radiation gain/loss that depends on the position of the weights. Clearly, there are a number of possibilities and it is not immediately obvious what is the mechanism(s) responsible for the observed temperature gradient correlation. This is an unexpected systematic effect that we did not anticipate during the design of SMILE and will have to be addressed in future versions of SMILE.

4.5.4 Changes in ambient light

Besides the correlations observed in the vacuum chamber's position, we also observed a remnant non-zero correlation in the intensity of the probe laser as measured by a quadrant photo-diode before the beam entered the vacuum chamber. Figure 4.41 shows a correlation of $\sim$ 3 μV after the weights have come to a stop. We note that the time dependence of the correlation depicted in Figure 4.41 is reminiscent of Figure 4.32 since the correlation here also tracks the position of the weights in that it switches between one level to another during the first 5 seconds while the weights are in motion and then remains at that level for the next 5 seconds while the weights are at rest.

Even though the optical enclosures are all covered with blackout fabric and the room lights are turned off during data taking, the time dependence of the correlation in Figure 4.41 suggests that it might be due to changes in the remnant ambient light as the weights alternately reverse positions. After all, if the probe laser's intensity was truly changing, one might expect the peak correlation to occur during the acceleration of the weights when there is the largest amount of mechanical and electromagnetic noise. To check if the correlation in Figure 4.41 is due to changes in the ambient light as a result of the weights' changing positions, we performed a test run in which the weights were moved as usual but the probe laser was turned off so that any measured

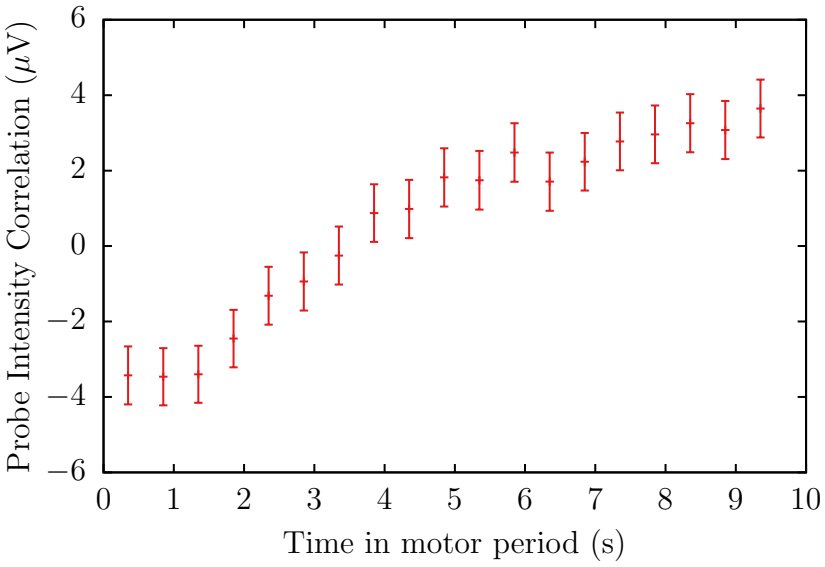

Figure 4.41: Measured correlation of probe intensity from quadrant photo-diode before the vacuum chamber.

correlation would be due only[59] to changes in the ambient room light. It typically requires a fairly long time of integration to achieve the level of uncertainty in Figure 4.41, especially since the signal of the quadrant photo-diode in Figure 4.41 is acquired using a NI-DAQ card with ~ 0.3 mV of resolution and there is additional noise from the probe beam. We have therefore, for the sake of expedience, used a Keithley 7510 DMM with 7 digits of precision to acquire the quadrant photo-diode's signal during this test run.

Figure 4.42 shows the result of this test run. We note that the correlation measured during the test run with the probe laser off and acquired using the DMM7510 has the same time dependence as the correlation measured during the SMILE run and acquired with a NI-DAQ card. However, the measured correlation of the test run is somewhat smaller than in the SMILE run and subtracting the background correlation (the test case) from the correlation in the SMILE run yields Figure 4.43, where there is arguably still a faint trace of a correlation at the end of the motor's motion.

[59]Technically, it could also be due to some electronic effect but that seems unlikely given the time dependence of the correlation.

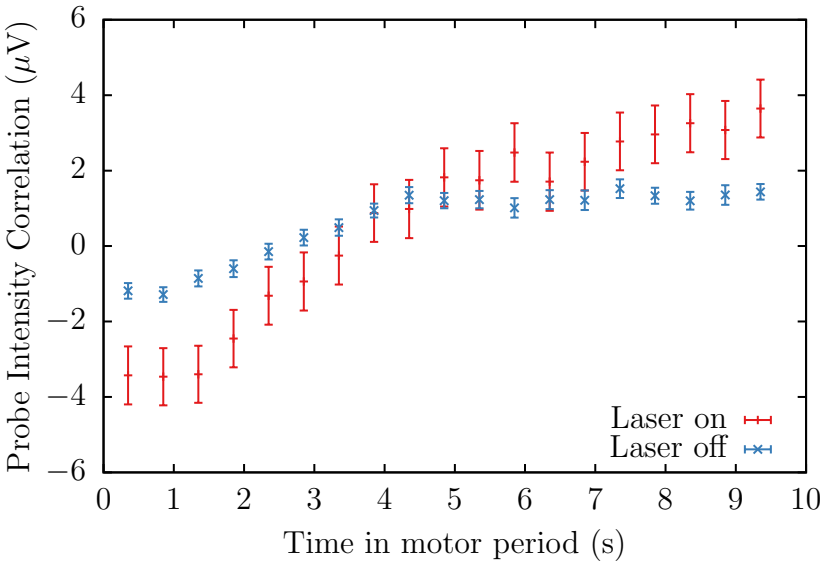

Figure 4.42: Measured correlation due to ambient light.

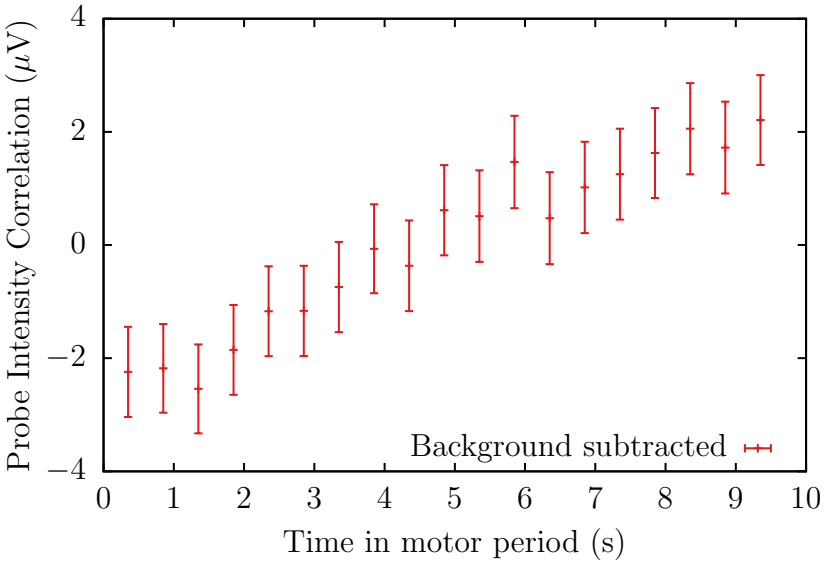

Figure 4.43: Measured correlation of probe intensity after background subtraction.

Nevertheless, we do not believe that this is real (in the sense that it stems from a real fluctuation of the probe beam intensity during the SMILE run) for a number of reasons. Firstly, the fact that both the background and actual SMILE run have the same time dependence for the correlation of the probe beam intensity (as measured from that particular quadrant photo-diode) suggest that the correlation measured during the SMILE run is due to changes in the ambient room light. Secondly, although

the measured correlation during the background run is somewhat smaller than during the actual SMILE run, this can be easily attributed to the difference in accuracy of the calibration of the Keithley DMM 7510 and NI-DAQ card, which is older and probably has a less accurate calibration compared to the Keithley DMM.

In any case, even if the remaining correlation is real and is due to real correlations of the probe beam intensity, it is too small to seriously affect the final results for SMILE. We may calibrate the effect of a real fluctuation of the probe beam's intensity on the co-magnetometer's signal by deliberately modulating the probe laser's current and measuring the response in both the co-magnetometer and the quadrant photo-diode. Applying this calibration to the "remnant" correlation in Figure 4.43 yields a correlation of about 20 aT whereas the final statistical uncertainty of SMILE is 70 aT. Perhaps more importantly, other sensors that also measure the intensity of the probe laser such as another quadrant photo-diode located after the vacuum chamber and the second harmonic of the lock-in's input signal did not register any significant correlation. Indeed, the final correlation measurement of the probe beam's intensity from that other quadrant photo-diode was -7 ± 6 aT. Consequently, we feel justified in ignoring the small "correlation" observed in this particular quadrant photo-diode.

4.6 Constraining Anomalous Spin-Mass Couplings

We present here the final results of SMILE and derive their constrains on anomalous spin-mass couplings of unpolarized fermions to (spin) polarized neutrons and electrons. As discussed in section 4.3, we search for a correlation between the co-magnetometer's signal and the position of the weights. More specifically, during the SMILE data runs, the motor move the weights in 5 seconds and waits for another 5 seconds before reversing their position. For the final analysis of SMILE, we measured the correlation of the signal with the position of the weights during the last 2 seconds

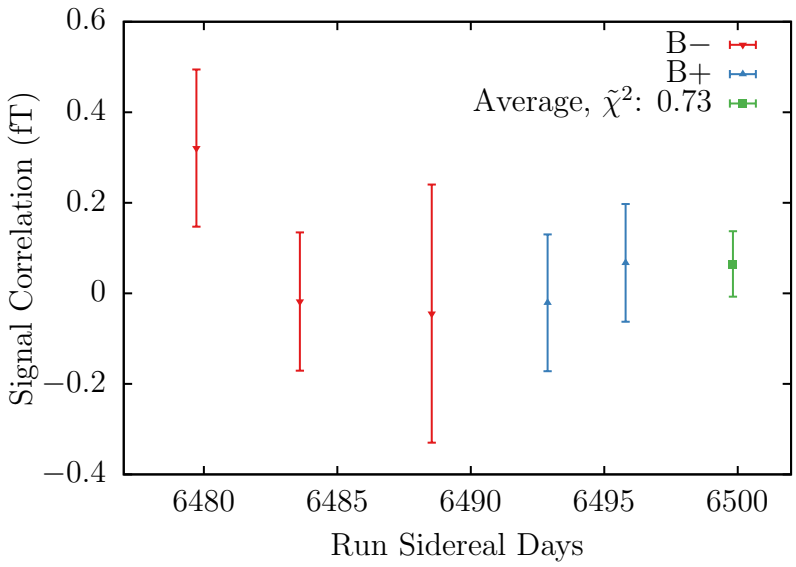

Figure 4.44: Measured correlation of co-magnetometer's signal for different SMILE runs.

of the waiting period to let any transients die away. The correlation during the last two seconds of the waiting period is then calculated using the string analysis method detailed in section 4.4.1. As explained at the end of section 4.3, SMILE was ran in two magnetic field configurations, $B+$ and $B-$, to cancel out spurious effects that do not couple to the spins of the atoms. Figure 4.44 shows the result of 5 data runs with different B field configurations. $B-$ runs are denoted with red triangles pointing down while $B+$ runs are denoted with blue triangles pointing up. The weighted average is given by the green square point. For 4 degrees of freedom, the $\tilde{\chi}^2$ is 0.73.

Estimates of systematic effects may also be obtained by measuring the correlations of various other experimental parameters during the same last two seconds of the motor's waiting period and then multiplying them by an appropriate calibration factor. The calibration factor measures the sensitivity of the co-magnetometer's signal to an experimental parameter and may be measured by applying an appropriate excitation and then measuring the response from both the co-magnetometer and the sensor monitoring the parameter. For example, the sensitivity of the co-magnetometer to external $\mathbf{B}$ field was measured as discussed in section 4.2.4 and its sensitivity to the

position of the vacuum chamber may be calibrated as discussed at the end of section 4.5.2. Similarly, the co-magnetometer's sensitivity to the position and intensity of the laser beams may be calibrated by respectively moving the beams with a piezo mirror and modulating the laser current while observing both the co-magnetometer and quadrant photo-diode's response. Table 4.2 delineates the measured calibrated correlations from various experimental parameters as well as the correlation from the co-magnetometer signal in both the $B+$ and $B-$ configurations followed by the final weighted average co-magnetometer correlation of all the runs in both configurations.

Experimental parameter	Calibrated Correlation (aT)
Pump position X	2 ± 4
Pump position Y	-12 ± 7
Pump intensity	2 ± 5
Fluxgate B_x	-0.24 ± 0.02
Fluxgate B_y	0.03 ± 0.01
Fluxgate B_z	-0.19 ± 0.03
Oven heater output	-1 ± 1
Vacuum chamber position	-13 ± 13
Pump glass tube position	2 ± 2
Probe position X	-12 ± 9
Probe position Y	-3 ± 6
Probe intensity	-7 ± 6
Rotation Ω_x	1 ± 1
Rotation Ω_y	0.1 ± 0.7
Total	-41 ± 20
Signal (B+)	-5 ± 100
Signal (B−)	70 ± 100
Signal	32 ± 70

Table 4.2: Summary of measured correlations in the signal and other calibrated sensors.

In addition to the experimental parameters listed in Table 4.2, we also measured various other parameters that were not calibrated in the manner described above. Nevertheless, we present them in Table 4.3 for completeness. We note that "oven analog control" in Table 4.3 is not the same parameter as "oven heater output" in Table 4.2. "Oven heater output" refers to the de-modulated amplitude of the actual AC heating waveform going into the oven whereas "oven analog control" refers to the control voltage that the temperature controller sends into the oven's power amplifier.

Experimental parameter	Correlation
Signal 2nd harmonic	5 ± 3 μV
Pump intensity set point	50 ± 60 nV
Vibration DC offset	125 ± 25 μV
Optics air temperature	0.04 ± 1 μV
Oven analog control	3 ± 3 μV
AOM control voltage	-3.7 ± 1.5 μV
Optical table height	200 ± 150 nV
Vacuum chamber temperature gradient	1 ± 0.009 m°C

Table 4.3: Summary of measured correlations in other non-calibrated sensors.

We also note that two parameters in Table 4.3 show a clear correlation with the position of the weights: the vibration DC offset and the vacuum chamber's temperature gradient. The measurement of the vacuum chamber's temperature gradient and its potential causes were discussed in section 4.5.3, and as explained in section 4.5.2, the vibration sensor's DC offset is due to a correlation of its electronics' temperature with the position of the weights. Since the systematic effects from the various parameters listed in Table 4.2 should be independent, their uncertainties may be combined in quadrature to give an estimate of the overall systematic uncertainty. Moreover, as Table 4.2 shows, the final calibrated correlations of these experimental parameters are not statistically significant and we therefore do not use them to correct the final correlation from the co-magnetometer's signal. Accordingly, we quote as the final result,

$$\beta^n - \beta^e < (32 \pm 70_{\text{stat}} \pm 20_{\text{syst}}) \text{ aT},$$

which gives an upper limit $|\beta^{e,n}| < 155$ aT at 95% C.L.

If we make the typical assumption that the coupling to unpolarized fermions g_s^N is the same for neutrons and protons and is zero for electrons in the unpolarized mass, then we may, barring accidentally cancellation of β^e and β^n, derive constraints on $g_p^n g_s^N$ from these limits by noting that the neutron is 87% polarized in ^{3}He [212, 213], which implies that we may set

$$\mu_{^3\text{He}} \beta^n > g_p^n g_s^N 0.87 A, \tag{4.70}$$

where $\mu_{^3\mathrm{He}}$ is the magnetic dipole moment of ^{3}He and A is the numerical factor from the integration of (1.35) over all the nucleons in the Pb mass. Similarly, we may write

$$\mu_B \beta^e > g_p^e g_s^N A, \tag{4.71}$$

where μ_B is the Bohr magneton, to derive the limits on $g_p^e g_s^N$. Figure 4.45 shows the new constraints that this work places on $g_p^n g_s^N$. We note that in Figure 4.45, the limits in [48, 50] were multiplied by 2 to obtain a 95% CL while those from [51] was extrapolated by integrating over the Earth's mass density for heavier axions. [214] uses astrophysical constraints to limit g_p^n and the solid red line (1) in Figure 4.45 represents the constraints set by SMILE.

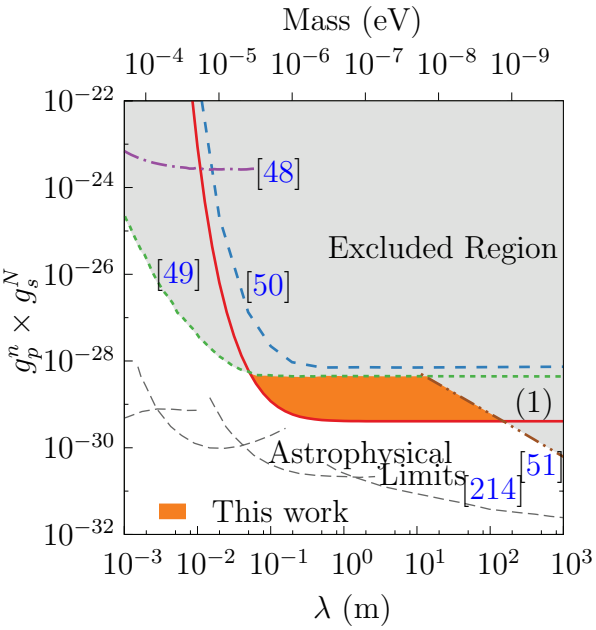

Figure 4.45: Constraints (95% CL) on $g_p^n g_s^N$ for the neutron.

Similarly, Figure 4.46 shows the new limits that SMILE places on $g_p^e g_s^N$ for the electron. As before, the solid red line (1) represents the results of this work and the limits in [50] were multiplied by 2 to obtain a 95% CL while those from [214] uses astrophysical observations.

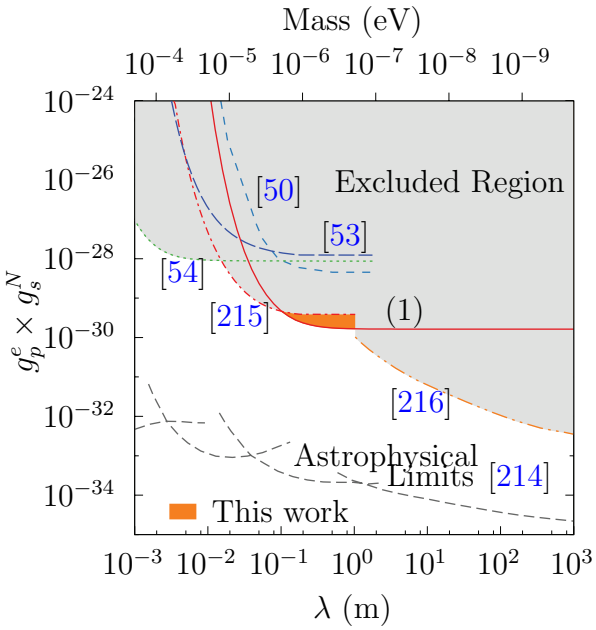

Figure 4.46: Constraints (95% CL) on $g_p^e g_s^N$ for the electron.

Our results represent, by an order of magnitude, the most stringent laboratory limits on $g_p^n g_s^N$ for axion-like particles (ALP) with masses lighter than 3×10^{-6} eV, although we note that for much lighter ALP masses ($\sim< 10^{-9}$ eV), additional constraints can be derived from experiments using the Earth as a source mass [51, 216].

Chapter 5

Pulsed Co-magnetometer

In chapter 3, we introduced the continuously pumped[1] co-magnetometer and showed in section 3.1 that at the compensation point, it has a suppressed response to ordinary **B** fields while retaining first order sensitivity to anomalous fields. Moreover, as we demonstrate in section 3.3 and 4.2.4, the CW co-magnetometer also has a suppressed response to slow changes in **B**. However, the Achilles' heel of the CW co-magnetometer is that although it has suppressed response to **B** fields at the compensation point, deflections of the pump and probe beam still nevertheless, as a cursory glance at (3.30) confirms, affects its signal at the same level as an anomalous field. Physically, we may understand this as a geometric effect since at the compensation point, the alkali atoms are in a low **B** field environment and they are therefore, to a good approximation, polarized along the direction of the pump beam. Since the probe beam measures the x projection of the alkali's electronic polarization, any projections of the pump beam in the x direction will appear as an un-suppressed first order term in the co-magnetometer's signal. The CW co-magnetometer's first order sensitivity to pump and probe beam deflections typically limits its low frequency sensitivity as was the case in SMILE (see section 4.2.6) and has long been a bane to achieving better sensitivities at low frequencies.

[1] We shall also for brevity refer to this as the CW co-magnetometer.

The pulsed co-magnetometer however, has the potential to overcome these limitations of the CW co-magnetometer and enable a whole new generation of alkali-noble gas co-magnetometer that is capable of achieving significantly better low frequency sensitivity. Since the pump beam affects the co-magnetometer's signal at leading order, the simplest solution would be to turn it off. However, since we need to spin polarize the atoms, we cannot afford to have it off all the time. Consequently, the compromise is to pump the atoms with short intense pulses and then to watch them decay in the dark with a weak probe beam. Nevertheless, there remains the problem of interpreting the decay and extracting useful information from it. Obviously, our steady state treatment of the CW co-magnetometer in section 3.1 will be of no avail here and in fact, the Bloch equation (2.361) that describes the macroscopic polarization of the alkali atoms is somewhat less valid in this case since the polarization of the alkali atoms will vary significantly during the decay and consequently, the slowing down factor Q, which is assumed constant in (2.361), will also vary[2]. In the sections below, we shall numerically investigate several properties of the pulsed co-magnetometer but it is helpful to first gain an intuitive understanding of the pulsed co-magnetometer's signal.

As in the CW co-magnetometer, the spin orientation of the alkali atoms is read out via optical rotation of a linearly polarized off-resonant probe beam and the signal of the pulsed co-magnetometer is therefore proportional to the x projection of the alkali's electronic polarization. If the pump beam is exactly co-linear with the ambient $\mathbf{B}$ field, the atom's spin polarization will simply decay along the $\mathbf{B}$ field's direction without precessing during the dark period. If in addition the probe beam is exactly orthogonal to the pump beam/$\mathbf{B}$ field, then there will be zero signal. However, if the probe is misaligned with the pump/$\mathbf{B}$ field so that its inner product with them is

[2]This is less of a problem for the CW co-magnetometer since it's polarization is relatively constant during operation and so the slowing down factor can quite reasonably be taken to be constant.

non-zero, then one would observe an almost[3] exponentially decaying signal. Suppose now that the probe beam is orthogonal to the **B** field but there is a misalignment between the pump beam and the **B** field. Since the pump beam is not aligned with the **B** field, the spin polarization of the alkali atoms will not be co-linear with the **B** field and consequently, when the pump beam turns off, the spins will precess about the **B** field. In this case, the signal will be an decaying (due to the spins' transverse relaxation) oscillation. In the most general case, the probe beam will not be exactly orthogonal to the **B** field and consequently, the signal will also contain an (almost) exponentially decaying term on top of the decaying oscillation. We therefore expect a decay signal of the form

$$P_x^e(t) \propto S(t) = e^{-t/T_2}[A\sin(2\pi ft + \phi) + D\cos(2\pi ft + \phi)] + Be^{-t/T_1} + C, \qquad (5.1)$$

where we have included a constant offset C here to take into account a possible DC offset from the optical rotation signal. A, D, B, C, T_1 and T_2 are in general all fit parameters while ϕ is a fixed phase that the user provides.

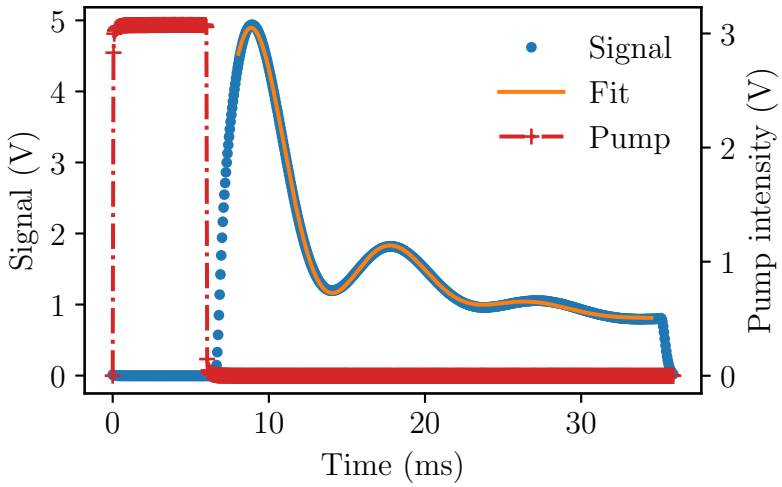

Figure 5.1: Fit of decay signal in a pulsed co-magnetometer.

[3]It's technically only exponential at late time due to the non-constant slowing down factor.

Figure 5.1 shows an example of a typical pump and decay signal from the pulsed co-magnetometer. The pump intensity (red dash-dot) turns on for 6 ms before turning off for 30 ms during which the spins precess and decay. The orange line is a fit of (5.1) to the lock-in amplifier's output (blue dots). Note that to prevent the lock-in amplifier from over-loading during the pump phase, we gate its input so that it only sees a constant DC signal when the pump is on, which explains the signal's zero value during the pump phase. After the pump turns off, the lock-in amplifier receives the the signal from the photodiode and we wait for $\sim$ 2 ms before fitting (5.1) to the data. As Figure 5.1 shows, the decay is fairly well described by (5.1) although we note that there is an observable change in the signal's frequency at the end of the decay due to the changing slowing down factor which is not described by (5.1).

From the discussion above, it is evident tha misalignments between the pump and $\mathbf{B}$ field will result in an oscillating decay. Similarly, anomalous fields, which will serve to misalign the effective $\mathbf{B}$ field away from the pump beam, will also result in an oscillating decay. The signal of interest in the pulsed co-magnetometer is therefore its oscillating decay component. In the CW co-magnetometer, we defined a compensation field $B_c = -B_e - B_n$ that is the sum of the alkali and noble gas' effective magnetization and showed that the co-magnetometer exhibits suppression of $\mathbf{B}$ fields at that particular value of B_z. We expect that to be true of the pulsed co-magnetometer as well except that in this case, B_e is the average alkali effective magnetization over a pump and decay period. This has important implications for the choice of alkali/noble gas species in the pulsed co-magnetometer. Since the signal of interest in the pulsed co-magnetometer is the oscillating component of the decay, it is critical that the frequency of the oscillations is sufficiently rapid so that there are at least a few cycles of oscillations within the decay time. However, the frequency of the oscillations at the compensation point is determined by the magnitude of the alkali's effective magnetization $|B_e|$ and consequently, we need an alkali-noble gas pair with

a sufficiently large contact interaction so that there are a few oscillations during the decay time[4]. It turns out that the contact interaction between K and ^{3}He is too small but Rb and ^{21}Ne, which as Table 2.3 shows has a contact interaction ~ 5 times larger than K and ^{3}He, will suffice. Accordingly, although a Rb-^{21}Ne co-magnetometer is somewhat less sensitive compared to K-^{3}He because of Rb's faster relaxation, we work with Rb-^{21}Ne in the rest of this chapter on the pulsed co-magnetometer.

5.1 Density Matrix Simulations

To further investigate the properties of the pulsed co-magnetometer, we turn now to numerical simulations. We begin by noting that the use of ^{21}Ne introduces a few complications. Firstly, as discussed briefly in section 2.9, the pre-dominant relaxation of the $K = 3/2$, ^{21}Ne is due to the interaction of its quadrupole moments with induced electric fields during collisions with other atoms. Consequently, its relaxation rate is determined by the number density of the surrounding buffer gas, which in this case is predominantly Ne itself. Ghosh and Romalis have experimentally measured the T_1 of Ne to scale as [95]

$$T_1 = \frac{214 \pm 10}{n} \quad \text{min}, \tag{5.2}$$

where n here is the number density in amagat. Secondly, the higher nuclear spin of ^{21}Ne compared to ^{3}He invalidates the spin-exchange rate equation with alkali atoms found in (2.350) by interchanging $\mathbf{S} \leftrightarrow \mathbf{K}$. Rather, from [116] and [95] we expect the polarization of ^{21}Ne to evolve as

$$\frac{d\mathbf{P}^n}{dt} = \gamma_n \left(\mathbf{B} + \lambda M_e \mathbf{P}^e + \boldsymbol{\beta}^n + \frac{\Omega}{\gamma_n} \right) \times \mathbf{P}^n + R_{se}^{ne} \left(\frac{\epsilon(K, P^n) S}{K} \mathbf{P}^e - \mathbf{P}^n \right) - R_{sd}^n \mathbf{P}^n, \tag{5.3}$$

[4] We note that B_e depends also on the density of alkali atoms so going to higher temperatures will also help. However, there is a limit to how high the temperature can be raised before the alkali atoms start attacking the glass cell.

where $S = 1/2$ and $K = 3/2$ is the electron and noble gas spin respectively, and $\epsilon(K, P^n)$ is the paramagnetic coefficient as defined in (2.115), except that K and P^n are now the spin and polarization of ^{21}Ne. Compared with (2.356), the main difference here is the presence of the paramagnetic coefficient ϵ, which is here a measure of how efficiently the noble gas atom with spin K depolarize/polarize the alkali atoms with electronic spin S [75]. As we noted above, the Bloch equations in (2.361) for the alkali atom will be quantitatively wrong since it assumes a constant slowing down factor. This assumption is true to an excellent approximation in the CW co-magnetometer since the bulk of its polarization is longitudinal and constant. However, in the case of the pulsed co-magnetometer where the alkali polarization will vary significantly during each pump and decay cycle, it is best to model its dynamics using a density matrix formulation that will accurately take into account the changing slowing down factors. One key distinction between the pulsed co-magnetometer and its CW counterpart is that in the pulsed co-magnetometer, we aim to fully polarize all of the alkali atoms during the short intense pulses. In the CW co-magnetometer, fully polarizing the atoms will result in poor sensitivity to anomalous fields since the spin orientation of the atoms will then be mostly dominated by the pump beam. However, this is no longer a problem in the pulsed co-magnetometer since the atoms will precess freely in the dark during the measuring interval. A corollary of this is that in the pulsed co-magnetometer, there should ideally be no polarization gradient (except near the walls) since all of the atoms in the bulk are fully polarized during the pump pulses. Consequently, there is no need for hybrid pumping. We therefore pump the alkali

atoms directly and model them with the density matrix equation

$$\begin{aligned}\frac{d\rho^i}{dt} = \frac{1}{i\hbar}[\tilde{H} + \delta\mathscr{E}_{se} - 2\mathscr{E}_m \mathbf{s}_m \cdot \mathbf{S} - 2\mathscr{E}_p \mathbf{s}_p \cdot \mathbf{S}, \rho] + R_m(\phi^i(1 + 2\mathbf{s}_m \cdot \mathbf{S}) - \rho^i) \\ + R_p(\phi^i(1 + 2\mathbf{s}_p \cdot \mathbf{S}) - \rho^i) + R^i_{sd}(\phi^i - \rho^i) + R^{en}_{se}(\phi^i(1 + 4\langle \mathbf{K} \rangle \cdot \mathbf{S}) - \rho^i) \\ + \sum_j R^{ij}_{ex}(\phi^i(1 + 4\langle \mathbf{S}^i \rangle \cdot \mathbf{S}) - \rho^i), \end{aligned} \tag{5.4}$$

where we have set $\mathbf{q}_{m,p} = 2\mathbf{s}_{m,p}$ for $\mathcal{D}_1$ pumping and all the terms are as described in (2.357) and (2.358). We have retained the superscript i here since in natural abundance Rb, which we used in one of our cells, there is a significant amount of both ^{85}Rb with $I = 5/2$ and ^{87}Rb with $I = 3/2$. Consequently, we include both species (labeled by the superscript i) to take into account their different slowing down factors. We note that to be fully accurate there should be a correction in the R^{en}_{se} term corresponding to the ϵ factor in (5.3). However, we have for simplicity omitted that correction in these simulations. We note that in general the inclusion of that correction will modify how effectively the noble gas depolarizes the alkali atoms via spin-exchange collisions and its absence will therefore have the effect of underestimating the alkali's spin relaxation.

Simulating the density matrix equations (5.4) can be quite computationally expensive, especially since the full system has $8 \times 8 + 12 \times 12 = 208$ complex elements and the ground-state hyperfine constant is in the GHz range, which will necessitate a very small integration time step. However, since we are interested in the behavior of the system at much longer time scales, and the density matrix elements that are off-diagonal in F will be oscillating at hyperfine frequencies, we may regard them as effectively averaged to zero. Consequently, we follow [217] and set the off-diagonal terms in F to zero. We have verified that there is no discrepancy in the behavior of the system at our time scales of interest when this major simplification is used.

Simulations in this chapter were all performed in Python since its object-oriented structure made it significantly easier to construct modular and re-usable code. For example, an alkali atom class can be defined just once and different instances of the class corresponding to different alkali atoms containing all the necessary member spin operators relevant to it can be easily generated later on. Using Python also allows us to easily re-use a set of fitting routines written in C to automatically fit the decays to (5.1). As we will discuss in more detail later, these routines were first developed and written in C to allow LabVIEW to fit the measured decays in real-time and has been indispensable in allowing us to interact with the system in real-time. By using the same fit routines in the simulations as in the experiment, we eliminate one possible source of artificial discrepancy between the both of them. More practically, this makes maintaining all the various codes much easier since there is less unnecessary duplication and more portability. Git was used to help with version control of bug fixes and upgrades while PyTables was used to organize most of the simulation results in a hdf5 file so that simulation parameters and results can be stored and viewed together. Although (5.4) is a differential equation of the density matrix, we have followed [75] in converting it into a Liouville vector, which has allowed us to easily use standard ODE solvers in SciPy.

5.1.1 Suppression of pump beam deflections

One of the prime motivation behind the pulsed co-magnetometer is the hope that it will provide some suppression to misalignment of the pump beam. Since the pump beam is off during the dark measuring period, it might seem at first sight that all dependence on the pump beam should be removed from the pulsed co-magnetometer. However, this is an oversimplification since the system retains a "memory" of the pump beam's direction that is imprinted in the alkali's initial spin orientation before they decay. Indeed, unless the pump beam is exactly co-linear with the **B** field, the

alkali atoms will in general freely precess around the **B** field during the dark period. Nevertheless, we can still expect some suppression due to the noble gas. Consider a pump beam misalignment away from the **B** field. The beam's misalignment polarizes the alkali atoms away from the **B** field, which then creates a transverse effective field for the noble gas atoms in the opposite direction[5]. The rotation of the total field the noble gas experiences causes them to orient away from the alkali, which in turn causes a transverse effective field for the alkali atoms. This effective field rotates the total **B** field the alkali experiences closer to its polarization orientation, which reduces the amplitude of its oscillating decay. Notice that while the noble gas' polarization will also re-orient in a similar manner in the CW co-magnetometer, its re-orientation does not cause the alkali to re-align back to it's original orientation and the effect of a pump misalignment is therefore not suppressed. On the other hand, since the signal of interest in the pulsed co-magnetometer is the oscillating part of the decay, the field's re-orientation does suppress the effect of a pump misalignment by reducing the amplitude of the oscillations.

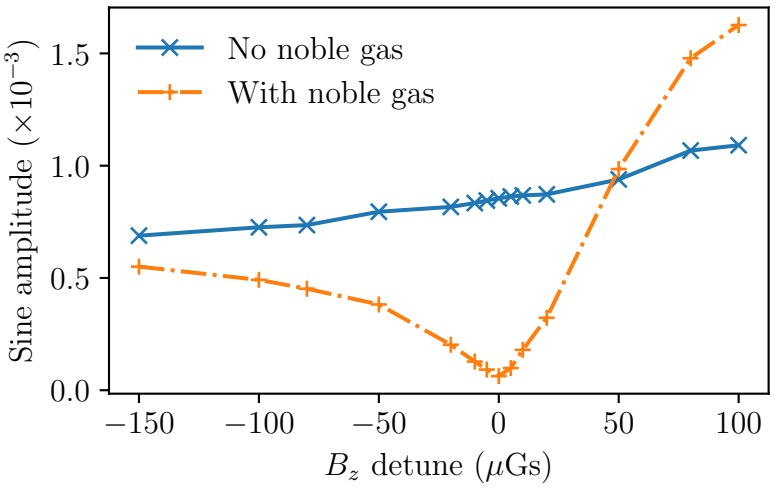

Figure 5.2: Total oscillation amplitude after a pump beam misalignment in the y-direction.

[5]It's opposite since the g-factor is negative.

We may verify this by numerically solving the coupled differential equations (5.4) and (5.3) for a fixed pump beam misalignment of 0.1° in the y direction while scanning B_z and fitting the decay to (5.1) after the system reaches steady state from the excitation of the misalignment. Figure 5.2 shows the total oscillation amplitude ($\sqrt{A^2 + D^2}$ from (5.1)) as a function of B_z detuning from the expected compensation point $B_c = -B_n - \langle B_e \rangle$, where by $\langle B_e \rangle$ we mean here the average of B_e over a pump/decay cycle. As the orange dash-dot line in Figure 5.2 shows, there is a clear dip in the magnitude of the oscillations at the compensation point due to a pump beam misalignment. It is interesting to compare this with the case where this is no noble gas. To make this a fair comparison, the applied **B** field has to be reduced to ensure that the alkali atoms see $|\mathbf{B}| = B_e$ at zero detuning in both cases. As the blue line depicts, there is, as expected, no suppression of the pump beam misalignment in this case.

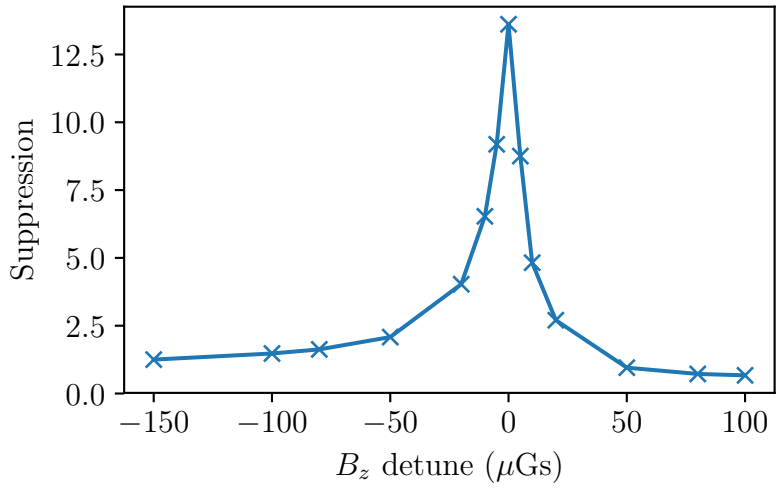

Figure 5.3: Pulsed co-magnetometer suppression of pump beam misalignment in the y-direction.

We may define the pulsed co-magnetometer's suppression to pump beam misalignment as the ratio of the oscillation amplitude in a pulsed magnetometer (i.e. no noble gas) to that of a pulsed co-magnetometer. Dividing the blue line with the

orange dash-dot line yields Figure 5.3, which shows that the pulsed co-magnetometer has a suppression of ~ 10 for the parameters used in the simulation. As mentioned above, we used natural abundance Rb here with rates $R_{np} = R_m + R_{sd}^e + R_{se}^{en} = 493$ /s and $R_p = 4434$ /s so that the maximum Rb polarization is about 90%. $|B_n|$ was 4.52 mGs and $|B_e|$ was 285 μGs, corresponding to an average (over a full pump/decay cycle) polarization of 2.43 % and 36.7 % respectively. The average polarization of the alkali during the dark period is slightly lower at 28.6%. We note that the HWHM of the suppression curve is $\sim R_{np}/(Q\gamma_e) \approx 16$ μGs, for a Q of 10.

5.1.2 Suppression of magnetic fields

Besides suppressing pump beam deflections, we expect that the pulsed co-magnetometer, like the CW co-magnetometer, will be capable of suppressing **B** fields as well. As in the preceding section, we have verified this numerically with the same simulation parameters as in section 5.1.1 but without any pump beam misalignment. Rather, we deliberately apply a B_y field of 10 μGs and scan the B_z field across the expected compensation point. In the CW co-magnetometer, the suppression of **B** fields is compared relative to the (first-order) response of the co-magnetometer to an anomalous field. Accordingly, we compare the pulsed co-magnetometer's response to a B_y and β_y^n field of the same magnitude (10 μGs) in Figure 5.4. In order to not obscure details from each response, the pulsed co-magnetometer's total oscillation amplitude ($\sqrt{A^2 + D^2}$ from (5.1)) response to β_y^n field (blue line) is plotted on the left axis while its response to B_y field (orange dash-dot) is plotted on the right axis. It is interesting to note that the pulsed co-magnetometer's peak sensitivity to anomalous fields does not exactly coincide with maximal suppression of B_y fields and that it increases for positive B_z detuning. We will discuss this more fully in section 5.1.3 but for now, we note that there is indeed maximal suppression of B_y fields at the compensation point as expected.

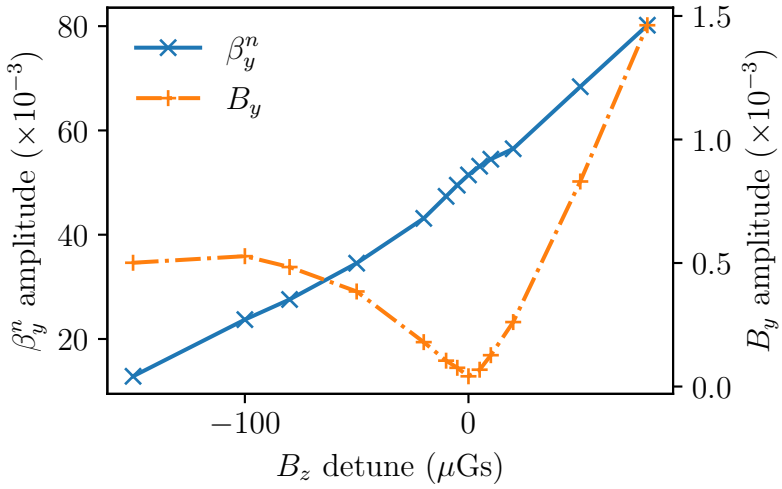

Figure 5.4: Total oscillation amplitude due to a B_y field.

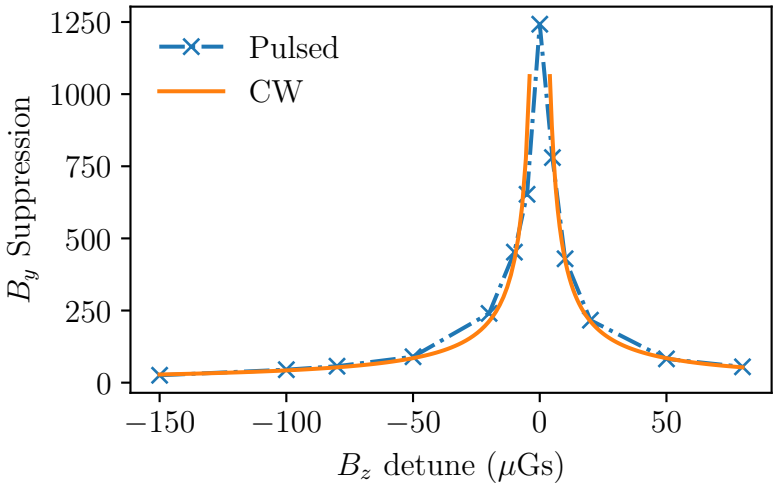

Figure 5.5: Pulsed co-magnetometer's suppression of B_y fields.

Figure 5.5 shows the pulsed co-magnetometer's suppression to B_y fields (blue crosses), which we have defined here as the ratio β_y^n/B_y. We may compare this to the suppression of B_y fields in the CW co-magnetometer. From (3.30), the ratio of the CW co-magnetometer's steady state response to β_y^n and B_y is simply B_n/B_z, where B_z is the detuning of the longitudinal magnetic field away from the compensation point. As in section 5.1.1, B_n in the simulation here is 4.52 mGs. Dividing this by the (absolute)

B_z detuning over a partial range of Figure 5.5 yields the orange CW curve, which shows good agreement with the pulsed co-magnetometer's suppression. We note that the agreement becomes significantly worst at smaller (absolute) B_z detuning since the simple expression B_n/B_z would naively predict infinite suppression whereas the pulsed co-magnetometer simulations obviously predict a finite suppression. This is not surprising since there are higher order terms in (3.30) that we have left out (such as terms due to spin-exchange between the alkali and noble gas atoms) that will give the CW co-magnetometer a small but non-zero B_y response even at zero B_z detuning.

It is interesting to note that for the same simulation parameters, the pulsed co-magnetometer exhibits significantly more suppression to B_y compared to pump beam misalignments in the y-direction. We believe that this is not an accident since there are subtle differences in the suppression mechanisms of the two cases. In the case of **B** field suppression, the noble gas reacts directly to the change in **B** and moves to orient itself parallel to the new **B** field. In doing so, its effective magnetic field cancels out part of the change in **B** that the alkali atoms would have otherwise experienced and consequently, the co-magnetometer's response to **B** is suppressed. On the other hand, in the case of pump suppression, the noble gas reacts to the change of the effective magnetization from the alkali atoms and it suppresses the oscillation by rotating the total effective **B** that the alkali atoms experiences to align with the pump beam.

5.1.3 Simultaneous dual axis sensitivity

In the CW co-magnetometer, we are as (3.30) shows, primarily only sensitive to anomalous coupling fields in the y direction. Physically, this is not surprising since the probe beam is only sensitive to P_x^e, the projection of the alkali polarization in the x direction, which is exactly the direction that an anomalous field in the y direction will tilt the alkali spins in. It is however, not sensitive to anomalous coupling fields in the x direction since they cause the spins to tilt in the y direction, which the

probe beam cannot detect. In the pulsed co-magnetometer, the probe beam is also only sensitive to P_x^e. Nevertheless, there is a subtle difference since in the pulsed co-magnetometer, the signal consist of the oscillation amplitude of the precessing alkali polarization during the dark period. If the **B** field is exactly aligned with the pump beam, then the magnitude of those oscillations is a measure of how much the anomalous coupling fields tilt the effective **B** field of the alkali atoms away from the pump beam. But since an anomalous field in the x direction can cause a misalignment as well as an anomalous field in the y direction, we expect that in contrast to the CW co-magnetometer, the pulsed co-magnetometer will exhibit first order sensitivity to anomalous fields in both the x and y directions.

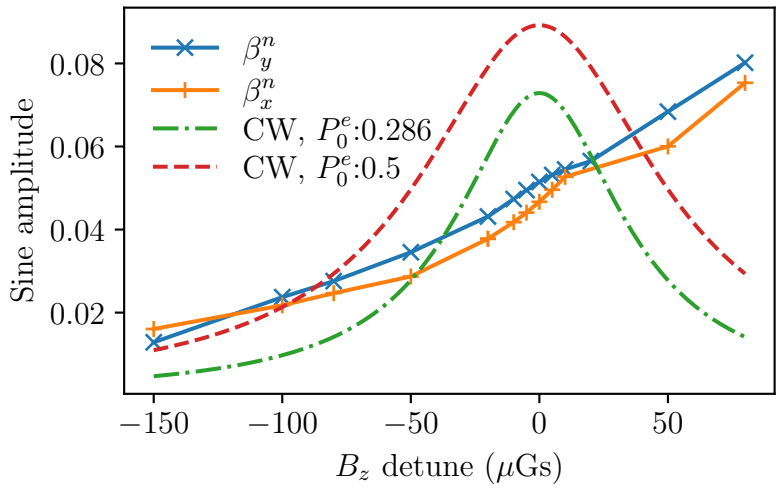

Figure 5.6: Sensitivity of the pulsed co-magnetometer to β_x^n and β_y^n as a function of B_z detuning.

Figure 5.6 shows the simulated magnitude of the oscillations due (separately) to an applied β_x^n and β_y^n of 10 μGs and demonstrates that there is no significant difference in the pulsed co-magnetometer's response to anomalous fields in the x or y directions. The simulation parameters used here are the same as in section 5.1.1. We may also compare the pulsed co-magnetometer's sensitivity to β_x^n and β_y^n fields with the CW co-magnetometer's sensitivity to β_y^n fields as a function of

B_z detuning. As explained at the beginning of this chapter, the signal of interest in the pulsed co-magnetometer is in the amplitude of the oscillations whereas in the CW co-magnetometer, the signal of interest is simply the steady state value of P_x^e given by (3.30). We may therefore compare the magnitude of the pulsed co-magnetometer's oscillations to the CW co-magnetometer's response given in (3.30) due to an anomalous field $\beta_y^n = 10$ μGs. In Figure 5.6, we also show calculations of the CW co-magnetometer's response given the same $R_{np} = 493$ /s relaxation rates of the pulsed co-magnetometer's simulations. The green dash-dot line shows the CW co-magnetometer's response to $\beta_y^n = 10$ μGs with a longitudinal alkali polarization P_0^e of 28.6%, which corresponds to the average alkali polarization of the pulsed co-magnetometer (in the simulations of Figure 5.6) during the dark measuring period, while the red dashed line shows the CW co-magnetometer's response with an optimum (see section 3.2) longitudinal alkali polarization of 50%. Evidently, the green dash-dot line corresponding to calculations using the average alkali polarization of the pulsed co-magnetometer during the dark, measuring period is a better match to the simulated magnitude of the oscillations of the pulsed co-magnetometer at zero B_z detuning.

It is interesting to note that in the CW co-magnetometer, the sensitivity to anomalous fields is maximal at the compensation point and falls off as $1/({R_{tot}^e}^2 + \gamma_e^2 B_z^2)$ per (3.30) whereas in the case of the pulsed co-magnetometer, the sensitivity to anomalous fields seem to increase at positive B_z detuning away from the compensation point, which corresponds in the simulations of Figure 5.6, to a smaller longitudinal **B** field for the atoms. This has two important implications for the pulsed co-magnetometer. Firstly, positive detuning of B_z in this case reduces the frequency of the alkali's oscillations and can completely eliminate it when the total applied longitudinal magnetic field cancels out the noble gas' effective magnetization. Practically, this means that at certain values of positive B_z detuning where $|B_n - B_z|$ is small, it is no longer

possible to fit the decay to (5.1) since there are not enough oscillations within the dark period and the magnitude of the oscillations then becomes ill defined. For the simulations in Figure 5.6, this occurs at a B_z detuning of around 80 μGs, which explains its upper B_z limit. Secondly, as a positive B_z detuning reduces the longitudinal **B** field that the atoms experience, the total rotation/misalignment of the effective field that the atoms experience increases for a fixed magnitude of anomalous field. Indeed, when the positive detuning exactly cancels out the noble gas' effective magnetization so that the alkali atoms experience zero **B** field, an anomalous electron coupling field in the y-direction will cause the alkali atoms to see a maximal 90° misalignment between the pump and its effective magnetic field (assuming that the pump is aligned with the longitudinal magnetic field) during the dark period. This will cause it to precess completely in the x-z plane and result, barring relaxation and decoherence, in maximal oscillation amplitude of P_x^e. However, this effect is not measurable for small β_y^e fields since the frequency of these oscillations will be too slow compared to both the lifetime of the alkali's polarization and the dark period. In reality, we can therefore only observe an increase in anomalous field sensitivity due to an increased misalignment of the effective field until the oscillations become too slow to measure as Figure 5.6 shows. We note that the dynamics is quite different in the CW co-magnetometer's case since the presence of the pump beam and its strong pumping rate there means that the atoms are mostly oblivious to these changes in misalignments as B_z is changed. Rather, the dependence of the CW's co-magnetometer's sensitivity to anomalous fields on B_z detuning is likely due to changes in how strongly the alkali and noble gas atoms are coupled to each other.

Besides having equal sensitivity to anomalous fields in both x and y directions, we expect that the oscillations in a pulsed co-magnetometer due to an anomalous field in the x direction will be 90° out of phase with oscillations due to an anomalous field in the y direction, which implies that we can simultaneously measure anomalous

fields in the x and y directions by simultaneously measuring the in and out-of-phase components of the oscillating decay. Figure 5.7, which shows the decay of P_x^e due

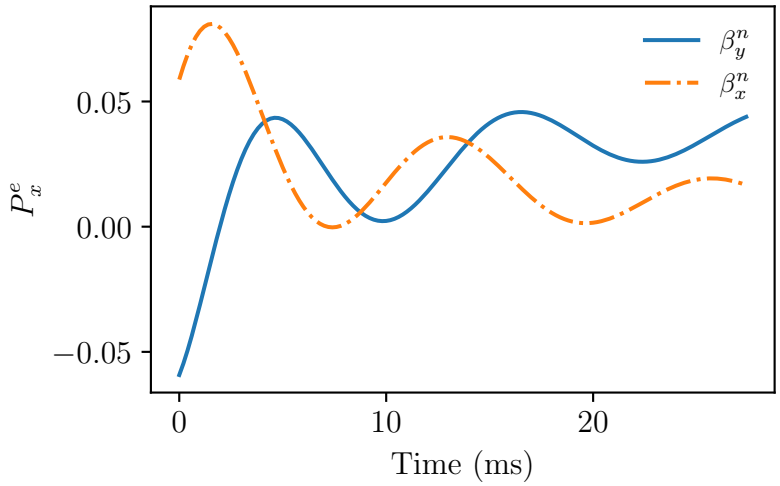

Figure 5.7: Decay of the pulsed co-magnetometer to β_x^n and β_y^n as a function of B_z detuning.

to a β_x^n and β_y^n field, reveals that this expectation is well founded. We note that for ease of comparison, the plot for the β_y^n decay has been offset by 0.05. The phase difference between these two oscillations can be quantified by fitting them to (5.1) and varying the fixed parameter ϕ over 2π and choosing the value of ϕ that maximizes the fit parameter A (or D). If we perform this procedure, we find that there is a 81° phase difference between the decay due to β_x^n and β_y^n. The exact reason for this 9° departure from 90° is currently unknown but we believe that it may be due to the slight exponential character of the decays and/or the slightly changing frequency of each decay due to the variable slowing down factor, which makes (5.1) only an approximation.

5.2 Experimental Implementation

The pulsed co-magnetometer has been experimentally implemented on an rotating apparatus that was originally designed to search for Lorentz violation [140, 206]. Detailed information about the experimental setup can be found in [152] and we do not reproduce it here. Rather, we discuss the modifications made to the setup for the purposes of implementing the pulsed co-magnetometer.

5.2.1 Pump laser

Originally, the rotating apparatus employed a K-^{3}He co-magnetometer cell and relied on direct pumping of K using a distributed feedback laser diode providing 8.3 mW of pumping light [152]. In [140], ^{3}He was replaced with ^{21}Ne to enable measurements of tensor anisotropy. To effectively pump ^{21}Ne via spin-exchange collisions, Rb, which has a higher spin-exchange cross-section with ^{21}Ne than K (see Table 2.2), was used instead. Also, hybrid pumping with K as the lean, donor species was employed to allow an optically thick vapor of Rb to be pumped without generating large polarization gradients. However, as we noted in section 5.1, the pulsed co-magnetometer does not in theory require hybrid pumping since the goal is to completely polarize the alkali atoms during the short intense laser pulses, which will automatically eliminate any polarization gradient in the bulk. Consequently, we directly pumped Rb in our Rb-^{21}Ne cells and swapped out the seed diode laser and tapered amplifier (TA) in [140] for a distributed Bragg reflector 795 nm seed diode laser and a 3W, 4A 795 nm TA from m2k similar to the one employed in SMILE and described in section 4.1.6. As in [152] and [140], we expand the pump beam to the size of the cell and have a linear polarizer and $\lambda/4$ wave-plate combination to circularly polarize the pumping light.

Initially, the "pulses" were simply generated by quickly modulating the laser current of the tapered amplifier. However, to avoid potential instabilities arising from significant modulation of the pump laser current (the max operating current can be as high as 4.2A), we decided to use an acoustic-optical modulator (AOM) instead. By using the first order diffracted beam of the AOM to illuminate the cell, we can ensure that almost no pumping light reaches the cell during the dark period without having to modulate the laser current of the TA. The disadvantage to operating in this mode is that there is less transmission of the beam during the bright period. Using a commercial RF amplifier, we were able to achieve a diffraction efficiency of about 70% into the first order mode. It is likely that focusing the beam down to a point and employing a mechanical chopper will retain similar modulation depths while having higher transmission during the bright period. This has been tested but not yet implemented since there are also possible problems ranging from vibration of the chopper's motor to greater difficulty in the synchronization of the pump/decay cycle with other parts of the experiment that we discuss in further detail below.

5.2.2 Electronics

Operating in the pulsed mode requires additional synchronization between various parts of the experiment. For example, since the signal of interest is in the oscillating part of the decay, we would like to fit the decays in real time to (5.1), which implies that the data acquisition has to be synchronized to the pump/decay cycle. This is accomplished by setting up a NI M Series data acquisition card to perform re-triggerable finite acquisition that re-triggers at the start of each pump cycle on a synchronization TTL output from the function generator modulating the AOM's RF amplifier. We have found that this provides sufficient synchronization between the data acquisition and pump/decay cycle over long time scales.

An additional complication arises when the pump beam is fully on since scattered light from the cell is then sufficient to saturate the signal's photo-diode. The photo-diode itself can recover quickly from saturation since its electronics were designed to have a bandwidth above 100 kHz. However, as in the case of SMILE, the photodiode's output is fed into a lock-in amplifier that de-modulates the photodiode's signal[6] that was previously modulated at 50 kHz by a photo-elastic modulator (PEM). When the photo-diode saturates, the sudden jump in the lock-in's input causes it to overload and its recovery time can be, depending on its time constant, significantly longer. To prevent the lock-in from overloading, we therefore switch its input between an adjustable DC level and the photodiode's output. A second channel on the AOM's function generator provides a synchronized 0 to -3 V square wave[7] that switches the lock-in amplifier's input to the DC level during the bright period and back to the photodiode's output during the dark period. By adjusting the DC level to closely match the mean voltage level of the photodiode's output, we were able to prevent the lock-in from overloading during the transition between bright and dark periods.

5.2.3 Real time curve fitting

One of the practical challenges to operating the pulsed co-magnetometer is to have real-time feedback from the system. Since the useful information is now encoded in the amplitude of the oscillations, we would like to be able to extract that information in real-time while adjusting various experimental parameters rather than downloading and analyzing them later, which would make operation of the pulsed co-

[6]We note that in the experimental setup here, a $\lambda/4$ plate and PEM is used to modulate the polarization of the light in a way that is reminiscent of SMILE in section 4.1.5. However, here the position of the $\lambda/4$ plate and PEM are reversed. Nevertheless, it is shown in [178] that the de-modulated first harmonic signal is still proportional to the optical rotation caused by the atoms.

[7]The 0 to -3V square wave used to switch the lock-in's input is a historical relic from the time when the pump beam was modulated via modulation of the laser current and the function generator only had one output, which necessitated the use of a comparator to convert the 0 to -3V square wave into a 0 to 5 V waveform that was then fed into the switch. Currently, the comparator is no longer necessary since the function generator has two outputs but since it works just fine, it has not been removed.

magnetometer rather clunky and un-intuitive. The data acquisition scheme described above in section 5.2.2 allows us to acquire data in a fashion that is synchronized to the pump/decay cycle so that we are always looking at the same portion of the pump/decay cycle. However, we need still need to fit the decay data to (5.1) to obtain useful information. Early attempts to use LabVIEW's native curve fitting functions did not prove too successful since it was not sufficiently fast and the fits simply could not keep up with the data acquisition rate. Since the period of the pump/decay cycle was 36 ms, we would require the fits to be completed in less than that time to ensure real-time operation of the pulsed co-magnetometer and a simple application of LabVIEW's curve fitting functions were inadequate for that purpose. Although it's possible that additional clever programming and algorithms in LabVIEW will allow it to meet these requirements, it was deemed that adding this complexity on a LabVIEW's programming GUI will turn it into a hideous monstrosity. Besides, there was also need for such a set of curve fitting routines in the simulations and therefore, it makes sense to develop just one set of curve fitting routines that can be used in both the simulations and experiment, which means that programming in LabVIEW would be out of the question. Consequently, we elected to write a set of curve fitting routines in C, compile it into a Dynamically Linked Library (DLL), and have LabVIEW call it using its Call Library Function Node.

The curve fitting functions were written with the aid of the least-square fitting library in the GNU Scientific Library (GSL) and compiled into a DLL with Visual Studio 2017. Consequently, it is necessary to install the (free) Microsoft Visual C++ Redistributable for Visual Studio 2017 packages on the target computer since the target computer might not otherwise have the necessary run-time components needed for the DLL to work correctly. For compatibility with older continuously pumped co-magnetometer LabVIEW VIs, the pulsed co-magnetometer VIs were also written as 32-bit LabVIEW VIs, which means that they have to interface with a DLL

that is compiled for x86. Since we typically employ 64-bit programs in the simulations however, we compile the DLL in both x86 and x64 versions. For LabVIEW to use the routines in these DLL reliably, it is crucial to prevent memory leaks that might otherwise inadvertently appear in the interface between them. In particular, it is important that the DLL does not create any object that is then passed out to LabVIEW, since those objects will likely not be cleaned up by either the DLL or LabVIEW. Consequently, all fitting routines in the DLL were written as void functions. The onus is on LabVIEW to create correctly sized arrays and to provide their pointers to the DLL, which will then write into them without performing any memory allocation or de-allocation. LabVIEW is then fully responsible for managing the allocation/de-allocation of those arrays. Although functions in the DLL should automatically de-allocate any C variables created within it when it exits, they might not de-allocate memory from a GSL object and therefore any GSL objects should be explicitly de-allocated before the function exits.

The ability of these curve fitting functions to quickly fit a decay to (5.1) in less that 36 ms depends crucially on obtaining good initial guesses. Over the course of the pulsed co-magnetometer implementation, we have written various routines that treat different variables in (5.1) as fit variables. Obviously, once the system is relatively stable at the compensation point, it is ideal to treat "non-essential" variables (such as T_1, T_2, C and f) as fixed so that we only need to vary the amplitude of the oscillations, which is what we are ultimately most interested in. This linearizes the fit and simplifies the fitting. Nevertheless, we require a more general fitting routine while attempting to zero the pulsed co-magnetometer where all of these parameters (especially f) can vary substantially.

Here we sketch out our strategy behind automatically obtaining good guesses for the decay in the most general case where we fit the decay to a variant of (5.1)

$$S(t) = Ae^{-t/T_2}\sin(2\pi ft + \phi) + Be^{-t/T_1} + C, \tag{5.5}$$

with A, T_2, f, ϕ, B, T_1 and C as free fit parameters. In this case, the strategy to obtaining a good initial guess for (5.5) comes down to first attempting to separate out the exponential component from the oscillating component. We do so by first fitting the decay to an exponential decay

$$S(t) = Be^{-t/T_1} + C. \tag{5.6}$$

If the best fit T_1[8] is absurd, i.e. it is zero, negative or too large (which we define as 4 times the decay interval), then we subject the decay to a linear fit and estimate B, T_1 and C from a first order expansion of (5.6). The estimated values of B, T_1 and C are then used to subtract the exponential and constant term from (5.5). We then obtain an estimate of f by performing a Fast Fourier Transform (FFT) on the exponential (and constant) subtracted decay signal. Armed with an estimate of f, we may then guess ϕ by searching for the maximum stationary point in one period and measuring its distance from the origin (t=0). If this does not exist due to the phase of the decay signal and/or the quality of the prior background subtraction, we use the maximum stationary point in the second period instead. Getting an estimate on T_2 and A is somewhat more involved and would ideally require a minimum of two or more periods in the decay interval to be successful. The basic idea is to use the maximum stationary points in the first two periods and to estimate T_2 and A from them. However, we are occasionally unable, as in the case of the ϕ estimate, to obtain a maximum stationary point in the first period. In that case, if the decay interval

[8] We typically use $R_1 \equiv 1/T_1$ in the actual code.

contains 3 decay periods, we use the maximum stationary points of the second and third period to estimate T_2 and A, which should be more reliable since the "edge effect" of the background subtraction becomes less important at late times although the signal is also admittedly smaller. If the decay interval only contains 2 decay periods, we use the maximum and minimum in the second period to estimate T_2 and A as a last resort. After obtaining A, T_2, f and ϕ, we then re-estimate B, T_1 and C by subtracting the first term of (5.5) from the decay signal and then subjecting it again to either an exponential or linear fit per the conditions outlined above.

Although the strategy above is not perfect and can still sometimes cause the fit to fail to converge, it has proven useful and robust over a wide range of parameters. Obviously, if there are very small oscillations, then this most general fit will fail since it will not be able to accurately estimate the frequency. In that case, it is advisable to switch to a routine in which f, T_2, T_1 and C (or some combination of them) is fixed. The fitting routines in the DLL can be programmed via an input to accept an initial guess from the user instead of automatically calculating their own guesses using strategies similar to the one outlined above. This is especially useful in their implementation in LabVIEW since upon a first successful fit, LabVIEW can pass the fit parameters from the last fit as the initial guess of the next fit and will only revert to an automatic guess when the previous fit fails for whatever reason. This helps reduce unnecessary computation and helps the fits keep up with the acquisition. Lastly, we note that it is important to employ a producer/consumer loop architecture in LabVIEW that is linked together by first-in first-out (FIFO) queues, which allow the acquisition and fitting to be performed in separate while loops. This ensures that the acquisition buffer does not fill up or miss a trigger even if the fitting falls behind the acquisition.

5.3 Calibration and Measurement of Earth's Rotation

In section 3.6, we described two ways of calibrating the CW co-magnetometer's sensitivity to anomalous fields. The first relied on the B_z zeroing procedure first described in section 3.5, which made use of the quasi-static steady state response of the CW co-magnetometer. The second relied on the co-magnetometer's response to a low frequency B_x modulation. In the case of the pulsed co-magnetometer, we would not expect the first method that is based on the quasi-static response to work but as we saw from above, the pulsed co-magnetometer still exhibits suppression to **B** fields and we therefore expect that it might have a similar behavior to the CW co-magnetometer in response to a slow changing B_x field. Consequently, we expect in analogy to the slow B_x calibration of the CW co-magnetometer that the amplitude (A or D of (5.1)) of oscillations in the pulsed co-magnetometer will vary in response to a slow $B_x = B_0 \cos \omega t$ modulation as

$$A(t) = a \sin \omega t + b \cos \omega t \approx a \sin \omega t = \frac{1}{C} \frac{\omega}{\gamma_n B_n} B_0 \sin \omega t, \tag{5.7}$$

where a, b here are respectively the measured out and in-phase response of the amplitude A in response to a $B_x = B_0 \cos \omega t$ modulation, C is the desired calibration constant and B_n is the noble gas' effective magnetization. Ideally, b should be close to zero for a sufficiently slow B_x modulation (see (3.50)). In the pulsed co-magnetometer, B_n can be easily measured as the limiting value of B_z where the frequency of oscillations goes to zero. (5.7) also assumes that D in (5.1) is effectively zero throughout the entire B_x modulation. In general, this will not be true since the ratio of A to D will depend on the fixed phase parameter ϕ. However, we can re-analyze the data from the calibration for different ϕ and select the ϕ that minimizes D. As we saw in section

5.1.3, A and D in (5.1) can be viewed as the pulsed co-magnetometer's response to orthogonal anomalous fields. In the CW co-magnetometer, the slow B_x modulation yields the co-magnetometer's sensitivity to anomalous fields in the y direction. We therefore expect that fixing ϕ by choosing a value that minimizes D in response to a slow B_x modulation effectively sets the amplitude A and D to measure anomalous fields in the y and x direction (as defined by the field coils) respectively.

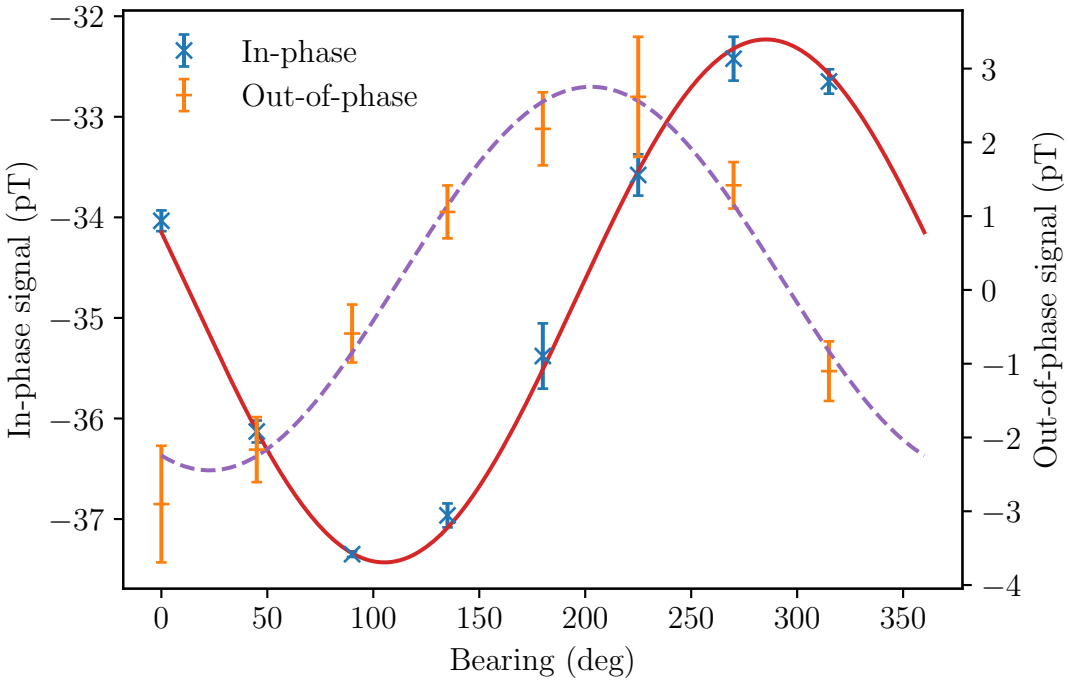

Figure 5.8: Pulsed co-magnetometer's measurement of Earth's rotation.

Since the pulsed co-magnetometer was implemented on a rotating platform, we may verify the accuracy of this slow B_x modulation by rotating the apparatus 360° and measuring Earth's rotation, which is an example of an anomalous field. Figure 5.8 shows the result of a typical Earth rotation measurement[9]. In obtaining Figure 5.8, we have simultaneously measured A and D in (5.1) while rotating the apparatus 360°. Due to magnetic field offsets, there is a large constant offset in the out-of-phase

[9] 0 deg bearing in Figure 5.8 does not correspond to North.

component and we have therefore plotted the in and out-of-phase components on different y axes to better demonstrate their orthogonality to each other. We note that as expected, the pulsed co-magnetometer demonstrates dual axis sensitivity and accurately measures Earth's rotation along two orthogonal axes as it rotates about the vertical axis by 360°. The calibration obtained with a slow B_x modulation gives the correct magnitude of Earth's rotation in Princeton to within 30%. We are currently working on a zeroing procedure to zero out magnetic field offsets that should, in principle, remove the offsets in the Earth rotation curves of Figure 5.8.

Chapter 6

Conclusion

We have in this work placed new limits on possible anomalous spin-mass interactions that can arise from a variety of sources including the QCD axion, axion-like particles and very light spin-1 bosons that have CP-violating couplings to fermions. In particular, we have, using a K-^{3}He co-magnetometer and two 250 kg Pb source masses, improved the best existing laboratory constraints on $g_p^n g_s^N$, the product of the axion's pseudoscalar and scalar coupling to neutrons and nucleons respectively, by an order of magnitude over two decades of axion mass range from $1 - 0.01$ μeV. At a 95 % confidence level (C.L), we have set an upper bound of $g_p^n g_s^N < 4.2 \times 10^{-30}$ for axions lighter than 1 μeV. Similarly, we set an upper bound of $g_p^e g_s^N$, the product of the axion's pseudoscalar and scalar coupling to electrons and nucleons respectively, of $g_p^e g_s^N < 1.7 \times 10^{-30}$ at a 95 % C.L for axions lighter than 1 μeV.

These results can still be significantly improved. The co-magnetometer's low frequency sensitivity is currently limited by optical rotation and pump beam deflection noise. We have pinpointed the source of optical rotation noise as arising primarily from the inhomogeneously birefrigent vacuum windows, which can potentially be greatly reduced by using dense flint glass like SF57 that have extremely low stress induced birefrigence. Noise arising from pump beam deflection is somewhat more

challenging to defeat. One approach would be to further reduce the optical path between the cell and pump beam's optical fiber. This is not, in principle, difficult to accomplish but would require additional clearance below the vacuum chamber. Assuming that the co-magnetometer's low frequency sensitivity is no longer limited by optical rotation or pump deflection noise, our analysis of the correlation data during the experiment indicates that unforeseen thermal effects that were correlated with the position of the source masses are likely to become a significant systematic effect. Consequently, it will be imperative to either control these thermal effects or to reduce the co-magnetometer's sensitivity to them. We note that if the co-magnetometer's low frequency sensitivity is improved by about an order of magnitude, then the sensitivity of multiple sensors will also have to concomitantly be improved to ensure that they can continue to constrain other systematic effects below the level of the co-magnetometer's sensitivity.

Finally, we presented work on a new pulsed co-magnetometer that can potentially help defeat noise due to deflections of the pump beam. Simulations of the pulsed co-magnetometer indicate that it should be able to suppress noise due to pump beam deflections by slightly more than an order of magnitude. In addition, the pulsed co-magnetometer retains the CW co-magnetometer's high suppression of ordinary magnetic fields and has the additional feature of being sensitive to anomalous fields in both x and y directions simultaneously. These developments can potentially help alkali-noble gas co-magnetometers to achieve previously unattainable low frequency performance and enable them to perform even more precise measurements of anomalous spin coupling fields that are a harbinger of new physics beyond the Standard Model.

Appendix A

Angular Momentum in Quantum Mechanics

A.1 Spherical Tensors

The computation of matrix elements in quantum mechanics often requires the selection of an appropriate basis that is diagonal with respect to the operators involved in the calculation. In problems involving angular momentum where the total angular momentum $\mathbf{J}$ is conserved, the $\{|j, m_j\rangle\}$ basis is frequently used in computations since they are eigenstates of the total angular momentum operator $\mathbf{J}^2$ and the z-projection angular momentum operator J_z. By Noether's theorem, if the total angular momentum is conserved, then the system is also rotationally symmetric and a convenient basis is thus one in which the operators and wavefunctions of the system transform as irreducible tensors under rotation. Such a basis is convenient because irreducible tensors cannot, by definition, be decomposed into parts that transform differently. Spherical tensors are tensors expressed in a spherical coordinate representation so that they are irreducible under rotation.

We follow Rose and define the (irreducible) spherical tensor T^L_M of rank L as a member of a set of $2L+1$ operators ($M = -L, -L+1 \ldots, L-1, L$) that transform according to the $2L+1$ dimensional representation of the rotation group [218]. In other words, the result of a rotation operation on T^L_M can be expressed as a $2L+1$ linear combination of the elements in the set

$$R\, T^L_M\, R^{-1} = \sum_{M'} D^L_{M,M'} T^L_{M'}, \tag{A.1}$$

where in the equation above, we have denoted the rotation operator as R and $D^L_{M,M'}$ are its matrix elements in the LM basis. Equivalently, as Racah first showed [219–221], a spherical tensor T^L_M transforms according to the $2L+1$ dimensional representation of the rotation group if it obeys the commutator relations with the angular momentum operators J_i:

$$[J_x \pm i J_y, T^L_M] = \sqrt{(L \mp M)(L \pm M + 1)}\, T^L_{M\pm 1} \tag{A.2}$$

$$[J_z, T^L_M] = M T^L_M. \tag{A.3}$$

A new spherical tensor T^L_M can be formed by the sum[1] of the products of two (lower rank) spherical tensors Y^l_m and X^λ_μ:

$$T^L_M = \sum_{m\mu} Y^l_m X^\lambda_\mu C(l\lambda L; m\mu M). \tag{A.4}$$

The coefficient $C(l\lambda L; m\mu M)$ are the usual Clebsch-Gordan co-efficients[2] for coupling two angular momentum states $|l, m\rangle$ and $|\lambda, \mu\rangle$ (which are examples of spherical tensors) to form the coupled state $|L, M\rangle$ (which is also a spherical tensor).

[1] As usual, when the limits of summation are not explicit, we mean to sum over all possible values.
[2] We follow the Clebsch-Gordan notation of [218] here and elsewhere in this work.

Use of the orthogonality relation (A.54) of the Clebsh-Gordan co-efficients allows us to obtain the inverse to (A.4)

$$Y_m^l X_\mu^\lambda = \sum_L T_{m+\mu}^L C(l\lambda L; m\mu). \tag{A.5}$$

In problems involving angular momentum, it is frequently useful to express spatial vectors in the spherical basis since they are spherical tensors of rank 1 and transform conveniently as irreducible tensors under rotations. The spherical basis consist of the basis vectors

$$\begin{aligned} \mathbf{i}_1 &= -\frac{\mathbf{i}_x + i\,\mathbf{i}_y}{\sqrt{2}} \\ \mathbf{i}_0 &= \mathbf{i}_z \\ \mathbf{i}_{-1} &= \frac{\mathbf{i}_x - i\,\mathbf{i}_y}{\sqrt{2}}. \end{aligned} \tag{A.6}$$

The spherical basis vectors are orthgonal to each other and have the relations

$$\mathbf{i}_\mu^* \cdot \mathbf{i}_\nu = \delta_{\mu\nu} \tag{A.7}$$

$$\mathbf{i}_\mu^* = (-1)^\mu \mathbf{i}_{-\mu}. \tag{A.8}$$

Spatial vectors may be expanded in the spherical basis as

$$\mathbf{r} = \sum_\mu (-1)^\mu r_\mu \mathbf{i}_{-\mu}. \tag{A.9}$$

Operators like the polarizability operator $\overleftrightarrow{\alpha} \propto \kappa \propto \mathbf{pp}$ are spatial tensors of rank 2 and it is convenient to express them as spherical tensors. We follow [130] and introduce a set of basis dyadics $\mathbf{Q}_M^L$ that follows from (A.4) apart from a normalization

factor

$$\mathbf{Q}_M^L = \sum_\mu \mathbf{i}_\mu (\mathbf{i}_{\mu-M})^* (-1)^{\mu-M-1} C(11L; \mu, M-\mu). \tag{A.10}$$

As in (A.5), use of the orthogonality relation (A.54) gives the inverse relationship

$$\mathbf{i}_\nu \mathbf{i}_\mu = -\sum_L \mathbf{Q}_{\mu+\nu}^L C(11L; \nu, \mu). \tag{A.11}$$

The unit dyadic is

$$\mathbf{1} = \mathbf{i}_x \mathbf{i}_x + \mathbf{i}_y \mathbf{i}_y + \mathbf{i}_z \mathbf{i}_z = \sum_\mu \mathbf{i}_\mu (\mathbf{i}_\mu)^* = \sqrt{3}\mathbf{Q}_0^0, \tag{A.12}$$

and the cross product of two vectors may be expressed in terms of the basis dyadics $\mathbf{Q}_M^1$ as

$$\mathbf{A} \times \mathbf{B} = -i\sqrt{2} \sum_M (-1)^M A_{-M} \mathbf{Q}_M^1 \cdot \mathbf{B}. \tag{A.13}$$

In particular, the cross-product $\mathbf{e} \times \mathbf{e}^*$ is given by

$$\mathbf{e} \times \mathbf{e}^* = -i\sqrt{2} \sum_{M\mu} (-1)^M e_\mu^* e_{-M} \mathbf{Q}_M^1 \cdot \mathbf{i}_\mu, \tag{A.14}$$

where $\mathbf{e}$ is any vector and $\mathbf{e}^*$ is its complex conjugate (the expansion of $\mathbf{e}^*$ can be performed by expanding $\mathbf{e}$ using (A.9) and using (A.8) after taking its complex conjugate). Taking the complex conjugate, expanding $\mathbf{Q}_M^1$ with (A.10) and using (A.8) gives

$$\mathbf{e}^* \times \mathbf{e} = -i\sqrt{2} \sum_{M\mu} e_{-M}^* e_{\mu-M} C(111; \mu, M-\mu) \mathbf{i}_{-\mu}, \tag{A.15}$$

so that if $\mathbf{e}$ is the (complex) polarization vector of a propagating light wave, then the mean photon spin $\mathbf{s}$ is

$$\mathbf{s} \equiv \frac{\mathbf{e}^* \times \mathbf{e}}{i} = -\sqrt{2} \sum_{M\mu} e_{-M}^* e_{\mu-M} C(111; \mu, M-\mu) \mathbf{i}_{-\mu}. \tag{A.16}$$

Moreover, we have from (A.9), (A.8) and (A.7) for any vector $\mathbf{A}$

$$\mathbf{A}\cdot\mathbf{s} = -\sqrt{2}\sum_{M\mu} A_M e^*_{-\mu} e_{-\mu-M} C(111; -M, M+\mu). \tag{A.17}$$

The hyperfine eigenstates $|F = I + J, \mu\rangle$ are spherical tensors of rank F and operators between these hyperfine states can be expressed as spherical tensors using (A.4). As before, we follow the normalization in [130] and introduce the spherical tensor operators $T^L_M(F, F')$

$$T^L_M(F,F') = \sum_{\mu} |F,\mu\rangle \langle F', \mu - M| (-1)^{\mu-M-F'} C(FF'L; \mu, M-\mu). \tag{A.18}$$

The inverse relationship, which follows from application of (A.54), is

$$|F,\mu\rangle \langle F',\nu| = \sum_{L} T^L_{\mu-\nu}(F,F')(-1)^{\nu-F'} C(FF'L;\mu,-\nu). \tag{A.19}$$

Moreover, the operators $\{T^L_M(F,F')\}$ are orthonormal, that is

$$\begin{aligned}\mathrm{Tr}\left[T^L_M(F,F')\left[T^l_m(f,f')\right]^\dagger\right] &= \sum_{G\rho} \langle G,\rho| T^L_M(F,F')\left[T^l_m(f,f')\right]^\dagger |G,\rho\rangle \\ &= \delta_{Ll}\delta_{Mm}\delta_{Ff}\delta_{F'f'}.\end{aligned} \tag{A.20}$$

Accordingly, $\{T^L_M(F,F')\}$ can be used as an orthonormal basis for ground state operators and any such operator O can be expanded as

$$O = \sum_{LMFF'} O^L_M(F,F') T^L_M(F,F'), \tag{A.21}$$

where the coefficients $O_M^L(F,F')$ can be evaluated by applying the orthonormality conditions (A.20) to (A.21) to obtain

$$O_M^L(F,F') = \mathrm{Tr}\left[O\, T_M^L(F,F')^\dagger\right]. \tag{A.22}$$

Alternatively, the ground state operator O can also be expanded in terms of the uncoupled basis operators $T_M^K(I,I)T_N^L(S,S)$ as

$$O = \sum_{KMLN} O(KM;LN)T_M^K(I,I)T_N^L(S,S). \tag{A.23}$$

Since $S = 1/2$, we may explicitly compute $T_N^L(S,S)$ using (A.18) as

$$\begin{aligned} T_M^L\left(\tfrac{1}{2},\tfrac{1}{2}\right) &= \left|\tfrac{1}{2},\tfrac{1}{2}\right\rangle\left\langle\tfrac{1}{2},\tfrac{1}{2}-M\right|(-1)^M C\left(\tfrac{1}{2}\tfrac{1}{2}L;\tfrac{1}{2},M-\tfrac{1}{2}\right) \\ &\quad + \left|\tfrac{1}{2},-\tfrac{1}{2}\right\rangle\left\langle\tfrac{1}{2},-\tfrac{1}{2}-M\right|(-1)^{-1-M} C\left(\tfrac{1}{2}\tfrac{1}{2}L;-\tfrac{1}{2},M+\tfrac{1}{2}\right), \end{aligned} \tag{A.24}$$

where the Clebsch-Gordan coefficients can be evaluated using (A.65) and (A.66). Doing so, we obtain

$$\begin{aligned} T_1^1\left(\tfrac{1}{2},\tfrac{1}{2}\right) &= -\left|\tfrac{1}{2},\tfrac{1}{2}\right\rangle\left\langle\tfrac{1}{2},-\tfrac{1}{2}\right| = -S_+ = \sqrt{2}S_1 \\ T_0^1\left(\tfrac{1}{2},\tfrac{1}{2}\right) &= \sqrt{2}\left(\tfrac{1}{2}\left|\tfrac{1}{2},\tfrac{1}{2}\right\rangle\left\langle\tfrac{1}{2},\tfrac{1}{2}\right| - \tfrac{1}{2}\left|\tfrac{1}{2},-\tfrac{1}{2}\right\rangle\left\langle\tfrac{1}{2},-\tfrac{1}{2}\right|\right) = \sqrt{2}S_z \\ T_{-1}^1\left(\tfrac{1}{2},\tfrac{1}{2}\right) &= \left|\tfrac{1}{2},-\tfrac{1}{2}\right\rangle\left\langle\tfrac{1}{2},\tfrac{1}{2}\right| = S_- = \sqrt{2}S_{-1} \\ T_0^0\left(\tfrac{1}{2},\tfrac{1}{2}\right) &= \tfrac{1}{\sqrt{2}}\left(\left|\tfrac{1}{2},\tfrac{1}{2}\right\rangle\left\langle\tfrac{1}{2},\tfrac{1}{2}\right| + \left|\tfrac{1}{2},-\tfrac{1}{2}\right\rangle\left\langle\tfrac{1}{2},-\tfrac{1}{2}\right|\right) = \tfrac{1}{\sqrt{2}}\mathbb{1}, \end{aligned} \tag{A.25}$$

where S_+, S_- are the raising/lowering operators and $S_{\pm 1}$, S_z are the spherical basis components of the electron spin operator $\mathbf{S}$ (A.38).

In the coupled basis, the expansion coefficients $J^L_M(F,F')$ of the electron angular momentum operator $\mathbf{J}$ can be computed as

$$\begin{aligned} J^L_M(F,F') &= \sum_{G\rho\mu} \langle G,\rho\,|\mathbf{J}|\,F',\mu-M\rangle \underbrace{\langle F,\mu|\,G,\rho\rangle}_{\delta_{FG}\delta_{\mu\rho}} (-1)^{\mu-M-F'} C(FF'L;\mu,M-\mu) \\ &= \sum_{\mu} \langle F,\mu\,|\mathbf{J}|\,F',\mu-M\rangle\,(-1)^{\mu-M-F'} C(FF'L,\mu,M-\mu). \end{aligned} \tag{A.26}$$

The matrix element $\langle F,\mu\,|\mathbf{J}|\,F',\mu-M\rangle$ can be evaluated by means of the Wigner-Eckhart theorem (A.89) to obtain

$$\langle F,\mu\,|\mathbf{J}|\,F',\mu-M\rangle = \sum_{\rho}(-1)^{\rho}\mathbf{i}_{-\rho}C(F'1F;\mu-M,\rho,\mu)\,\langle F\,||\mathbf{J}||\,F\rangle\,, \tag{A.27}$$

while the reduced matrix element $\langle F\,||\mathbf{J}||\,F\rangle$ can be computed with the aid of a corollary to the Wigner-Eckhart theorem (A.90) to give

$$\begin{aligned} \langle F\,||\mathbf{J}||\,F\rangle = \langle IJ_gF\,||\mathbf{J}||\,IJ_gF\rangle &= (-1)^{I+1-Jg-F}\sqrt{(2J_g+1)(2F'+1)} \\ &\quad\times W(J_gF'J_gF;I1)\,\langle J_g\,||\mathbf{J}||\,J_g\rangle\,, \end{aligned} \tag{A.28}$$

but the reduced matrix element $\langle J_g\,||\mathbf{J}||\,J_g\rangle$ is given simply by

$$\begin{aligned} \left\langle J_g,m_g\,|J_z|\,J_g,m'_g\right\rangle = m'_g\delta_{m_gm'_g} &= C(J_g1J_g;m'_g0m_g)\,\langle J_g\,||\mathbf{J}||\,J_g\rangle \\ \implies \langle J_g\,||\mathbf{J}||\,J_g\rangle &= \sqrt{J_g(J_g+1)}, \end{aligned} \tag{A.29}$$

and therefore the matrix element $\langle F,\mu\,|\mathbf{J}|\,F',\mu-M\rangle$ is (after application of the W symmetry relation (A.81) and recalling that $I-J_g-F'\in\mathbb{Z}$)

$$\begin{aligned} \langle F,\mu\,|\mathbf{J}|\,F',\mu-M\rangle &= (-1)^{F'-F}\sqrt{J_g(J_g+1)(2J_g+1)(2F'+1)}W(1J_gFI;J_gF') \\ &\quad\times\sum_{\rho}(-1)^{\rho}\mathbf{i}_{-\rho}C(F'1F;\mu-M,\rho,\mu). \end{aligned} \tag{A.30}$$

Substituion of (A.30) into (A.26) yields after applying the Clebsch-Gordan symmetry relation (A.61) and property (A.55a)

$$J_M^L(F,F') = (-1)^{F'-F}\sqrt{\frac{J_g(J_g+1)(2J_g+1)(2F'+1)(2F+1)}{3}}\sum_\rho \mathbf{i}_{-\rho}(-1)^\rho \times \underbrace{\sum_\mu C(FF'1;\mu,M-\mu,\rho)C(FF'L;\mu,M-\mu)}_{\delta_{1L}}\delta_{M\rho}$$
$$= (-1)^{F'-F+M}\mathbf{i}_{-M}\sqrt{\frac{J_g(J_g+1)(2J_g+1)(2F'+1)(2F+1)}{3}}W(1J_gFI;J_gF')\delta_{1L}, \tag{A.31}$$

and the electronic angular momentum operator $\mathbf{J}$ is therefore[3], in terms of the spherical tensor operator T_M^L,

$$\mathbf{J} = \sum_{MFF'}(-1)^{F'-F+M}\mathbf{i}_{-M}\sqrt{\frac{J_g(J_g+1)(2J_g+1)(2F'+1)(2F+1)}{3}} \times T_M^1(F,F')W(1J_gFI;J_gF'). \tag{A.32}$$

A.2 Angular momentum operators

Angular momentum operators in quantum mechanics possess several generic and useful properties that we state here for convenience. For a general angular momentum operator $\mathbf{J}$, its cartesian components obey the commutation relation

$$[J_i,J_j] = i\,\epsilon_{ijk}J^k, \tag{A.33}$$

[3]We note that there is a sign difference here compared to [130] that seems to stem from differences in (A.90). This is not too much of an issue though because the signs eventually cancel out and we obtain the same multipole components of the polarizability tensor as in [130].

where Einstein's summation notation is implied and ϵ_{ijk} is here the anti-symmetric Levi-Civita symbol with the following useful summation identities in 3D

$$\epsilon_{ijk}\epsilon^{imn} = \delta_j^{\ m}\delta_k^{\ n} - \delta_j^{\ n}\delta_k^{\ m} \tag{A.34}$$

$$\epsilon_{imn}\epsilon^{jmn} = 2\delta_i^{\ j} \tag{A.35}$$

$$\epsilon_{ijk}\epsilon^{ijk} = 6. \tag{A.36}$$

The raising J_+ and lowering J_- operators are defined as

$$J_\pm \equiv J_x \pm i\, J_y. \tag{A.37}$$

J may then, in analogy to (A.6), be expanded in spherical basis as

$$\begin{aligned} J_1 &= -\frac{J_x + i\, J_y}{\sqrt{2}} = -\frac{1}{\sqrt{2}} J_+ \\ J_0 &= J_z \\ J_{-1} &= \frac{J_x - i\, J_y}{\sqrt{2}} = \frac{J_-}{\sqrt{2}}. \end{aligned} \tag{A.38}$$

From the commutation relation (A.33) and the definitions of J_+ and J_-, it follows that

$$[J_z, J_\pm] = \pm J_\pm \tag{A.39}$$

$$[J_+, J_-] = 2J_z. \tag{A.40}$$

Similarly, it is straightforward to show that

$$J_- J_+ = J^2 - J_z^2 - J_z \tag{A.41}$$

$$J_+ J_- = J^2 - J_z^2 + J_z. \tag{A.42}$$

Using the Condon-Shortley phase convention, the action of the raising/lowering operator on a $|j, m_j\rangle$ state is

$$J_+ |j, m_j\rangle = \sqrt{j(j+1) - m_j(m_j+1)}\, |j, m_j + 1\rangle \tag{A.43}$$

$$J_- |j, m_j\rangle = \sqrt{j(j+1) - m_j(m_j-1)}\, |j, m_j - 1\rangle\,. \tag{A.44}$$

The angular momentum operators are all traceless since in the spherical basis,

$$\mathrm{Tr}[J_0] = \mathrm{Tr}[J_z] = \sum_{m_j=-j}^{j} \langle j, m_j |J_z| j, m_j\rangle = \sum_{m_j=-j}^{j} m_j = \frac{(2j+1)(j-j)}{2} = 0, \tag{A.45}$$

and

$$\mathrm{Tr}[J_{\pm 1}] = \mp\frac{1}{\sqrt{2}}\,\mathrm{Tr}[J_\pm] = \mp\frac{1}{\sqrt{2}} \sum_{m_j=-j}^{j} \langle j, m_j |J_\pm| j, m_j\rangle = 0. \tag{A.46}$$

Besides possessing all of the above generic properties, the electron spin operator also obey the anti-commutation relation

$$\{S_i, S_j\} = \frac{1}{2}\delta_{ij}. \tag{A.47}$$

Adding the commutator (A.33) and anti-commutator (A.47) yields the useful identity

$$S_i S_j = \frac{1}{4}\delta_{ij} + \frac{i}{2}\epsilon_{ijk} S^k. \tag{A.48}$$

Using (A.48), we can derive another useful property

$$\begin{aligned} S_j S_i S^j &= S_j \left(\frac{1}{4}\delta_i^{\ j} + \frac{i}{2}\epsilon_i^{\ jk} S_k \right) \\ &= \frac{1}{4} S_i + \frac{i}{2}\epsilon_i^{\ jk} \left(\frac{1}{4}\delta_{jk} + \frac{i}{2}\epsilon_{jkl} S^l \right) \\ &= \frac{1}{4} S_i - \frac{1}{4} \underbrace{\epsilon_i^{\ jk}\epsilon_{ljk}}_{2\delta_{il}} S^l \\ &= \frac{1}{4} S_i - \frac{1}{2} S_i = -\frac{1}{4} S_i, \end{aligned} \tag{A.49}$$

where in the third line we have made use of (A.35). The electron spin operator $\mathbf{S}$ is also a generator of rotations and the operator $e^{-i\theta S_i}$ rotates a state by θ about the i axis. More generally, $e^{-i\boldsymbol{\Theta}\cdot\mathbf{S}}$ may be expressed as

$$\begin{aligned} e^{-i\boldsymbol{\Theta}\cdot\mathbf{S}} = e^{-i\Theta^i S_i} &= \sum_{m=0}^{\infty} \frac{(-i\Theta^i S_i)^{2m}}{2m!} + \sum_{m=0}^{\infty} \frac{(-i\Theta^i S_i)^{2m+1}}{(2m+1)!} \\ &= \sum_{m=0}^{\infty} \frac{(-1)^m}{2m!} \underbrace{(\Theta^i S_i)^{2m}}_{(|\Theta|/2)^{2m}} - i\Theta^i S_i \sum_{m=0}^{\infty} \frac{(-1)^m}{(2m+1)!} \underbrace{(\Theta^i S_i)^{2m}}_{(|\Theta|/2)^{2m}} \\ &= \cos\left(\frac{1}{2}\Theta\right) - i2\hat{\boldsymbol{\Theta}}\cdot\mathbf{S}\sin\left(\frac{1}{2}\Theta\right). \end{aligned} \tag{A.50}$$

A rotated spin operator S_j is therefore

$$e^{i\boldsymbol{\Theta}\cdot\mathbf{S}} S_j e^{-i\boldsymbol{\Theta}\cdot\mathbf{S}} = S_j\cos\Theta + (\hat{\boldsymbol{\Theta}}\times\mathbf{S})_j\sin\Theta + 2\hat{\boldsymbol{\Theta}}_j\,\hat{\boldsymbol{\Theta}}\cdot\mathbf{S}\sin^2\left(\frac{\Theta}{2}\right). \tag{A.51}$$

A.3 Clebsch-Gordan coefficients

In the context of quantum mechanics, Clebsch-Gordan coefficients typically arise as the expansion coefficients of a coupled angular momentum state $|j_3, m_3\rangle$ in terms of

its uncoupled basis states $|j_1, m_1\rangle\,|j_2, m_2\rangle$

$$|j_3, m_3\rangle = \sum_{m_1 m_2} C(j_1 j_2 j_3; m_1 m_2 m_3)\,|j_1, m_1\rangle\,|j_2, m_2\rangle\,. \tag{A.52}$$

Equivalently, they are the matrix elements of a unitary transformation from one basis to another and are sometimes written as $\langle j_1 m_1 j_2 m_2|\, j_3, m_3\rangle$. Accordingly, they are subject to the orthonormality conditions

$$\sum_{m_1} C(j_1 j_2 j; m_1, m - m_1) C(j_1 j_2 j'; m_1, m - m_1) = \delta_{jj'} \tag{A.53}$$

$$\sum_{j} C(j_1 j_2 j; m_1, m - m_1) C(j_1 j_2 j; m_1', m' - m_1') = \delta_{m_1 m_1'} \delta_{m m'}, \tag{A.54}$$

where we have used the notational short hand $C(j_1 j_2 j; m_1, m - m_1) = C(j_1 j_2 j; m_1 m_2 m)$ in the equations above since the Clebsch-Gordan coefficients are zero unless $m_2 = m - m_1$. Indeed, the Clebsch-Gordan coefficients are in general subject to the conditions

$$C(j_1 j_2 j; m_1 m_2 m) = 0 \text{ unless } \begin{cases} m_1 + m_2 = m & \text{(A.55a)} \\ -(j_1 + j_2) \le m \le j_1 + j_2 & \text{(A.55b)} \\ |j_1 - j_2| \le j \le j_1 + j_2 & \text{(A.55c)} \\ m, j \in \mathbb{Z} \text{ or } m, j \in \left(\mathbb{Z} + \dfrac{1}{2}\right). & \text{(A.55d)} \end{cases}$$

The conditions (A.55c) and (A.55d) are often combined together and stated as the triangular inequality $\Delta(j_1 j_2 j)$

$$|j_1 - j_2|, |j_1 - j_2| + 1, \ldots, j, \ldots, j_1 + j_2 - 1, j_1 + j_2. \tag{A.56}$$

We note here that the relations (A.55b) and (A.55c) typically make it unnecessary to specify the limits of summations over m and j as in (A.53) and (A.54) and in general,

where the limits of summation is not explicit, it is taken to be over all possible values consistent with (A.55b) and (A.55c). Moreover, (A.55a) implies that for fixed m, a sum over m_1 or m_2 is equivalent to a double sum over m_1 and m_2. The Clebsch-Gordan coefficients can be chosen to be real and they possess the following useful symmetry relations

$$C(j_1 j_2 j_3; m_1 m_2 m_3) = (-1)^{j_1+j_2-j_3} C(j_1 j_2 j_3; -m_1, -m_2, -m_3) \tag{A.57}$$

$$= (-1)^{j_1+j_2-j_3} C(j_2 j_1 j_3; m_2 m_1 m_3) \tag{A.58}$$

$$= (-1)^{j_1-m_1} \sqrt{\frac{2j_3+1}{2j_2+1}} C(j_1 j_3 j_2; m_1, -m_3, -m_2) \tag{A.59}$$

$$= (-1)^{j_2+m_2} \sqrt{\frac{2j_3+1}{2j_1+1}} C(j_3 j_2 j_1; -m_3, m_2, -m_1) \tag{A.60}$$

$$= (-1)^{j_1-m_1} \sqrt{\frac{2j_3+1}{2j_2+1}} C(j_3 j_1 j_2; m_3, -m_1, m_2) \tag{A.61}$$

$$= (-1)^{j_2+m_2} \sqrt{\frac{2j_3+1}{2j_1+1}} C(j_2 j_3 j_1; -m_2, m_3, m_1). \tag{A.62}$$

Moreover, by considering the seemingly trivial case of coupling no angular momentum to an angular momentum state,

$$|j_1, m_1\rangle = C(j_1 0 j_1; m_1 0 m_1) \, |j_1, m_1\rangle \, |0, 0\rangle \,, \tag{A.63}$$

we obtain a useful relation

$$C(j_1 0 j_3; m_1 0 m_3) = \delta_{j_1 j_3} \delta_{m_1 m_2}, \tag{A.64}$$

that together with the symmetry relations above allows us to compute any Clebsch-Gordan coefficient when either j_1, j_2 or j_3 is zero. For the typical case of coupling to

an electron spin with $j_2 = 1/2$, the Clebsh-Gordan coefficients are [218]:

$$C(j_1, \frac{1}{2}, j_1 \pm \frac{1}{2}; m_3 - \frac{1}{2}, \frac{1}{2}, m_3) = \pm\sqrt{\frac{j_1 + \frac{1}{2} \pm m_3}{2j_1 + 1}} \tag{A.65}$$

$$C(j_1, \frac{1}{2}, j_1 \pm \frac{1}{2}; m_3 + \frac{1}{2}, -\frac{1}{2}, m_3) = \sqrt{\frac{j_1 + \frac{1}{2} \mp m_3}{2j_1 + 1}}. \tag{A.66}$$

A.4 Racah W Coefficients and Wigner 6-j Symbols

The Clebsch-Gordan coefficients $C(j_1 j_2 j; m_1 m_2 m)$, as we saw earlier, are the matrix elements of a unitary transformation between the uncoupled basis of two angular momentum states $\{|j_1, m_1\rangle |j_2, m_2\rangle\}$ and the coupled basis $\{|j, m\rangle\}$. Racah W coefficients arise similarly in the coupling of three angular momentum states. To be more specific, we consider three uncoupled angular momentum states $|j_1, m_1\rangle$, $|j_2, m_2\rangle$, $|j_3, m_3\rangle$ and the final coupled state $|j, m\rangle$. There are three ways to add $|j_1, m_1\rangle$, $|j_2, m_2\rangle$, $|j_3, m_3\rangle$ to obtain $|j, m\rangle$:

$$|j_3 j_1 j_2 j, m\rangle = |j_3, m_3\rangle \otimes (|j_1, m_1\rangle \otimes |j_2, m_2\rangle) = |j_3, m_3\rangle \otimes |j_1 j_2 j', m'\rangle \tag{A.67}$$

$$|j_1 j_2 j_3 j, m\rangle = |j_1, m_1\rangle \otimes (|j_2, m_2\rangle \otimes |j_3, m_3\rangle) = |j_1, m_1\rangle \otimes |j_2 j_3 j'', m''\rangle \tag{A.68}$$

$$|j_2 j_1 j_3 j, m\rangle = |j_2, m_2\rangle \otimes (|j_1, m_1\rangle \otimes |j_3, m_3\rangle) = |j_2, m_2\rangle \otimes |j_1 j_3 j''', m'''\rangle \,. \tag{A.69}$$

The three representations are related to each other by a unitary transformation. For example, if $R_{j'j''}$ is the matrix element of that unitary transformation, then

$$|j_3, m_3\rangle \otimes |j_1 j_2 j', m'\rangle = \sum_{j''} R_{j'j''} |j_1, m_1\rangle \otimes |j_2 j_3 j'', m''\rangle \,. \tag{A.70}$$

The Racah W coefficient is in turn defined by:

$$W(j_1 j_2 j j_3; j' j'') = \frac{1}{\sqrt{(2j'' + 1)(2j' + 1)}} R_{j'j''}. \tag{A.71}$$

These W coefficients obey the following equivalent relations[4] that we shall state without proof. The interested reader may find their derivations in [218].

$$\sum_{j''} \sqrt{(2j'+1)(2j''+1)}\, W(j_1 j_2 j j_3; j' j'') C(j_2 j_3 j''; m_2 m_3) C(j_1 j'' j; m_1, m_2+m_3)$$
$$= C(j_1 j_2 j'; m_1 m_2) C(j' j_3 j; m_1+m_2, m_3) \tag{A.72}$$

$$\sqrt{(2j'+1)(2j''+1)}\, W(j_1 j_2 j j_3; j' j'') C(j_1 j'' j; m_1, m_2+m_3)$$
$$= \sum_{m_2} C(j_1 j_2 j'; m_1 m_2) C(j' j_3 j; m_1+m_2, m_3) C(j_2 j_3 j''; m_2 m_3) \tag{A.73}$$

$$\sqrt{(2j'+1)(2j''+1)}\, W(j_1 j_2 j j_3; j' j'')$$
$$= \sum_{m_1 m_2} C(j_1 j_2 j'; m_1 m_2) C(j' j_3 j; m_1+m_2, m_3) C(j_2 j_3 j''; m_2 m_3) C(j_1 j'' j; m_1, m_2+m_3). \tag{A.74}$$

In addition to the relations above, the W coefficients also obey the following sum rules due to Racah [220, 221] and Biedenharn [222] respectively

$$\sum_{j'} (2j'+1)(-1)^{j_1+j_2-j'} W(j_1 j_2 j j_3; j' j'') W(j_2 j_1 j j_3; j' j''') = W(j_1 j'' j''' j_2; j j_3) \tag{A.75}$$

$$\sum_{g} (2g+1) W(a' g d c; a c') W(b g e c'; b' c) W(a' g f b; a b') = W(a d b e; c f) W(a' d b' e; c' f), \tag{A.76}$$

and they are also orthonormal in the sense that

$$\sum_{j'} (2j'+1)(2j''+1) W(j_1 j_2 j j_3; j' j'') W(j_1 j_2 j j_3; j' j''') = \delta_{j'', j'''}. \tag{A.77}$$

[4] (A.73) and (A.74) follow from (A.72) by multiplying the appropriate Clebsch-Gordan coefficient, summing and using (A.53). We note that $m_2 + m_3 =$ constant and $m_1 + m_2 + m_3 =$ constant in (A.73) and (A.74) respectively.

In the special case when one of the angular momentum argument vanishes, the W coefficient evaluates to a particularly simple form

$$W(abcd;e0f) = \frac{(-1)^{f-b-d}\delta_{ab}\delta_{cd}}{\sqrt{(2b+1)(2d+1)}}. \tag{A.78}$$

Moreover, it is evident from the definition of the angular momenta in the argument of the W coefficient that they must obey the underlying triangular inequalities (defined in (A.56)):

$$W(j_1 j_2 j j_3; j' j'') = 0 \text{ unless } \begin{cases} \Delta(j_1 j_2 j'), \Delta(j' j_3 j) & \text{(A.79a)} \\ \Delta(j_2 j_3 j''), \Delta(j_1 j'' j). & \text{(A.79b)} \end{cases}$$

The Racah W coefficient has a large number of symmetries under the interchange of the six angular momenta [218]:

$$\begin{aligned} W(abcd;ef) &= W(badc;ef) = W(cdab;ef) = W(dcba;ef) = W(acbd;fe) \\ &= W(cadb;fe) = W(bdac;fe) = W(dbca;fe) \end{aligned} \tag{A.80}$$

$$\begin{aligned} (-1)^{b+c-e-f} W(abcd;ef) &= W(aefd;bc) = W(eadf;bc) = W(fdae;bc) = W(dfea;bc) \\ &= W(afed;cb) = W(fade;cb) = W(edaf;cb) = W(defa;cb) \end{aligned} \tag{A.81}$$

$$\begin{aligned} (-1)^{a+d-e-f} W(abcd;ef) &= W(ebcf;ad) = W(befc;ad) = W(cfeb;ad) = W(fcbe;ad) \\ &= W(ecbf;da) = W(cefb;da) = W(bfec;da) = W(fbce;da). \end{aligned} \tag{A.82}$$

As expressed above, the symmetries of the W coefficient can be difficult to remember and apply. These symmetries are usually most readily exploited when the coefficient

is expressed as a Wigner 6-j symbol[5]:

$$W(j_1 j_2 j_5 j_4; j_3 j_6) = (-1)^{(j_1+j_2+j_4+j_5)} \begin{Bmatrix} j_1 & j_2 & j_3 \\ j_4 & j_5 & j_6 \end{Bmatrix}. \tag{A.83}$$

The Wigner 6-j symbol has convenient and memorable symmetries. It is invariant under any permutation of its columns and it is also invariant if the upper and lower arguments are interchanged in any two columns:

$$\begin{Bmatrix} j_1 & j_2 & j_3 \\ j_4 & j_5 & j_6 \end{Bmatrix} = \begin{Bmatrix} j_2 & j_1 & j_3 \\ j_5 & j_4 & j_6 \end{Bmatrix} \tag{A.84}$$

$$\begin{Bmatrix} j_1 & j_2 & j_3 \\ j_4 & j_5 & j_6 \end{Bmatrix} = \begin{Bmatrix} j_4 & j_5 & j_3 \\ j_1 & j_2 & j_6 \end{Bmatrix}. \tag{A.85}$$

Moreover, as is evident from its relationship with the Racah W coefficient, the Wigner 6-j symbol is zero unless j_1, j_2, j_3 satisfy the triangle conditions: $j_1 = |j_2 - j_3|, |j_2 - j_3| + 1, \ldots, j_2 + j_3 - 1, j_2 + j_3$. Due to the large number of angular momenta involved, the sum rules (A.75) and (A.76) are typically easiest to use when expressed in the Wigner 6-j symbols, which are easier to maniupulate due to their simpler symmetries. In terms of the Wigner 6-j symbols, (A.75) and (A.76) are respectively

$$\begin{aligned} \sum_{j'} (2j'+1)(-1)^{j_1+j_2-j'} \begin{Bmatrix} j_1 & j_2 & j' \\ j_3 & j & j'' \end{Bmatrix} \begin{Bmatrix} j_2 & j_1 & j' \\ j_3 & j & j''' \end{Bmatrix} &= W(j_1 j'' j''' j_2; j j_3) \\ &= (-1)^{j_1+j_2+j''+j'''} \begin{Bmatrix} j_1 & j'' & j \\ j_2 & j''' & j_3 \end{Bmatrix} \end{aligned} \tag{A.86}$$

[5]We note that $j_1 + j_2 + j_4 + j_5 \in \mathbb{Z}$ and so the pre-factor can be either $(-1)^{(j_1+j_2+j_4+j_5)}$ or $(-1)^{-(j_1+j_2+j_4+j_5)}$. This is true since if $j_1+j_2+j_4 \in (\mathbb{Z}+1/2)$, then $j_5 \in (\mathbb{Z}+1/2)$ and $j_1+j_2+j_4+j_5 \in \mathbb{Z}$. Alternatively, if $j_1 + j_2 + j_4 \in \mathbb{Z}$, then $j_5 \in \mathbb{Z}$ and $j_1 + j_2 + j_4 + j_5 \in \mathbb{Z}$.

$$\sum_g (2g+1)(-1)^{3g} \begin{Bmatrix} a' & g & a \\ c & d & c' \end{Bmatrix} \begin{Bmatrix} b & g & b' \\ c' & e & c \end{Bmatrix} \begin{Bmatrix} a' & g & a \\ b & f & b' \end{Bmatrix}$$
$$= (-1)^{-(2a'+2b+c+d+e+c'+f)} W(adbe; cf) W(a'db'e; c'f). \tag{A.87}$$

We conclude this discussion on the Racah W coefficients by reproducing the expression of some simple W coefficients used in this work that was compiled and listed in [218]:

$$W(aacc; 1f) = (-1)^{a+c-f-1} \frac{a(a+1) + c(c+1) - f(f+1)}{\sqrt{4a(a+1)(2a+1)c(c+1)(2c+1)}}. \tag{A.88}$$

A.5 Wigner-Eckhart Theorem

The Wigner-Echkart theorem states that the matrix element of a spherical tensor operator T^L_M can be expressed as a product of a Clebsch-Gordan coefficient and a reduced matrix element that does not depend on the orientation of the system

$$\left\langle j_1, m_1 \left| T^L_M \right| j_2, m_2 \right\rangle = C(j_2 L j_1; m_2 M m_1) \left\langle j_1 \left|\left| T^L \right|\right| j_2 \right\rangle. \tag{A.89}$$

This is a powerful result as it enables the separation of the physics due to rotational symmetry, which is now encoded in the Clebsch-Gordan coefficient where all dependence of m_1, m_2 and M now lies, and the remaining physics of the system that is encoded in the reduced matrix element $\left\langle j_1 \left|\left| T^L \right|\right| j_2 \right\rangle$, which is independent of m_1, m_2 and M. This significantly eases the computation of the (full) matrix elements since the reduced matrix element need only to be computed once for fixed L, j_1 and j_2 and the matrix elements $\left\langle j_1, m_1 \left| T^L_M \right| j_2, m_2 \right\rangle$ are then easily obtained for all valid m_1 and m_2 by multiplying the reduced matrix element with the appropriate Clebsch-Gordan coefficient.

The Wigner-Echkart theorem also allows us[6] to obtain a relationship between the reduced matrix element of a spherical tensor operator $T^L(1)$, which only acts in the space of $|j_1, m_1\rangle$ in the $|j_1, m_1\rangle \otimes |j_2, m_2\rangle$ coupled representation, to its reduced matrix element in the uncoupled representation:

$$\left\langle j_1' j_2' j' \left|\left| T^L(1) \right|\right| j_1 j_2 j \right\rangle = \delta_{j_2' j_2} (-1)^{j_2 + L - j_1 - j'} \sqrt{(2j_1' + 1)(2j + 1)} \times W(j_1 j j_1' j'; j_2 L) \left\langle j_1' \left|\left| T^L(1) \right|\right| j_1 \right\rangle . \tag{A.90}$$

[6]The interested reader may find a derivation of this in [218].

Bibliography

[1] G. 't Hooft, "Symmetry Breaking through Bell-Jackiw Anomalies," Phys. Rev. Lett. **37**, 8–11 (1976).

[2] G. 't Hooft, "Computation of the quantum effects due to a four-dimensional pseudoparticle," Phys. Rev. D **14**, 3432–3450 (1976).

[3] R. Jackiw and C. Rebbi, "Vacuum Periodicity in a Yang-Mills Quantum Theory," Phys. Rev. Lett. **37**, 172–175 (1976).

[4] C. Callan, R. Dashen, and D. Gross, "The structure of the gauge theory vacuum," Physics Letters B **63**, 334 – 340 (1976).

[5] J. Schwinger, "The Theory of Quantized Fields. I," Phys. Rev. **82**, 914–927 (1951).

[6] M. Pospelov and A. Ritz, "Theta-Induced Electric Dipole Moment of the Neutron via QCD Sum Rules," Phys. Rev. Lett. **83**, 2526–2529 (1999).

[7] J. M. Pendlebury *et al.*, "Revised experimental upper limit on the electric dipole moment of the neutron," Phys. Rev. D **92**, 092003 (2015).

[8] D. R. Nelson, G. T. Fleming, and G. W. Kilcup, "Up Quark Mass in Lattice QCD with Three Light Dynamical Quarks and Implications for Strong CP Invariance," Phys. Rev. Lett. **90**, 021601 (2003).

[9] C. Amsler *et al.*, "Review of particle physics," Physics Letters B **667**, 1 – 6 (2008).

[10] R. D. Peccei and H. R. Quinn, "CP Conservation in the Presence of Pseudoparticles," Phys. Rev. Lett. **38**, 1440–1443 (1977).

[11] R. D. Peccei and H. R. Quinn, "Constraints imposed by CP conservation in the presence of pseudoparticles," Phys. Rev. D **16**, 1791–1797 (1977).

[12] S. Weinberg, "A New Light Boson?" Phys. Rev. Lett. **40**, 223–226 (1978).

[13] F. Wilczek, "Problem of Strong P and T Invariance in the Presence of Instantons," Phys. Rev. Lett. **40**, 279–282 (1978).

[14] F. A. Wilczek, "Asymptotic Freedom: From Paradox to Paradigm," (2004).

[15] T. W. Donnelly, S. J. Freedman, R. S. Lytel, R. D. Peccei, and M. Schwartz, "Do axions exist?" Phys. Rev. D **18**, 1607–1620 (1978).

[16] A. Zehnder, "Axion search in a monochromatic -transition: A new lower limit for the axion mass," Physics Letters B **104**, 494 – 498 (1981).

[17] M. Dine, W. Fischler, and M. Srednicki, "A simple solution to the strong CP problem with a harmless axion," Physics Letters B **104**, 199 – 202 (1981).

[18] A. R. Zhitnitsky, "On Possible Suppression of the Axion Hadron Interactions. (In Russian)," Sov. J. Nucl. Phys. **31**, 260 (1980).

[19] J. E. Kim, "Weak-Interaction Singlet and Strong CP Invariance," Phys. Rev. Lett. **43**, 103–107 (1979).

[20] M. Shifman, A. Vainshtein, and V. Zakharov, "Can confinement ensure natural CP invariance of strong interactions?" Nuclear Physics B **166**, 493 – 506 (1980).

[21] L. Di Luzio, F. Mescia, and E. Nardi, "Redefining the Axion Window," Phys. Rev. Lett. **118**, 031801 (2017).

[22] A. G. Dias, A. C. B. Machado, C. C. Nishi, A. Ringwald, and P. Vaudrevange, "The quest for an intermediate-scale accidental axion and further ALPs," Journal of High Energy Physics **2014**, 37 (2014).

[23] E. Ma, T. Ohata, and K. Tsumura, "Majoron as the QCD axion in a radiative seesaw model," Phys. Rev. D **96**, 075039 (2017).

[24] F. Wilczek, "Axions and Family Symmetry Breaking," Phys. Rev. Lett. **49**, 1549–1552 (1982).

[25] F. Arias-Aragón and L. Merlo, "The minimal flavour violating axion," Journal of High Energy Physics **2017**, 168 (2017).

[26] Y. Ema, K. Hamaguchi, T. Moroi, and K. Nakayama, "Flaxion: a minimal extension to solve puzzles in the standard model," Journal of High Energy Physics **2017**, 96 (2017).

[27] L. Calibbi, F. Goertz, D. Redigolo, R. Ziegler, and J. Zupan, "Minimal axion model from flavor," Phys. Rev. D **95**, 095009 (2017).

[28] H. P. Nilles and S. Raby, "Supersymmetry and the strong CP problem," Nuclear Physics B **198**, 102 – 112 (1982).

[29] M. B. Wise, H. Georgi, and S. L. Glashow, "SU(5) and the Invisible Axion," Phys. Rev. Lett. **47**, 402–404 (1981).

[30] E. Witten, "Some properties of O(32) superstrings," Phys. Lett. B **149**, 351 (1984).

[31] P. Svrcek and E. Witten, "Axions in string theory," Journal of High Energy Physics **2006**, 051 (2006).

[32] A. Arvanitaki, S. Dimopoulos, S. Dubovsky, N. Kaloper, and J. March-Russell, "String axiverse," Phys. Rev. D **81**, 123530 (2010).

[33] S. S. McGaugh, W. J. G. de Blok, J. M. Schombert, R. K. de Naray, and J. H. Kim, "The Rotation Velocity Attributable to Dark Matter at Intermediate Radii in Disk Galaxies," The Astrophysical Journal **659**, 149–161 (2007).

[34] J. Kapteyn, "First Attempt at a Theory of the Arrangement and Motion of the Sidereal System," The Astrophysical Journal **55**, 302 (1922).

[35] F. Zwicky, "The redshift of extragalactic nebulae," Helvetica Physica Acta **6**, 110 (1933).

[36] F. Zwicky, "On the Masses of Nebulae and of Clusters of Nebulae," The Astrophysical Journal **86**, 217 (1937).

[37] D. Clowe, M. Bradač, A. H. Gonzalez, M. Markevitch, S. W. Randall, C. Jones, and D. Zaritsky, "A Direct Empirical Proof of the Existence of Dark Matter," The Astrophysical Journal **648**, L109–L113 (2006).

[38] M. J. Jee, H. C. Ford, G. D. Illingworth, R. L. White, T. J. Broadhurst, D. A. Coe, G. R. Meurer, A. van der Wel, N. Benitez, J. P. Blakeslee, R. J. Bouwens, L. D. Bradley, R. Demarco, N. L. Homeier, A. R. Martel, and S. Mei, "Discovery of a Ringlike Dark Matter Structure in the Core of the Galaxy Cluster Cl 0024+17," The Astrophysical Journal **661**, 728–749 (2007).

[39] J. Preskill, M. B. Wise, and F. Wilczek, "Cosmology of the invisible axion," Physics Letters B **120**, 127 – 132 (1983).

[40] M. Dine and W. Fischler, "The not-so-harmless axion," Physics Letters B **120**, 137 – 141 (1983).

[41] L. Abbott and P. Sikivie, "A cosmological bound on the invisible axion," Physics Letters B **120**, 133 – 136 (1983).

[42] C. Collaboration, "New CAST limit on the axionphoton interaction," Nature Physics **13**, 584 (2017).

[43] E. F. Ribas *et al.*, "The IAXO Helioscope," Journal of Physics: Conference Series **650**, 012009 (2015).

[44] R. Ballou *et al.* (OSQAR Collaboration), "New exclusion limits on scalar and pseudoscalar axionlike particles from light shining through a wall," Phys. Rev. D **92**, 092002 (2015).

[45] R. Bradley, J. Clarke, D. Kinion, L. J. Rosenberg, K. van Bibber, S. Matsuki, M. Mück, and P. Sikivie, "Microwave cavity searches for dark-matter axions," Rev. Mod. Phys. **75**, 777–817 (2003).

[46] J. Hoskins, J. Hwang, C. Martin, P. Sikivie, N. S. Sullivan, D. B. Tanner, M. Hotz, L. J. Rosenberg, G. Rybka, A. Wagner, S. J. Asztalos, G. Carosi, C. Hagmann, D. Kinion, K. van Bibber, R. Bradley, and J. Clarke, "Search for nonvirialized axionic dark matter," Phys. Rev. D **84**, 121302 (2011).

[47] E. G. Adelberger, B. R. Heckel, S. Hoedl, C. D. Hoyle, D. J. Kapner, and A. Upadhye, "Particle-Physics Implications of a Recent Test of the Gravitational Inverse-Square Law," Phys. Rev. Lett. **98**, 131104 (2007).

[48] M. Bulatowicz, R. Griffith, M. Larsen, J. Mirijanian, C. B. Fu, E. Smith, W. M. Snow, H. Yan, and T. G. Walker, "Laboratory Search for a Long-Range T-Odd, P-Odd Interaction from Axionlike Particles Using Dual-Species Nuclear Magnetic Resonance with Polarized ^{129}Xe and ^{131}Xe Gas," Phys. Rev. Lett. **111**, 102001 (2013).

[49] K. Tullney *et al.*, "Constraints on Spin-Dependent Short-Range Interaction between Nucleons," Phys. Rev. Lett. **111**, 100801 (2013).

[50] A. N. Youdin, D. Krause, Jr., K. Jagannathan, L. R. Hunter, and S. K. Lamoreaux, "Limits on Spin-Mass Couplings within the Axion Window," Phys. Rev. Lett. **77**, 2170–2173 (1996).

[51] B. J. Venema, P. K. Majumder, S. K. Lamoreaux, B. R. Heckel, and E. N. Fortson, "Search for a coupling of the Earth's gravitational field to nuclear spins in atomic mercury," Phys. Rev. Lett. **68**, 135–138 (1992).

[52] D. J. Wineland, J. J. Bollinger, D. J. Heinzen, W. M. Itano, and M. G. Raizen, "Search for anomalous spin-dependent forces using stored-ion spectroscopy," Phys. Rev. Lett. **67**, 1735–1738 (1991).

[53] W.-T. Ni, S.-s. Pan, H.-C. Yeh, L.-S. Hou, and J. Wan, "Search for an Axionlike Spin Coupling Using a Paramagnetic Salt with a dc SQUID," Phys. Rev. Lett. **82**, 2439–2442 (1999).

[54] W. A. Terrano, E. G. Adelberger, J. G. Lee, and B. R. Heckel, "Short-Range, Spin-Dependent Interactions of Electrons: A Probe for Exotic Pseudo-Goldstone Bosons," Phys. Rev. Lett. **115**, 201801 (2015).

[55] G. Vasilakis, J. M. Brown, T. W. Kornack, and M. V. Romalis, "Limits on new long range nuclear spin-dependent forces set with a K$-^3$He comagnetometer," Phys. Rev. Lett. **103**, 261801 (2009).

[56] P. W. Graham and S. Rajendran, "New observables for direct detection of axion dark matter," Phys. Rev. D **88**, 035023 (2013).

[57] A. Arvanitaki and A. A. Geraci, "Resonantly detecting axion-mediated forces with nuclear magnetic resonance," Phys. Rev. Lett. **113**, 161801 (2014).

[58] D. Budker, P. W. Graham, M. Ledbetter, S. Rajendran, and A. O. Sushkov, "Proposal for a Cosmic Axion Spin Precession Experiment (CASPEr)," Phys. Rev. X **4**, 021030 (2014).

[59] J. E. Moody and F. Wilczek, "New macroscopic forces?" Phys. Rev. D **30**, 130–138 (1984).

[60] M. Tanabashi *et al.* (Particle Data Group), "Review of particle physics," Phys. Rev. D **98**, 030001 (2018).

[61] M. Srednicki, "Axion couplings to matter: (I). CP-conserving parts," Nuclear Physics B **260**, 689 – 700 (1985).

[62] D. B. Kaplan, "Opening the axion window," Nuclear Physics B **260**, 215 – 226 (1985).

[63] G. G. di Cortona, E. Hardy, J. P. Vega, and G. Villadoro, "The QCD axion, precisely," Journal of High Energy Physics **2016**, 34 (2016).

[64] P. Fayet, "New interactions and the standard models," Classical and Quantum Gravity **13**, A19 (1996).

[65] B. A. Dobrescu and I. Mocioiu, "Spin-dependent macroscopic forces from new particle exchange," Journal of High Energy Physics **2006**, 005 (2006).

[66] David R. Lide (Editor-in-chief), *CRC Handbook of Chemistry and Physics* (CRC Press, 1994).

[67] C. B. Alcock, V. P. Itkin, and M. K. Horrigan, "Vapour pressure equations for the metallic elements: 298 − 2500 K," Canadian Metallurgical Quarterly **23**, 309–313 (1984).

[68] M. E. Wagshul and T. E. Chupp, "Laser optical pumping of high-density Rb in polarized ^{3}He targets," Phys. Rev. A **49**, 3854–3869 (1994).

[69] B. Chann, E. Babcock, L. W. Anderson, and T. G. Walker, "Measurements of ^{3}He spin-exchange rates," Phys. Rev. A **66**, 032703 (2002).

[70] D. K. Walter, W. M. Griffith, and W. Happer, "Energy transport in high-density spin-exchange optical pumping cells," Phys. Rev. Lett. **86**, 3264–3267 (2001).

[71] E. Arimondo, M. Inguscio, and P. Violino, "Experimental determinations of the hyperfine structure in the alkali atoms," Rev. Mod. Phys. **49**, 31–75 (1977).

[72] J. J. Sakurai, *Modern quantum mechanics*, edited by S. F. Tuan (Addison-Wesley Publishing Company, 1994).

[73] S. Appelt, A. B.-A. Baranga, C. J. Erickson, M. V. Romalis, A. R. Young, and W. Happer, "Theory of spin-exchange optical pumping of ^{3}He and ^{129}Xe," Phys. Rev. A **58**, 1412–1439 (1998).

[74] U. Fano, "Description of states in quantum mechanics by density matrix and operator techniques," Rev. Mod. Phys. **29**, 74–93 (1957).

[75] W. Happer, Y.-Y. Jau, and T. Walker, *Optically Pumped Atoms* (Wiley-VCH Verlag GmbH and Co. KGaA, 2010).

[76] S. Kadlecek, L. W. Anderson, and T. G. Walker, "Field Dependence of Spin Relaxation in a Dense Rb Vapor," Phys. Rev. Lett. **80**, 5512–5515 (1998).

[77] S. Kadlecek, L. W. Anderson, C. J. Erickson, and T. G. Walker, "Spin relaxation in alkali-metal $^1\Sigma_g^+$ dimers," Phys. Rev. A **64**, 052717 (2001).

[78] J. P. Wittke and R. H. Dicke, "Redetermination of the hyperfine splitting in the ground state of atomic hydrogen," Phys. Rev. **103**, 620–631 (1956).

[79] E. M. Purcell and G. B. Field, "Influence of collisions upon population of hyperfine states in hydrogen." Astrophysical Journal **124**, 542 (1956).

[80] W. Happer, "Optical pumping," Rev. Mod. Phys. **44**, 169–249 (1972).

[81] Grossetête, Françoise, "Relaxation par collisions d'échange de spin," J. Phys. France **25**, 383–396 (1964).

[82] Grossetête, F., "Relaxation par collisions d'échange de spins. (ii)," J. Phys. France **29**, 456–466 (1968).

[83] L. C. Balling, R. J. Hanson, and F. M. Pipkin, "Frequency shifts in spin-exchange optical pumping experiments," Phys. Rev. **133**, A607–A626 (1964).

[84] L. C. Balling and F. M. Pipkin, "Spin exchange in a cesium-electron system," Phys. Rev. **136**, A46–A53 (1964).

[85] N. W. Ressler, R. H. Sands, and T. E. Stark, "Measurement of spin-exchange cross sections for Cs^{133}, Rb^{87}, Rb^{85}, K^{39}, and Na^{23}," Phys. Rev. **184**, 102–118 (1969).

[86] A. Moretti and F. Strumia, "Hyperfine optical pumping of sodium vapors," Phys. Rev. A **3**, 349–354 (1971).

[87] N. Ioli, P. Violino, and M. Meucci, "A new technique for measuring the spin-exchange cross-section between different atoms," Zeitschrift für Physik A Atoms and Nuclei **285**, 107–110 (1978).

[88] S. M. Jarrett, "Spin-exchange cross section for Rb^{85}-Rb^{87} collisions," Phys. Rev. **133**, A111–A117 (1964).

[89] H. M. Gibbs and R. J. Hull, "Spin-exchange cross sections for Rb^{87}-Rb^{87} and Rb^{87}-Cs^{133} collisions," Phys. Rev. **153**, 132–151 (1967).

[90] K. Ernst and F. Strumia, "High efficiency hyperfine pumping of cesium vapor," Phys. Rev. **170**, 48–49 (1968).

[91] E. Fermi, "Über die magnetischen momente der atomkerne," Zeitschrift für Physik **60**, 320–333 (1930).

[92] R. M. Herman, "Theory of spin exchange between optically pumped rubidium and foreign gas nuclei," Phys. Rev. **137**, A1062–A1065 (1965).

[93] D. K. Walter, W. Happer, and T. G. Walker, "Estimates of the relative magnitudes of the isotropic and anisotropic magnetic-dipole hyperfine interactions in alkali-metal–noble-gas systems," Phys. Rev. A **58**, 3642–3653 (1998).

[94] A. Ben-Amar Baranga, S. Appelt, M. V. Romalis, C. J. Erickson, A. R. Young, G. D. Cates, and W. Happer, "Polarization of ^{3}He by Spin Exchange with Optically Pumped Rb and K Vapors," Phys. Rev. Lett. **80**, 2801–2804 (1998).

[95] R. K. Ghosh and M. V. Romalis, "Measurement of spin-exchange and relaxation parameters for polarizing ^{21}Ne with K and Rb," Phys. Rev. A **81**, 043415 (2010).

[96] T. G. Walker, I. A. Nelson, and S. Kadlecek, "Method for deducing anisotropic spin-exchange rates," Phys. Rev. A **81**, 032709 (2010).

[97] E. Babcock, I. Nelson, S. Kadlecek, B. Driehuys, L. W. Anderson, F. W. Hersman, and T. G. Walker, "Hybrid Spin-Exchange Optical Pumping of ^{3}He," Phys. Rev. Lett. **91**, 123003 (2003).

[98] E. D. Babcock, *Spin-exchange optical pumping with alkali-metal vapours*, Ph.D. thesis, University of Wisconsin-Madison (2005).

[99] J. T. Singh, P. A. M. Dolph, W. A. Tobias, T. D. Averett, A. Kelleher, K. E. Mooney, V. V. Nelyubin, Y. Wang, Y. Zheng, and G. D. Cates, "Development of high-performance alkali-hybrid polarized ^{3}He targets for electron scattering," Phys. Rev. C **91**, 055205 (2015).

[100] T. V. Tscherbul, P. Zhang, H. R. Sadeghpour, and A. Dalgarno, "Anisotropic hyperfine interactions limit the efficiency of spin-exchange optical pumping of ^{3}He nuclei," Phys. Rev. Lett. **107**, 023204 (2011).

[101] E. Babcock, I. A. Nelson, S. Kadlecek, and T. G. Walker, "^{3}He polarization-dependent EPR frequency shifts of alkali-metal–^{3}He pairs," Phys. Rev. A **71**, 013414 (2005).

[102] R. E. Stoner and R. L. Walsworth, "Measurement of the ^{21}Ne zeeman frequency shift due to Rb−^{21}Ne collisions," Phys. Rev. A **66**, 032704 (2002).

[103] M. V. Romalis and G. D. Cates, "Accurate ^{3}He polarimetry using the rb zeeman frequency shift due to the Rb−^{3}He spin-exchange collisions," Phys. Rev. A **58**, 3004–3011 (1998).

[104] R. A. Bernheim, "Spin Relaxation in Optical Pumping," The Journal of Chemical Physics **36**, 135–140 (1962).

[105] T. G. Walker, J. H. Thywissen, and W. Happer, "Spin-rotation interaction of alkali-metal–He-atom pairs," Phys. Rev. A **56**, 2090–2094 (1997).

[106] W. Franzen, "Spin Relaxation of Optically Aligned Rubidium Vapor," Phys. Rev. **115**, 850–856 (1959).

[107] M. A. Bouchiat, J. Brossel, and L. C. Pottier, "Evidence for Rb−Rare−Gas Molecules from the Relaxation of Polarized Rb Atoms in a Rare Gas. Experimental Results," The Journal of Chemical Physics **56**, 3703–3714 (1972).

[108] R. R. Freeman, E. M. Mattison, D. E. Pritchard, and D. Kleppner, "The spinrotation interaction in the van der Waals molecule KAr," The Journal of Chemical Physics **64**, 1194–1203 (1976).

[109] W. E. Cooke and R. R. Freeman, "Molecular-beam magnetic-resonance measurement of the spin-rotational interaction in RbKr," Phys. Rev. A **16**, 2211–2215 (1977).

[110] Z. Wu, T. G. Walker, and W. Happer, "Spin-Rotation Interaction of Noble-Gas Alkali-Metal Atom Pairs," Phys. Rev. Lett. **54**, 1921–1924 (1985).

[111] F. Herman, C. D. Kuglin, K. F. Cuff, and R. L. Kortum, "Relativistic Corrections to the Band Structure of Tetrahedrally Bonded Semiconductors," Phys. Rev. Lett. **11**, 541–545 (1963).

[112] A. T. Ramsey and L. W. Anderson, "Spin relaxation in an optically oriented sodium vapor," II Nuovo Cimento **32**, 1151–1157 (1964).

[113] H. Soboll, "Spin exchange between optically oriented sodium and foreign gas nuclei," Physics Letters A **41**, 373 – 374 (1972).

[114] N. D. Bhaskar, J. Pietras, J. Camparo, W. Happer, and J. Liran, "Spin Destruction in Collisions between Cesium Atoms," Phys. Rev. Lett. **44**, 930–933 (1980).

[115] J. H. Van Vleck, "The coupling of angular momentum vectors in molecules," Rev. Mod. Phys. **23**, 213–227 (1951).

[116] T. G. Walker and W. Happer, "Spin-exchange optical pumping of noble-gas nuclei," Rev. Mod. Phys. **69**, 629–642 (1997).

[117] J. Liran, J. Pietras, J. Camparo, and W. Happer, "Optical pumping of cesium atoms with second resonance light," Optics Communications **31**, 169 – 173 (1979).

[118] C. J. Erickson, D. Levron, W. Happer, S. Kadlecek, B. Chann, L. W. Anderson, and T. G. Walker, "Spin Relaxation Resonances due to the Spin-Axis Interaction in Dense Rubidium and Cesium Vapor," Phys. Rev. Lett. **85**, 4237–4240 (2000).

[119] M. Tinkham and M. W. P. Strandberg, "Theory of the fine structure of the molecular oxygen ground state," Phys. Rev. **97**, 937–951 (1955).

[120] J. M. Daniels and P. B. Dorain, "Electron Paramagnetic Resonance of Sulfur Monoxide," The Journal of Chemical Physics **45**, 26–34 (1966).

[121] T. R. Gentile, P. J. Nacher, B. Saam, and T. G. Walker, "Optically polarized ^{3}He," Rev. Mod. Phys. **89**, 045004 (2017).

[122] D. K. Walter, W. M. Griffith, and W. Happer, "Magnetic Slowing Down of Spin Relaxation due to Binary Collisions of Alkali-Metal Atoms with Buffer-Gas Atoms," Phys. Rev. Lett. **88**, 093004 (2002).

[123] S. Kadlecek, T. Walker, D. K. Walter, C. Erickson, and W. Happer, "Spin-axis relaxation in spin-exchange collisions of alkali-metal atoms," Phys. Rev. A **63**, 052717 (2001).

[124] R. J. Knize, "Spin destruction in rubidium-rubidium and potassium-potassium collisions," Phys. Rev. A **40**, 6219–6222 (1989).

[125] L. W. Anderson, F. M. Pipkin, and J. C. Baird, "N^{14}-N^{15} Hyperfine Anomaly," Phys. Rev. **116**, 87–98 (1959).

[126] M. I. Darby, "Tables of the Brillouin function and of the related function for the spontaneous magnetization," British Journal of Applied Physics **18**, 1415–1417 (1967).

[127] J. C. Allred, R. N. Lyman, T. W. Kornack, and M. V. Romalis, "High-Sensitivity Atomic Magnetometer Unaffected by Spin-Exchange Relaxation," Phys. Rev. Lett. **89**, 130801 (2002).

[128] W. Happer and H. Tang, "Spin-exchange shift and narrowing of magnetic resonance lines in optically pumped alkali vapors," Phys. Rev. Lett. **31**, 273–276 (1973).

[129] W. Happer and A. C. Tam, "Effect of rapid spin exchange on the magnetic-resonance spectrum of alkali vapors," Phys. Rev. A **16**, 1877–1891 (1977).

[130] W. Happer and B. S. Mathur, "Effective Operator Formalism in Optical Pumping," Phys. Rev. **163**, 12–25 (1967).

[131] B. Fried and S. Conte, *The Plasma Dispersion Function* (Academic Press Inc., New York, 1961).

[132] E. U. Condon and G. H. Shortley, *The Theory of Atomic Spectra* (Cambridge University Press, 1957).

[133] E. W. Foster, "The measurement of oscillator strengths in atomic spectra," Reports on Progress in Physics **27**, 469 (1964).

[134] Larson, B. et. al, "Asymmetries in elastic scattering of 100 MeV π^+ from a polarized ^{3}He target," Phys. Rev. Lett. **67**, 3356–3359 (1991).

[135] Abe, K. et. al (E154 Collaboration), "Precision determination of the neutron spin structure function g_1^n," Phys. Rev. Lett. **79**, 26–30 (1997).

[136] T. Katabuchi, S. Buscemi, J. M. Cesaratto, T. B. Clegg, T. V. Daniels, M. Fassler, R. B. Neufeld, and S. Kadlecek, "Spin-exchange optically pumped polarized ^{3}He target for low-energy charged particle scattering experiments," Review of Scientific Instruments **76**, 033503 (2005).

[137] A. Ioffe, E. Babcock, and T. Gutberlet, "JCNS workshop on modern trends in production and applications of polarized ^{3}He," Journal of Physics: Conference Series **294**, 011001 (2011).

[138] H. E. Möller *et al.*, "MRI of the lungs using hyperpolarized noble gases," Magnetic Resonance in Medicine **47**, 1029–1051 (2002).

[139] J. C. Leawoods, D. A. Yablonskiy, B. Saam, D. S. Gierada, and M. S. Conradi, "Hyperpolarized ^{3}He gas production and MR imaging of the lung," Concepts in Magnetic Resonance **13**, 277–293 (2001).

[140] M. Smiciklas, J. M. Brown, L. W. Cheuk, S. J. Smullin, and M. V. Romalis, "New test of local lorentz invariance using a ^{21}Ne−Rb−K comagnetometer," Phys. Rev. Lett. **107**, 171604 (2011).

[141] B. Lancor and T. G. Walker, "Effects of nitrogen quenching gas on spin-exchange optical pumping of ^{3}He," Phys. Rev. A **82**, 043417 (2010).

[142] Y. F. Verolanen and A. Y. Nikolaich, "Radiative lifetimes of excited states of atoms," Sov. Phys. Usp. **25**, 431 (1982).

[143] L. Krause, "Sensitized fluorescence and quenching," in *Advances in Chemical Physics* (John Wiley and Sons, Ltd, 2007) pp. 267–316.

[144] D. A. McGillis and L. Krause, "Inelastic collisions between excited alkali atoms and molecules. i. sensitized fluorescence and quenching in Cs-N_2 and Cs-H_2 systems," Phys. Rev. **153**, 44–50 (1967).

[145] J. A. Bellisio, P. Davidovits, and P. J. Kindlmann, "Quenching of rubidium resonance radiation by nitrogen and the noble gases," The Journal of Chemical Physics **48**, 2376–2377 (1968).

[146] E. S. Hrycyshyn and L. Krause, "Inelastic collisions between excited alkali atoms and molecules. vii. sensitized fluorescence and quenching in mixtures of rubidium with H_2, HD, D_2, N_2, CH_4, CD_4, C_2H_4, and C_2H_6," Canadian Journal of Physics **48**, 2761–2768 (1970).

[147] J. N. Dodd, E. Enemark, and A. Gallagher, "Quenching of cesium resonance radiation by helium," The Journal of Chemical Physics **50**, 4838–4842 (1969).

[148] A. Sieradzan and F. A. Franz, "Quenching, depolarization, and transfer of spin polarization in Rb-N_2 collisions," Phys. Rev. A **25**, 2985–2995 (1982).

[149] M. V. Romalis, "Hybrid Optical Pumping of Optically Dense Alkali-Metal Vapor without Quenching Gas," Phys. Rev. Lett. **105**, 243001 (2010).

[150] W. C. Chen, T. R. Gentile, T. G. Walker, and E. Babcock, "Spin-exchange optical pumping of ^{3}He with Rb-K mixtures and pure K," Phys. Rev. A **75**, 013416 (2007).

[151] R. M. Corless, G. H. Gonnet, D. E. G. Hare, D. J. Jeffrey, and D. E. Knuth, "On the Lambert W function," Advances in Computational Mathematics **5**, 329–359 (1996).

[152] J. M. Brown, *A New Limit on Lorentz- and CPT-Violating Neutron Spin Interactions Using a Potassium-Helium Comagnetometer*, Ph.D. thesis, Princeton University (2011).

[153] G. D. Cates, S. R. Schaefer, and W. Happer, "Relaxation of spins due to field inhomogeneities in gaseous samples at low magnetic fields and low pressures," Phys. Rev. A **37**, 2877–2885 (1988).

[154] L. D. Schearer and G. K. Walters, "Nuclear Spin-Lattice Relaxation in the Presence of Magnetic-Field Gradients," Phys. Rev. **139**, A1398–A1402 (1965).

[155] R. L. Gamblin and T. R. Carver, "Polarization and Relaxation Processes in He^3 Gas," Phys. Rev. **138**, A946–A960 (1965).

[156] S. Gozzini, G. Nienhuis, E. Mariotti, G. Paffuti, C. Gabbanini, and L. Moi, "Wall effects on light-induced drift," Optics Communications **88**, 341 – 346 (1992).

[157] H. G. C. Werij, J. E. M. Haverkort, and J. P. Woerdman, "Study of the optical piston," Phys. Rev. A **33**, 3270–3281 (1986).

[158] S. Grafström and D. Suter, "Interaction of spin-polarized atoms with a surface studied by optical-reflection spectroscopy," Phys. Rev. A **54**, 2169–2179 (1996).

[159] M. A. Bouchiat and J. Brossel, "Relaxation of Optically Pumped Rb Atoms on Paraffin-Coated Walls," Phys. Rev. **147**, 41–54 (1966).

[160] S. J. Seltzer and M. V. Romalis, "High-temperature alkali vapor cells with antirelaxation surface coatings," Journal of Applied Physics **106**, 114905 (2009).

[161] M. Aymar, M. Bouchiat, and J. Brossel, "Étude expérimentale de la relaxation du rubidium en présence d'hélium," J. Phys. France **30**, 619–629 (1969).

[162] F. A. Franz and C. Volk, "Electronic spin relaxation of the $4^2S_{\frac{1}{2}}$ state of K induced by K-He and K-Ne collisions," Phys. Rev. A **26**, 85–92 (1982).

[163] J. Vanier, J.-F. Simard, and J.-S. Boulanger, "Relaxation and frequency shifts in the ground state of Rb^{85}," Phys. Rev. A **9**, 1031–1040 (1974).

[164] K. Ishikawa and T. Yabuzaki, "Diffusion coefficient and sublevel coherence of Rb atoms in N_2 buffer gas," Phys. Rev. A **62**, 065401 (2000).

[165] W. A. Fitzsimmons, L. L. Tankersley, and G. K. Walters, "Nature of Surface-Induced Nuclear-Spin Relaxation of Gaseous He^3," Phys. Rev. **179**, 156–165 (1969).

[166] R. Jacob, B. Driehuys, and B. Saam, "Fundamental mechanisms of 3He relaxation on glass," Chemical Physics Letters **370**, 261 – 267 (2003).

[167] E. Babcock, B. Chann, T. G. Walker, W. C. Chen, and T. R. Gentile, "Limits to the Polarization for Spin-Exchange Optical Pumping of ^{3}He," Phys. Rev. Lett. **96**, 083003 (2006).

[168] Q. Ye, T. Gentile, J. Anderson, C. Broholm, W. Chen, Z. DeLand, R. Erwin, C. Fu, J. Fuller, A. Kirchhoff, J. Rodriguez-Rivera, V. Thampy, T. Walker, and S. Watson, "Wide Angle Polarization Analysis with Neutron Spin Filters," Physics Procedia **42**, 206 – 212 (2013).

[169] Q. Ye, G. Laskaris, W. Chen, H. Gao, W. Zheng, X. Zong, T. Averett, G. D. Cates, and W. A. Tobias, "A high-pressure polarized 3He gas target for nuclear-physics experiments using a polarized photon beam," The European Physical Journal A **44**, 55–61 (2010).

[170] S. Parnell, E. Babcock, K. Nnighoff, M. Skoda, S. Boag, S. Masalovich, W. Chen, R. Georgii, J. Wild, and C. Frost, "Study of spin-exchange optically pumped 3he cells with high polarisation and long lifetimes," Nuclear Instruments and Methods in Physics Research Section A: Accelerators, Spectrometers, Detectors and Associated Equipment **598**, 774 – 778 (2009).

[171] R. E. Jacob, S. W. Morgan, B. Saam, and J. C. Leawoods, "Wall Relaxation of ^{3}He in Spin-Exchange Cells," Phys. Rev. Lett. **87**, 143004 (2001).

[172] J. S. Teter, *Wall Relaxation Studies of Hyperpolarized ^3He*, Ph.D. thesis, University of Utah (2005).

[173] N. R. Newbury, A. S. Barton, G. D. Cates, W. Happer, and H. Middleton, "Gaseous ^{3}–^{3}He magnetic dipolar spin relaxation," Phys. Rev. A **48**, 4411–4420 (1993).

[174] H. C. Torrey, "Chemical Shift and Relaxation of Xe^{129} in Xenon Gas," Phys. Rev. **130**, 2306–2312 (1963).

[175] E. R. Hunt and H. Y. Carr, "Nuclear Magnetic Resonance of Xe^{129} in Natural Xenon," Phys. Rev. **130**, 2302–2305 (1963).

[176] D. Brinkmann, E. Brown, and H. Staub, "Kernresonanz im gasförmigen Xenon," Helvetica Physica Acta **35**, 431.

[177] T. W. Kornack, *A test of CPT and Lorentz symmetry using a potassium-helium-3 co-magnetometer*, Ph.D. thesis, Princeton University (2005).

[178] G. Vasilakis, *Precision measurements of spin interactions with high density atomic vapors*, Ph.D. thesis, Princeton University (2011).

[179] T. W. Kornack and M. V. Romalis, "Dynamics of Two Overlapping Spin Ensembles Interacting by Spin Exchange," Phys. Rev. Lett. **89**, 253002 (2002).

[180] T. W. Kominis, I. K.and Kornack, J. C. Allred, and M. V. Romalis, "A subfemtotesla multichannel atomic magnetometer," Nature **422**, 596 (2003).

[181] D. Bear, R. E. Stoner, R. L. Walsworth, V. A. Kostelecký, and C. D. Lane, "Limit on Lorentz and CPT Violation of the Neutron Using a Two-Species Noble-Gas Maser," Phys. Rev. Lett. **85**, 5038–5041 (2000).

[182] T. E. Chupp, R. J. Hoare, R. A. Loveman, E. R. Oteiza, J. M. Richardson, M. E. Wagshul, and A. K. Thompson, "Results of a new test of local Lorentz invariance: A search for mass anisotropy in ^{21}Ne," Phys. Rev. Lett. **63**, 1541–1545 (1989).

[183] C. Gemmel, W. Heil, S. Karpuk, K. Lenz, Y. Sobolev, K. Tullney, M. Burghoff, W. Kilian, S. Knappe-Grüneberg, W. Müller, A. Schnabel, F. Seifert, L. Trahms, and U. Schmidt, "Limit on Lorentz and CPT violation of the bound neutron using a free precession ^{3}He/^{129}Xe comagnetometer," Phys. Rev. D **82**, 111901 (2010).

[184] M. Auzinsh, D. Budker, D. F. Kimball, S. M. Rochester, J. E. Stalnaker, A. O. Sushkov, and V. V. Yashchuk, "Can a Quantum Nondemolition Measurement Improve the Sensitivity of an Atomic Magnetometer?" Phys. Rev. Lett. **93**, 173002 (2004).

[185] I. M. Savukov, S. J. Seltzer, M. V. Romalis, and K. L. Sauer, "Tunable Atomic Magnetometer for Detection of Radio-Frequency Magnetic Fields," Phys. Rev. Lett. **95**, 063004 (2005).

[186] M. P. Ledbetter, I. M. Savukov, V. M. Acosta, D. Budker, and M. V. Romalis, "Spin-exchange-relaxation-free magnetometry with Cs vapor," Phys. Rev. A **77**, 033408 (2008).

[187] J. Lee, A. Almasi, and M. Romalis, "Improved limits on spin-mass interactions," Phys. Rev. Lett. **120**, 161801 (2018).

[188] L. Laux and G. Schulz, "A sodium-resistant glass cell by coating with CaF2," Journal of Physics E: Scientific Instruments **13**, 823–824 (1980).

[189] Schmiedeskamp, J., Heil, W., Otten, E. W., Kremer, R. K., Simon, A., and Zimmer, J., "Paramagnetic relaxation of spin polarized 3He at bare glass surfaces - Part I," Eur. Phys. J. D **38**, 427–438 (2006).

[190] E. Hearn, *Mechanics of Materials 1*, third edition ed. (Butterworth-Heinemann, 1997).

[191] N. Dural and M. V. Romalis, "Gallium phosphide as a new material for anodically bonded atomic sensors," APL Materials **2**, 086101 (2014).

[192] A. W. Rücker F.R.S., "VII. On the magnetic shielding of concentric spherical shells," The London, Edinburgh, and Dublin Philosophical Magazine and Journal of Science **37**, 95–130 (1894).

[193] J. Nenonen, J. Montonen, and T. Katila, "Thermal noise in biomagnetic measurements," Review of Scientific Instruments **67**, 2397–2405 (1996).

[194] T. W. Kornack, S. J. Smullin, S.-K. Lee, and M. V. Romalis, "A low-noise ferrite magnetic shield," Applied Physics Letters **90**, 223501 (2007).

[195] E. Paperno, S. Peliwal, M. V. Romalis, and A. Plotkin, "Optimum shell separation for closed axial cylindrical magnetic shields," Journal of Applied Physics **97**, 10Q104 (2005).

[196] E. Paperno, M. V. Romalis, and Y. Noam, "Optimization of five-shell axial magnetic shields having openings in the end-caps," IEEE Transactions on Magnetics **40**, 2170–2172 (2004).

[197] T. J. Sumner, J. M. Pendlebury, and K. F. Smith, "Convectional magnetic shielding," Journal of Physics D: Applied Physics **20**, 1095–1101 (1987).

[198] A. Mager, "Magnetic shields," IEEE Transactions on Magnetics **6**, 67–75 (1970).

[199] A. A. Tovar and L. W. Casperson, "Generalized beam matrices: Gaussian beam propagation in misaligned complex optical systems," J. Opt. Soc. Am. A **12**, 1522–1533 (1995).

[200] C. Fiebig, V. Z. Tronciu, M. Lichtner, K. Paschke, and H. Wenzel, "Experimental and numerical study of distributed-bragg-reflector tapered lasers," Applied Physics B **99**, 209–214 (2010).

[201] L. Goldberg, M. R. Surette, and D. Mehuys, "Filament formation in a tapered gaalas optical amplifier," Applied Physics Letters **62**, 2304–2306 (1993).

[202] J. C. B. Kangara, A. J. Hachtel, M. C. Gillette, J. T. Barkeloo, E. R. Clements, S. Bali, B. E. Unks, N. A. Proite, D. D. Yavuz, P. J. Martin, J. J. Thorn, and D. A. Steck, "Design and construction of cost-effective tapered amplifier systems for laser cooling and trapping experiments," American Journal of Physics **82**, 805–817 (2014).

[203] Y. Xiong, S. Murphy, J. L. Carlsten, and K. S. Repasky, "Design and characteristics of a tapered amplifier diode system by seeding with continuous-wave and mode-locked external cavity diode laser," Optical Engineering **45**, 124205 (2006).

[204] K. A. Kluttz, T. D. Averett, and B. A. Wolin, "Pressure broadening and frequency shift of the D_1 and D_2 lines of Rb and K in the presence of ^{3}He and N_2," Phys. Rev. A **87**, 032516 (2013).

[205] E. L. Koschmieder, *Bénard Cells and Taylor Vortices* (Cambridge University Press, 1993).

[206] J. M. Brown, S. J. Smullin, T. W. Kornack, and M. V. Romalis, "New Limit on Lorentz- and CPT-Violating Neutron Spin Interactions," Phys. Rev. Lett. **105**, 151604 (2010).

[207] G. Meier and H. Kriegs, "A high pressure cell for dynamic light scattering up to 2kbars with conservation of plane of polarization," Review of Scientific Instruments **79**, 013102 (2008).

[208] S. Brakhane, W. Alt, D. Meschede, C. Robens, G. Moon, and A. Alberti, "Note: Ultra-low birefringence dodecagonal vacuum glass cell," Review of Scientific Instruments **86**, 126108 (2015).

[209] S. Brakhane and A. Alberti, *Technical note: Stress-Induced Birefringence in Vacuum Systems*, Tech. Rep. (2017).

[210] W. B. Dress, P. D. Miller, J. M. Pendlebury, P. Perrin, and N. F. Ramsey, "Search for an electric dipole moment of the neutron," Phys. Rev. D **15**, 9–21 (1977).

[211] J. R. Taylor, *An Introduction to Error Analysis: The Study of Uncertainties in Physical Measurements*, 2nd ed. (University Science Books, 1997).

[212] J. L. Friar, B. F. Gibson, G. L. Payne, A. M. Bernstein, and T. E. Chupp, "Neutron polarization in polarized ^{3}He targets," Phys. Rev. C **42**, 2310–2314 (1990).

[213] J. J. Ethier and W. Melnitchouk, "Comparative study of nuclear effects in polarized electron scattering from ^{3}He," Phys. Rev. C **88**, 054001 (2013).

[214] G. Raffelt, "Limits on a CP-violating scalar axion-nucleon interaction," Phys. Rev. D **86**, 015001 (2012).

[215] N. Crescini, C. Braggio, G. Carugno, P. Falferi, A. Ortolan, and G. Ruoso, "Improved constraints on monopoledipole interaction mediated by pseudo-scalar bosons," Physics Letters B **773**, 677 – 680 (2017).

[216] B. R. Heckel, E. G. Adelberger, C. E. Cramer, T. S. Cook, S. Schlamminger, and U. Schmidt, "Preferred-frame and CP-violation tests with polarized electrons," Phys. Rev. D **78**, 092006 (2008).

[217] I. M. Savukov and M. V. Romalis, "Effects of spin-exchange collisions in a high-density alkali-metal vapor in low magnetic fields," Phys. Rev. A **71**, 023405 (2005).

[218] M. E. Rose, *Elementary Theory of Angular Momentum* (John Wiley and Sons, Inc., 1957).

[219] G. Racah, "Theory of Complex Spectra. I," Phys. Rev. **61**, 186–197 (1942).

[220] G. Racah, "Theory of Complex Spectra. II," Phys. Rev. **62**, 438–462 (1942).

[221] G. Racah, "Theory of Complex Spectra. III," Phys. Rev. **63**, 367–382 (1943).

[222] L. C. Biedenharn, "An Identity Satisfied by the Racah Coefficients," Journal of Mathematics and Physics **31**, 287–293 (1952).